

PREPARATION AND CHARACTERISATION OF NANOSTRUCTURED BULK Bi_2Te_3 THERMOELECTRIC MATERIALS USING ULTRASOUND MILLING

A thesis submitted to Cardiff University in the candidature for
the degree of

Doctor of Philosophy

by

Lourdes Márquez García

Institute of Energy
School of Engineering
Cardiff University

April 2016



SUMMARY

Thermoelectric materials have been intensively investigated during the last years for energy harvesting applications. The main drawback of this technology is the low efficiency of the current materials. Significant advances in this respect have been recently achieved by nanostructuring, to mainly reduce the thermal conductivity. In this approach a bulk sample is milled into a nanostructured powder that is then compacted to form a nanobulk sample.

The main objective of this thesis is to explore and introduce a new technique, ultrasound milling, based on the crushing of bulk samples by means of ultrasound effects taking place in a liquid medium, for the preparation of nanostructured bulk materials. Bismuth telluride alloys are the industrial standard in thermoelectrics and has been chosen as the material to perform this investigation.

The most suitable conditions for the preparation of the nanostructured powders by the ultrasound milling technique have been identified. The optimised powders were used to prepare compacted nanobulk samples. The thermoelectric properties of these samples were finally characterised at room temperature and their performance related to their microstructure.

Extraordinarily low thermal conductivity was obtained for both n- and p-type samples prepared (0.5 and 0.35 W/Km respectively), which are within the lowest reported values for any thermoelectric alloy. This reduction was accompanied with a significant decrease in electrical conductivity which led to a non-significant improvement in the figure of merit (Z).

However, high ZT values (1 and 1.4 for n- and p-type bismuth telluride respectively) were identified in non-treated samples after a very simple grinding process which was employed as pre-treatment. The figure of merit of these two materials prepared by this simple methodology is close to the best reported values for Bi_2Te_3 .

Our results identify ultrasound milling and the simple crushing method as promising tools for the fabrication of nanostructured bulk thermoelectric materials.

DECLARATION AND STATEMENTS

DECLARATION

This work has not previously been accepted in substance for any degree and is not concurrently submitted in candidature for any degree.

Signed..... (Lourdes Marquez Garcia) Date.....

STATEMENT 1

This thesis is being submitted in partial fulfilment of the requirements for the degree of Doctor of Philosophy (PhD).

Signed..... (Lourdes Marquez Garcia) Date.....

STATEMENT 2

This thesis is the result of my own independent work/investigation, except where otherwise stated. Other sources are acknowledged by explicit references.

Signed..... (Lourdes Marquez Garcia) Date.....

STATEMENT 3

I hereby give consent for my thesis, if accepted, to be available for photocopying and for interlibrary loan, and for the title and summary to be made available to outside organisations.

Signed..... (Lourdes Marquez Garcia) Date.....

ACKNOWLEDGMENTS

First of all, I would like to express my gratitude to my supervisor, Dr Gao Min to give me the possibility to work in his group and change completely my research area. His guidance and comments have been essential to make me understand the new knowledge of this work. But, it is more in the human sense where I am very thankful to him. It would have been impossible to get so far without your support and understanding of my sickness. Thanks from my heart.

I would also like to recognise the effort made by my second supervisor, Prof. Nick Jenkins, in having meetings with me and trying to understand my research.

Then, I am very grateful to all the colleagues that I have met in this thermoelectric group. I have learnt something from everyone and it was nice to share funny moments with all of you. I would like to express my gratitude to everyone in the electrical and mechanical workshops because they have been always trying to help me. But especially, I would like to thank Malcolm Seaborne for everything, you are a very nice person, I will never forget you.

Especial thanks are going to Paul Malpas in the mechanical workshop and Sophie in the Pharmacy department, to allow me using the Mastersizer equipment as it was mine. Also Prof. David Barrow and Dr. Li Jin to permit measuring my samples in his optical microscope.

On the other hand, I would like to thank Anthony Oldroyd for his support in the XRD analysis and provide results in a very short period of time. I should also thank the technicians that helped me with the SEM and EDX measurements. My especial thanks are for Prof. Anthony Powell to allow me using the laser flash equipment and Dr. Jesús Prado-Gonjal for his help using this technique, his explanations and inputs in the XRD measurements.

Finally this thesis would have not been possible without the financially support of the European Commission under the Globasol project (309194).

Esta tesis nunca hubiera visto la luz sin el esfuerzo, el cariño y la educación recibida por parte de mis padres. A ellos les debo todo lo que soy y todo lo que hago, gracias a su educación basada en el esfuerzo y en seguir adelante siempre para conseguir lo que uno se propone he llegado hasta aquí. Sois la razón de mi existir, gracias por todo aunque nunca podré agradecerlos lo suficiente todo lo que habéis hecho en vuestra vida por mí, sois INIGUALABLES, para mí los MEJORES. Gracias por confiar siempre en mí y en mis posibilidades, hacer que nunca me rindiera y aceptar mis decisiones aunque sé que algunas no hayan sido de vuestro agrado. Perdonar por los nervios en mis momentos de exámenes y por alguna que otra mala contestación pero el estrés... Mi hermano, esto también es un fruto tuyo, tu eres mi media mitad que a todos sitios donde voy y en todo lo que hago

siempre me acompaña, gracias por confiar siempre en mí y gracias por esos momentos compartidos de juegos y risas desde pequeños, TE QUIERO. Espero que vosotros tres sintáis este trabajo como si fuera vuestro, porque lo es, sin vosotros nunca hubiera sido capaz de llegar hasta aquí. OS ADORO!!

Esta tesis no sería lo que es e incluso no hubiera salido adelante, sin mi compañero de viajes desde hace 7 años y medio, mi Pich. Esta tesis es en gran parte obra tuya, así que espero que la sientas como tal. Jorge sabes que sin ti yo no hubiera sido capaz de terminar esto, sin tus correcciones, tus consejos, tu ayuda en todo momento, sin esos momentos de bajón a tu lado... en fin, que nunca podré agradecerte lo mucho que has hecho por mi e incluso al dejar tus cosas de lado para mirar las mías, sólo puede haber una frase que mejor te define: ¡¡ERES EL MEJOR. GRACIAS POR ESTAR AHÍ, TE QUIERO MUCHO!!

También me gustaría dar las gracias a toda mi familia porque siempre han confiado mucho en mí desde pequeña, han preguntado y preocupado por mis. Me gustaría hacer una especial mención a mi abuela Fulgencia, que con una memoria que para mí la quisiera, no se ha olvidado nunca de mis exámenes, abuela mira a donde ha llegado uno de los suyos. Chacha aunque a veces digas que estropeo la carrera por como hablo, espero que consideres esto como parte tuya también, gracias por estar siempre ahí al lado nuestro y por ser para mí como una segunda madre. ¡¡OS QUIERO MUCHO FAMILIA!!

Gracias chicas, María y Lledó, por ser como sois. Sois unas amigas INMEJORABLES, a pesar de la distancia siempre me he sentido cerca. Gracias por esos ánimos y por confiar tanto en que yo podría con esto y mucho más, gracias por esas risas nerviosas de antes de los exámenes, por las noches de fiesta, por estar siempre ahí, en fin por todo lo vivido y lo que nos queda juntas. Sois muy especiales, esto también es en parte gracias a vosotras o sea que espero que lo sintáis así.

No podría olvidarme nunca de mis compañeros de la Universitat Jaume I, con ellos empecé mi andadura en esto de la ciencia. Vosotros habéis sido el mejor grupo en el que he estado, gracias por esos inolvidables momentos que pasamos. De ahí no sólo me llevo las vivencias, la gente y la ciencia que aprendí, sino lo mejor que podría haber encontrado en mi vida, a mi Pich.

Gracias a mi compañera inseparable del master Anais, que bonito fue y que bien lo pasamos, pero lo más bonito fue conocerte y tenerte como amiga, eres un sol.

Silvia Villarroya muchas gracias por la oportunidad que me concediste de trabajar en Cardiff y tu amistad, eres grande!. A mis amigas "galesas" Lia, Ana, Lorena, y a Ángel, el culero, que tanto me ha ayudado en esta tesis, sin tu ayuda no hubiera conseguido algunos resultados, eres un buen chico y un buen científico, siempre te recordaré.

¡¡Gracias a todos los que han hecho esto posible porque al final es un trabajo en el que ha participado mucha gente de manera directa o indirecta!!

PUBLICATIONS

- L. Marquez-Garcia, Wei Li, J. J. Bompfrey, D. J. Jarvis, Gao Min. Preparation of Nanoparticles of Thermoelectric Materials by Ultrasonic Milling. *Journal of electronic materials*, 44, 2172-2176, 2015.
- International Conference on Thermoelectrics 2015, Dresden (Germany) - 28 June to 2 July 2015. Poster presentation: L. Marquez-García, J. García-Cañadas and G. Min. *Fabrication of nanostructured bulk Bi₂Te₃ materials by ultrasonic milling*.
- Ultralow thermal conductivity for Bi₂Te₃ materials prepared by Ultrasonic milling (under preparation).
- Significant Thermal conductivity reduction for Bi₂Te₃ materials via a simple crushing process (under preparation)

CONTENTS

SUMMARY	i
DECLARATION AND STATEMENTS	iii
ACKNOWLEDGMENTS	v
PUBLICATIONS	viii
CONTENTS	x
LIST OF SYMBOLS	xiv
LIST OF ABBREVIATIONS	xvi
LIST OF FIGURES	xviii
LIST OF TABLES.....	xxvi
Chapter 1: Introduction	1
1.1 Background to the present research.....	2
1.2 Aim and objectives	4
1.3 Thesis outline	4
1.3.1 Chapter 1: Introduction	4
1.3.2 Chapter 2: Introduction to thermoelectricity and state-of-the-art.....	4
1.3.3 Chapter 3: Experimental methods	5
1.3.4 Chapter 4: Preparation of bismuth telluride nanopowder	5
1.3.5 Chapter 5: Optimisation of the hot press compaction method.....	5
1.3.6 Chapter 6: Thermoelectric properties of nanobulk materials	5
1.3.7 Chapter 7: Thermoelectric modules fabrication.....	6
1.3.8 Chapter 8: Conclusions and future work.....	6
Chapter 2 : Introduction to Thermoelectricity and State-of-the-art	7
2.1 Introduction	8
2.2 History of thermoelectricity.....	8
2.3 Thermoelectric effects	11
2.3.1 Seebeck effect.....	11
2.3.2 Peltier effect	12
2.3.3 Thomson effect.....	13

2.3.4	Kelvin relationships	14
2.4	Thermoelectric devices	14
2.4.1	Structure of thermoelectric generators.....	15
2.4.2	Conversion efficiency and Power output	16
2.5	Thermoelectric materials	18
2.6	Strategies to improve ZT	25
2.7	Nanostructuring methods	27
2.8	Methods to prepare nanobulk thermoelectric materials.....	35
Chapter 3	: Experimental Methods	39
3.1	Introduction	40
3.2	Nanopowder fabrication methods	40
3.2.1	Ball Milling (BM)	40
3.2.2	Ultrasonic Milling (UM)	41
3.3	Powder characterisation methods.....	43
3.3.1	Shaker.....	44
3.3.2	Laser diffraction particle size analyser	44
3.3.3	SEM and EDX	45
3.3.4	XRD	47
3.3.5	Optical microscope	48
3.4	Thermoelectric characterisation methods.....	49
3.4.1	Hot probe.....	49
3.4.2	4-probe technique	50
3.4.3	4-multifunctional probe technique	51
3.4.4	Laser flash instrument.....	53
3.4.5	Impedance spectroscopy	54
Chapter 4	: Preparation of Bismuth Telluride Nanopowder	57
4.1	Introduction	58
4.2	Experimental part	58
4.3	Optimisation of ball milling	59
4.3.1	Particle size distribution	59
4.3.2	Morphological characterisation	65
4.3.3	Structural characterisation	67

4.4	Optimisation of ultrasound milling	69
4.4.1	Particle size distribution	71
4.4.2	Morphological characterisation	82
4.4.3	Structural characterisation	88
4.5	Comparison between ball and ultrasound milling techniques	90
4.5.1	Morphological characterisation	90
4.5.2	Structural characterisation	92
4.6	Conclusions	94
Chapter 5 : Optimisation of the Hot Press Compaction Method		97
5.1	Introduction	98
5.2	Construction of the hot press station.....	98
5.3	Optimisation of the sintering process	99
5.3.1	Time and temperature optimisation	100
5.3.2	Pressure optimisation.....	103
5.4	Conclusions	105
Chapter 6 : Thermoelectric Properties of Nanobulk Materials.....		107
6.1	Introduction	108
6.2	Characterisation of non-treated samples	109
6.2.1	Thermoelectric properties.....	109
6.2.2	XRD	116
6.2.3	Optical microscope	118
6.3	Characterisation of milled samples	122
6.3.1	Thermoelectric properties.....	123
6.3.2	XRD	128
6.3.3	Optical microscope	130
6.4	Conclusions	133
Chapter 7 : Thermoelectric Modules Fabrication		136
7.1	Introduction	137
7.2	Module fabrication procedure.....	137
7.3	Module characterisation.....	139
7.4	Conclusions	141

Chapter 8 : Conclusions and Future Work	144
8.1 Conclusions	145
8.2 Future work	147
References	150
Appendix A.....	157

LIST OF SYMBOLS

Z	Figure of merit
ZT	Dimensionless figure of merit
Z'	Real impedance term
Z''	Imaginary impedance term
α	Seebeck coefficient or thermopower
σ	Electrical conductivity
λ	Thermal conductivity
λ_L	Lattice thermal conductivity
λ_E	Electronic thermal conductivity
λ_b	Beam wavelength
T	Temperature
V	Voltage
ΔT	Temperature difference
E	Energy
π	Peltier coefficient
Q	Heat transfer rate
Q_T	Total heat rate
Q_{in}	Heat input
I	Electric current
β	Thomson coefficient
η	Conversion efficiency
η_{max}	Maximum conversion efficiency
P	Power
P_{max}	maximum power output
N	Number of couples
R	Electrical resistance
R_L	Load resistance
R_s	Sheet resistance
R_{TE}	Thermoelectric resistance
R_Ω	Ohmic resistance
m	Ratio between the resistance of thermoelectric elements and the load resistance
K	Thermal conductance

T_{avg}	Average temperature
T_{H}	Hot side temperature
T_{C}	Cold side temperature
θ	Beam irradiation angle
n	Order of beam reflection
a	Distance between lattice planes
s	Probe spacing
d	Sample diameter
W	Sample thickness
F, C	Geometrical correction factors
ρ	Electrical resistivity
D	Thermal diffusivity
C_p	Specific heat
ρ_m	Mass density
t	Time
t_{50}	Half-rise time
m_m	Mass
q	Heat
ϕ	Phase angle
ω	Angular frequency

LIST OF ABBREVIATIONS

AC	Alternating current
BM	Ball milling
BSE	Back-scattered electrons
CVD	Chemical vapor deposition
DC	Direct current
DIC	Differential interference contrast
DMF	Dimethyl-formamide
ECD	Electrochemical deposition
ED	Electroless deposition
EDX	Energy dispersive X-ray spectroscopy
EtOH	Ethanol
FAST	Field assisted sintering technique
FCC	Face centred cubic
HH	Half-heusler
HTS	Hydrothermal and solvothermal
IGPC	Inert-gas phase condensation
IR	Infrared
LCVD	Laser chemical vapour deposition
LED	Light-emitting diode
LLCT	Lytotropic liquid crystal templates
LP	Laser pyrolysis
P ² C	Plasma pressure compaction
PAS	Plasma-activated sintering
PECS	Pulse electric current sintering
PEDOT	Poly(3,4-ethylenedioxythiophene)
PG	Propylene glycol
PLA	Pulsed laser ablation
PVD	Physical vapor deposition
SAA	Surface active agent
SCR	Sono-chemical reduction
SE	Secondary electrons
SEM	Scanning electron microscopy

SP	Spray pyrolysis
SPS	Spark plasma sintering
ST	Sputtering technique
TEG	Thermoelectric generator
TEM	Thermoelectric module
TTF	Tetrathiafulvalene
UM	Ultrasound milling
XRD	X-ray diffraction

LIST OF FIGURES

Fig. 2.1. Instrument used by Seebeck for the discovery of the Seebeck effect.	12
Fig. 2.2. Illustration of the Seebeck effect where two different conductors (orange and green), forming an electrical circuit, produce a voltage under a temperature difference at their junctions.....	15
Fig. 2.3. Diagram of the Peltier effect in a circuit formed by 2 dissimilar conductors (orange and green). When electrons cross the top junction they have to absorb energy, producing cooling. The opposite occurs at the bottom junction where electrons release energy when they cross it, producing heating.....	16
Fig. 2.4. Basic unit (thermocouple) of a thermoelectric device under Seebeck mode operation. The electric power generated is delivered to the load resistance R_L	18
Fig. 2.5. Sketch of a thermoelectric device.....	19
Fig. 2.6. Schematic of the rhombohedral structure of quintuple layer of Bi_2Te_3	22
Fig. 2.7. Seebeck coefficient, power factor and electrical conductivity versus log (carrier concentration).....	28
Fig. 2.8. Energy diagrams describing the higher excitation needed for the electrons in the valence band when the majority carrier concentration is increased.....	29
Fig. 2.9. Scheme of top-down and bottom-up approaches for the preparation of nanoparticles.....	32
Fig. 3.1 (a) Trace of motions performed by the SPEX 8000M. (b) Photograph of SPEX 8000M employed in this work. (c) Container with the balls and bismuth telluride powder after a ball milling experiment.....	46
Fig. 3.2. Cavitation process, bubble size and behaviour in response to ultrasound waves. Outset, growth, oscillation and collapse of bubbles within a fluid driven by a sound field. ...	47
Fig. 3.3 (a) Image of the ultrasound milling with the generator from the supplier (www.hielscher.com). (b) Experimental set up of the ultrasound milling showing key parts. (c) Milling cell with the heat sink and the typical Bi_2Te_3 solution used for these experiments....	48
Fig. 3.4 (a) Sonic sifter shaker. (b) Sieves stacked up for separation of different particle size.....	49
Fig. 3.5. Mastersizer 3000 for measuring particle size distribution.....	50
Fig. 3.6. Philips XL 30 SEM apparatus.....	51
Fig. 3.7 Experimental results obtained from EDX for an n-type Bi_2Te_3 sample. (a) Quantitative data. (b) SEM image of the part of the sample analysed. (c) Spectrum showing the characteristic peaks of the elements that form the sample.....	52
Fig. 3.8 (a) Scheme of the X-ray diffraction following the Bragg equation. (b) Schematic operation of the XRD apparatus.....	53
Fig. 3.9. Optical microscope Nikon MM-800/SL.....	54
Fig. 3.10 (a) Schematic diagram of the hot probe. (b) Photograph of the actual hot probe apparatus.....	55
Fig. 3.11 (a) Schematic diagram of the 4-probes. (b) Top view of the 4-probe apparatus. (c) Front view of the 4-probe technique.....	55
Fig. 3.12 (a) Sketch of a multifunctional probe and (b) Top view of the 4-multifunctional probe apparatus.....	56
Fig. 3.13 (a) Laser flash equipment and (b) Typical measurement performed by the laser flash instrument.....	58

Fig. 3.14. (a) Applied and response signals in an impedance experiment. (b) Point representation in the complex impedance plane.	59
Fig. 3.15. Nyquist plot of a commercial 254-leg thermoelectric module and the characteristic parameters R_{Ω} and R_{TE} . The inset shows a magnification of the high-frequency part. Image taken from reference	60
Fig. 4.1 (a) Micro hammer-cutter mill utilised for the pre-treatment. (b) Schematic process to prepare the powder from the ingot by the milling processes.....	66
Fig. 4.2. Particle size distribution in number density of n-type Bi_2Te_3 after ball milling using a balls:material ratio 20:1 at different times. Parameters N_M , D_M and D_L indicate the maximum number density percentage, the particle size corresponding to this maximum and the lowest particle size identified, respectively.	67
Fig. 4.3. Representation of the smallest particle size (blue) and the number of particles smaller than 1 μm (red) achieved for n-type Bi_2Te_3 after ball milling experiments under different times and 5:1 balls:material ratio.	70
Fig. 4.4. Smallest particle size (blue) and percentage of the number of particles smaller than 1 μm (red) obtained for ball milling experiments of p-type Bi_2Te_3 at different times and 20:1 balls:material ratio.	72
Fig. 4.5. SEM images of n- Bi_2Te_3 (a-d) before ball milling and after ball milling experiments at 5:1 ratio at different times: (e-h) 2 h, (i-l) 8 h, (m-p) 24 h and (q-t) 48 h from left to right, scale bar: 200 μm , 50 μm , 5 μm and 2 μm	73
Fig. 4.6. SEM images of p- Bi_2Te_3 (a-d) before and after ball milling experiments at 20:1 ratio at different times: (e-h) 2 h, (i-l) 8 h and (m-p) 24 h from left to right, scale bar: 200 μm , 50 μm , 5 μm and 2 μm	74
Fig. 4.7. XRD patterns of n-type $\text{Bi}_2\text{Te}_{2.79}\text{Se}_{0.21}$: (blue) theoretical, (red) ingot sample, (green) reference before milling and (purple) after ball milling experiment performed at 24 h and 5:1 balls:material ratio.	75
Fig. 4.8. XRD patterns of p-type $\text{Bi}_{0.5}\text{Te}_{2.5}\text{Sb}_{1.5}$: (blue) theoretical, (red) ingot sample, (green) reference before milling and (purple) after ball milling experiments performed for 8 h at 10:1 balls:material ratio.	76
Fig. 4.9. Particle size distribution in number density of n-type Bi_2Te_3 powder after ultrasound milling experiments which produce the smallest particle size under different conditions.....	82
Fig. 4.10. Representation of the smallest particle size (blue) and number of particles smaller than 1 μm achieved for n-type Bi_2Te_3 after ultrasound milling experiments for different optimum conditions.	85
Fig. 4.11. Particle size distribution in number density of p-type Bi_2Te_3 after ultrasound milling experiments of optimum conditions.	88
Fig. 4.12. Representation of the smallest particle size (blue) and percentage of particles smaller than 1 μm achieved for p-type Bi_2Te_3 after ultrasound milling experiments at different conditions.....	90
Fig. 4.13. SEM images of n- Bi_2Te_3 powder (a-d) before ultrasound milling treatment, after ultrasound milling treatment at (e-h) 100 % amplitude and 2 coolers for 30 min, (i-l) 100 % amplitude, 2 coolers and 1 % of PG for 30 min, (m-p) 60 % amplitude, 2 coolers for 4 h, and (q-t) 60 % amplitude, 1 cooler for 10 h from left to right, scale bar: 200 μm , 50 μm , 5 μm and 2 μm	91
Fig. 4.14. SEM images of n- Bi_2Te_3 (a-d) before ultrasound milling treatment, after ultrasound milling treatment at 100 % amplitude, 2 coolers for (e-h) 30 min, (i-l) 2 h, (m-q) 4 h, (r-v) 6 h, and (w-a_1) 8 h from left to right, scale bar: 200 μm , 50 μm , 5 μm , 2 μm and 1 μm	93

Fig. 4.15. Dried samples after ultrasound milling treatment at 30 min (left) and 8 h (right and the corresponding magnified image) with the presence of curly features.....	94
Fig. 4.16. SEM images of n-Bi ₂ Te ₃ after ultrasound milling treatment at 100 % amplitude, [powder]=0.0166 M and 2 coolers for 6 h (a-e) and for 8 h (f-j) from left to right, scale bar: 200 μm, 50 μm, 5 μm, 2 μm and 1 μm.	94
Fig. 4.17. SEM images of p-Bi ₂ Te ₃ (a-d) before ultrasound milling treatment and after ultrasound milling at (e-h) 100 % amplitude, 2 coolers for 6 h, (i-l) 100 % amplitude, 2 coolers, 1 % of PG for 8 h, (m-p) 60 % amplitude, 2 coolers for 6 h, and (q-t) 60 % amplitude, 1 cooler for 4 h from left to right, scale bar: 200 μm, 50 μm, 5 μm, and 2 μm.....	96
Fig. 4.18. SEM images of p-Bi ₂ Te ₃ after ultrasound milling at (a-d) 100 % amplitude, 2 coolers, 6 and (e-i) 8 h, (j-n) 100 % amplitude, 2 coolers, [powder]=0.0166 M, 6 h and (o-s) 8 h from left to right, scale bar: 200 μm, 50 μm, 5 μm, 2 μm and 1 μm.....	97
Fig. 4.19. Theoretical XRD pattern of n-type Bi ₅ Te _{2.79} Se _{0.21} (blue) and patterns of the ingot sample (red), reference sample before milling (green) and after ultrasound milling treatment performed at 100 % amplitude, 2 coolers and for 8h (pink).	98
Fig. 4.20. Theoretical XRD pattern of the p-type Bi _{0.5} Te ₃ Se _{1.5} (blue), ingot sample (red), reference sample before milling (green) and after ultrasound milling treatment performed at 100 % amplitude, 2 coolers and for 8 h (pink).	99
Fig. 4.21. SEM images of n-Bi ₂ Te ₃ after (a-d) ball milling process at 24 h and ratio 5:1 and ultrasound milling treatment at (e-h) 100 % amplitude, 2 coolers and [powder]=8.3·10 ⁻³ M for 30 min, and (i-m) 100 % amplitude, 2 coolers and [powder]=0.0166 M for 8 h from left to right, scale bar: 200 μm, 50 μm, 5 μm, 2 μm and 1 μm.	100
Fig. 4.22. SEM images of p-Bi ₂ Te ₃ (a-d) after ball milling process at 8 h, ratio 20:1 and (e-j) ultrasound milling treatment at 100 % amplitude, 2 coolers, 8 h, [powder]=8.3·10 ⁻³ M and (j-n) [powder]=0.0166 M from left to right, scale bar: 200 μm, 50 μm, 5 μm, 2 μm and 1 μm.	101
Fig. 4.23. XRD patterns of the n-type Bi ₂ Te _{2.79} Se _{0.21} after ball milling, 24 h and ratio 5:1 (purple), and after ultrasound milling performed at 100 % amplitude, 2 coolers and 8 h (pink).	102
Fig. 4.24. XRD patterns of p-type Bi _{0.5} Te ₃ Sb _{1.5} after ball milling at 8 h and ratio 20:1 (purple) and after ultrasound milling treatment performed at 100 % amplitude, 2 coolers and for 8 h (pink).....	102
Fig. 5.1. (a) Hot pressed system built in the laboratory and (b) die set.	108
Fig. 5.2. Schematic process of fabrication of sample discs.....	109
Fig. 5.3. Scheme of the experiments performed for the optimisation of time and temperature of the compaction process.	110
Fig. 5.4. Density vs. sintering temperature of compacted discs at different times, 25 s (blue), 30 min (red) and 60 min (green). The density value of the reference sample (cyan line) is also represented.	110
Fig. 5.5. Seebeck coefficient (a), electrical conductivity (b) and power factor (c) as a function of the sintering temperature at different times.	111
Fig. 5.6. Diagram of the procedure followed to prepare disc samples at different pressures.	112
Fig. 5.7. Density (blue) and relative density (red) of powders treated at different pressures. The pressing temperature (250 °C) and the duration of the treatment (60 min) were the same for all the experiments.	113
Fig. 5.8. Seebeck coefficient (a), electrical conductivity (b) and power factor (c) as a function of the sintering pressure. The same duration (30 min) and temperature (250 °C) were used in all experiments.	113

Fig. 6.1. (a) Density, (b) Seebeck coefficient, (c) in-plane electrical conductivity and (d) power factor of n-type discs prepared under two different sintering temperatures (250 and 350 °C), 5 tons of weight and for 30 min. Results are shown for samples compacted from powders of different particle size ranges.	121
Fig. 6.2. (a) Cross-plane thermal conductivity and (b) ZT of n-type discs prepared at 350 °C, 5 Tons of weight for 30 min. Results are shown for samples compacted from powders of different particle size ranges.	122
Fig. 6.3. Example of a disc sample with the different directions employed for the measurements and pressing.	123
Fig. 6.4. (a) Density, (b) Seebeck coefficient, (c) in-plane electrical conductivity and (d) power factor of p-type discs prepared under two different sintering temperatures (250 and 350 °C), 5 tons of weight and for 30 min. Results are shown for samples compacted from powders of different particle size ranges.	124
Fig. 6.5. (a) Cross-plane thermal conductivity, (b) electrical thermal conductivity and (c) lattice thermal conductivity of p-type discs prepared at 250 °C and 350 °C, 5 tons of weight for 30 min from different size fractions of powder. Thermal conductivity and the different contributions at (d) 250 °C and (e) 350 °C. (f) ZT values for 250 and 350 °C sintering temperatures.	126
Fig. 6.6. Theoretical XRD pattern of non-treated n-type $\text{Bi}_2\text{Te}_{2.79}\text{Se}_{0.21}$ (blue), ingot sample (red), particle size 250-106 μm (green), particle size <106 μm (pink), particle size 106-45 μm (grey) and particle size 45-20 μm (dark green) discs sintered at 250 °C for 30 min with 5 tons of weight.	128
Fig. 6.7. Theoretical XRD pattern of non-treated p-type $\text{Bi}_5\text{Te}_{2.79}\text{Se}_{0.21}$ (blue), reference sample before milling (red), particle size 250-106 μm (green), particle size <106 μm (pink), particle size 106-45 μm (grey) and particle size 45-20 μm (dark green) discs sintered at 350 °C for 30 min with 5 tons of weight.	129
Fig. 6.8. Microscope images of n-type disc samples (a) reference, (b) size 250-106 μm , (c) size < 106 μm , (d) size 106-45 μm and size (e) 45-20 μm	131
Fig. 6.9. Microscope images of p-type disc samples (a) reference, (b) size 250-106 μm , (c) size <106 μm , (d) size 106-45 μm and size (e) 45-20 μm	133
Fig. 6.10. (a) Density, (b) Seebeck coefficient, (c) electrical conductivity and (d) power factor of the n-type non-treated (350 °C) and ball milling and ultrasound milling samples prepared at 250 °C and 5 tons of weight for 30 min (optimum conditions).	135
Fig. 6.11. (a) Thermal conductivity, (b) electrical thermal conductivity, (c) lattice thermal conductivity and (d) ZT of the n-type non-treated (350 °C), BM and UM samples prepared at 250 °C and 5 tons of weight for 30 min (optimum conditions).	137
Fig. 6.12. (a) Density, (b) Seebeck coefficient, (c) electrical thermal conductivity and (d) power factor, of p-type non-treated, UM and reference samples prepared at 350 °C and 5 tons of weight for 30 min.	138
Fig. 6.13. a) Thermal conductivity, (b) electrical thermal conductivity, (c) lattice thermal conductivity and (d) ZT of p-type non-treated and UM samples prepared at 350 °C and 5 tons of weight for 30 min.	139
Fig. 6.14. XRD patterns of n-type $\text{Bi}_{0.5}\text{Te}_3\text{Sb}_{1.5}$ (blue), non-treated reference (red), after ball milling treatment with particle size 106-45 μm (green), 45-20 μm (pink), 20-10 μm (grey) and after ultrasound milling treatment (dark green).	140
Fig. 6.15. XRD patterns of p-type $\text{Bi}_{0.5}\text{Te}_3\text{Sb}_{1.5}$ (blue), reference cut from the ingot (red) and after ultrasound milling experiment (dark green).	141

Fig. 6.16. Microscope images of n-type disc samples treated by ball milling using the optimum conditions and separated in different size ranges (a) 106-45 μm , (b) 45-20 μm and (c) 20-10 μm .	143
Fig. 6.17. Microscope images of n- (a-b) and p-type (c-d) disc samples treated by ultrasound milling.	144
Fig. 7.1. Schemes of (a) material and (b) substrate preparation for the thermoelectric module fabrication.	150
Fig. 7.2. Scheme of the assembly process for the module fabrication.	151
Fig. 7.3. (a) Burnt and (b) shiny joints in the fabricated modules after soldering treatment for 30 and 25 min, respectively.	152
Fig. 7.4. Impedance spectra of the best modules prepared with the (blue) reference and (red) prepared material with particle size range 250-106 μm .	153
Fig. A.1. Particle size distribution in volume density of n-type Bi_2Te_3 after ball milling using balls:material ratio 20:1 at different times.	169
Fig. A.2. Particle size distribution in volume density of n-type Bi_2Te_3 after ball milling using balls:material ratio 5:1 at different times.	169
Fig. A.3. Particle size distribution in number density of n-type Bi_2Te_3 after ball milling using balls:material ratio 5:1 at different times.	170
Fig. A.4. Particle size distribution in volume density of n-type Bi_2Te_3 after ball milling using different balls:material ratio at 24 h.	170
Fig. A.5. Particle size distribution in number density of n-type Bi_2Te_3 after ball milling using different balls:material ratios at 24 h.	171
Fig. A.6. Representation of the smallest particle size achieved for n-type Bi_2Te_3 after ball milling under different times and ratio balls:material 5:1.	171
Fig. A.7. Representation of the number of particles with a size smaller than 1 μm achieved for n-type Bi_2Te_3 after ball milling under different times and ratio balls:material 5:1.	172
Fig. A.8. Particle size distribution in volume density of p-type Bi_2Te_3 after ball milling using balls:material ratio 20:1 at all the different times performed.	172
Fig. A.9. Particle size distribution in number density of p-type Bi_2Te_3 after ball milling using balls:material ratio 20:1 at all the different times performed.	173
Fig. A.10. Particle size distribution in volume density of p-type Bi_2Te_3 after ball milling using different balls:material ratio at 8 h.	173
Fig. A.11. Particle size distribution in number density of p-type Bi_2Te_3 after ball milling using different balls:material ratio at 8 h.	174
Fig. A.12. Representation of the smallest particle size achieved for p-type Bi_2Te_3 after ball milling under different times and ratio balls:material 20:1.	174
Fig. A.13. Representation of the number of particles with a size smaller than 1 μm achieved for p-type Bi_2Te_3 after ball milling under different times and ratio balls:material 20:1.	175
Fig. A.14. Density measurements of the n-type Bi_2Te_3 discs prepared by ultrasound milling (2 h, 100 % amplitude and 2 coolers) using different solvents.	175
Fig. A.15. Seebeck coefficient results of the n-type Bi_2Te_3 discs prepared by ultrasound milling (2 h, 100 % amplitude and 2 coolers) using different solvents.	176
Fig. A.16. Electrical conductivity results of the n-type Bi_2Te_3 discs prepared by ultrasound milling (2 h, 100 % amplitude and 2 coolers) using different solvents.	176
Fig. A.17. Power factor results of the n-type Bi_2Te_3 discs prepared by ultrasound milling (2 h, 100 % amplitude and 2 coolers) using different solvents.	177

Fig. A.18. Particle size distribution in volume density of n-type Bi ₂ Te ₃ powder after ultrasound milling treatment performed without PG additive at 100 % amplitude, 2 coolers and at different times.....	177
Fig. A.19. Particle size distribution in number density of n-type Bi ₂ Te ₃ powder after ultrasound milling treatment performed without PG additive at 100 % amplitude, 2 coolers and at different times.....	178
Fig. A.20. Particle size distribution in volume density of n-type Bi ₂ Te ₃ after ultrasound milling performed at 100 % amplitude, 2 coolers, 1 % of additive PG and at different times.	178
Fig. A.21. Particle size distribution in number density of n-type Bi ₂ Te ₃ powder after ultrasound milling experiments performed at 100 % amplitude, 2 coolers, 1 % of PG additive and at different times.....	179
Fig. A.22. Particle size distribution in volume density of n-type Bi ₂ Te ₃ after ultrasound milling performed at 60 % amplitude, 2 coolers and at different times.	179
Fig. A.23. Particle size distribution in number density of n-type Bi ₂ Te ₃ after ultrasound milling experiments performed at 60 % amplitude, 2 coolers and at different times.	180
Fig. A.24. Particle size distribution in volume density of n-type Bi ₂ Te ₃ after ultrasound milling performed at 60 % of amplitude, 1 cooler and at different times.	180
Fig. A.25. Particle size distribution in number density of n-type Bi ₂ Te ₃ after ultrasound milling performed at 60 % amplitude, 1 cooler and at different times.....	181
Fig. A.26. Particle size distribution in volume density of n-type Bi ₂ Te ₃ powder after ultrasound milling experiments which produce the smallest particle size under different conditions.....	181
Fig. A.27. Particle size distribution in volume density of n-type Bi ₂ Te ₃ after ultrasound milling experiments performed at 100 % amplitude, 2 coolers, double powder concentration (0.0166 M) and at different times.	182
Fig. A.28. Particle size distribution in number density of n-type Bi ₂ Te ₃ after ultrasound milling experiments performed at 100 % amplitude, 2 coolers, double powder concentration (0.0166 M) and at different times.	182
Fig. A.29. Representation of the smallest particle size achieved for n-type Bi ₂ Te ₃ after ultrasound millings which the smallest particle size is achieved for every different variable changed.	183
Fig. A.30. Representation of the number of particles smaller than 1 μm achieved for n-type Bi ₂ Te ₃ after ultrasound millings which the smallest particle size is achieved for every different variable changed.....	183
Fig. A.31. Particle size distribution in volume density of p-type Bi ₂ Te ₃ after ultrasound milling experiments performed at 100 % amplitude, 2 coolers and at different times without PG additive.	184
Fig. A.32. Particle size distribution in number density of p-type Bi ₂ Te ₃ after ultrasound milling experiments performed at 100 % amplitude, 2 coolers and at different times without PG additive.	184
Fig. A.33. Particle size distribution in volume density of p-type Bi ₂ Te ₃ after ultrasound milling experiments performed at 100 % amplitude, 2 coolers, 1% of additive (PG) and at different times.	185
Fig. A.34. Particle size distribution in number density of p-type Bi ₂ Te ₃ after ultrasound milling experiments performed at 100 % amplitude, 2 coolers, 1 % of additive (PG) and at different times.	185
Fig. A.35. Particle size distribution in volume density of p-type Bi ₂ Te ₃ after ultrasound milling experiments performed at 60 % amplitude, 2 coolers and at different times.	186

Fig. A.36. Particle size distribution in number density of p-type Bi_2Te_3 after ultrasound milling experiments performed at 60 % amplitude, 2 coolers and at different times.	186
Fig. A.37. Particle size distribution in volume density of p-type Bi_2Te_3 after ultrasound milling experiments performed at 60 % amplitude, 1 cooler and at different times.....	187
Fig. A.38. Particle size distribution in number density of p-type Bi_2Te_3 after ultrasound milling experiments performed at 60 % amplitude, 1 cooler and at different times.....	187
Fig. A.39. Particle size distribution in volume density of p-type Bi_2Te_3 after ultrasound millings experiments of optimum conditions.	188
Fig. A.40. Particle size distribution in volume density of p-type Bi_2Te_3 after ultrasound milling experiments performed at 60 % amplitude, 1 cooler, 4 h and at different concentrations. .	188
Fig. A.41. Particle size distribution in number density of p-type Bi_2Te_3 after ultrasound milling experiments performed at 60 % amplitude, 1 cooler, 4 h and at different concentrations. .	189
Fig. A.42. Representation of the smallest particle size achieved for p-type Bi_2Te_3 after ultrasound millings which the smallest particle size is achieved for every different variable changed.....	189
Fig. A.43. Representation of the number of particles smaller than $1\mu\text{m}$ achieved for p-type Bi_2Te_3 after ultrasound millings which the smallest particle size is achieved for every different variable changed.....	190
Fig. A.44. Theoretical XRD pattern of non-treated n-type $\text{Bi}_2\text{Te}_{2.79}\text{Se}_{0.21}$ (blue), particle size $250\text{-}106\mu\text{m}$ (red), particle size $<106\mu\text{m}$ (green), particle size $106\text{-}45\mu\text{m}$ (pink) and particle size $45\text{-}20\mu\text{m}$ (grey) powder.....	190
Fig. A.45. Theoretical XRD pattern of non-treated p-type $\text{Bi}_{0.5}\text{Te}_3\text{Se}_{1.5}$ (blue), particle size $250\text{-}106\mu\text{m}$ (red), particle size $<106\mu\text{m}$ (green), particle size $106\text{-}45\mu\text{m}$ (pink) and particle size $45\text{-}20\mu\text{m}$ (grey) powder.....	191
Fig. A.46. F value corrections to calculate the electrical conductivity measured by 4-probe technique.	192
Fig. A.47. C value corrections to calculate the electrical conductivity measured by 4-probe technique.	193

LIST OF TABLES

Table 4.1. Ball milling experiments performed at different times for n-type Bi ₂ Te ₃ at the 20:1 balls:material ratio.	67
Table 4.2. Ball milling experiments performed at different times for n-type Bi ₂ Te ₃ at the 5:1 balls:material ratio. Parameters N _M , D _M and D _L indicate the maximum number density percentage, the particle size corresponding to this maximum and the lowest particle size identified, respectively.	68
Table 4.3. Variation of the balls:material ratio for ball milling experiments of n-type Bi ₂ Te ₃ at a fixed time of 24 h. Parameters N _M , D _M and D _L indicate the maximum number density percentage, the particle size corresponding to this maximum and the lowest particle size identified, respectively.	69
Table 4.4. Results of the minimum particle size and the percentage of number of particles smaller than 1 μm achieved after ball milling experiments at different times but under the same balls:Bi ₂ Te ₃ ratio (5:1) for the n-type material.	69
Table 4.5. Variation of the ball milling time under the same balls:material ratio for p-type Bi ₂ Te ₃ . Parameters N _M , D _M and D _L indicate the maximum number density percentage, the particle size corresponding to this maximum and the lowest particle size identified, respectively.	71
Table 4.6. Variation of the balls:material ratio at a fixed treatment time of 8 h for ball milling experiments of p-type Bi ₂ Te ₃ . Parameters N _M , D _M and D _L indicate the maximum number density percentage, the particle size corresponding to this maximum and the lowest particle size identified, respectively.	71
Table 4.7. Minimum particle size and percentage of the number of particles smaller than 1 μm obtained after ball milling experiments at different times under the same balls:Bi ₂ Te ₃ ratio (20:1) for the p-type material.	72
Table 4.8. Solvents utilised to perform the ultrasound milling experiments and their flash point.	77
Table 4.9. Density, Seebeck coefficient, electrical conductivity and power factor values obtained for the discs prepared with powder treated by ultrasound milling at 100 % amplitude, 2 coolers and for 2 h using different solvents.	78
Table 4.10. Ultrasound milling experiments carried out at different times, 100 % amplitude, 2 coolers and with and without the addition of propylene glycol (PG) for n-type Bi ₂ Te ₃ . Parameters N _M , D _M and D _L indicate the maximum number density percentage, the particle size corresponding to this maximum and the lowest particle size identified, respectively. ...	79
Table 4.11. Ultrasound milling experiments carried out at different times, 60 % amplitude, 2 coolers for n-type Bi ₂ Te ₃ . Parameters N _M , D _M and D _L indicate the maximum number density percentage, the particle size corresponding to this maximum and the lowest particle size identified, respectively.	80
Table 4.12. Ultrasound milling experiments carried out at different times, 60 % amplitude, 1 cooler system for n-type Bi ₂ Te ₃ . Parameters N _M , D _M and D _L indicate the maximum number density percentage, the particle size corresponding to this maximum and the lowest particle size identified, respectively.	81
Table 4.13. Ultrasound milling experiments carried out at different times, 100 % amplitude, 2 cooler systems and [powder]=0.0166 M for n-type Bi ₂ Te ₃ . Parameters N _M , D _M and D _L	

indicate the maximum number density percentage, the particle size corresponding to this maximum and the lowest particle size identified, respectively.	83
Table 4.14. Summary of the values of the smallest particle size and the number of particles smaller than 1 μm achieved for n-type Bi_2Te_3 powder treated by ultrasound milling.	84
Table 4.15. Ultrasound milling experiments carried out at different times at 100 % amplitude, 2 coolers and with and without the propylene glycol (PG) additive for p-type Bi_2Te_3 . Parameters N_M , D_M and D_L indicate the maximum number density percentage, the particle size corresponding to this maximum and the lowest particle size identified, respectively. ...	86
Table. 4.16. Ultrasound milling experiments carried out at different times at 60 % amplitude, 2 coolers for p-type Bi_2Te_3 . Parameters N_M , D_M and D_L indicate the maximum number density percentage, the particle size corresponding to this maximum and the lowest particle size identified, respectively.....	87
Table. 4.17. Ultrasound milling experiments carried out at different times at 60 % amplitude, 1 cooler system for p-type Bi_2Te_3 . Parameters N_M , D_M and D_L indicate the maximum number density percentage, the particle size corresponding to this maximum and the lowest particle size identified, respectively.....	87
Table 4.18. Different concentrations employed in the ultrasound milling experiments performed at 60 % amplitude, 1 cooler and during 4 h. Parameters N_M , D_M and D_L indicate the maximum number density percentage, the particle size corresponding to this maximum and the lowest particle size identified, respectively.	89
Table 4.19. Values of the smallest particle size and the number of particles smaller than 1 μm achieved for p-type Bi_2Te_3 powder under different ultrasound milling treatments.....	90
Table 4.20. Relation of SEM images from Fig. 4.13 with the different conditions that produced the smallest particle size utilised to perform ultrasound milling experiments for the n-type Bi_2Te_3	92
Table 4.21. Different optimum conditions utilised to perform ultrasound milling experiments using the p-type Bi_2Te_3	95
Table 6.1. Conditions of the stain etching treatment for the n-type non-treated disc samples.	130
Table 6.2. Conditions of the stain etching treatment for the non-treated p-type disc samples.	132
Table 6.3. Conditions of the stain etching treatment for the n-type samples treated by BM.	141
Table 6.4. Conditions of the stain etching treatment for the n- and p-type samples treated by UM.	143
Table 7.1. Experimental conditions, total ohmic resistance, leg length and $(ZT)_{\text{module}}$ results for different modules prepared with original ingot materials.....	152
Table 7.2. Experimental conditions, total ohmic resistance, leg length and $(ZT)_{\text{module}}$ results for the modules prepared using materials prepared from powders with particle size (250-106 μm).	153

Chapter 1: Introduction

- 1.1 Background to the present research
- 1.2 Aim and objectives
- 1.3 Thesis outline

Chapter 1

1.1 Background to the present research

Nowadays, the world is facing the enormous challenge of finding new energy sources. The insufficient fossil-fuel reserves and the negative impact that they cause in the environment create the need to search for alternative energy sources, more environmentally friendly and able to cover the increasing energetic demand in the society. Alternative energy sources such as photovoltaics, wind power or hydrogen-based technologies have been intensively studied as a replacement to fossil fuels. In light of the importance of the problem, also improving the efficiency of the current energy use can significantly help.

These days around 60 % of the energy produced is lost in terms of heat, especially in electrical power generation and transport. For example, around 60 % of the energy extracted at the power plants is lost as waste heat during its generation,⁽¹⁾ and between 8 % and 15 % is lost as heat during its transport and transformation in the electrical lines.⁽¹⁾ Another major example is the waste heat in our cars, which is around 70 %, apart from the associated CO₂ emissions due to the extra 70 % of fuel needed. Under this scenario, materials able to transform waste heat into electrical power are highly valuable.

Thermoelectric materials are a promising candidate in this respect due to their capacity to convert temperature differences into electrical power, i.e., producing power from waste heat. Thermoelectric materials present the advantage of being formed by no-moving parts that make them more durable and silent. They are also easy to miniaturise and can be utilised for cooling and heating applications, since a temperature difference can be generated when applying an electrical current in the device. The main disadvantage of thermoelectric devices is their low efficiency (low figure of merit ZT), which makes them not competitive to other technologies in the market. To date, most of materials present ZT values slightly higher than 1 while more applications need ZT values around 2 or higher. Bismuth telluride based alloys are the dominant materials in the market since 1950s. Since then, no other material has been found to replace it. They can operate under maximum hot side temperatures of around 250 °C.

Seebeck coefficient, electrical and thermal conductivity are the parameters that govern the performance of the materials (ZT). These properties are interrelated, which makes it very difficult to increase or decrease one of them without affecting the others, so a compromise has to be commonly adopted to maximise the ZT value. There are many different strategies to improve thermoelectric materials. Some of the main approaches under intense investigation are:

- a) Preparation of new materials with complex band structures, which will increase the Seebeck coefficient without affecting the electrical conductivity and the electronic thermal conductivity.^(2, 3)
- b) Using the concept of electron crystals and phonon glasses, increasing the electrical conductivity and reducing the lattice thermal conductivity due to the rattling effect.⁽⁴⁾
- c) Nanostructuring, which could produce an increase of the Seebeck coefficient due to quantum confinement effects, and the decrease of the thermal conductivity due to the phonons scattering.^(5, 6)

The latter strategy is being the most intensively studied due to the latest improvements achieved in the figure of merit.⁽⁷⁾ There are mainly two approaches employed to produce nanoparticles in the thermoelectric field, which are then compacted to form nanostructured bulk materials, top-down and bottom-up. The former has been the most successful to date, specially employing the ball milling (mechanical alloying) method.⁽⁸⁾ For example, the performance of bismuth telluride materials has been significantly improved using this method.⁽⁹⁾

In this thesis ultrasound milling is presented as a new method to produce nanostructured thermoelectric materials. Bismuth telluride alloys, both n- and p-type, have been chosen to explore this new approach and results are compared to the ball milling technique. The new method benefits in requiring shorter times than ball milling and produces very low thermal conductivity materials, within the lowest values reported in the literature (0.50 W/Km and 0.35 W/Km for n- and p-type respectively). This reduced thermal conductivity values are due to the presence of highly aggregated nanoparticles that form a uniform granular microstructure after compaction. Unfortunately, electrical conductivity is also reduced significantly, which leads to no significant final improvement in ZT.

The ultrasound milling process is preceded by a simple crushing pre-treatment performed by a micro hammer-cutter mill, producing mainly micrometre size powder. Powders obtained in this way, separated in different particle sizes, present high ZT values (≈ 1.4 for p-type material) close to the best ones reported in the literature.⁽¹⁰⁾

1.2 Aim and objectives

The aim of this thesis is the evaluation of ultrasound milling technique as a new method able to produce nanostructured thermoelectric materials. Bismuth telluride alloys, as the standard thermoelectric materials at room temperature, were chosen as the material to be treated by this top-down approach. Results achieved are compared to the ball milling technique.

The objectives to be achieved are:

- Identification of the optimum conditions to prepare nanostructured n- and p-type bismuth telluride powders by ultrasound and ball milling methods.
- Identification of the most suitable conditions to prepare nanostructured bulk samples by hot pressing method from the powders prepared.
- Morphological, structural and thermoelectric characterisation of the materials fabricated by these two milling techniques.
- Correlate the thermoelectric performance to the microstructure of the nanobulk materials characterised.
- Demonstrate the capability to integrate the fabricated nanobulk materials into a thermoelectric device.

1.3 Thesis outline

1.3.1 Chapter 1: Introduction

In chapter 1, a brief contextualization of the research is introduced. The main achievements of this thesis are summarised and it provides an outline of the thesis, where a short explanation of every chapter is shown.

1.3.2 Chapter 2: Introduction to thermoelectricity and state-of-the-art

Chapter 2 presents a review of the history of thermoelectricity and its fundamentals. It includes a brief description of the main thermoelectric materials currently under research. The most widely used strategies to enhance the performance of the thermoelectric materials

are also exposed. Finally, the most common nanostructuring methods and the techniques employed to fabricate bulk thermoelectric materials are reviewed.

1.3.3 Chapter 3: Experimental methods

The third chapter covers the experimental methods and techniques employed in this thesis for the preparation and characterisation of thermoelectric materials and modules. Firstly, the two experimental methods of fabrication of bismuth telluride nanoparticles are described, the ball milling and the novel ultrasound milling. Then, a description of the techniques employed to characterise the powders is presented, which include particle size, morphology and structural characterisation. Finally, the methods employed for the thermoelectric characterisation of bulk materials are shown.

1.3.4 Chapter 4: Preparation of bismuth telluride nanopowder

The fourth chapter focuses on the evaluation of the optimum parameters to prepare n- and p-type bismuth telluride nanoparticles by ball milling and ultrasound milling methods. Balls:powder ratio and time were optimised for the ball milling technique while in the ultrasound milling method conditions such as solvent, time, amplitude of the ultrasound, cooling systems and powder concentration. To perform the optimisation, the resulting powders are analysed using a particle size analyser, SEM and XRD. Finally, in the last section a comparison of both methods is shown.

1.3.5 Chapter 5: Optimisation of the hot press compaction method

This chapter describes the construction of a hot press from a standard press. It also shows the optimisation of the sintering method (time, temperature and pressure) for the fabrication of highly dense nanostructured bulk disc samples from the powders by hot pressing.

1.3.6 Chapter 6: Thermoelectric properties of nanobulk materials

Chapter 6 includes the structural and thermoelectric characterisation of the n- and p-type bismuth telluride nanobulk samples prepared under the optimised conditions of the previous chapter. Firstly, the non-treated samples (simply crushed in an intimal pre-treatment) are analysed. Then, the results of the characterisation of the samples produced by ultrasound and ball milling methods under the optimised conditions are presented.

1.3.7 Chapter 7: Thermoelectric modules fabrication

In this chapter, the fabrication and characterisation of thermoelectric modules is shown. These modules are prepared using the reference materials (from the commercial ingots) and the best performing materials prepared in the thesis. In the module fabrication process the soldering treatment is optimised and then the module ZT is determined by impedance spectroscopy to evaluate the performance of the devices.

1.3.8 Chapter 8: Conclusions and future work

Chapter 8 comprises a summary of the main achievements and conclusions of this thesis and some proposals for future work.

Chapter 2 : Introduction to Thermoelectricity and State-of-the-art

2.1 Introduction

2.2 History of thermoelectricity

2.3 Thermoelectric effects

2.3.1 Seebeck effect

2.3.2 Peltier effect

2.3.3 Thomson effect

2.3.4 Kelvin relationships

2.4 Thermoelectric devices

2.4.1 Structure of thermoelectric generators

2.4.2 Conversion efficiency and Power output

2.5 Thermoelectric materials

2.6 Strategies to improve ZT

2.7 Nanostructuring methods

2.8 Methods to prepare nanobulk thermoelectric materials

Chapter 2

2.1 Introduction

The aim of this chapter is to provide an overview of the history of thermoelectricity, its fundamentals and the main thermoelectric materials currently under development. In addition, the most common strategies to improve the performance of thermoelectric materials are also briefly reviewed.

On the other hand, since the research developed in this thesis is related to the nanostructuring of materials, a review of the state-of-the-art of the current nanostructuring methods is provided, including the different techniques to prepare compacted nanobulk thermoelectric materials from nanostructured powders.

2.2 History of thermoelectricity

The history of thermoelectricity commenced in 1822 when Thomas Johann Seebeck reported⁽¹¹⁾ the deflection of a compass needle in a circuit formed by two different conductors with the junctions at different temperatures. Seebeck initially thought that this was due to a magnetic effect produced by the temperature difference. However, Hans Christian Ørsted explained the actual physics of the phenomenon. The movement of the needle was caused by a magnetic field induced by an electric current flowing in the circuit.⁽¹²⁾ This current was due to the movement of electrical charges (electrons or holes) away from the heat source.

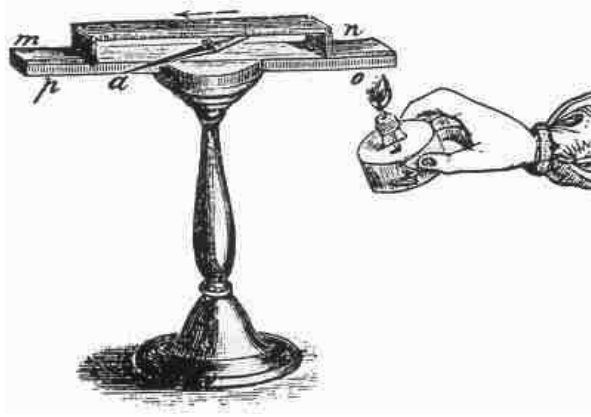


Fig. 2.1. Instrument used by Seebeck for the discovery of the Seebeck effect.⁽¹³⁾

In 1834, Jean Charles Peltier discovered the *Peltier effect*. He noticed that when a current passed across a circuit formed by two dissimilar conductors a change in temperature at the proximity of the junctions was observed. Despite the physical explanation for the Seebeck effect was known at that time, he was unable to explain the nature of his observations. However, in 1838 Lenz⁽¹⁴⁾ performed an experiment to explain the Peltier effect, consisting in freezing water at a bismuth-antimony junction and melting ice back by reversing the direction of the current. That proved that depending on the direction of the current flow, heat was absorbed or generated at the junction.

In the late 1860s, the first design of a thermoelectric generator (TEG) was developed by M. Clamond. He used a thermoelectric battery made of iron combined with zinc-alloyed antimony to generate electricity for lighting. This design was employed to produce light at some companies in Paris since 1875 and also at the Royal Albert Hall in London.⁽¹⁵⁾ However, these systems utilised metallic junctions with low conversion efficiency and, as a consequence, the devices were very bulky. The first commercial TEG available in the United Kingdom appeared in 1925, the gas-powered Thermattaix. It was used for charging batteries in radio devices.

Rayleigh, although incorrectly, was the first one to calculate the efficiency of a TEG in 1885. In 1909⁽¹⁶⁾ and 1911⁽¹⁷⁾ Altenkirch developed a theory of thermoelectric generation and refrigeration and presented the characteristics that a good thermoelectric material should show.

Thermoelectricity experienced a growth in the late 1930s due to the development of semiconductor materials, which presented absolute Seebeck coefficients above $100 \mu\text{V}/\text{K}$, and the fabrication of a generator that operated with an efficiency around 5 % in 1947 by Telkes.⁽¹⁸⁾ In addition, the use of p- and n-type PbS semiconductors by Abram Fedorovich Ioffe drove him in 1950 to publish the theory of thermoelectric energy conversion by semiconductors.⁽¹⁹⁾

Nowadays, this theory is used worldwide to characterise new materials employing the “thermoelectric figure of merit” $Z=\alpha^2\sigma/\lambda$, where α is the thermopower or Seebeck coefficient, σ is the electrical conductivity and λ is the thermal conductivity. Apart from these contributions, it is worth mentioning his ring-shaped TEG used with paraffin lamps to power radio devices.⁽¹⁹⁾

In 1951,⁽²⁰⁾ W. Thomson (Lord Kelvin) published the relationship between the Seebeck and Peltier coefficients and prognosticated another thermoelectric effect called the *Thomson effect*, which describes the heating or cooling within a single homogeneous conductor when a current passes through it under a temperature gradient. Afterwards, he observed this effect experimentally.

Inspired by possible military applications, an enormous effort to produce new thermoelectric materials was carried out in the late 1950s, resulting in the preparation of few semiconductors with ZT around 1.5, with T the absolute temperature⁽²¹⁾. Bi_2Te_3 or $\text{Si}_{1-x}\text{Ge}_x$ alloys were widely investigated for their use in thermoelectric applications⁽²²⁾. Based on these systems, Ioffe prepared different temperature materials such as PbSe-PbTe and $\text{Bi}_2\text{Te}_3\text{-Sb}_2\text{Te}_3$,⁽¹⁴⁾ which were utilised to produce new devices which showed high efficiencies. However, these devices presented some disadvantages such as high price, toxicity, and scarcity of the materials used. Bismuth telluride was used at low temperatures in sensors in thermal vision systems and heat-seeking missiles.⁽²³⁾

Only nearly 10 years later, in the early 1960s, some applications emerged to use TEGs for autonomous sources of electric power for the space, medical physics and Earth’s resources exploitation in remote locations.⁽²⁴⁾ Moreover, at that time, another significant development emerged, which was the use of SiGe in high temperature devices such as radioisotope TEGs. These devices convert heat released from nuclear materials into electricity^(25, 26) and they can operate unattended for prolonged periods. In the 1990s, NASA employed this technology in satellites, deep-space probes and lunar or planetary landers.

Due to the increment of the price of crude oil in 1974, the problem of the damage of the ozone layer in the late 1980s, and the spreading interest in environmentally friendly energy sources, the use of thermoelectric generation as a source of large-scale electric power using waste heat^(27, 28) lived an important revival. In fact, over the past two decades, new concepts of materials, including bulk and thin-film, complex structures and geometries, material synthesis, theory and characterisation have been introduced.

The concept of phonon glass electron crystal, designed by Glen Slack⁽⁴⁾ was used to investigate bulk thermoelectric materials, thin-film and superlattice structures, and electric and heat transport across interfaces. He conjectured that a good thermoelectric material should possess the electrical properties of a crystalline material and the thermal properties of a glass.

On the other hand, in 1993, Hicks and Dresselhaus predicted that higher ZT values could be achieved when the dimensions of thermoelectric materials are reduced in quantum well structures (quantum confinement).^(5, 29) The ZT improvement is produced as a result of enhancing the density of states which causes higher mobility and thermopower when the quantum well width reduces from a “bulk-like” term. Their predictions were verified in a large number of experiments and the belief still endures.⁽³⁰⁻³⁴⁾

Glen Slack gave a talk at the 1998 Fall Materials Research Society meeting under the title “Holey and Unholy Semiconductors and Thermoelectric Refrigeration Materials” where the term holey semiconductors or cage-structure materials that use “rattling” atoms to scatter phonons and reduce the lattice thermal conductivity of a material was presented.⁽³⁵⁾ Skutterudites are an example of a holey semiconductor, whereas half-Heusler alloys, BiSb and quasicrystals are unholey materials. The last ones reduce the lattice thermal conductivity depending on ordinary scattering mechanisms, such as mass fluctuation scattering.

In the late 1980s, considerable progress was made in the miniaturization of thermoelectric devices, specially detectors and sensors^(36, 37) and power sources.⁽³⁸⁾ From 1970s until 1996 a significant amount of the research on thermoelectric materials was published in conference proceedings and for this reason there are not very abundant publications in scientific journals from that period.

2.3 Thermoelectric effects

Thermoelectricity refers to the coupling of thermal and electrical phenomena in a material and offers a route by which thermal energy can be transformed into electricity and electricity can be used for heating or refrigeration.

There are three thermoelectric effects, the Seebeck effect, the Peltier effect and the Thomson effect. They are interrelated by the Kelvin relationships and form the basis of thermoelectricity.

2.3.1 Seebeck effect

The Seebeck effect was discovered in 1822 by Thomas Johann Seebeck.⁽¹¹⁾ This effect describes that when a temperature difference is applied across the junctions of two dissimilar conductors, a voltage difference is produced at open circuit as shown in Fig. 2.2.

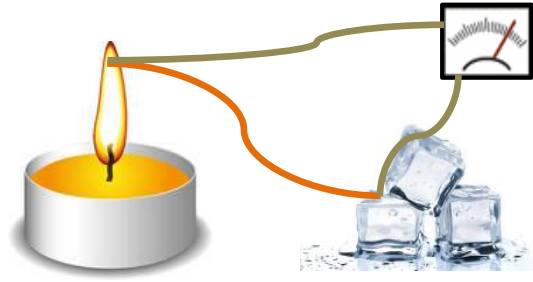


Fig. 2.2. Illustration of the Seebeck effect where two different conductors (orange and green), forming an electrical circuit, produce a voltage under a temperature difference at their junctions.

The voltage difference V_{ab} or Seebeck voltage is given by,

$$V_{ab} = \alpha_{ab} \Delta T \quad (2.1)$$

where $\Delta T = (T_{\text{Hot}} - T_{\text{Cold}})$ is the temperature difference between the hot and cold junctions and $\alpha_{ab} = \alpha_a - \alpha_b$ is the relative Seebeck coefficient. When material a is a good thermoelectric material ($|\alpha_a| > 100 \mu\text{V/K}$) and metallic leads, which present Seebeck coefficient values of a few or tens of $\mu\text{V/K}$, are used as material b to measure the voltage difference, $\alpha_a \gg \alpha_b$ and $\alpha_{ab} \approx \alpha_a$. On the other hand, the Seebeck coefficient varies as a function of temperature and hence it is typically defined under a small temperature difference,

$$\alpha_{ab} \approx \frac{V_{ab}}{\Delta T}, \quad \Delta T \rightarrow 0 \quad (2.2)$$

The Seebeck voltage is conventionally measured vs the hot side and it can be positive (p-type semiconductors) or negative (n-type semiconductors).^(24, 39) When heat is applied to one of the junctions, the majority charge carriers (electrons or holes) at this side acquire higher energy than the ones at the cold side, so the hot carriers diffuse from the hot to the cold side.

When a thermoelectric device converts heat into electricity, it is said that it is operating in Seebeck mode and it is called a *generator*.

2.3.2 Peltier effect

The Peltier effect was discovered in 1834 by the physicist Jean Charles Peltier.⁽⁴⁰⁾ This effect is the opposite of the Seebeck effect. In this case, when a voltage is applied to a circuit formed by two different conductors an electric current flows through the circuit and one of the junctions becomes hot and the other becomes cold. This temperature change at the junctions is a consequence of the gain/release of energy when the carriers move through the junction of the two materials, leading to heat absorption/dissipation respectively (see Fig.

2.3). The heating/cooling at the junctions is reversed if the direction of the current is switched. This effect is the basis of the thermoelectric heating and refrigeration.

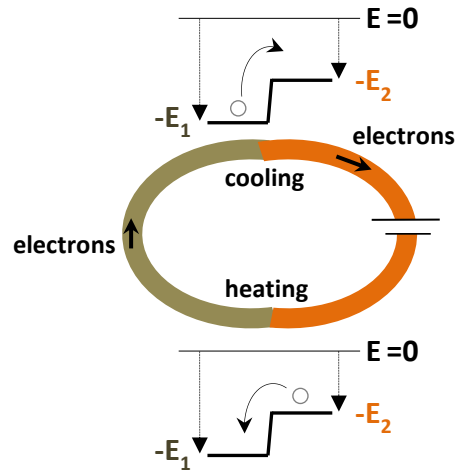


Fig. 2.3. Diagram of the Peltier effect in a circuit formed by 2 dissimilar conductors (orange and green). When electrons cross the top junction they have to absorb energy, producing cooling. The opposite occurs at the bottom junction where electrons release energy when they cross it, producing heating.

The Peltier coefficient determines the magnitude of the heating or cooling that happens at a junction of two different materials. It has dimensions of volts (V). Therefore, the Peltier coefficient measured under isothermal conditions ($\Delta T=0$, both junctions are kept at the same temperature), is defined as

$$\pi_{ab} = \frac{Q}{I}, \quad \text{at } \Delta T = 0 \quad (2.3)$$

Where $\pi_{ab}=\pi_a-\pi_b$ is the relative Peltier coefficient, I is the electric current flowing through the circuit and Q is the heat transfer rate at the junction, or alternatively, it can be defined as the amount of heat removed per unit time from one junction to another.

When a thermoelectric device pumps heat from one junction to another, it is operating in Peltier mode and it is called a *refrigerator* or a *heater*.

2.3.3 Thomson effect

The Thomson effect was discovered in 1851 by the physicist William Thomson (Lord Kelvin).⁽²⁰⁾ This effect describes the absorption or dissipation of heat across a homogeneous conductor when subjected simultaneously to a temperature difference and an electric current.⁽⁴¹⁾

The Thomson coefficient β is determined by the total heat (absorption or dissipation) rate Q_T in a single material per unit current and temperature difference. The dimensions of the Thomson coefficient are V/K.

$$\beta = \frac{Q_T}{I \cdot \Delta T} \quad (2.4)$$

Despite the fact that this effect is present in all thermoelectric devices and its contribution can be significant especially when a large temperature difference exists across the device,⁽⁴²⁾ it is normally ignored in the evaluation of the devices due to its low value which is usually much smaller than Joule heating.

2.3.4 Kelvin relationships

The Kelvin relationships were published by Lord Kelvin.^(14, 24, 39) They provide the relationship between the three thermoelectric coefficients, which are interrelated. Furthermore, from these relationships it is clearly understood that the three thermoelectric effects occur together in any thermoelectric device under operation (electrical current and temperature difference). These relationships were derived from the first and second laws of thermodynamics.

The Seebeck and Peltier effects are linked by the following equation,

$$\pi_{ab} = \alpha_{ab} \cdot T_j, \quad (2.5)$$

where T_j is the temperature at the junction. This equation provides a straightforward way to determine the Peltier coefficient, since measuring voltages and temperatures, required in the Seebeck coefficient, is easier than measuring precisely the heat absorption or dissipation at the junctions, which is needed for a direct calculation of the Peltier coefficient. Moreover, this equation suggests that materials that are appropriate for power generation are also suitable for refrigeration due to its direct relationship.

The Seebeck and Thomson coefficients are related by,

$$\frac{d\alpha_{ab}}{dT} = \frac{\beta_a - \beta_b}{T} \quad (2.6)$$

2.4 Thermoelectric devices

As was mentioned above, thermoelectric devices can operate as heaters or refrigerators (Peltier mode) or power generators (Seebeck mode). Its operation as heaters is

much less common, since other devices operate more efficiently. Thermoelectric devices have been employed in diverse applications for both operating modes.^(21, 43) However, since the focus of this thesis is on energy harvesting, only the power generation operation is described in this section.

2.4.1 Structure of thermoelectric generators

The basic unit of a thermoelectric device or thermoelectric module (TEM) is a couple (also called thermocouple) of two doped semiconductor legs, one p-type and the other n-type, connected electrically in series by metallic strips (usually copper) acting as electrodes as shown in Fig. 2.4. The structure of a module consists essentially of multiple thermocouples connected electrically in series but thermally in parallel⁽⁴⁴⁾ and finally sandwiched between two thermal insulator materials (usually ceramic plates) which constitute the substrates of the device, as shown in Fig. 2.5.

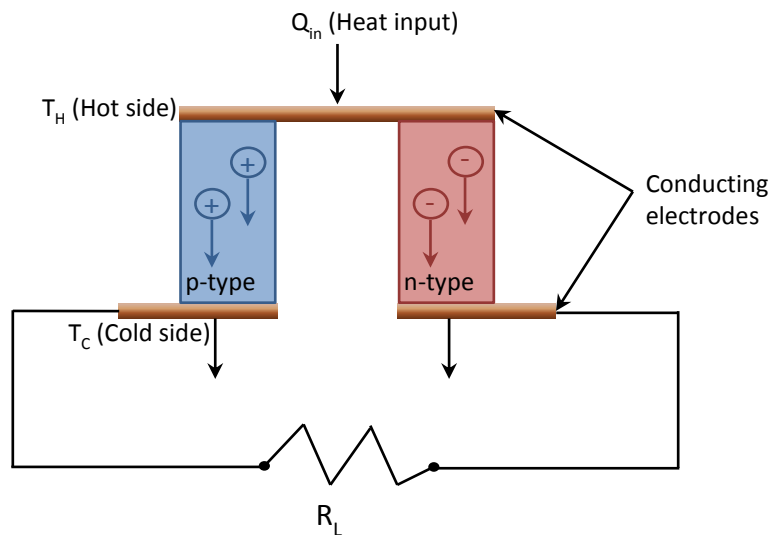


Fig. 2.4. Basic unit (thermocouple) of a thermoelectric device under Seebeck mode operation. The electric power generated is delivered to the load resistance R_L .

Under operation, the external heat source is applied to the hot side ceramic and a heat sink is attached to the ceramic at the cold side, which removes the heat and keeps the cold side as cold as possible.

Highly-doped semiconductor materials are typically selected in the devices, since they exhibit the best thermoelectric properties. Bismuth telluride is the most widely used material in temperature ranges from room temperature to around 250 °C. For higher temperature ranges, such as the ones required for automotive and industrial applications,^(45, 46) other materials like cobalt oxides, silicides, skutterudites and sulfides are being explored.

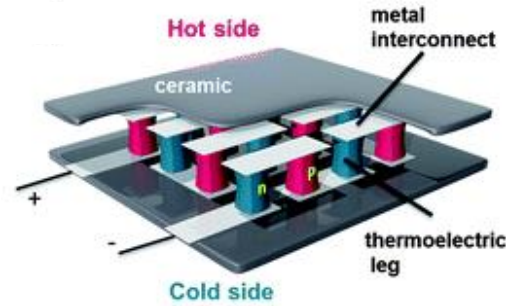


Fig. 2.5. Sketch of a thermoelectric device.⁽⁴⁷⁾

2.4.2 Conversion efficiency and Power output

The conversion efficiency η and power output P are the two main parameters which determine the performance of a TEM. These parameters can be evaluated by the simplistic theoretical model developed by Ioffe,⁽¹⁴⁾ which does not consider the influence of the thermal and electrical resistances of the ceramics and metal strips. A more complete theory that considers the influence of the ceramic and metal strips is available elsewhere.⁽⁴⁸⁻⁵⁶⁾

The conversion efficiency is presented here for only one thermocouple for simplicity. A real device possesses N of these pairs and hence the theory can be easily adapted by multiplying/dividing by N in the corresponding terms.

The conversion efficiency is given by the relation between the power delivered to the load and the heat input at the hot side,

$$\eta = \frac{P}{Q_{in}}. \quad (2.7)$$

At steady-state the voltage difference at the load V_L is given by,

$$V_L = IR_L = \alpha_{np}\Delta T - IR, \quad (2.8)$$

being R_L the load resistance, $\alpha_{np}\Delta T$ the open-circuit voltage, with $\alpha_{np}=\alpha_p-\alpha_n$ the total Seebeck coefficient of the couple, and IR the voltage drop due to the electrical resistance R of both n and p -type thermoelectric materials. From Eq. (2.8), the current can be determined as,

$$I = \frac{\alpha_{np}\Delta T}{R + R_L}. \quad (2.9)$$

Finally, the power output $P=IV_L$ can be obtained as,

$$P = \left(\frac{\alpha_{np}\Delta T}{R+R_L} \right)^2 R_L. \quad (2.10)$$

If $m=R/R_L$ is the ratio between the resistance of the thermoelectric elements and the load resistance,

$$P = \frac{m}{(1+m)^2} \frac{(\alpha_{np}\Delta T)^2}{R}. \quad (2.11)$$

The maximum power output can be obtained by adjusting the ratio m , which is maximum when $R_L=R$, resulting in a maximum power output,

$$P_{max} = \frac{(\alpha_{np}\Delta T)^2}{4R} \quad (2.12)$$

It can be seen from Eq. (2.12) that the maximum power output increases parabolically with the increase in the temperature difference. However, this parabolic relationship is not perfect due to the variation with temperature of α_{np} and R .

Once the power output has been obtained, we need to calculate the heat input in order to provide the efficiency. It can be calculated using the heat balance at the hot junction, where Peltier heat and thermal conductivity (Fourier's law) take place. Q_{in} is given by,

$$Q_{in} = \alpha_{np}IT_H + K(T_H - T_C) - \frac{1}{2}I^2R, \quad (2.13)$$

where K is the total thermal conductance of the thermoelectric couple. It should be noticed that half of the Joule heating appears in the equation since this effect modifies the temperature gradient dT/dx at the junction, which governs the conduction of heat. Finally, the conversion efficiency of a thermoelectric couple is given by,

$$\eta = \frac{P}{Q_{in}} = \frac{I^2R_L}{\alpha_{np}IT_H + K(T_H - T_C) - \frac{1}{2}I^2R}, \quad (2.14)$$

which can be rewritten as,

$$\eta = \left(\frac{T_H - T_C}{T_H} \right) \left[\frac{m}{(1+m) - \left(\frac{T_H - T_C}{2T_H} \right) + \frac{(1+m)^2}{ZT_H}} \right], \quad (2.15)$$

where $Z = \alpha_{np}^2 / (RK)$ is known as the thermoelectric figure of merit, which also equals for the case of a single material to $Z = \alpha^2 \sigma / \lambda$. As occurred with the power output, the conversion

efficiency also depends on the ratio m and it is maximised when $m = \sqrt{1 + ZT_{avg}}$. Therefore, the maximum conversion efficiency is given by,

$$\eta_{max} = \left(\frac{T_H - T_C}{T_H} \right) \frac{\sqrt{1 + ZT_{avg}} - 1}{\sqrt{1 + ZT_{avg}} + \frac{T_C}{T_H}}, \quad (2.16)$$

where T_{avg} is the mean temperature across the thermoelements, $T_{avg} = (T_H + T_C)/2$ and $(T_H - T_C)/T_H$ corresponds to the Carnot efficiency, that is the theoretical maximum efficiency of an energy convertor between a heat sink and a heat source. It can be observed from Eq. (2.16) that in order to have high efficiencies, both ΔT and Z should be as large as possible. Since Z only depends on materials properties, it is used as the main parameter to quantify in order to assess the performance of a thermoelectric material. When Z is multiplied by the temperature at which the materials properties have been measured, it becomes the dimensionless figure of merit ZT .

2.5 Thermoelectric materials

Since thermoelectricity commenced in 1822, numerous investigations about new thermoelectric materials have been performed to develop materials with higher ZT values. There is a wide range of thermoelectric materials which have been developed over the time. In this section, we briefly show the most promising and more intensively studied ones. It has to be taken into account that every material has an optimum operating temperature and accordingly they are useful for different applications.

Chalcogenide compounds

They have been studied since the discovery of semiconductors. Most of them are semiconductors, stable in air and possess high melting points. They are mainly formed by sulphur, selenium, tellurium and bismuth in different stoichiometry to obtain semiconductors with pertinent energy gaps for thermoelectric applications (0.1-0.8 eV). The two most important chalcogenide systems which have been investigated for a long time are Bi_2Te_3 for room temperature and PbTe for intermediate temperatures.

Bismuth telluride (Bi_2Te_3) is the main thermoelectric material for room temperature (300-500 K) applications and therefore for thermoelectric cooling technology. It is a semiconductor with an indirect bandgap of approximately 0.15 eV. Due to this, it is a partially degenerated semiconductor, with the Fermi level close to the conduction band at room temperature. The material presents high carrier concentration, which can be modified by

using an excess of bismuth or tellurium or dopant impurities that could be from the group IV and V and also halogens atoms. It crystallises in a rhombohedral structure with five atomic layers stacked, where the bismuth atoms are coordinated with six tellurium atoms and every block of five atomic layers is connected by van der Waals forces along the c-axis. It presents for this reason anisotropic properties. The p-type Bi_2Te_3 is comprised of Sb as in the formula $\text{Bi}_{2-x}\text{Sb}_x\text{Te}_3$ ($x \approx 1.5$), while the n-type has the form $\text{Bi}_2\text{Te}_{3-y}\text{Se}_y$ ($y \approx 0.3$). Both show similar ZT values of around 1.

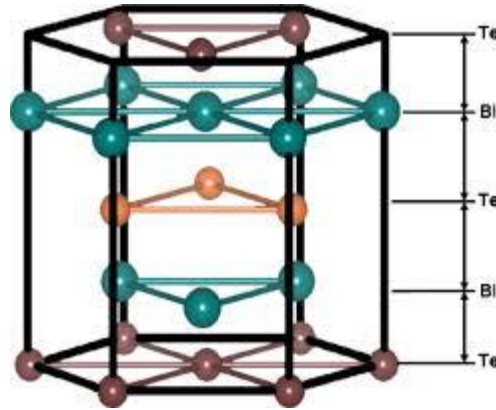


Fig. 2.6. Schematic of the rhombohedral structure of quintuple layer of Bi_2Te_3 .⁽⁵⁷⁾

Nanostructuring of Bi_2Te_3 provides a way to increase its ZT value. In the case of the p-type, a nanostructured $\text{Bi}_{0.5}\text{Sb}_{1.5}\text{Te}_3$ material subsequently sintered using a simple liquid-phase compacting process has been reported to present the highest $\text{ZT} \approx 1.86$ at 320 K.⁽⁵⁸⁾ The compaction process was performed applying pressure and transient flow of the liquid phase. It is a material made with periodic dislocations at low-energy grain boundaries. The reason for this ZT enhancement is the diminution of the lattice thermal conductivity by phonon scattering. On the other hand, the highest ZT value for the nanostructured n-type counterpart was 1.25 at 420 K, being the material prepared using hydrothermal synthesis with nanotubes embedded in a Bi_2Te_3 matrix, grown by the zone melting technique.⁽⁵⁹⁾

Other Bi_2Te_3 systems have been prepared that show ZT of 2.4 at room temperature.⁽⁶⁰⁾ These systems are thin-film materials called superlattices and are comprised of an alternating assembly of nanosize films of Bi_2Te_3 and Sb_2Te_3 . This extraordinarily high ZT value is explained to be due to two factors: an extremely low lattice thermal conductivity ($\approx 0.24 \text{ W/m}\cdot\text{K}$) caused by phonon back reflection at the $\text{Bi}_2\text{Te}_3/\text{Sb}_2\text{Te}_3$ interfaces and cross-plane and in-plane electron mobility are equal. It has not been reported yet a validation of this ZT value.⁽⁶¹⁾

PbTe is the other well studied chalcogenide material used in applications in the mid-range temperature 600-900 K. It is an isotropic material and crystallises in the NaCl structure where Pb atoms occupy the Na sites and the Te the anionic sites. Its bandgap (0.32 eV)⁽⁶¹⁾ is slightly larger than in Bi_2Te_3 . Its thermal conductivity is quite high at room temperature ≈ 2.2

$W/m\cdot K^{(61)}$ but it decreases in the ratio $1/T$ with increasing temperature. The most successful ways of improving the thermoelectric properties of this material have been achieved by means of nanostructuring and by modification of the density of states to create resonance levels in the conduction band for the increase of the Seebeck coefficient. Since nanostructured PbTe have a wide variety of thermal and charge-transport properties, it will be studied within the nanostructured materials below.

Following these two approaches, PbTe can be doped with n- and p-dopants which can insert electronic states able to resonate with the PbTe matrix.⁽⁶²⁻⁶⁵⁾ In this direction a system consisting of PbTe:TI, where TI was added to the matrix, achieved a large ZT of 1.5 at 773 K.⁽⁶⁶⁾ The maximum ZT reported was 1.8, reached at 850 K using Na as dopant in the $PbTe_{1-x}Se_x$ alloy.⁽⁶⁷⁾ Snyder's group demonstrated that either TI or Na modifies the electronic structure of the crystal, raising the electrical conductivity. They also confirmed that Se increases the electrical conductivity and decreases the thermal conductivity.

One of the drawbacks of these compounds is the use of lead which is very toxic. Moreover, tellurium shows low abundance. All this makes these compounds expensive and limit their application.

Skutterudites

They are single-phase materials and crystallise in the $CoAs_3$ -type cubic structure, which is an altered version of the perovskite AB_3 structure. They are formed by an eight corner-shared XY_6 (X: Co, Rh, Ir and Y: P, As, Sb) octahedral. The cluster $(XY_6)_8$ shows a void at the centre of the cubic lattice where the eight octahedrons are linked. Consequently, the structure of these materials are $M_2X_8Y_{24}$ where M are the voids that can be filled with rare elements or alkaline-earth elements and Y are pnictogen atoms (e.g. $[P_4]^{4-}$, $[As_4]^{4-}$, etc).

The first skutterudite prepared was $CoSb_3$ which presented a very high power factor, but its thermal conductivity at room temperature was very high (10 $W/m\cdot K$). Researchers intended to improve this material by filling the central void with low-coordination ions (usually rare elements, the smaller and heavier the ion, the larger the disorder it produces, resulting in greater decrease in the lattice thermal conductivity), which can improve the thermoelectric properties by mainly reducing the thermal conductivity without decreasing the electrical conductivity.⁽⁶⁸⁻⁷⁰⁾ Even though it is thought that reduction of the thermal conductivity produced by the void-filled atoms is due to the "rattling" property, it has not been demonstrated that "rattling" induces phonon scattering, since there are other effects such as lattice disorder and point defects that cannot be separated from "rattling" effects. The skutterudite antimonides present a prominent position to be studied for thermoelectric applications since they show the largest voids.

Some examples of ZT larger than 1 are $\text{Ba}_{0.30}\text{Ni}_{0.05}\text{Co}_{3.95}\text{Sb}_{12}$ ($\text{ZT}\approx 1.25$ at 900 K)⁽⁷¹⁾ and $\text{Ca}_{0.18}\text{Ni}_{0.03}\text{Co}_{3.97}\text{Sb}_{12.4}$ ($\text{ZT}\approx 1$ at 800 K),⁽⁷²⁾ and it was reported that partially filling the void produces higher ZT than the full filling. Without adding any Ni, the ZT decreases significantly, as in $\text{Ba}_x\text{Co}_4\text{Sb}_{12}$ ($\text{ZT}\approx 0.8$ at 800 K)⁽⁷³⁾ and $\text{Ca}_x\text{Co}_4\text{Sb}_{12}$ ($\text{ZT}\approx 0.45$ at 800 K).^(70, 74)

Half-Heusler (HH) Intermetallic compounds

They are single-phase materials, very promising for power generation at high temperatures (800-1000 K), since they have high melting points (1100-1300 °C) and chemical stability, with no sublimation at temperatures close to 1000 °C. Other advantages of these materials are their relatively simple synthesis and the fact that they are fairly cheap.⁽⁷⁵⁾ Moreover, due to their large Seebeck coefficient at room temperature (100 $\mu\text{V}/\text{K}$) and high electrical conductivities (1000-10000 S/cm),⁽⁷⁶⁻⁸⁰⁾ these compounds have been investigated in depth for thermoelectric applications.

The HH intermetallic alloys present a general structure XYZ, which consists of two transition metals XY and the other element Z from a main-group (metal or metalloid).⁽⁴¹⁾ The most common formulation is XNiSn (X: Ti, Hf, Zr) and the crystal structure consists of three filled interpenetrating face centred cubic (FCC) sublattices and one vacant sublattice.

One of the HH alloy systems is the TiNiSn where Ti and Sn crystallise in the NaCl structure and Ni occupies the FCC sublattice. Meanwhile the Heusler intermetallic compounds have a fully filled sublattice with metals (full-Heusler alloys), the HH compounds with the Ni vacant sites provoke the formation of d-orbital hybridisation and a considerable semiconductor character is achieved.^(41, 81-83) As a consequence, these compounds present large effective mass and large thermopower.⁽⁷⁶⁾

The highest ZT value reported for HH alloys was around 1.4 at 700 K for n-type $(\text{Zr}_{0.5}\text{Hf}_{0.5})_{0.5}\text{Ti}_{0.5}\text{NiSn}_{1-y}\text{Sb}_y$,⁽⁸⁴⁾ but it has not been possible to reproduce it. It has been predicted that Co-, Rh- and Fe-based HH alloys could be good p-type materials whereas others like LaPdBi (n-type) might present a large power factor.

Silicide compounds

They are good thermoelectric materials for the mid-temperature range, since their figure-of-merit is of the same order of magnitude ⁽⁸⁵⁻⁹²⁾ as other materials used nowadays. They present high abundance of their precursor materials (silicon is the second highest abundant material in the earth's crust and magnesium the eighth⁽⁹³⁾), low production cost, and are environmentally friendly.

Magnesium silicide compounds have $\text{Mg}_2(\text{Si-Sn})$ molecular formula and their density is quite low $\approx 3 \text{ g}/\text{cm}^3$ compared to other thermoelectric materials like Bi_2Te_3 ($7.93 \text{ g}/\text{cm}^3$) and PbTe ($8.27 \text{ g}/\text{cm}^3$), which leads to very light devices. They crystallise in the antifluorite

structure where Mg occupies tetrahedral positions and Si FCC positions. In contrast to pure compounds, the Mg_2Si and Mg_2Sn compounds and their solid solutions present a very low thermal conductivity. Although they have been intensely studied⁽⁹⁴⁾ there is still more room for improvement of their performance.

Undoped $Mg_2(Si-Sn)$ based materials show a small $ZT \approx 0.18$ at 540 K,⁽⁹⁵⁾ and the highest ZT reported increased from ≈ 0.4 at 500 K⁽⁹⁴⁾ to 1.3 at 740 K⁽⁹⁶⁾ for the compound $Mg_2Si_{0.6}Sn_{0.4}$.

Silicon germanium

These alloys are excellent for high temperature (over 1000 K) applications. Their usage is limited by their high price, mainly due to germanium. They present a very high stability since they can operate up to 1300 K without performance degradation. The ideal composition is typically $Si_{0.8}Ge_{0.2}$.⁽²¹⁾ Similarly to other materials, nanostructuring generates higher ZT values as the SiGe composite with $ZT \approx 1.5$ at 1173 K.⁽⁹⁷⁾ In contrast, at the same temperature its bulk (non-nanostructured) alloy has almost half $ZT \approx 0.9$.⁽²¹⁾

Due to its robustness and high performance at high temperatures, their applications have been focused on radioisotope thermoelectric generators for spacecraft.⁽²¹⁾

Metal oxides

They are single-phase materials and very promising at high temperatures (900-1000 K) due to their high thermal and chemical stability (high oxidation resistance) in air, large thermopower, low thermal conductivity and non-toxicity. On the other hand, these compounds present crucial disadvantages such as low ZT values for the moment and problems in the fabrication of modules, which present quite high contact resistances at the oxide/metal electrode junction. In addition, during operation cycles they suffer cracking or exfoliation of the pellets due to differences in the thermal expansions.⁽⁹⁸⁾

The structure of p-type metal oxides based on Co is $MCoO_2$ (M: metal), in which CoO_2 layers are formed and serve as electronic transport sheets. These layers seem to be the main reason for their good thermoelectric performance. Moreover, the intercalated Na ions serve as phonon-scattering zones and produce low thermal conductivity.

The first p-type oxide that showed significant thermoelectric properties was Na_xCoO_2 . A clear example is $NaCo_2O_4$, which presents a good thermopower ($150 \mu V/K$) due to its large entropy.^(99, 100) As a single-crystal, this material shows $ZT > 1$ at 800 K,⁽¹⁰¹⁾ whereas for polycrystalline compound the ZT is ≈ 0.8 at 1000 K.^(102, 103) Other composites like $Ca_3Co_4O_9$,⁽¹⁰⁴⁾ $(Bi,Pb)_2Sr_2Co_2O_8$,⁽¹⁰⁵⁻¹⁰⁷⁾ $TiSr_2Co_2O_y$,⁽¹⁰⁸⁾ and $(Hg,Pb)_2Sr_2Co_2O_y$ ⁽¹⁰⁹⁾ show good thermoelectric performance.

On the other hand, n-type metal oxides present lower ZT values. In the best of the cases a $ZT \approx 0.37$ at 1000 K for SrTiO_3 highly doped with Nb was found.⁽¹¹⁰⁾ Similar to p-type oxides, n-type counterparts present large Seebeck coefficients, however the thermal conductivity is very high (10 W/m·K at 300 K).

Recent new materials

- *Organic thermoelectrics*: despite organic materials have been studied for a long time, thermoelectric measurements of organic materials⁽¹¹¹⁾ and conducting polymers⁽¹¹²⁾ were performed in the 1970s. It was not until the 21st century when organic materials, particularly conductive polymers,⁽¹¹³⁻¹¹⁵⁾ were considered as strong candidates for thermoelectric applications.

Contrary to the conventional inorganic thermoelectric materials mentioned above that typically present high cost of production, scarcity and toxicity, which restrict their use in everyday life, organic thermoelectric materials show numerous advantages such as low cost, earth abundant materials, light weight, flexibility, large area deposition, low temperature solution processability, and innate low thermal conductivity. These benefits make organic thermoelectric semiconductors to be also considered for wearable devices operated by body heat and flexible devices.⁽¹¹⁶⁻¹¹⁸⁾ They also show electronic structures that can be easily modified by chemical and doping treatments.⁽¹¹⁹⁾ In spite of all these advantages, organic thermoelectric materials show some drawbacks such as poor stability due to their sensitivity to moisture and oxygen and low carrier mobility which affects the electrical conductivity.

Most organic thermoelectric materials are based on π -conjugated polymers (or conducting polymers) such as polyacetylene, polypyrrole, polythiophene, polyaniline, polyphenylene and poly(3,4-ethylenedioxythiophene) (PEDOT). In addition, small organic molecules such as pentacene, fullerene, tetrathiafulvalene (TTF) and 2,3,5,6-tetrafluoro-7,7,8,8-tetracyanoquinodimethane (F_4TCNQ) have also been studied. The highest ZT achieved for a conducting polymer is 0.45⁽¹²⁰⁾ at room temperature for PEDOT:PSS (PSS: poly(styrenesulfonate), which acts as counter ion).

Coordination polymers, composed of metal ions and ligands that act as connectors and linkers respectively, reached a ZT 0.2 at 400 K for $\text{poly}[\text{K}_x(\text{Ni-ett})]$ (ett: 1,1,2,2-ethenetetrathiolate as a linking bridge).⁽¹²¹⁾ Moreover, the nature of the compound (n- or p-type-like) can be modified by the metal ion.

- *SnSe*: This single crystal shows the highest ZT value reported so far, 2.62 at 923 K,⁽¹²²⁾ due to its extraordinarily low lattice thermal conductivity (0.23 W/m·K) along the b-axis of the orthorhombic crystal. The compound is highly anisotropic and presents different ZT values along the different axis. In this way, for the c-axis the ZT value is 2.32 and in the a-

axis it is quite low, 0.8. In this material, the electrical conductivity and thermal conductivity show nearly constant trend over the temperature range 750 K to 923 K. Apart from the high ZT, this thermoelectric material presents the advantage of being formed by two non-toxic and abundant elements.

Due to the recent discovery of this material, its stability and thermal cycling behaviour has to be explored further. The properties of the polycrystalline samples need to be analysed to see whether they preserve the same properties as the crystal. The production of single crystals for scaling up is very expensive.

- *Tetrahedrites*: They are natural minerals that can be used directly as thermoelectric materials. They belong to the tetrahedrite family which consists of sulfosalts with a formula $Cu_{12-x}M_xSb_4S_{13}$, where M is a transition metal such as Fe or Zn. These materials have the benefit of being formed by earth-abundant elements and, as natural minerals, have low cost. A promising ZT near 1 has been reported.⁽¹²³⁾ However, further investigations are needed to improve its performance and prove its stability and availability for scaling up. Recently, a thermoelectric generator which uses tetrahedrites, produced by Alphabet Energy (www.alphabetenergy.com), has been built for commercialisation. It can be attached to the exhaust pipe of common regulators and it can reach 5 to 10 % efficiency.

- *MgAgSb*: It structurally and compositionally belongs to half-Heusler materials but it was reported to exist in three different crystal structures in the temperature range 27 to 420 °C.⁽¹²⁴⁾ Thus, at high temperature (above 360 °C) the phase γ -MgAgSb is presented, consisting of a Mg-Sb cube with half-Heusler structure. At intermediate (300-360 °C) and room temperatures, the phases β -MgAgSb and α -MgAgSb exist.

This compound seems to be able to compete with bismuth telluride for room temperature applications, since both present comparable ZT values and good thermal stability. $MgAg_{0.97}Sb_{0.99}$ shows a ZT of ≈ 0.7 at 300 K and 1.2 at 450 K.⁽¹²⁵⁾ Moreover, higher ZT values were reported using a very small amount of Ni in $MgAg_{0.965}Ni_{0.005}Sb_{0.99}$, obtaining $ZT \approx 1$ at 325 K and 1.4 at 450 K.⁽¹²⁵⁾ Furthermore, a record thermoelectric conversion efficiency of 8.5 % in the temperature range 20-245 °C was reported recently⁽⁸⁾ for a single leg of p-type MgAgSb-based compound. This efficiency was improved to ≈ 10 % by changing the hot side temperature to 295 °C.⁽⁸⁾

Another significant feature of this material is that its ZT shows a weak temperature dependence over a wide temperature range (up to 300 °C).⁽¹²⁶⁾ However, an analogous n-type thermoelectric leg is not currently available and will have to be produced with similar performance under the same temperature range.

2.6 Strategies to improve ZT

The task of improving the ZT value is quite complex since the parameters which govern the performance of thermoelectric materials are closely interrelated (see Fig. 2.7) and typically an increase of one of them produces a decrease of the other. This makes it very difficult to improve the ZT values and a compromise is required in most of the cases.

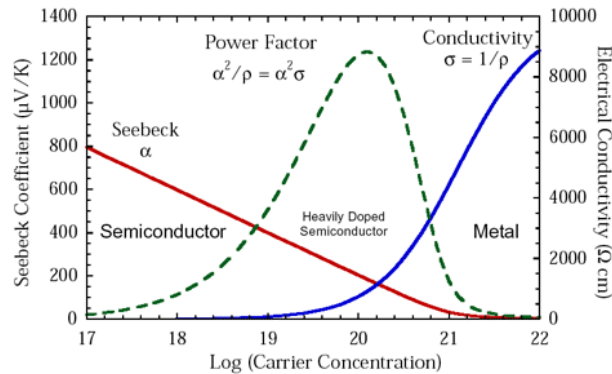


Fig. 2.7. Seebeck coefficient, power factor and electrical conductivity versus log (carrier concentration).⁽¹³⁾

Two main strategies have been followed to date to improve the figure-of-merit:

- a) **Maximising the power factor** by band engineering,^(127, 128) focusing on the improvement of the Seebeck coefficient without decreasing the electrical conductivity. This approach mainly aims to enhance the peak ZT, even though it should be taken into consideration that thermoelectric devices need to perform under a large temperature gradient to reach high overall device efficiency. This approximation involves optimisation by doping of existing materials and the preparation of nanomaterials.⁽⁶¹⁾ The most common band-engineering approaches studied are:

- Band structure modification by degeneration of multiple valleys:⁽¹²⁹⁾ Both Seebeck coefficient and electrical conductivity are enhanced when the number of degenerate valleys or carrier pockets in the band structure is increased.
- Band structure modification by electronic resonance states:⁽¹³⁰⁾ dopants can create resonant levels which can alter the density of states near the Fermi level and increase the thermopower^(2, 131) due to an enhancement of the effective mass of the carriers without modifying their concentration. The effect of resonant states vanishes at high temperature.

- Band structure modification by depressing bipolar effect at high temperature:⁽¹³²⁾ bipolar effect occurs when both holes and electrons contribute to the transport process creating electron-hole pairs. The likelihood of this effect is quite high due to the typically narrow bandgap of thermoelectric materials. Electrons in the valence band can be thermally excited to the conduction band and vice versa, which considerably reduces the Seebeck coefficient. Three approaches are followed to reduce the bipolar effect:

1) By increasing the carrier concentration more energy levels in the conduction band become occupied and higher energy is required for the electrons in the valence band (VB) to be excited to the conduction band (CB), in the n-type material case (see Fig. 2.8).

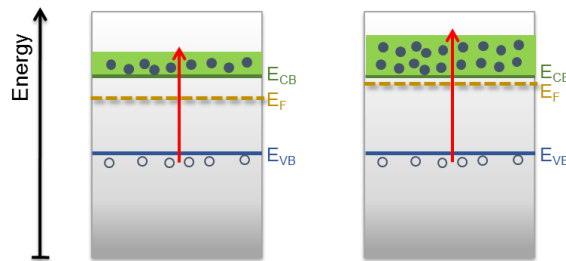


Fig. 2.8. Energy diagrams describing the higher excitation needed for the electrons in the valence band when the majority carrier concentration is increased.

- 2) Increasing the bandgap reduces the number of minority carriers thermally activated⁽¹³³⁾ at high temperature.
- 3) Synthesis of meso-scale microstructures with grain boundaries.^(10, 132) Normally interfaces at grain boundaries cause an interfacial potential that can scatter electrons and holes in a different way, which produces a degradation of the bipolar effect.⁽¹⁰⁾

b) **Minimising the thermal conductivity.** The thermal conductivity has two different contributions, the *lattice thermal conductivity* (λ_L) and the *electronic thermal conductivity* (λ_E). The λ_E is determined by the Wiedemann-Franz law: $\lambda_E = L\sigma T$, where $L = 2.0 \cdot 10^{-8} \text{ V}^2/\text{K}^2$ is the Lorentz number for the case of heavily doped semiconductors.⁽¹³⁴⁾ Hence, the electrical thermal conductivity is influenced by the carrier concentration and increases with the electrical conductivity. On the other hand, the λ_L is influenced by different parameters such as the mass of the unit cell and the grain size.

Thermal conductivity could be minimised mainly by two approaches that essentially consist in the insertion of scattering centres (point defects and interfaces) through

the synthesis of isostructural solid solution alloys which produce strong phonon scattering that blocks phonon propagation. The interparticle spacing, which is associated to the particle size, concentration and distribution of the secondary phase, and the matrix grain size, are the most significant parameters which affect the effect of phonon scattering.⁽¹³⁵⁾ Every structural constituent (point defects, strain, dislocations, nanoparticles, displacement layers, etc.) in the bulk material can contribute to phonon scattering, so they can potentially scatter different frequency heat-carrying phonons. The two principal mechanisms that have been utilised to reduce the thermal conductivity are:

- Nanostructuring of existing materials: this approach is likely to produce an increase of the Seebeck coefficient due to quantum confinement effects,⁽⁵⁾ but the main expected benefit is the reduction of the lattice thermal conductivity due to the efficient scattering of phonons at the grain boundaries in the interfaces.⁽⁶⁾ Due to nanostructuring, the number of interfaces (grain boundaries) is significantly increased.

Phonon scattering depends on the mass difference between the host material and nanoparticles, bond rigidity and the phonon frequency or wavelength.⁽¹³⁶⁾ Previous investigations^(132, 137) suggest that phonons with high-frequency are mainly scattered by an alloy mass-mismatch mechanism (point defects created for example by substitution), and atomic vacancies, whereas low-frequency phonons are notably scattered by nanoparticles or interfaces which present larger length scale disorder.

- Synthesis of new materials based on the “phonon glass electron crystal” concept. These materials contain cages or tunnels in their crystal structure inside which reside massive atoms that are small enough relative to the cage to “rattle”. Heavy elements can fill the cages and tunnels in the crystal structure of these materials to produce rattling and an increment in the number of phonon scattering centres, which leads to a significant reduction in the lattice thermal conductivity. Moreover, these materials present high carrier mobility (as crystals) but behave as amorphous materials as the lattice thermal conductivity is concerned. These compounds involve mainly skutterudites and clathrates.

2.7 Nanostructuring methods

The work presented in this thesis is developed following the approach of nanostructuring to improve the thermoelectric performance of materials. In this section, the main existing methods to produce nanostructures are reviewed.

Typically, there are two approaches for the preparation of nanoparticles (see Fig. 2.9), which are:

- **Bottom-up:** is a conventional material synthesis widely used in the industry for a long time which consists in building up things from atomic or molecular level until the nanoparticle is attained, atom-by-atom, molecular-by-molecular or cluster-by-cluster on a very large scale from the bottom. In the majority of the materials prepared by this approach when they present the same chemical composition, crystallinity and microstructure, there is not much variation in the physical properties of materials depending on the different synthesis routes. But obviously, there are different synthesis methods that produce significant differences in the chemical composition, crystallinity, physical properties and microstructure of the material due to kinetic reasons.

This means of production of nanostructures generates samples with more homogeneous chemical composition, small amount of defects in the structures and better range ordering. This approach is based on the reduction of the Gibbs free energy where the produced nanostructures and nanomaterials are close to the thermodynamic equilibrium state. A colloidal dispersion is one of the best examples of the bottom-up approach.

- **Top-down:** involves successive crushing of the bulk material until the nanoparticles are formed. This method leads to bulk production of nanoparticles. Attrition or milling is a typical top-down method, which will be explained further in chapter 3. One of the disadvantages of this approach is the fact that since the starting material has to break down into small pieces, there are imperfections or defects on the surface structure of the particles that could cause a significant impact on the physical properties and surface chemistry of the nanostructures. For example, these surfaces could reduce the electrical conductivity due to inelastic surface scattering. Other problems are the internal stress and contaminations that this approach might introduce.

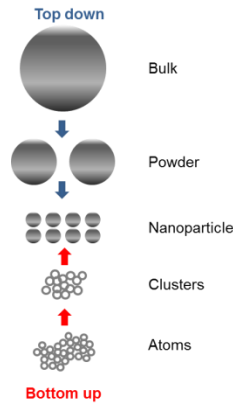


Fig. 2.9. Scheme of top-down and bottom-up approaches for the preparation of nanoparticles.

The fabrication methods to produce nanostructured materials depend on the dimensions and the application required. There are four general strategies that have been used to prepare nanomaterials, which are:

- A group of techniques that produces isolated ultrafine crystallites with uncontaminated free surfaces followed by a consolidation process at low and high temperatures. Some of the techniques are inert-gas condensation⁽¹³⁸⁻¹⁴⁰⁾, decomposition of the precursors and precipitation from solutions.
- Deposition of atoms or molecules on an appropriate substrate. Chemical vapour deposition (CVD), physical vapour deposition (PVD)^(141, 142) and some electrochemical methods^(143, 144) can be employed.
- New nanostructured materials can be formed when defects as dislocations or grain boundaries are introduced in a perfect crystal. These defects can be produced a high energy technique such as ball milling, extrusion, shear strain or high-energy irradiation.^(145, 146)
- Crystallisation from glasses or precipitation from supersaturated solid or liquid solutions^(147, 148) of condensed matter.

Although these are the main approaches to prepare nanoparticles, the techniques are mainly separated in two groups and the most common ones to prepare Bi_2Te_3 nanoparticles⁽¹⁴⁹⁾ are detailed below:

1. Physical methods:

- **Inert-gas phase condensation (IGPC):**⁽¹⁵⁰⁻¹⁵²⁾ it synthesises single-phase materials such as atom clusters by evaporating a precursor material (single metal or a compound) in a gas at low pressure, usually below 1 atm. The evaporated atoms or molecules experience/suffer a homogeneous condensation to form atom clusters when they collapse with adjacent gas atoms or molecules on a cold-powder collection surface. When the clusters are formed they are

removed from the deposited place to prevent aggregation and fusion of the clusters.

- **Physical vapor deposition (PVD):**⁽¹⁵³⁾ growth species are transferred or deposited from a source or target to a substrate to form a film. The thickness of the films can change from angstroms to millimetres. Different techniques exist:

- **Sputtering technique (ST):**⁽¹⁵⁰⁻¹⁵³⁾ can produce nanostructured clusters and thin films (metallic and ceramic) by bombarding the surface of the target material. Target and substrate are facing, an inert gas is introduced into the system as the medium to initiate and maintain a discharge, then an electrical field is applied to the electrodes and the discharge commences. The electrical field accelerates the free electrons that have enough energy to ionise argon atoms (Ar^+), which bombards the target causing the expulsion of neutral target atoms that pass through the discharge and deposit on the opposite electrode (substrate). Metallic or ceramic multilayers can be deposited.

- **Evaporation technique (ET):**^(152, 153) the growth species are removed from the source by thermal means. The system consists of a vacuum chamber which contains an evaporation source where the desired material is placed to be vaporised and a substrate situated an adequate distance away, facing the evaporation source. Intense heat is applied to vaporise the material (solid or liquid) to a vapour state and the vapour flux of the material condenses onto the cooler substrate to form a solid film or onto a cool finger to form powders. The pressure in the chamber has to be low ($< 10^{-4}$ mtorr).

- **Lithographic processes:**⁽¹⁵⁴⁻¹⁵⁶⁾ it transfers a drawing onto a substrate using a mask that contains the pattern by a radiation that impacts onto a flat coated with a photoresist. Thus specific areas (exposed) of the surface are chemically treated/modified which can be done by wet or dry etchants. Normally the substrate is covered with a photoresist mask (metal or organic polymer) layer deposited by spin coating or sprayed on a glass plate. After exposure the unexposed photoresist can be removed and chemical treatment occurs only in the uncovered areas. This technique allows selective chemical processing. Many techniques have been developed and utilised to fabricate nanoparticles such as photolithography, electron beam lithography, X-ray lithography that present different radiation sources (photons, X-rays, electrons, ions and neutral atoms) and lens but they are not going to be developed further because these techniques are not the ones used in this thesis. It is the most used method.

- **Spray pyrolysis (SP):**^(151, 157) it is also known as aerosol thermolysis, mist decomposition, evaporation decomposition of solutions, high-temperature aerosol decomposition or aerosol high-temperature decomposition. It consists basically of a solution process to prepare powder or thin films of metal and metal oxides. The procedure is mainly divided in 5 steps: (1) generation of precursor droplets, (2) evaporation of the solvent, (3) condensation of solute, (4) decomposition and reaction of solute, and (5) sintering of solid particles.
- **Pulsed laser ablation (PLA):**^(150, 151) it is a deposition process by which a material or target is evaporated after being irradiated by a focused pulsed laser beam. When the sample is irradiated, it becomes hot and the evaporation starts, atoms and clusters are removed from the sample and deposited onto a substrate. It can be used to synthesise nanocrystalline films and powders. The wavelength and pulse width of the laser play an important role in the ablation mechanism. The most employed laser is the excimer one (ArF) due to its short wavelength (193 nm) and small pulse width (6-12 ns). This technique is able to control the vapour composition, so that, it is able to control the stoichiometry and produce multicomponent materials, which are great advantages that have the capability to prepare complex materials such as multicomponent oxides used in different applications. But, on the other hand, it presents some drawbacks, e.g. the design of the system is quite complex, it is not always possible to find the desired laser wavelength for evaporation, low energy conversion efficiency and high production cost.
- **Sonochemical reduction (SCR):** a reduction of the target in a solution occurs due to the reaction with reducing species formed from the sonolysis (formation of free radicals) of organic additives and solvent. The rate and intensity of reduction can be controlled by altering the types and concentration of additives, acoustic frequency, acoustic intensity, bulk temperature, static pressure and the choice of liquid or dissolved gas.⁽¹⁵⁸⁾ The particle size of the reduction of ions is affected dramatically by the rate of reduction, so smaller metal particles are generated when the rate of reduction is higher. The chemical effects of ultrasound are caused by acoustic cavitation that involves nucleation, growth and collapse of bubbles in a liquid.⁽¹⁵⁸⁾ A cavity is a volume (empty or any gas or vapour) rounded by a liquid. The collapse of bubbles generates localised extreme conditions (gas at 5000 °C and the liquid around the cavity at 2100 °C and pressure around 500 atm⁽¹⁵⁸⁾) and the formation of nanoparticles is produced. Cavitations concentrate the diffuse energy of sound into

microreactors. It can produce nanoparticles of desirable size range, bimetallic alloys or nanoparticles with core-shell morphology depending on the experimental conditions utilised during the process. This process will be explained further in the next chapter due to this is one of the techniques utilised in this thesis to produce nanoparticles.

2. Chemical methods: they present some advantages with respect to the physical ones which are (1) versatility in designing and synthesizing new material, (2) good chemical homogeneity due to chemical synthesis performed at the molecular level. On the other hand, they also present some problems with regards to complexity, contamination of generated secondary products, agglomeration and hazardous synthesis. Within these methods, the most common ones to prepare Bi_2Te_3 nanoparticles are:

- **Electrochemical deposition (ECD)**:^(159, 160) it is also known as electrodeposition and electroplating when a metallic coating is prepared. It involves a special electrolysis by which a solid metal film is deposited from a solution of ions onto an electrically conducting surface (electrode). Therefore, only conductive materials such as metals, alloys, semiconductors and electrical conductive polymers can be used in this technique. The process involves the connection of two different electrodes immersed into an electrolyte solution to an external circuit and owing to the difference electrode potentials between the two electrodes, a migration of electrons occurs from the electrode with higher electrode potential to the lower one, resulting in an oxidation and reduction processes, accompanied by deposition. Apart from the low cost process, electrodeposition presents the ability to deposit relatively thick films (several tens of microns or more) and in a large area which make this technique very promising to scale up thin-film to produce a multi-layered structural material with individual layer thickness but with an overall thickness and in-plane area.

- **Electroless deposition (ED)**:⁽¹⁶¹⁾ it fabricates nanowires and nanorods.⁽¹⁶²⁻¹⁶⁵⁾ It is a chemical deposition and involves the usage of a chemical agent to cover a material from the surrounding phase onto a template surface without an external current source.⁽¹⁶⁶⁾ This technique does not require electrically conductive materials and the deposition starts from the pore wall and continues inside, so that, there is a formation of growth void fibrils or nanotubes. The thickness of the nanotubes depends on the variation of deposition time (longer times resulting in thicker walls and a prolonged deposition may prepare a solid nanorods, even though extended times do not guarantee the formation of solid nanorods).

- **Hydrothermal and solvothermal techniques (HTS):**⁽¹⁶⁷⁾ they are techniques to prepare chemical compounds and materials by placing them in a stainless steel autoclave (closed system) with a solvent at high temperatures and pressures (≈ 500 °C and 10-80 MPa). The main difference between the two techniques is the solvent utilised in each reaction, water is the one for the hydrothermal technique and non-aqueous solvent is for solvothermal techniques. They are based on the ability of the solvent to dilute substances that are practically insoluble under normal conditions such as: oxides, silicates, sulphides and zeolites. Frequently, a surface active agents (SAA) or surfactant is necessary because it reduces the surface tension and helps the formation of oxide compounds in the hydrothermal solution. The main experimental parameters that affect the resulting products significantly are: initial pH of the medium, duration and temperature of the synthesis, pressure in the system and selection of solvents, precursors and surfactants. They can produce materials with a desirable pore size with a narrow distribution.

Hydrothermal technique: can sinter single crystals, oxides, silicates, sulphides, zeolites and nanopowders. Nanopowders can be formed either at high and room temperature reaction, where they are produced due to a fast crystallisation of some phases in hydrothermal conditions. Some advantages of this method are high quality and control of the composition of the crystals and the ability to form crystalline phases that are not stable at the melting point and disadvantages are mainly the cost of the equipment and the unfeasibility to see the growth of the crystals.

Solvothermal technique: can sinter single nanostructured titanium dioxide, graphene, carbon, etc. Some benefits of this technique are the usage of sol-gel and hydrothermal routes, the ability to control the particle size, shape distribution and crystallinity of metal-oxide nanoparticles or nanostructures.

- **Chemical vapour deposition (CVD):**^(150, 168) there is a chemical reaction between a volatile gaseous compound (precursor) with the material (wafer or substrate) to be deposited and produce a non-volatile thin solid film onto the substrate. The CVD system is formed of three main parts, (1) vapour precursor gas which is the desirable material, (2) the reactor where the deposition happens and (3) the effluent gas handling system to remove the by-products and the unreacted precursor. In conventional CVD, when gas compounds are unable to react at room temperature, are passed over a substrate heated to a convenient temperature where the reactants decompose or combine with other constituents to form a layer onto the substrate. Deposition occurs by different chemical

reactions such as reduction, oxidation and pyrolysis, compound formation, etc. This technique has been widely utilised due to the immense variety of chemical reactions that can be realised using different reactants or precursors and different ratios and deposited conditions (temperature, pressure and gas composition). Moreover, it can be associated with solid-state microelectronic and semiconductor industry to produce thin and multi-layered films, which are high quality and high performance. Apart from thin films, some people utilise this technique to fabricate nanowires.

- **Laser chemical vapour deposition (LCVD):**^(169, 170) it is a modification of the standard chemical vapour deposition and uses transparent reactants. It employs a laser to heat the surface and break the bonds to enable the deposition, the laser passes through a transparent window and the transparent reactants onto an absorbing surface, forming a localised hot spot where the reaction occurs. Two mechanisms are involved in this technique: pyrolytic and photolytic processes.^(171, 172) The procedure starts with the deposition of the vapour-phase of the compound into a vacuum system that contains the substrate. Then, the substrate is irradiated with laser light to initiate a pyrolytic chemical reaction that decomposes gases and enhances rates of chemical reaction and the photolytic process continues where the laser photons dissociate the precursor molecules in the gas phase and it leads to the deposition of the desirable compound onto the substrate. This laser's wavelength is determined by the absorptivities of the reactants.

- **Laser pyrolysis (LP):**^(173, 174) normally the reactants are in the gas-phase but liquid ones can be also treated by this technique placing them in a heated container where another gas is bubbled to produce its vapour into the chamber. Therefore, it is a vapour-phase synthesis and consists of heating a mixture flux of gases with a continuous wave CO₂ ($\lambda=10.6 \mu\text{m}$) laser, which initiates and maintains a chemical reaction. It is based on the resonance between the CO₂ wave laser and the infrared absorption band of the reactant⁽¹⁷⁵⁾ and the transfer of energy to the non-laser active molecules. When the laser beam irradiates the gas or vapour-phase precursors, the condensable products are formed due to the chemical reactions that the laser induces and an inert photo-sensitizer is added to the vapour phase mixture. Over certain pressure and laser power, there are enough nuclei in the reaction zone to start the homogeneous nucleation of particles which are transported to a filter by an inert gas. This method shows some marked features: it produces a small particle size (10-200 nm) with

remarkable narrow particle size distribution, barely presence of aggregation and has the ability to produce various classes of compounds such as oxides, nitrides, carbides, sulphides, etc. It generates nanopowders.

- **Lyotropic liquid crystal templates (LLCTs):**⁽¹⁷⁶⁾ it normally prepares porous organic polymers and inorganic nanomaterials with different morphologies^(177, 178) such as spherical particles, empty nanostructures, nanowire (1D), nanorods and nanotubes and two-dimensional ordered materials (arrays). LLCTs cover the structure of nanomaterials depending on the interaction of the inorganic ions and surfactants within the template. Therefore, the composition and concentration of the lyotropic liquid crystals (hydrophilic materials that love water) define the final morphology and the properties of the products. The most remarkable characteristics of this technique are the flexibility for transferring structures from templates to another substrate and the selection of the template phase of the liquid crystal can modify the shape and size of the final products. The phases for the LLCTs that control the structure and morphology of desirable nanomaterials can be lamellar, hexagonal and cubic, this long-ranged orientational order is produces by the solvent.

2.8 Methods to prepare nanobulk thermoelectric materials

Typically, there are many sintering techniques that are employed to prepare a bulk material, in this section the most representative are detailed:

- **Cold press:** it is a compacting method where the compaction is carried out applying pressure in a uniaxial direction at room temperature. Then, normally the compacted powders are heated at high temperatures inside an oven to improve the electrical conductivity within the material. The powder of material is placed into a mould and the pressure applied produces the compacted disc.
- **Hot press:**⁽¹⁷⁹⁾ it is a high-pressure (≈ 50 MPa) sintering method where the compaction is carried out applying simultaneously heat and pressure in uniaxial direction. Sintering temperatures are normally 650-2400 °C. It can be used to sinter samples pre-compacted already by cold press. Usually, the material (loose powder or pre-compacted) is placed into a mould that allows induction or resistance heating up to high temperatures, therefore, the sample is heated by heat transfer occurring by conduction form the external surface of the container to the powders. Heating can be classified into three different types:

1. *Inductive heating*: heat is produced within the mould when a high-frequency electromagnetic field is applied. This electromagnetic field is generated by an induction coil connected to an electronic generator. The mould is placed within the induction coil.

The main advantages of this heating are that the pressure and the applied power are independent, powders with a liquid phase can be treated by this method and low pressure can be utilised.

On the other hand, between the disadvantages, it is worth underlining the very expensive high-frequency generator, the mould has to be perfectly aligned to have a homogeneous heat distribution, the process needs a good inductive connection and thermal conductivity of the mould, due to the magnetic field can only penetrate the mould from 0.5 mm to 3 mm and then the heat has to be transmitted into the mould by the thermal conductivity of the mould and another problem might be possible heating rates, thus the mould could be damaged if the heating up rate is high due to the temperature difference between the surface and the core.

2. *Indirect resistance heating*: the mould is positioned in a heating chamber made of graphite heating elements which are heated by an electric current and the heat is transferred into the mould by convection. Owing to the heating is made in two different steps, first the graphite elements are heated and then the mould, this heating is called indirect resistance heating.

Some advantages are independent of heat, pressure and conductivity of the mould and high temperatures can be reached. And the main disadvantage is that it needs long times to heat up the mould since the furnace has to transfer the heat to the mould surface and then throughout the cross-section of the mould.

3. *Direct hot pressing*: the mould is directly connected to the electric powder (AC or DC) so heat is directly generated into the mould which produces high heating rates. Due to this, short cycle times (few minutes) and lower temperatures and pressure are needed to perform the compaction since heat is generated in the mould.

- Spark plasma sintering (SPS)⁽¹⁸⁰⁾ or Pulse electric current sintering (PECS) or Plasma pressure compaction (P²C)⁽¹⁸¹⁾ or Plasma-activated sintering (PAS)⁽¹⁸²⁾: the most common term is SPS but this is confusing/inaccurate since neither a spark nor a plasma are involved in the process where the densification is performed by a current. SPS is a modification of the hot pressing technique in that the heating of the sample is performed by a moderate uniaxial force/pressure and pulsed (on-off)

high direct electric current (DC) through the powder under low pressures and voltages to produce a rapid compaction of a wide range of powders. This direct way of heating produces high heating rates (> 300 °C/min, up to 1000 °C/min) and short sintering times (5-20 min), high quality densification, less grain growth, little modification of the grain size, eliminates powder decomposition and allows the maintenance of the intrinsic properties of the nanopowders in their compacted samples. It can reach over 2000 °C which is 200 to 500 °C lower than the conventional techniques such as hot press and also during the sintering process it can adjust temperature gradients thus, layered material structures with different properties can be fabricated (i.e. ZrO_2 /stainless steel).

The basic SPS system is constituted of a vertical single-axis pressing system, a water-cooled vessel, a vacuum chamber, atmosphere control inside the vessel and sintering DC pulse generator. The powder is placed between the die and punch on the sintering stage in the chamber and held between the electrodes. When pressure and pulse are applied, temperature increase to $1000\sim 2000$ °C above ambient temperature, producing a high quality sintered compacted sample in a few minutes.

Advantages of SPS respect to the conventional methods such as hot press (HP) sintering:

- Ease operation and accurate control of sintering conditions.
- High sintering speed, high reproducibility and reliability.
- Rapid consolidation of powders and ability to preserve nano-structures.
- Heat is homogeneously dissipated for whole sample producing less grain growth and eliminating powder decomposition.
- Heating generation is internal which means that it is not provided from other external elements so the heating is quite homogeneous with only small thermal gradients even at high heating rates, thus the usage of heat input is very efficient.

On the other hand, SPS presents problems which need to be mentioned, powders have to present an appropriate electrical conductivity and the sintering temperature gradient has to be control and minimised.

- Zone melting or zone refining or floating zone process: it is a process to purify crystals where part of the crystal is melted in a tube by a heater that applies a high frequency alternating current (AC) and the melting process progresses slowly along the material to the end, melting the impure solid that it is found. Therefore, there is a concentration of the impurities in the melted substance in one of the edges and in the other the pure crystal is solidified. This process can be employed in a wide variety of solute-solvent systems that have a considerable concentration difference between the solid and liquid phase at equilibrium. This process can be performed

as a batch or continuously, adding fresh impure material at one end and removing pure material from the other part.

The fundamental principle of this process is based in the ratio of the impurities contained in the solid phase and the liquid phase, which normally is below 1. Therefore, the impurity atoms will diffuse into the liquid region at solid/liquid interface producing a single crystal. If a high pure material is required, the impurity end of the material can be cut.

A variety of heaters can be employed such as induction coils, resistance heaters, gas flames, pass electric current directly through the ingot while it is in a magnetic field and optical heaters as a halogen or xenon lamps (to fabricate insulators). It is not used for diameters larger than 150 mm.

- Hot isostatic pressing: it is a process that reduces the porosity and increases the density and the strength of many materials using high temperatures (900-1250 °C and also higher) and isostatic (same pressure) pressures (100-200 MPa) in a high pressure vessel in a furnace using an inert gas, usually argon. The powder is placed into a flexible air-tight container, normally polyurethane and put inside a closed pressure vessel filled with liquid and the densification is produced by increasing the pressure within the vessel. After filling and closing the vessel with the desirable material, the air is removed. Then, the chamber is heated provoking an increase in the pressure of the argon gas inside the vessel due to a gas thermal expansion. The argon gas pressure change takes place across the liquid which applies a uniform pressure of the air tight- container resulting in uniform pressed sample with isotropic properties and 100 % densification.

As this technique employs simultaneously elevated temperatures and pressures to do the compaction, the resulting samples present almost no voids or porous or defects which improves significantly the mechanical properties of the samples. Moreover, this technique presents the advantage of bonding two or more materials together independent of whether they are in powder or in solid state. Moreover, another benefit of this technique is the wide variety of materials that can be utilised and cost-effective process for the fabrication of many metal or ceramic components, high-performance and quality.

Chapter 3 : Experimental Methods

3.1 Introduction

3.2 Nanopowder fabrication methods

3.2.1 Ball Milling (BM)

3.2.2 Ultrasonic Milling (UM)

3.3 Powder characterisation methods

3.3.1 Shaker

3.3.2 Laser diffraction particle size analyser

3.3.3 SEM and EDX

3.3.4 XRD

3.3.5 Optical microscope

3.4 Thermoelectric characterisation methods

3.4.1 Hot probe

3.4.2 4-probe technique

3.4.3 4-multifunctional probe technique

3.4.4 Laser flash instrument

3.4.5 Impedance spectroscopy

Chapter 3

3.1 Introduction

The purpose of this chapter is to describe the experimental methods used throughout this thesis. For the preparation of nanoparticles two methods have been employed, ball milling (BM) and ultrasound milling (UM). For the characterisation of the nanopowders, particle size analyser, scanning electron microscopy (SEM), energy dispersive X-ray spectroscopy (EDX) and X-ray diffraction (XRD) techniques have been used. A home-made hot-press was used to compact the thermoelectric powders into a disk pellet, which will be described in Chapter 5. Finally, for the characterisation of the thermoelectric properties of the bulk materials, hot probe, 4-probe methods, 4-multifunctional probes and laser flash were utilised.

3.2 Nanopowder fabrication methods

3.2.1 Ball Milling (BM)

BM is performed in a type of grinder used to crush materials into fine powders (including nanopowders). The fundamental process of ball milling is the impact between the balls and the materials, which result in the particle size reduction. The grinding media is the balls, which are made of steel (chrome steel), stainless steel or rubber. In the equipment used in this thesis the balls were made of stainless steel.

A ball mill usually consists of a cylindrical container (vial) rotating around its axis. The ball mill utilised in this work is a SPEX 8000M Miller, which performs complex vibrations to enhance impact as illustrated in Fig. 3.1 (a). An image of the equipment is shown in Fig. 3.1 (b). The frequency of the vibrations is 1200 times per minute. During these vibrations the vial is displaced violently laterally and vertically to hit all the portions of the substance in the vial, simultaneously milling the sample and blending it. Because of the amplitude and velocity of

the clamp's swing, each ball develops fairly high G forces, enough to pulverize the toughest materials (rocks, slags, cement, ceramics, etc.). In this work, the materials of research are bismuth telluride based materials.

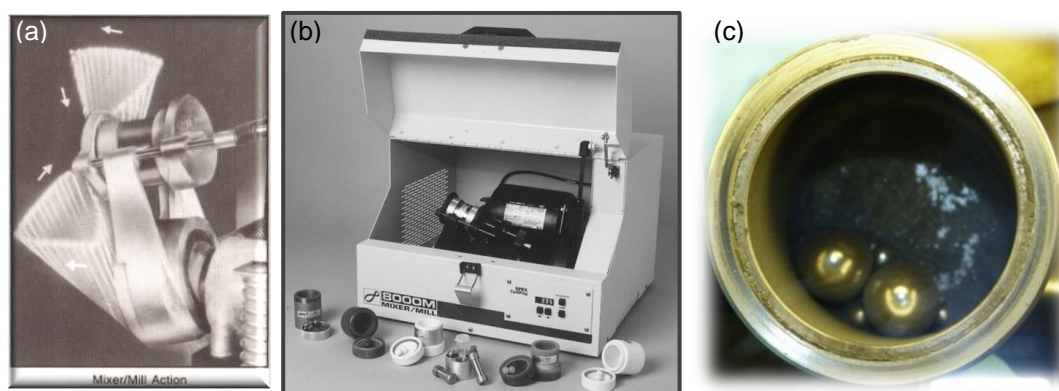


Fig. 3.1 (a) Trace of motions performed by the SPEX 8000M. (b) Photograph of SPEX 8000M employed in this work. (c) Container with the balls and bismuth telluride powder after a ball milling experiment.

The container is partially filled with balls and the material to be ground as it can be observed in Fig. 3.1 (c). The grinder and the balls are generally harder (251 knoop hardness) than the material to be crushed (155 knoop hardness for Bi_2Te_3) and should not interact with the substance to grind to avoid any contamination.

The container employed in this research is a stainless steel grinding vial set (8007), with both the vial and balls made of stainless steel. The main compositions are Fe and Cr with a small proportion of Ni, Mn, S and Si. Although stainless steel is durable, hard and suitable for most applications, the resulting samples can be contaminated by Fe and Cr when grinding tough materials. To avoid possible sample agglomeration or “cake” and also oxidation problems in dry grinding, which is the case in this work, the samples are loaded and unloaded into the container under argon atmosphere inside a glove box. No other chemicals are added to avoid caking due to the moisture. Even though the maximum volume of the vial is 65 mL, the recommended mixing load is only 25 mL and 3-10 g of grinding material.

BM presents several advantages over other systems: the cost of installation is low; it is suitable for both batch and continuous operation. In addition, it is suitable for materials of all degrees of hardness since a wide selection of grinding vials and balls are available.

3.2.2 Ultrasonic Milling (UM)

Ultrasonication is an efficient mean for the wet-milling and micro and nano-grinding of particles, in particular for the preparation of superfine-size slurries.⁽¹⁸³⁾ The particle milling effect is based on intense ultrasonic cavitation. This **cavitation** is the fundamental process

of UM. When liquids are sonicated at high intensities, the sound waves propagate into the liquid media producing alternating high pressure (compression) and low pressure (rarefaction) cycles, with rates depending on frequency. During the low pressure cycle, high-intensity ultrasonic waves create small vacuum bubbles or voids in the liquid. When the bubbles achieve a volume at which they can no longer absorb energy, they collapse violently during a high pressure cycle. Accordingly, the ultrasound field creates the bubbles within the liquid which gradually grow and implode at a certain size and energy is released in the form of heat (minor effect due to the heat dissipates quickly as a consequence of the small size of the bubbles) and pressure wave (major effect). Bubbles grow under low pressures and bubbles start to collapse under high pressure. After the bubble collapses, the cycle starts again. Since the powders do not have enough strength to withstand such force, the powders break into smaller pieces. Cavitation is a destructive process of non-linear nature as the applied ultrasound field increases in amplitude.⁽¹⁸⁴⁾ It should be mentioned that cavitation strongly depends on the fluid properties and particularly on the availability of sites for cavitation nucleation such as trapped air pockets in dust particles.

The rapid compression of gasses and vapours inside the bubbles produces massive temperatures (around 5000 K)⁽¹⁸⁵⁾ on the surface of the particles which are similar to the temperatures at the surface of the sun. The pressure inside the bubble is around 1000 atm while 10000 atm can be reached at the surrounding liquid of the resulting shock-wave. These temperatures are similar to those at the surface of the sun and pressure inside the bubble about 1000 atm, while the resulting shock-wave in the surrounding liquid may be as high as 10000 atm. These extreme conditions may cause chemical changes, acoustic signals, light emission, free-radical generation and surface erosion.

Since the bubbles are very small, the heat dissipates quickly (the cooling rate is on the order of 10 billion °C/second), thus the ambient conditions remains unaffected.

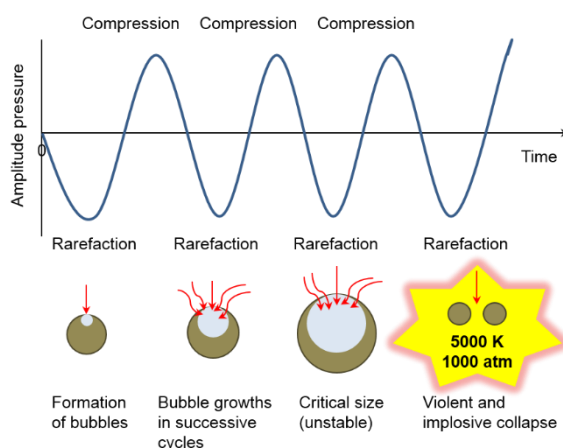


Fig. 3.2. Cavitation process, bubble size and behaviour in response to ultrasound waves. Outset, growth, oscillation and collapse of bubbles within a fluid driven by a sound field.

A diagram of the cavitation process is shown in Fig. 3.2. The implosion of the cavitation bubbles results in micro-turbulences and micro-jets of up to 1000 km/h.⁽¹⁸³⁾ Large particles may suffer surface erosion (via cavitation collapse in the surrounding liquid) or particle size reduction (due to fission through inter-particle collision or the collapse of cavitation bubbles formed on the surface). This leads to a sudden acceleration of diffusion, mass-transfer processes and solid phase reactions due to crystallite size and structure changing.⁽¹⁸³⁾

The ultrasonic processor used for the experiments of this research can generate high-intensity ultrasonic energy (vibrations at the frequency of 20 kHz, nominal power of 1 kW and an amplitude of 140 μm) from a UIP-1000 HD 60 transducer (Hielscher GmbH) (Fig. 3.3 (a) and (b)). The cell for dispersing and wet-milling of powders is a home-made copper vessel (approximately 5 cm diameter and 5-6 cm height) with a heat sink cooled by a water bath (Fig. 3.3 (c)).

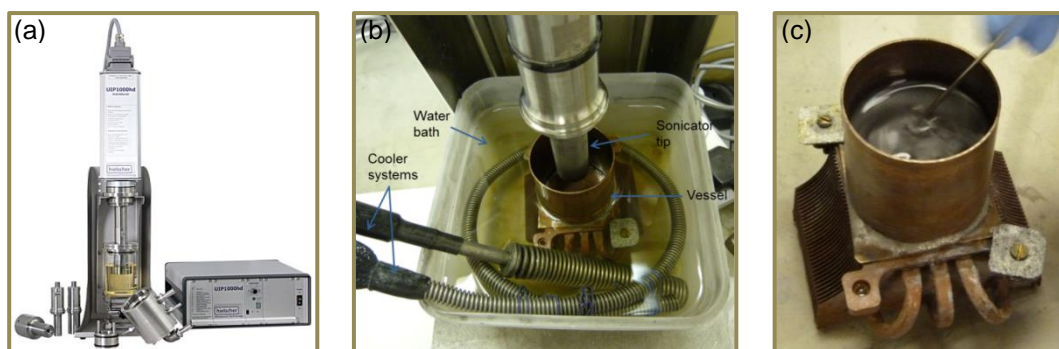


Fig. 3.3 (a) Image of the ultrasound milling with the generator from the supplier (www.hielscher.com). (b) Experimental set up of the ultrasound milling showing key parts. (c) Milling cell with the heat sink and the typical Bi₂Te₃ solution used for these experiments.

Ultrasonication presents some advantages compared to conventional particle size reduction equipment:

- Ultrasonic devices are very easy to install and operate. They have only two parts in contact with the material to be milled: the titanium sonotrode (tip) and the milling cell. Due to the simple design of these two parts, they can be cleaned quickly.
- Ultrasonic devices have a very high efficiency in the conversion of electrical into mechanical energy, thus normally less power is needed for the UM than for other conventional milling equipment.

Some disadvantages of this method are the high noise during operation and possible contamination with the solvent.

3.3 Powder characterisation methods

3.3.1 Shaker

The separation of the powders into different particle size ranges was carried out by a sonic sifter shaker (Endecotts) using sieves of different sizes (see Fig. 3.4). The equipment passes a vertical column of air through the sieves that contain the powder. The movement of the air alternatively lifts the sample, which facilitates the passage of the powder through the sieve apertures, achieving the separation, this mode of operation is totally different than the conventional vibrational shakers. The oscillation amplitude is variable and can be modified by the operator. Moreover, a horizontal mechanical pulse may also be applied to the sieves at regular intervals to break down any clustered particles and assist to eliminate any obstruction created on the sieves.

The shaker is able to separate samples down to 5 μm , although it takes a much longer time (around 24 h) than larger particles (around 1 h). It caused very little attrition of the sample and it operates quietly. However, sometimes the aggregation of the smaller particles can occur.

The range of the sieve apertures utilised in this thesis was:

- 106 μm .
- 45 μm .
- 20 μm .
- 10 μm .
- 5 μm .

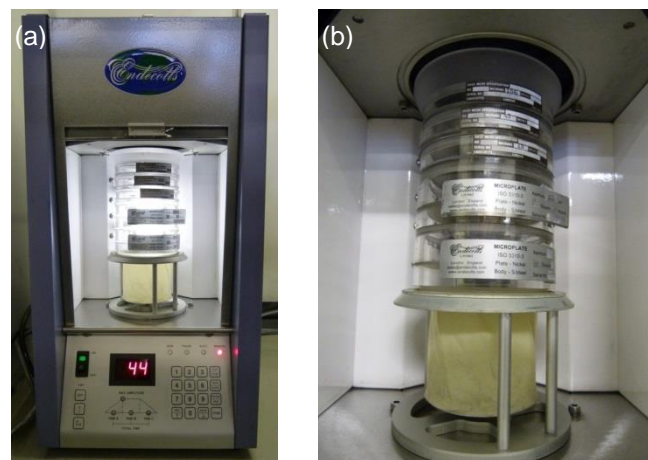


Fig. 3.4 (a) Sonic sifter shaker. (b) Sieves stacked up for separation of different particle size.

3.3.2 Laser diffraction particle size analyser

In this work, a Mastersizer 3000 particle size analyser was used to measure the particle size distribution in the range of 0.01-3500 μm . The instrument is based on the measurement of the intensity of the light scattered by passing a laser beam through the sample (in our experiments, the particles dispersed in water). Two light sources illuminate the sample, a red laser at 632.8 nm (He-Ne) and a blue LED at 470 nm. As can be seen in Fig. 3.5, the Mastersizer 3000 consists of an optical unit, a sample dispersion unit and a measurement cell.



Fig. 3.5. Mastersizer 3000 for measuring particle size distribution.

The measurements are performed in the optical unit, where the laser beam illuminates the dispersed particles when they pass across the optical bench. A series of detectors measure the intensity of the lights scattered by the particles over a wide range of angles for red and blue wavelengths.

The sample dispersion unit used in the measurements was a wet dispersion unit (Fig. 3.5), which suspended the sample in a liquid dispersant. In this study, deionised water with a resistivity of 18.2 $\text{M}\Omega\text{cm}$ was used. In order to keep the sample suspended and homogenized, the powder suspension is continuously recirculated through the measurement cell. In addition, stirring or agitation is also applied.

The Mastersizer is equipped with software that analyses the scattering data to calculate the particle size distribution. The software is also used to control the operation of the system (optical and dispersion units) during the measurement.

3.3.3 SEM and EDX

SEM is an electron microscope that produces images of a sample by scanning it with a focused beam of electrons instead of a beam of light. The electrons are accelerated by an electric field by means of a potential difference (1,000-30,000 V). Sensitive samples require

low voltage whereas metallic samples, typically less sensitive, are irradiated with higher voltage electrons in order to achieve better resolution.

As the beam is scanned over the specimen in the x- and y-directions, interactions between the electrons of the beam and the atoms in the sample produces secondary electrons (SE), back-scattered electrons (BSE) and characteristic X-rays. All of them can be detected and processed to provide information about the sample's surface topography and composition. Typically images are produced using the SE. While X-ray signals can be detected and analysed to determine the chemical composition of the specimen. This technique is referred to as EDX, which will be explained in more detail below.

A SEM basically consists of an electron gun where the electrons are accelerated, an electron column that focuses and illuminates the specimen, the electron beam, condenser and objective lens which reduce the beam are also present. An image of a Philips XL 30 SEM apparatus used in this work can be seen in Fig. 3.6.

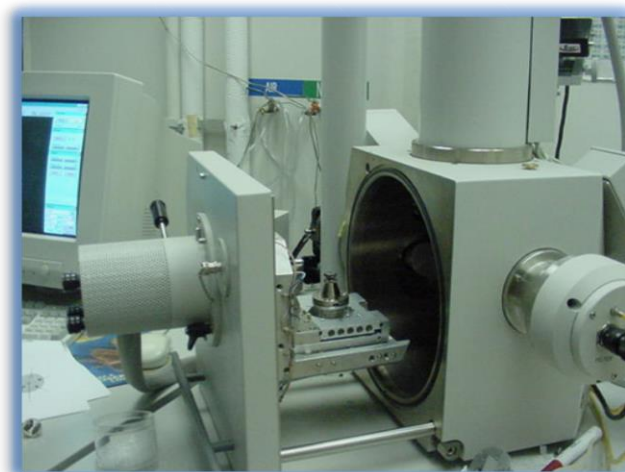


Fig. 3.6. Philips XL 30 SEM apparatus.

The SEM images have a very high resolution and samples can be examined using large amplifications (usually reaching up to a scale of few nm).

The samples measured by SEM need to be conductive. The non-conductive samples are usually coated with a thin layer of carbon or a metal like gold to provide the conductive behaviour in the sample.

EDX is a non-destructive analytical technique used for the identification of the elemental composition of materials. The technique can be used for qualitative and semi-quantitative analysis and is also able to provide spatial distribution of elements (mapping). EDX systems are connected to SEM or Transmission Electron Microscopy instruments, where using the images captured by the microscope, a part of the specimen is analysed. Fig. 3.7 shows experimental results obtained from EDX measurements.

As mentioned above, in this method, characteristic X-rays are created due to the impact of the electron beam with the atoms in the specimen. The incident beam excites an electron of the inner shell of the atoms, forming an electronic hole. Then, an electron from the outer shell with higher energy drops into the hole, releasing energy (an X-ray). The wavelength and energy of the X-rays emitted from the atoms can be measured by an energy-dispersive spectrometer and is characteristic of the atomic structure of the element, allowing the determination of the elemental composition of the specimen. Each element has a unique atomic structure which provides a unique set of peaks in the X-ray spectrum.

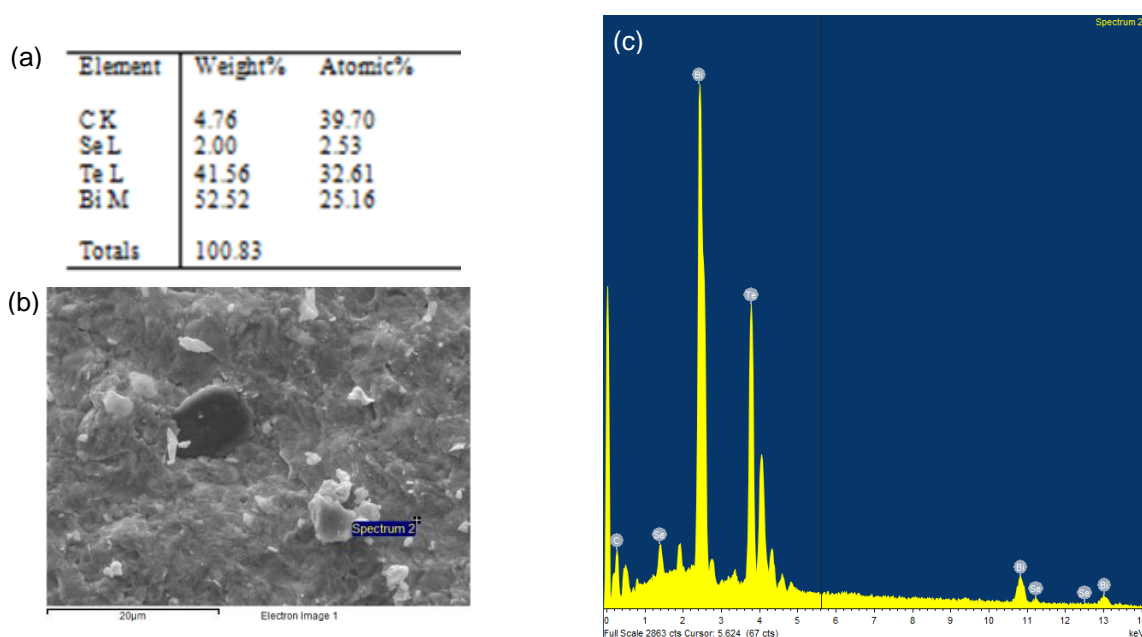


Fig. 3.7 Experimental results obtained from EDX for an n-type Bi_2Te_3 sample. (a) Quantitative data. (b) SEM image of the part of the sample analysed. (c) Spectrum showing the characteristic peaks of the elements that form the sample.

3.3.4 XRD

XRD is a non-destructive analytical technique where compounds with crystalline structure, either within a mixture or in a pure phase, can be identified and quantified. It does not provide a chemical compositional analysis but the identification of the phase or phases of a compound.

The atoms in crystals are ordered with certain periodicity, forming a lattice. The lattice planes are separated from each other by *a-distances* or *a-spacings*, which vary depending on the nature of the material (chemical composition) and the structure (planes exist in different orientations, each with distinct distances).

The phase identification is achieved by relating the angle of incidence of the X-rays to the distance between the atoms that form the crystal structure. According to the Laue prediction, when the atoms of a single crystal specimen impact with X-rays, the atomic

electrons diffract a parallel, monochromatic X-ray beam (coherent scatter) providing a series of diffracted beams whose directions and intensities would be dependent on the lattice structure and chemical composition of the crystal. Therefore, when a monochromatic X-ray beam with a known wavelength (λ_b) is irradiated on the lattice planes of a crystal at an angle θ , diffraction of the beam in different directions and intensities occurs due to reflections from successive planes, differing by a completed number (n) of λ_b . This pattern of diffraction follows the Bragg equation, $\lambda_b = 2a \sin \theta$, where n is the order of reflection and a is the distance between planes. In this way, a can be calculated as it can be seen in Fig. 3.8 (a).

By varying the angle θ , different a -spacings within the crystalline structure can be calculated. The different angular positions and intensities can be plotted to provide a unique characteristic X-ray pattern called diffractogram, which is the distinctive fingerprint of each crystal or mineral phase.

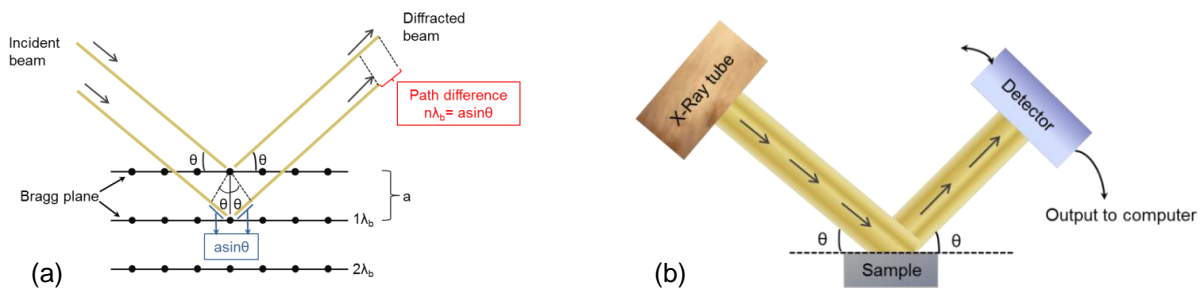


Fig. 3.8 (a) Scheme of the X-ray diffraction following the Bragg equation. (b) Schematic operation of the XRD apparatus.

The XRD consists of a generator of X-rays from X-ray tubes, a detector which moves to detect the angles of diffraction and a computer. In Fig. 3.8 (b) a simple scheme of the operating of the XRD is shown.

The X-ray instrument used in this study is a Philips PW1710 automated powder diffractometer where the X-rays are generated using copper ($\text{CuK}\alpha$) radiation at 35 kV and 40 mA. The equipment is controlled by a computer employing the PW1877 APD operating software and the PW1876 PC identification software. The sample in powder form was placed inside an aluminium holder which is mounted in the sample chamber of the diffractometer. The phases in the sample were identified by matching the obtained diffractograms against an available database of 70,000 known mineral phase diffractograms.

3.3.5 Optical microscope

An optical microscope uses visible light and a system of lenses to magnify details of samples. As other standard optical microscope, it offers different illuminators like brightfield, darkfield, sample polarising and differential interference contrast (DIC) to see invisible

features. The illuminator automatically sets optimum illumination through linkage to the shutter, field and aperture diaphragms. Up to five objectives (5x, 10x, 20x, 50x and 100x) may be mounted depending on the model. In this thesis a Nikon MM-800/SL (Fig. 3.9) was employed to analyse the microstructures of the nanostructured bulk samples prepared in chapter 6.



Fig. 3.9. Optical microscope Nikon MM-800/SL.

3.4 Thermoelectric characterisation methods

3.4.1 Hot probe

A homemade hot probe (Fig. 3.10) was used to measure the Seebeck coefficient (α). It consists of a copper hot probe with a hole close to its tip where a differential thermocouple is inserted. The hot probe is heated a few degrees above room temperature by a heater coil. The other junction of the differential thermocouple is inserted in a copper block that remains at room temperature and acts as heat sink.

To perform the measurement, the sample is sandwiched between the hot probe and the heat sink. This establishes a temperature difference (ΔT) across the sample, which is measured by the differential thermocouple. A Seebeck voltage (ΔV) is then generated and measured by Cu wires attached to the hot probe and the heat sink, that serve as well as electrical contacts (Fig. 3.10 (a)). The value of α can be determined by,

$$\alpha = \frac{\Delta V}{\Delta T} \quad (3.1)$$

where the contribution to the Seebeck coefficient from the copper wires is neglected, since it is very small ($1.8 \mu\text{V/K}$).⁽²¹⁾ The accuracy of the equipment, determined using the Bi_2Te_3 standard reference material from NIST (Ref. 3451) is 3 %.⁽¹⁸⁶⁾

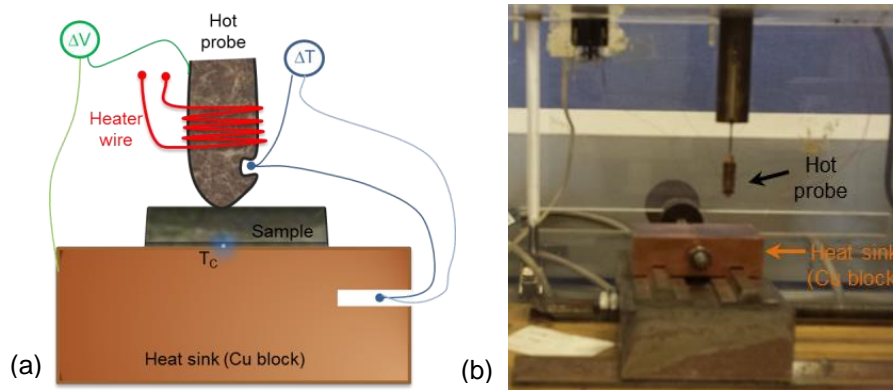


Fig. 3.10 (a) Schematic diagram of the hot probe. (b) Photograph of the actual hot probe apparatus.

3.4.2 4-probe technique

The most common method to measure the electrical resistivity ρ of bulk materials is the 4-probe technique. A commercial 4-probe apparatus (Microcontrole) has been used in this thesis (see Fig. 3.11 (b) and (c)). Since the measurement of electrical current and voltage is typically very accurate, the precision in the determination of electrical conductivity is usually limited by the measurement of the geometry of the sample and its homogeneity.

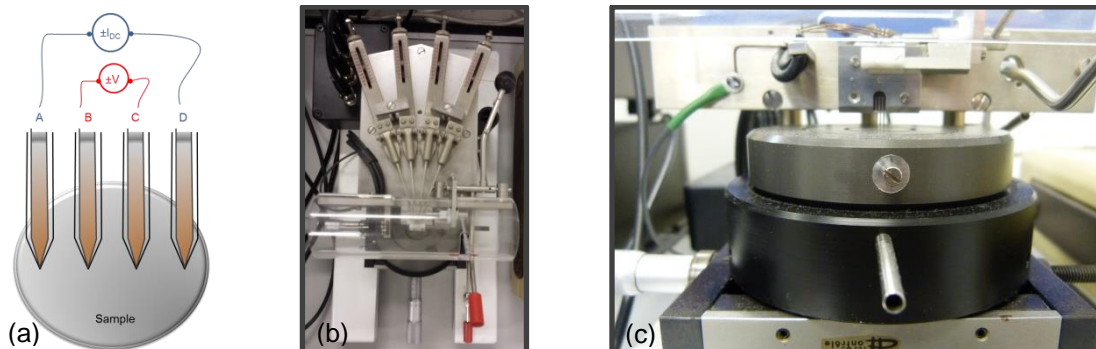


Fig. 3.11 (a) Schematic diagram of the 4-probes. (b) Top view of the 4-probe apparatus. (c) Front view of the 4-probe technique.

The measurement is performed applying a constant DC current I through the outer probes (A and D) and recording the open-circuit voltage V across the inner probes (B and C). In this way, the effect of contact resistances is suppressed and only the contribution from the sample is obtained (see Fig. 3.11 (a)). An additional measurement, changing the polarity of the current is performed and the average of the two measurements is used. This is performed to cancel out possible voltages induced by thermoelectric effects. To properly calculate the resistivity, the probe spacing s , sample diameter d , thickness W and geometrical corrections are required. The formula⁽¹⁸⁷⁾ to calculate ρ is given by,

$$\rho = FC \frac{V}{I} W \quad (3.2)$$

where F is one of the tabulated correction numbers, which is a function of the ratio W/s . The other correction number is C, which is also tabulated and depends on the ratio d/s .

3.4.3 4-multifunctional probe technique

It is a homemade apparatus⁽¹⁸⁶⁾ able to measure the Seebeck coefficient and electrical resistivity at room temperature in a very short time scale (around 20 s). The technique is based on a Van der Pauw setup⁽¹⁸⁸⁾ where 4 multifunctional probes contact the edges of the sample. The multifunctional probes are made up of a Cu tube where a constantan wire is introduced and welded at the tip⁽¹⁸⁹⁾ (Fig. 3.12). Then, the tube is sharpened to form a needle-like tip. A Cu wire is soldered to the upper part of the Cu tube, achieving a T-type thermocouple with the junction (temperature measurement point) at the tip. The Cu wires of the probes are used as electrical contacts. Inside one of the probes a heater coil was inserted to allow heating up to a few degrees above room temperature for the Seebeck coefficient measurements.

A triple channel DC power supply (Keithley 2230-30-1) connected to the computer by USB connection for automatic control, is utilised to supply the currents to the probes and heater. And a Keithley 2000 multimeter (input impedance $>10 \text{ G}\Omega$) was employed to measure voltage outputs and resistance. This is also connected to the computer by a GPIB to USB adaptor. For the rapid switching of the current outputs and voltage readings a USB 16 channel relay module (Denkovi DAE-CB/Ro16/Di4-USB) with remote control via USB was used. All the equipment and measurements are controlled by LabView 2011 in a PC which makes it a fully automated system.

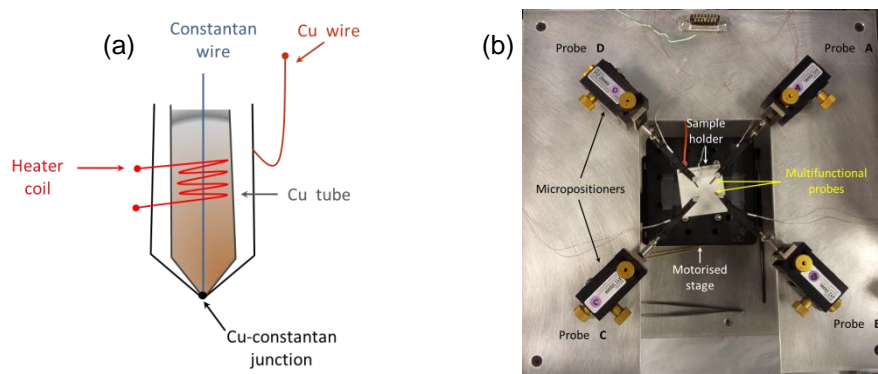


Fig. 3.12 (a) Sketch of a multifunctional probe and (b) Top view of the 4-multifunctional probe apparatus.

The Seebeck coefficient is calculated by measuring the open-circuit voltage ΔV produced when a temperature difference ΔT is applied across two points of the sample. To perform this measurement, probe A is heated around 3 degrees above room temperature by its internal heater. The open-circuit voltage generated between probes A and D is measured with the multimeter. Thus, α is calculated using,

$$\alpha = \frac{\Delta V}{\Delta T} + \alpha_{Cu} \quad (3.3)$$

where α_{Cu} is the absolute Seebeck coefficient of Cu.

The electrical resistivity is measured using the 4 probes and keeping probe A hot during the measurements. This avoids losing time in heating and cooling the probe. A constant DC current is applied between two probes, which induces a voltage difference across the other two probes. For example, if a current I_{AB} enters the sample through probe A and abandons from probe B, inducing a voltage difference between probes C and D, $\Delta V_{CD}=V_C-V_D$. Thus, a resistance $R_{AB,CD}=\Delta V_{CD}/I_{AB}$ can be calculated. $R_{BA,DC}=\Delta V_{DC}/I_{BA}$ was measured by simply changing the current direction. Likewise $R_{CD,AB}$ and $R_{DC,BA}$ can be calculated by applying current through probes C and D and registering the corresponding voltage between A and B. Averaging these 4 resistances $R_A=(R_{AB,CD}+R_{BA,DC}+R_{CD,AB}+R_{DC,BA})/4$, can be calculated. Similarly, $R_B=(R_{BC,AD}+R_{CB,DA}+R_{AD,BC}+R_{DA,CB})/4$, can be also obtained. Employing the Van der Pauw equation,⁽¹⁸⁸⁾ solved by iteration, the sheet resistance R_S can be determined,

$$e^{-\frac{\pi R_A}{R_S}} + e^{-\frac{\pi R_B}{R_S}} = 1 \quad (3.4)$$

From R_S , the electrical resistivity can be calculated by,

$$\rho = R_S W \quad (3.5)$$

It should be noted that thermoelectric voltages can be cancelled out by changing the current polarity when the average resistances are calculated. So measuring with probe A hot does not influence the electrical resistivity determination.

3.4.4 Laser flash instrument

A laser flash apparatus (Netzsch LFA 447 Nanoflash) was used to measure the thermal conductivity of the samples prepared in this thesis. The equipment measures the thermal diffusivity D and the specific heat C_p of the sample. The thermal conductivity λ is

calculated from the previous parameters and the mass density ρ_m . The sample mass was measured by a precision balance (Precisa 40SM-200A) with a precision of 10^{-5} g.

$$\lambda = DC_p\rho_m \quad (3.6)$$

The equipment (shown in Fig. 3.13 (a)) consists of a furnace that contains the sample aligned between a xenon flash tube and an indium antimonide IR detector. The operating temperatures are between 20 to 300 °C. The measurement starts by heating the sample until the desired temperature. Then, the laser from the flash lamp hits the front face of the sample, causing heat absorption in this face, increasing the temperature by 0.5-2 °C. The heat is then diffused across the cross plane of the sample and the temperature rise at the sample's back face is monitored by the IR detector Fig. 3.13 (b). From the registered transient change of the temperature, the thermal diffusivity can be calculated using the Parker expression,⁽¹⁹⁰⁾

$$D = \frac{0.1388W^2}{t_{50}} \quad (3.7)$$

where W is the thickness of the sample and t_{50} is the half-rise time (time for the rear face temperature to reach 50 % of its maximum value). The constant value 0.1388 is known as a Fourier number.⁽¹⁹¹⁾

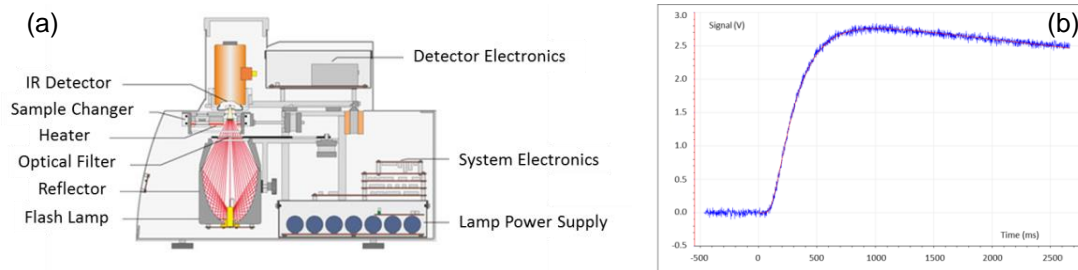


Fig. 3.13 (a) Laser flash equipment⁽¹⁹²⁾ and (b) Typical measurement performed by the laser flash instrument.

As the specific heat of a material is the amount of heat q per unit mass required to raise its temperature by 1 °C at a constant pressure,

$$q = C_p m_m \Delta T \quad (3.8)$$

where m_m is the mass and ΔT is the change in the temperature.

The specific heat can be determined with this equipment by comparing the temperature raise of the sample to that of a reference (with known specific heat) during the diffusivity measurement. So, the change in the temperature, monitored by other IR detector,

in the reference sample is measured and from its value q can be obtained. When a desirable material (unknown C_p) is measured, the same q is used and the C_p of the sample can be calculated using,

$$q = (m_m C_p \Delta T)_{ref} = (m_m C_p \Delta T)_{sample} \quad (3.9)$$

$$C_{p_{sample}} = \frac{(m_m C_p \Delta T)_{ref}}{(m_m \Delta T)_{sample}} \quad (3.10)$$

3.4.5 Impedance spectroscopy

Impedance spectroscopy is utilised to determine the module ZT value of thermoelectric modules. This method produces a small ac current (or voltage) signal in the system and registers the amplitude and phase change of the voltage (or current) response generated as a function of frequency (see Fig. 3.14 (a)). At high frequencies only quick processes show up (such as the total ohmic resistance), while at low frequencies the slow processes are allowed (like the Seebeck voltage induced by the rise of the temperature difference).

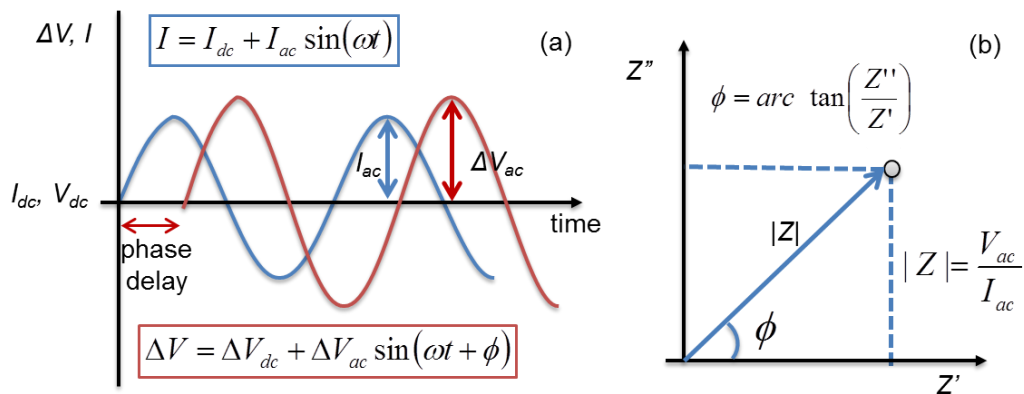


Fig. 3.14. (a) Applied and response signals in an impedance experiment. (b) Point representation in the complex impedance plane.

Impedance results are typically presented in the complex plane (Nyquist plot), where each point is given by a vector defined by the ratio of the amplitude of the voltage and current waves and the phase angle as shown in Fig. 3.14 (b). For a thermoelectric module under suspended conditions impedance spectroscopy allows the determination of the module ZT,⁽¹⁹³⁾ which can be obtained from the high frequency and low frequency intercepts with the real axis (zero phase points) of the impedance signal in the complex plane (see Fig. 3.15).

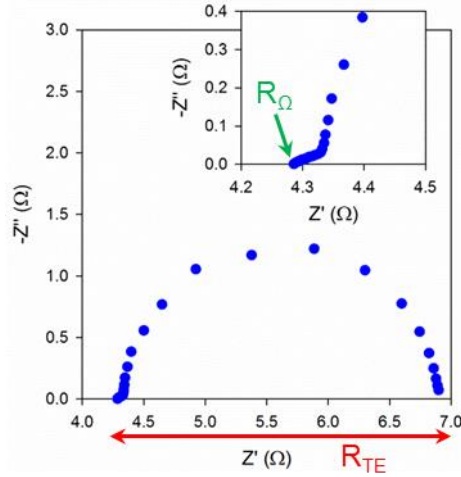


Fig. 3.15. Nyquist plot of a commercial 254-leg thermoelectric module and the characteristic parameters R_{Ω} and R_{TE} . The inset shows a magnification of the high-frequency part. Image taken from reference ⁽¹⁹⁴⁾.

In a thermoelectric module of $2N$ legs, being N the number of couples, the voltage difference in the device assuming identical properties for n and p-type materials is given by,

$$V = IR_{\Omega} + 2N\alpha\Delta T \quad (3.11)$$

considering α the absolute Seebeck coefficient of a single leg and R_{Ω} the total ohmic resistance of the device, which includes the parasitic resistance R_p contribution (wires, electrodes and contacts), and the contribution from the intrinsic resistance of the thermoelectric materials. From the energy balance at the hot side at steady-state, neglecting Joule effect and under adiabatic conditions, it is obtained,

$$\alpha IT_H = \frac{\lambda A}{L} \Delta T \quad (3.12)$$

being A and L the cross-sectional area and length of a leg. From this equation, ΔT can be extracted,

$$\Delta T = \frac{\alpha IT_H L}{\lambda A}. \quad (3.13)$$

The impedance function at steady state (frequency $\rightarrow 0$) can be determined using Eq. (3.11 and 3.13),

$$Z = \frac{V}{I} = R_{\Omega} + 2N \frac{\alpha^2 TL}{\lambda A}. \quad (3.14)$$

The last term in Eq. (3.14) is called a thermoelectric resistance R_{TE} , which only shows up when the ΔT is established in the device (low frequency). At high frequencies only R_{Ω} is present. From the ratio between R and R_{TE} , the module ZT can be calculated,

$$(ZT)_{module} = \frac{R_{TE}}{R_{\Omega}} = \frac{2N\alpha^2 TL}{\left(R_p + \frac{2NL}{\sigma A}\right)\lambda A}. \quad (3.15)$$

It should be noted that when the parasitic resistance is neglected, $(ZT)_{module}$ equals the material's ZT.

The equipment employed in this thesis for impedance measurements is an Autolab PGSTAT302N potentiostat equipped with FRA32M impedance module.

Chapter 4 : Preparation of Bismuth Telluride Nanopowder

4.1 Introduction

4.2 Experimental part

4.3 Optimisation of ball milling

4.3.1 Particle size distribution

4.3.2 Morphological characterisation

4.3.3 Structural characterisation

4.4 Optimisation of ultrasound milling

4.4.1 Particle size distribution

4.4.2 Morphological characterisation

4.4.3 Structural characterisation

4.5 Comparison between ball and ultrasound milling techniques

4.5.1 Morphological characterisation

4.5.2 Structural characterisation

4.6 Conclusions

Chapter 4

4.1 Introduction

The aim of this chapter is the identification of the optimal conditions to produce bismuth telluride nanoparticles using two different methods: ball milling (BM) and ultrasound milling (UM). BM is a well-established method, widely used in the preparation of Bi_2Te_3 nanoparticles.⁽¹⁾ However, UM has never been employed before and the conditions to achieve Bi_2Te_3 nanoparticles are described in this chapter for the first time. The different powders obtained are characterised using a particle size analyser, SEM and XRD.

The optimisation for the preparation of n- and p-type materials by BM method is described in section 4.3 after defining the general experimental conditions adopted for both methods in section 4.2. Then, the optimisation employing UM technique is presented in section 4.4. Finally, a comparison of both methods is shown in section 4.5.

4.2 Experimental part

The bulk precursor materials used to produce nanoparticles were n- and p-type bismuth telluride, purchased as an ingot from Thermonamic Electronics (China). The ingots were cut using a saw into small discs (3-5 cm diameter) that were crushed utilising a mortar and pestle to generate small pieces that were placed inside a micro hammer-cutter mill (Fig. 4.1 (a)) to perform an initial reduction of the particle size. Then, the resulting material was sieved using a 106 μm pore size sieve from Endecotts (Fig. 4.1 (b)). The powder that passed through the sieve ($< 106 \mu\text{m}$) is considered as the reference and was then treated by BM and UM methods. In this way, all the milling processes performed in this thesis started from a particle size smaller than 106 μm . A schematic process of the method to produce the powder to be treated by the milling process is shown in Fig. 4.1 (b).

We would like to remark that the 106 μm sieve aperture was used in order to start the milling treatments with the smallest particle size possible and thus reduce the efforts to achieve nanoparticles. The 106 μm sieve was the smallest available at that moment in the laboratory.

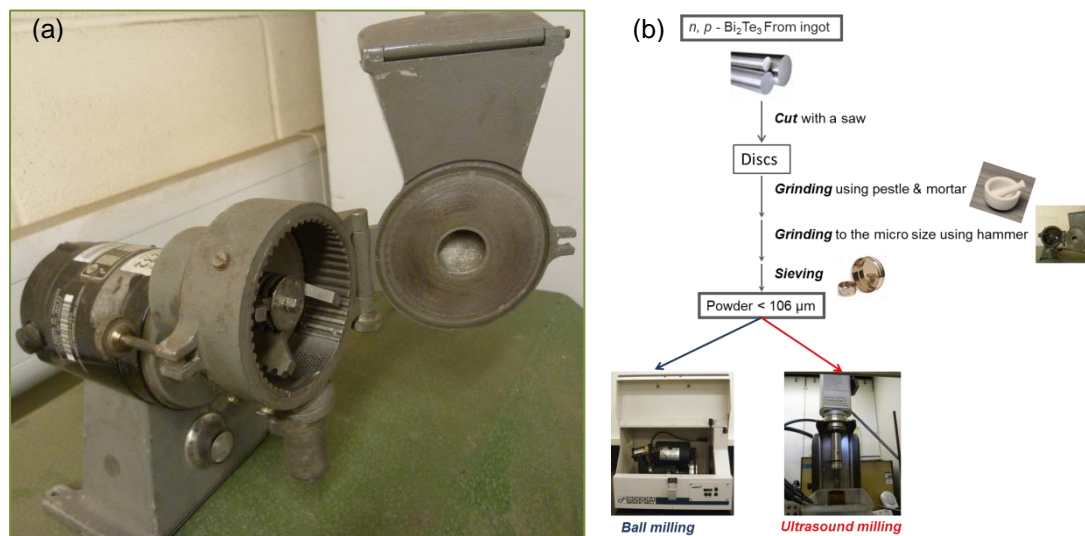


Fig. 4.1 (a) Micro hammer-cutter mill utilised for the pre-treatment. (b) Schematic process to prepare the powder from the ingot by the milling processes.

The distribution of the particle size of the powders was measured by the Mastersizer 3000 equipment (see section 3.3.2) adding a small amount of each powder to deionised water. In some cases, a soap was needed to help to segregate the sample. The results provided are the average of 11 measurements registered by the equipment for the same sample.

XRD measurements were obtained using the Philips PW1710 Automated Powder Diffractometer (see section 3.3.4) between 2 and 80 $2\theta^\circ$ with an angle step size of 0.04 and 1 s counting time. All XRD patterns were normalised. The phases of the ingot were identified using the ICSD Inorganic Crystal Structure Database.⁽¹⁹⁵⁾

4.3 Optimisation of ball milling

4.3.1 Particle size distribution

The parameters that were modified in order to optimise the production of nanoparticles by BM were the *milling time* and the *balls:material* weight ratio. As a common procedure adopted in all the BM experiments performed, the milling was operated employing intervals of 30 min operation followed by a 15 min break. This was carried out to avoid heating and possible chemical changes of the samples due to overheating, and the damage to the fuse

of the apparatus which is likely to occur if operated continuously during long times. Only the operation time is accounted for when the time of the experiment is reported, i. e., an experiment of 1 h involves two intervals of 30 min operation plus 15 min break (1 h and 15 min in total). The results are shown separately for the n- and p-type materials.

• **n-type $\text{Bi}_2\text{Te}_{2.79}\text{Se}_{0.21} + 0.001 \text{I}_2$:**

Time: To optimise the milling time, different BM experiments were performed at different times utilising the same balls: $\text{Bi}_2\text{Te}_{2.79}\text{Se}_{0.21}$ weight ratio.

Ratio \rightarrow 20:1: In Table 4.1 different times in which the BM was performed are shown.

Table 4.1. Ball milling experiments performed at different times for n-type Bi_2Te_3 at the 20:1 balls:material ratio.

Experiment	Milling Process	Ratio	Milling Time (h)
Reference	NO		
BM_2 h_20:1	30 min ON 15 min OFF	20:1	2
BM_8 h_20:1			8
BM_24 h_20:1			24
BM_48 h_20:1			48
BM_64 h_20:1			64

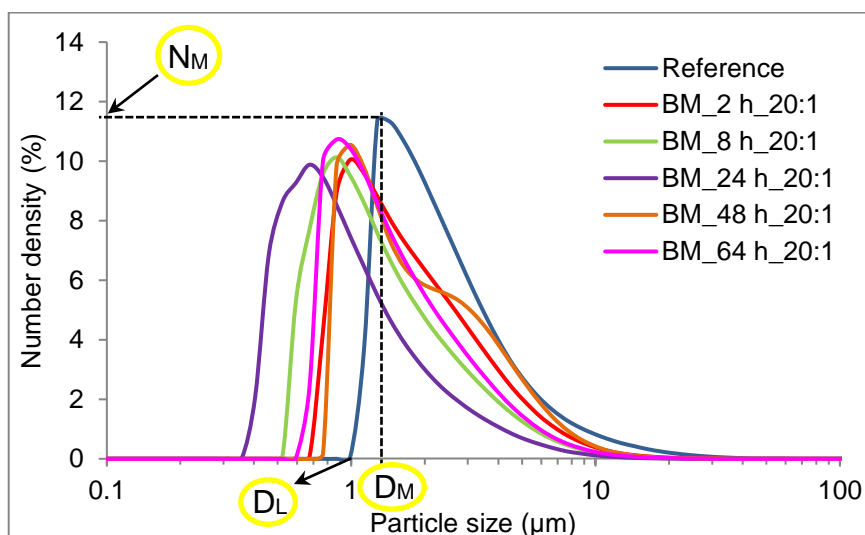


Fig. 4.2. Particle size distribution in number density of n-type Bi_2Te_3 after ball milling using a balls:material ratio 20:1 at different times. Parameters N_M , D_M and D_L indicate the maximum number density percentage, the particle size corresponding to this maximum and the lowest particle size identified, respectively.

Fig. 4.2 (number density) and Fig. A.1 (volume density) show that BM treatment produces a reduction in the particle size even when it is running only for two hours. However, the smallest particles are formed at 24 h, observing nanoparticles with

sizes around 350 nm. At 8 h there are nanoparticles in the range of 500 to 600 nm and similar size distributions are observed at 2, 48 and 64 h. From these results an optimum time of 24 h is considered.

Since a quite small amount of bismuth telluride is employed in the BM process when the ratio is 20:1, which leads to a limited amount of nano-powder available for further processing into pellets, other ratios were analysed. It will be evaluated if higher amount of bismuth telluride produces similar particle size distributions to that obtained at 24 h. If this is the case, less milling experiments will be required to obtain the necessary amount of bismuth telluride to prepare nanobulk discs. A ratio 5:1 was then analysed at different times to compare the results to the 20:1 ratio.

Ratio → 5:1: The BM experiments performed at 5:1 ratio are shown in Table 4.2. The particle size distributions in volume and number of these experiments are shown in Fig. A.2 and Fig. A.3 respectively. Similarly to the results obtained at 20:1 ratio, the smallest nanoparticles are obtained at 24 h for the 5:1 ratio. They show the smallest particle size around 400 nm, slightly higher than the size achieved at 20:1 ratio (≈ 350 nm). The particle size decreases from 2 to 24 h. However, at 48 h the size no longer decreases but increases as also observed in the 20:1 ratio, showing a profile similar to the 2 h experiment. It should be mentioned that at 5:1 ratio, the 64 h experiment was not performed, since the 48 h result already shows the increase in the particle size. Therefore, a ratio 5:1 and 24 h time is more convenient to achieve nanoparticles.

Table 4.2. Ball milling experiments performed at different times for n-type Bi₂Te₃ at the 5:1 balls:material ratio. Parameters N_M, D_M and D_L indicate the maximum number density percentage, the particle size corresponding to this maximum and the lowest particle size identified, respectively.

Experiment	Milling Process	Ratio	Milling Time (h)	D _L (nm)	D _M (nm)	N _M (%)
Reference	NO			991	1280	11.37
BM_2 h_5:1	30 min ON 15 min OFF	5 :1	2	675	872	11.49
BM_8 h_5:1			8	523	767	9.56
BM_24 h_5:1			24	405	523	12.20
BM_48 h_5:1			48	675	872	10.71

Ratio → 2:1 and 1:1: In a next optimisation step the amount of bismuth telluride is increased by using 2:1 and 1:1 ratios, keeping a fixed experiment time of 24 h. These experiments are compared with the previous 20:1 and 5:1 ratios as described in Table 4.3. The particle size distributions are plotted in Fig. A.5 (number density) and Fig. A.4 (volume density). From the results shown in Table 4.3 it can

be observed that the particle size distribution of the samples obtained using 20:1 and 5:1 ratios are similar, producing comparable smallest particle sizes. Utilising 2:1 and 1:1 ratios the smallest particle sizes increase significantly (≈ 700 and 600 nm respectively). Therefore, it can be concluded that the optimum conditions identified for BM experiments of n-type bismuth telluride are a **5:1 ratio** and **24 h time**.

Table 4.3. Variation of the balls:material ratio for ball milling experiments of n-type Bi_2Te_3 at a fixed time of 24 h. Parameters N_M , D_M and D_L indicate the maximum number density percentage, the particle size corresponding to this maximum and the lowest particle size identified, respectively.

Experiment	Milling Process	Ratio	Milling Time (h)	D_L (nm)	D_M (nm)	N_M (%)
Reference	NO			991	1280	11.37
BM_24 h_20:1	30 min ON 15 min OFF	20 :1	24	357	675	9.88
BM_24 h_5:1		5 :1		405	523	12.20
BM_24 h_2:1		2 :1		675	991	10.92
BM_24 h_1:1		1 :1		594	872	10.03

For a more detailed analysis of the amount of nanoparticles obtained, Table 4.4 shows the smallest particle sizes and the percentage of number of particles smaller than $1 \mu\text{m}$ for the 5:1 ratio and under different times to see how they change with the milling time.

Table 4.4. Results of the minimum particle size and the percentage of number of particles smaller than $1 \mu\text{m}$ achieved after ball milling experiments at different times but under the same balls: Bi_2Te_3 ratio (5:1) for the n-type material.

Experiment	Milling Time (h)	Smallest Particle Size (nm)	Percentage of Number of Particles $< 1 \mu\text{m}$
Reference	NO	991	0.011
BM_2 h_5:1	2	675	12.41
BM_8 h_5:1	8	523	13.09
BM_24 h_5:1	24	405	35.65
BM_48 h_5:1	48	675	11.02

At 24 h the largest production of particles smaller than $1 \mu\text{m}$ is achieved. The rest of experiments present quite similar percentages of number of particles smaller than $1 \mu\text{m}$ (11-13 %). This trend is shown in Fig. 4.3, Fig. A.6 and Fig. A.7.

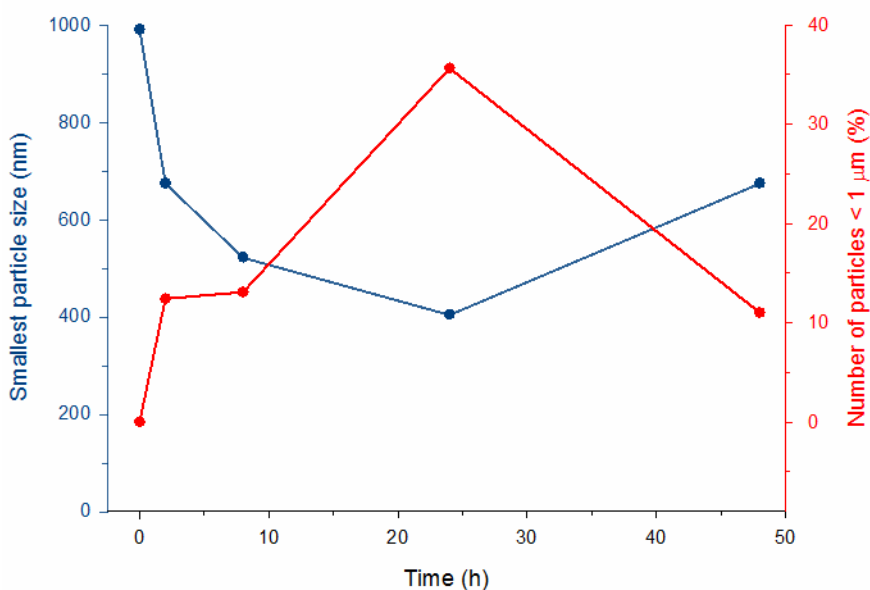


Fig. 4.3. Representation of the smallest particle size (blue) and the number of particles smaller than 1 μm (red) achieved for n-type Bi₂Te₃ after ball milling experiments under different times and 5:1 balls:material ratio.

• p-type Bi_{0.5}Te₃Sb_{1.5}:

Time: To optimise the time, different BM experiments were performed at different times utilising the same balls:Bi_{0.5}Te₃Sb_{1.5} weight ratio (20:1). The first experiments were performed at 2, 8 and 24 h. Since it was observed in the results that at 24 h an increase in the particle size occurred, more milling times were added for a more detailed optimisation. Table 4.5 shows the experiments carried out. All the experiments performed can be seen in Fig. A.8 (volume density) and Fig. A.9 (number density).

Ratio → 20:1: It can be observed in Table 4.5 that the reference sample already presents nanoparticles around 770 nm in size. This is due to the fact that when the p-type powder is crushed, it breaks down into fine particles. Some graphs show that at some milling times (2 h, 7 h and 9 h) the particle size is larger than the reference. Nevertheless, the smallest nanoparticles were formed at 8 h (around 600 nm). At 24 h a similar pattern to 8 h was observed although with slightly larger particle size. Therefore, for this particular ratio the optimum time for the BM treatment was 8 h.

Table 4.5. Variation of the ball milling time under the same balls:material ratio for p-type Bi₂Te₃. Parameters N_M, D_M and D_L indicate the maximum number density percentage, the particle size corresponding to this maximum and the lowest particle size identified, respectively.

Experiment	Milling Process	Ratio	Milling Time (h)	D _L (nm)	D _M (nm)	N _M (%)
Reference	NO			767	872	13.62
BM_2 h_20:1	30 min ON 15 min OFF	20 :1	2	872	1130	12.40
BM_3 h_20:1			3	767	991	12.39
BM_5 h_20:1			5	767	991	11.95
BM_6 h_20:1			6	872	1130	14.02
BM_7 h_20:1			7	872	1130	13.56
BM_8 h_20:1			8	594	872	10.34
BM_9 h_20:1			9	767	991	13.63
BM_10 h_20:1			10	767	991	13.14
BM_12 h_20:1			12	767	991	12.54
BM_24 h_20:1			24	675	872	10.16

As performed for the n-type bismuth telluride, different balls:material weight ratios were analysed at a fixed treatment time of 8 h and compared to the 20:1 ratio. Table 4.6 summarises the experiments and the obtained results are shown in Fig. A.11 (number density) and Fig. A.10 (volume density).

Different Ratios: Table 4.6 shows a significant increase of the smallest particle size from ≈ 600 nm for 20:1 ratio to 900 nm in the best of the cases (ratios 10:1 and 5:1). Consequently, the optimum conditions for BM experiments for the p-type bismuth telluride are the **20:1 ratio** and **8 h** time.

Table 4.6. Variation of the balls:material ratio at a fixed treatment time of 8 h for ball milling experiments of p-type Bi₂Te₃. Parameters N_M, D_M and D_L indicate the maximum number density percentage, the particle size corresponding to this maximum and the lowest particle size identified, respectively.

Experiment	Milling Process	Ratio	Milling Time (h)	D _L (nm)	D _M (nm)	N _M (%)
Reference	NO			767	872	13.62
BM_8 h_20:1	30 min ON 15 min OFF	20 :1	8	594	872	10.34
BM_8 h_10:1		10 :1		872	1280	14.65
BM_8 h_5:1		5 :1		872	991	14.95
BM_8 h_2:1		2 :1		991	1280	14.15

In Table 4.7 and Fig. 4.4, Fig. A.12 and Fig. A.13, the more detailed analysis of the nanoparticles obtained, which includes the smallest particle size and the percentage of number of nanoparticles smaller than 1 μ m, are presented for the 20:1 ratio at different times.

Table 4.7. Minimum particle size and percentage of the number of particles smaller than 1 μm obtained after ball milling experiments at different times under the same balls: Bi_2Te_3 ratio (20:1) for the p-type material.

Experiment	Milling Time (h)	Smallest Particle Size (nm)	Percentage of Number of Particles < 1 μm
Reference	NO	767	9.77
BM_2 h_20:1	2	872	2.22
BM_7 h_20:1	7	872	2.81
BM_8 h_20:1	8	594	12.61
BM_9 h_20:1	9	767	6.58
BM_24 h_20:1	24	675	7.72

A decrease in the smallest particle size was achieved at 8 h, which cannot be reduced at longer treatment times. At 8 h the largest production of particles smaller than 1 μm was also achieved ($\approx 13\%$).

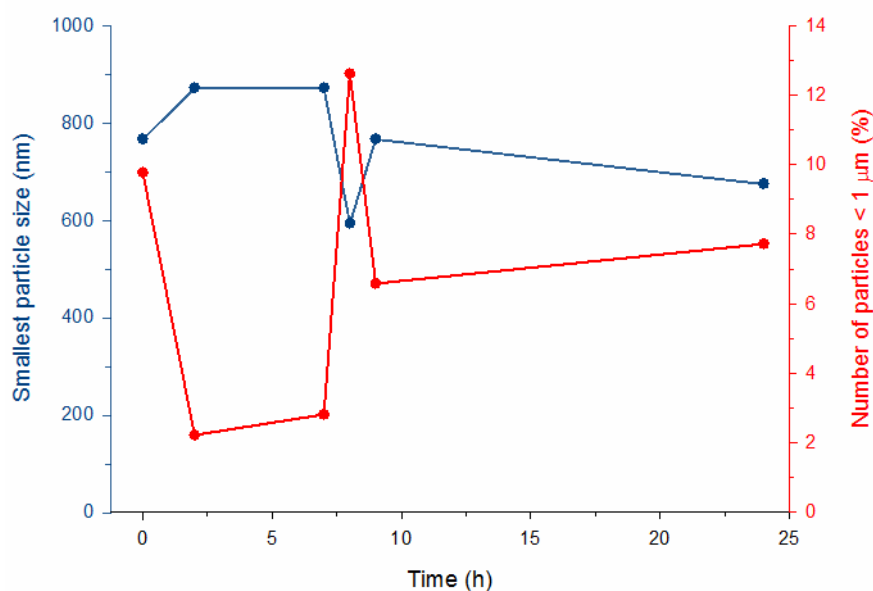


Fig. 4.4. Smallest particle size (blue) and percentage of the number of particles smaller than 1 μm (red) obtained for ball milling experiments of p-type Bi_2Te_3 at different times and 20:1 balls:material ratio.

4.3.2 Morphological characterisation

In order to evaluate the powders further, SEM experiments were performed.

• n-type $\text{Bi}_2\text{Te}_{2.79}\text{Se}_{0.21} + 0.001 \text{I}_2$:

Fig. 4.5 shows SEM images at different magnifications for n-type Bi_2Te_3 powders obtained before and after BM processes at different times (2, 8, 24 and 48 h) using the 5:1

optimum ratio (particle size analysis can be found in Table 4.2). There is a clear reduction in the particle size after the BM process at all times.

From the SEM images at the largest magnifications, it can be observed that average sizes of the smallest particles lie around 200 nm for the non-treated, 24 h and 48 h experiments, and around 350 nm for 2 and 8 h. It should be noted that the previous particle size analysis by laser diffraction was not able to detect these average sizes and provided smallest particle sizes which are from 120 up to 800 nm higher. For this reason laser diffraction results should be handled with care and SEM data is considered as a more reliable method for the detection of particle sizes.

On the other hand, it can be seen that finer powders are obtained at 24 and 48 h. Particle sizes at these two times do not seem to differ significantly, except for the fact of the existence of particles with larger sizes more dominantly at 48 h (Fig. 4.5 (q)). Regarding the morphology of the particles no relevant differences are observed between the non-treated and treated powders.

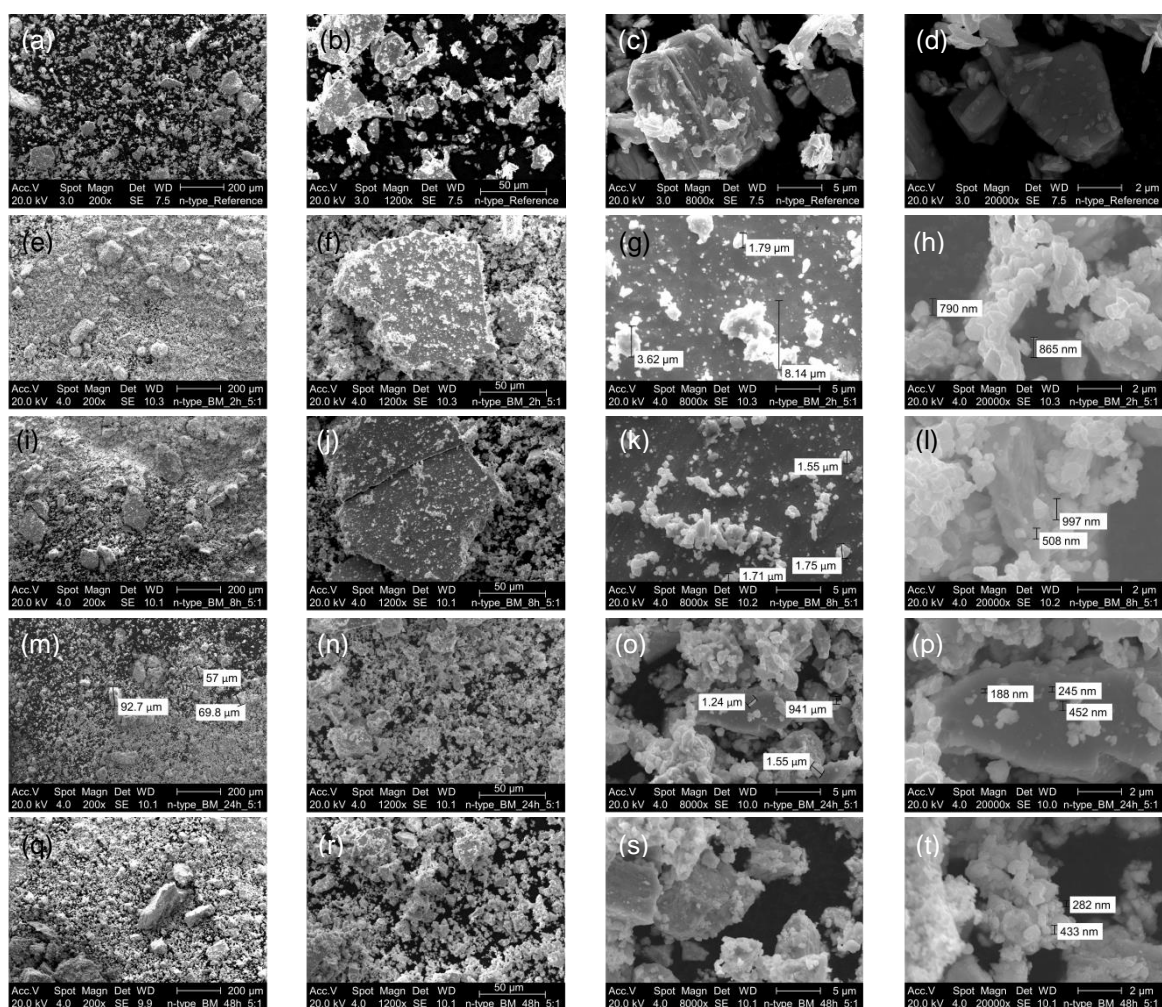


Fig. 4.5. SEM images of $n\text{-Bi}_2\text{Te}_3$ (a-d) before ball milling and after ball milling experiments at 5:1 ratio at different times: (e-h) 2 h, (i-l) 8 h, (m-p) 24 h and (q-t) 48 h from left to right, scale bar: 200 μm , 50 μm , 5 μm and 2 μm .

• *p*-type $\text{Bi}_{0.5}\text{Te}_3\text{Sb}_{1.5}$:

SEM images were also obtained for the *p*-type material. Non-treated and treated by BM samples at different times (2, 8 and 24 h) and using 20:1 ratio conditions are shown in Fig. 4.6. Particle size analysis for this experiment can be found in Table 4.5.

As occurred in the case of the *n*-type material, significant differences are observed between the SEM images and laser diffraction results in the smallest particle sizes. For all the treated powders the smallest particle sizes are around 300 nm (Fig. 4.6 (h, l and p)). However, the powder obtained at 2 h (Fig. 4.6 (h)) seems to present larger particles than the treatment at 8 and 24 h (Fig. 4.6 (l and p), respectively). Then, both 8 h and 24 h can be considered as optimum conditions. Since 8 h is a more convenient reduced time, these conditions will be finally adopted for the production of nanobulk samples in chapter 6. This selection is the same as chosen from the optimisation based on laser diffraction experiments.

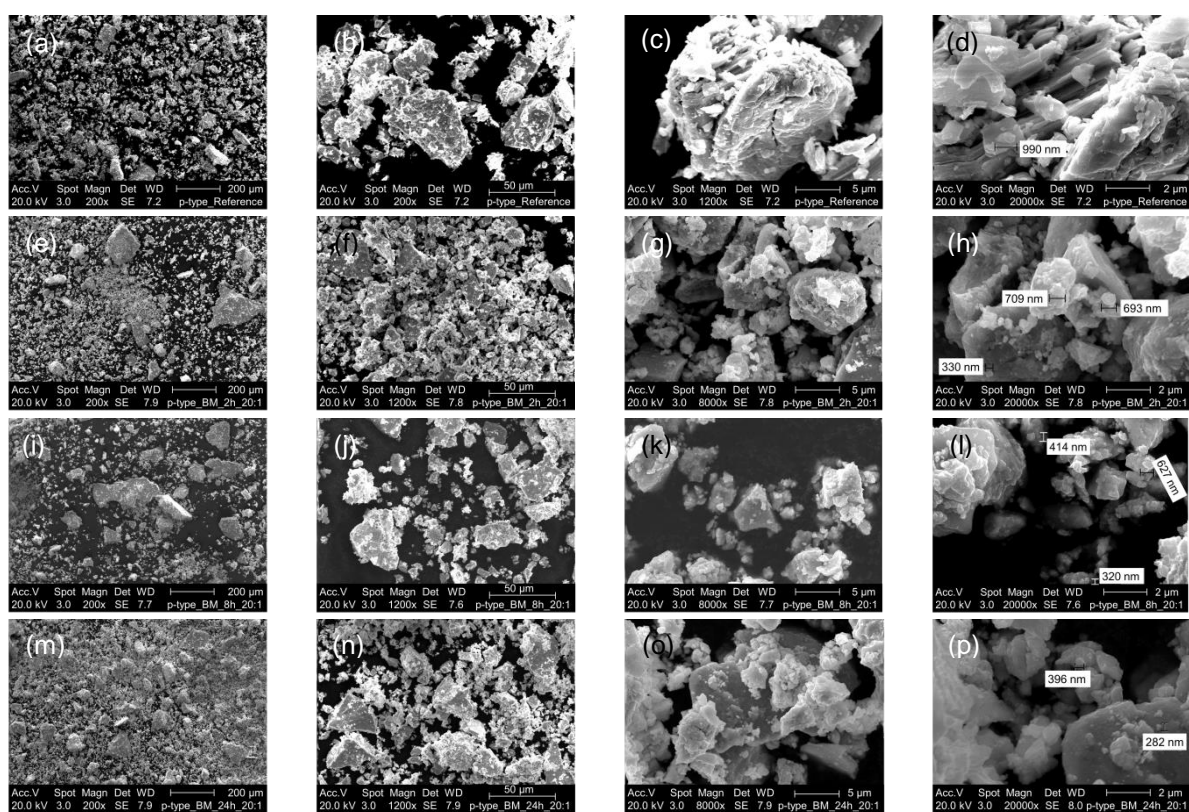


Fig. 4.6. SEM images of *p*- Bi_2Te_3 (a-d) before and after ball milling experiments at 20:1 ratio at different times: (e-h) 2 h, (i-l) 8 h and (m-p) 24 h from left to right, scale bar: 200 μm , 50 μm , 5 μm and 2 μm .

4.3.3 Structural characterisation

For both types (n- and p-) of bismuth telluride materials the phase structure and the grain orientation of a disc cut from the ingot, a reference sample with particle size $<106\ \mu\text{m}$ and the ball milled powders were analysed. As in previous experiments performed for the determination of particle size distributions, the reference sample corresponds to a crushed material which was sieved down to $106\ \mu\text{m}$. Only the identified optimum BM treated sample was analysed.

• **n-type $\text{Bi}_2\text{Te}_{2.79}\text{Se}_{0.21} + 0.001\ \text{I}_2$:**

The XRD patterns (Fig. 4.7) show that all the three samples are single-phase $\text{Bi}_2\text{Te}_{2.79}\text{Se}_{0.21}$, corresponding to a rhombohedral crystal geometry (space group $R\bar{3}m$)⁽¹⁹⁶⁾ with no detectable impurities of other phases. Nevertheless, after the crushing and BM processes, the preferred orientation changed from (110) for the ingot sample to (015) and (0015) for the reference, and (015) for the BM treated sample.

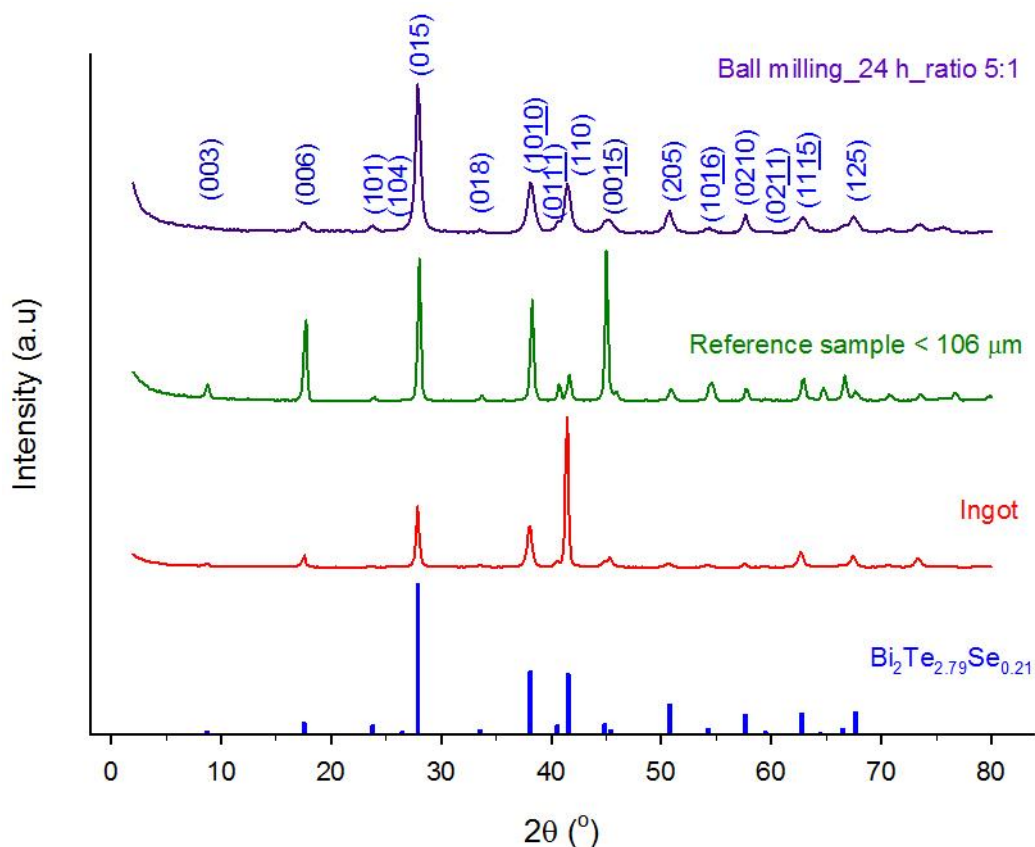


Fig. 4.7. XRD patterns of n-type $\text{Bi}_2\text{Te}_{2.79}\text{Se}_{0.21}$: (blue) theoretical, (red) ingot sample, (green) reference before milling and (purple) after ball milling experiment performed at 24 h and 5:1 balls:material ratio.

The peaks of the ingot and reference samples are sharper than the ball milled sample, which indicates a reduction in the particle size for the latter,⁽⁷⁾ where the sample became more polycrystalline as expected due to the reduction in the particle size.

• **p-type $\text{Bi}_{0.5}\text{Te}_3\text{Sb}_{1.5}$:**

All the three samples are single-phase $\text{Bi}_{0.5}\text{Te}_{2.5}\text{Sb}_{1.5}$ (space group $R\bar{3}m$).⁽¹⁹⁶⁾ Similarly to the n-type material, the p-type sample treated by BM (see Fig. 4.8) does not modify the rhombohedral geometry of the initial ingot. Furthermore, the preferred orientation (015) is maintained for all the samples except for the ingot in which the preferred orientation is (110). This could be due to the fact that the ingot sample is a pellet and it becomes more difficult to identify all the different orientations because the grains in the ingot are larger than in the powder and they contribute less to the total counts. The peaks of the ingot and reference samples are sharper and more intense than the ball milled sample, indicating again a reduction in the grain size in the latter.

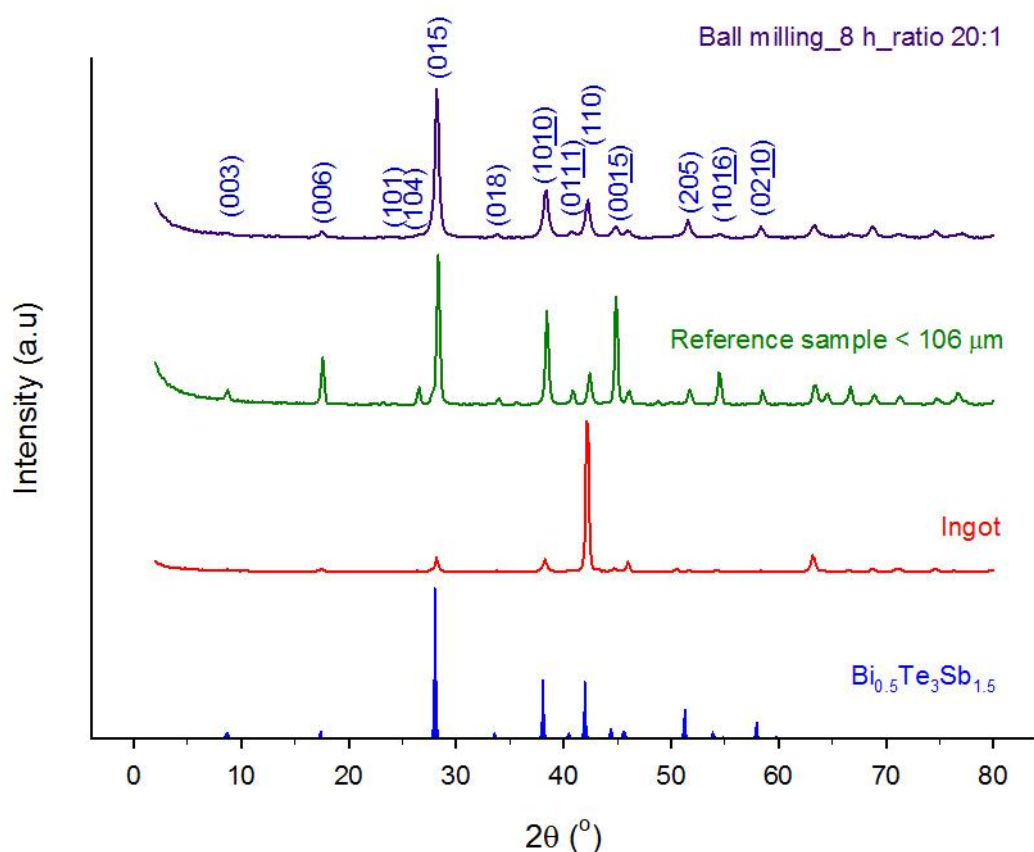


Fig. 4.8. XRD patterns of p-type $\text{Bi}_{0.5}\text{Te}_{2.5}\text{Sb}_{1.5}$: (blue) theoretical, (red) ingot sample, (green) reference before milling and (purple) after ball milling experiments performed for 8 h at 10:1 balls:material ratio.

4.4 Optimisation of ultrasound milling

The parameters to be optimised for the production of nanoparticles by UM are the *solvent*, *milling time*, *amplitude of the ultrasound*, *cooling system*, the use of *additives* and the *concentration*. Unlike BM, in UM the precursor powder is dispersed in a solvent during the treatment. The solvent was the only parameter that was examined only for the n-type bismuth telluride. The resulting solvent was also applied to the p-type material. The rest of parameters were evaluated for both n- and p-type materials.

• **n-type $\text{Bi}_2\text{Te}_{2.79}\text{Te}_{0.21} + 0.001 \text{ I}_2$** : It should be remembered that, as indicated in the experimental part above, in all these experiments the n-type bismuth telluride was broken down from the ingot and crushed into a powder, which was then sieved using a 106 μm pore size. This resulting powder is then placed in the UM vessel to be treated. A non-treated portion of the sieved powder (particle size $<106 \mu\text{m}$) was used as reference.

Solvent: The different solvents employed were 1-butanol, dimethyl-formamide (DMF), ethanol (EtOH) and decane. The concentration of the powder used in all the UM experiments was $8.3 \cdot 10^{-3}$ M. The selection of these solvents was based on different properties. A high flash point (lowest temperature at which vapours of a fluid will ignite) solvent was important to avoid combustion. A solvent easy to evaporate and unable to produce oxidation of the material was also required. In Table 4.8 the solvents and their corresponding flash points are shown.

Table 4.8. Solvents utilised to perform the ultrasound milling experiments and their flash point.

Solvent	Flash Point ($^{\circ}\text{C}$)
1-Butanol	35
DMF	58
EtOH	13
Decane	46
H ₂ O distilled	--

The UM experiments were performed for 2 h at 100 % amplitude and using 2 cooling systems. It should be mentioned that unlike the BM treatment, the UM process was run continuously, without any breaks. After the treatments the samples were dried under convective air flow of the fume hood and the collected powder was pressed into discs to measure its thermoelectric properties. The conditions for the cold pressing process were 5 ton (1513.7 MPa) for 30 s. After pressing, the specimens were heated at $\approx 360 \text{ }^{\circ}\text{C}$ for 45 min under argon atmosphere for sintering.

Density, Seebeck coefficient and electrical conductivity measurements were performed and used to select the optimum solvent. Seebeck coefficient was measured by the hot probe and electrical conductivity by a 4-probe technique (see section 3.4). The obtained values are shown in Table 4.9 and Fig. A.14 to A.17.

Table 4.9. Density, Seebeck coefficient, electrical conductivity and power factor values obtained for the discs prepared with powder treated by ultrasound milling at 100 % amplitude, 2 coolers and for 2 h using different solvents.

Solvent	Density (g/cm ³)	S (μV/K)	σ (Ω·cm) ⁻¹	Power Factor (mW/m·K ²)
Reference	6.51	-114.85	1265.64	1.670
1-Butanol	6.55	-123.15	759.70	1.152
DMF	6.46	-151.58	23.82	0.055
EtOH	6.50	-158.76	270.25	0.681
Decane	6.51	-189.23	69.92	0.250
Distilled H ₂ O	6.64	-127.77	95.95	0.157

There is not much difference in the density of the discs prepared. All of them present \approx 83-84 % of the density of the ingot provided from the company (7.83 g/cm³). The density values are somewhat low, since cold pressing was used instead of hot pressing (at that moment there was no hot press equipment available). We would like to remark that in the next chapter the hot press process is developed to identify adequate conditions to prepare discs with suitable densities.

There is a substantial variation of the Seebeck coefficient depending on the solvent utilised in the UM process. Decane presents the highest Seebeck coefficient value (-189 μV/K). DMF and EtOH show similar values (-150 and -160 μV/K respectively), whereas 1-butanol displays the lowest (-123 μV/K), very similar to the reference sample and the distilled water.

On the other hand, the electrical conductivity presented an opposite trend to that of the Seebeck coefficient, since in this case the reference sample showed a higher electrical conductivity than the ingot and the rest of the samples treated by the milling process.

Amongst the samples treated by UM, the solvent that presented the largest electrical conductivity was 1-butanol (\approx 760 (Ωcm)⁻¹) whereas in the rest of the cases a severe decrease was observed, reaching in some cases up to 10 times lower conductivity. This higher value of 1-butanol is dominant in the power factor and this solvent is selected for the UM treatments.

Once the solvent is chosen, the next experiments, to identify the rest of the optimum conditions, follow a similar structure to the optimisation of BM, that is, first the particle

size distribution is examined, then the morphological characterisation follows, and finally the structural characterisation is discussed.

4.4.1 Particle size distribution

Use of additives (PG): The additive employed during the treatment added to the solvent was propylene glycol (PG), which usually helps to avoid agglomerations of the particles. Its use was analysed by performing UM experiments at different times with or without the addition of PG. When added, the PG concentration was 1 % of the total volume. The concentration of powder was $8.3 \cdot 10^{-3}$ M. A summary of the experiments performed at 100 % amplitude, 2 cooling systems and with and without the addition of propylene glycol (PG) is given in Table 4.10.

The results obtained without the use of PG additive are shown in Fig. A.18 (volume density) and Fig. A.19 (number density). The smallest particles under these conditions were achieved at 30 min and 2 h (≈ 675 nm), while longer times result in larger particle size.

With the additive PG, the smallest particles were produced at 30 min (≈ 760 nm), which are larger than the results obtained without PG for the same time (≈ 675 nm). No improvement was observed at the other times either and consequently the use of PG was discarded. For more details, Fig. A.20 (volume density) and Fig. A.21 (number density) show the particle size distribution when PG additive is employed.

Table 4.10. Ultrasound milling experiments carried out at different times, 100 % amplitude, 2 coolers and with and without the addition of propylene glycol (PG) for n-type Bi_2Te_3 . Parameters N_M , D_M and D_L indicate the maximum number density percentage, the particle size corresponding to this maximum and the lowest particle size identified, respectively.

Experiment	Power Amplitude (%)	Additive	Cooling System	Milling Time (h)	D_L (nm)	D_M (nm)	N_M (%)
Reference					991	1280	11.37
UM_0.5 h	100	NO	2	0.5	675	872	10.31
UM_2 h				2	675	872	11.17
UM_4 h				4	872	991	17.41
UM_6 h				6	872	991	18.71
UM_8 h				8	872	1130	18.91
UM_10 h				10	767	991	18.29
UM_0.5 h_PG				1 % Vol PG	0.5	767	991
UM_2 h_PG		2			872	1130	13.74
UM_4 h_PG		4			872	1280	15.38
UM_6 h_PG		6			872	1130	15.83
UM_8 h_PG		8			991	1130	25.96
UM_10 h_PG		10			872	991	17.07

Amplitude of the ultrasound: To evaluate the effect of the oscillation amplitude of the ultrasound tip in the treated powders, different experiments were performed at an amplitude (60 %) different from the previously used value (100 %). It should be mentioned that the minimum amplitude that can be set in the equipment is 50 %. Using 60 % amplitude, the smallest particles were obtained at 4 and 6 h (≈ 460 nm) as it can be observed in Table. 4.11, Fig. A.23 (number density) and Fig. A.22 (volume density). Comparing these results to the same experiments performed at 100 % amplitude (Fig. A.19) significant differences can be observed. At 100 % amplitude the smallest particle size (675 nm) was achieved at 30 min and 2 h, which is more than 200 nm higher size than the smallest sizes found using 60 % (at 4 and 6 h). In addition, at these times (30 min and 2 h) the smallest particle size at 60 % amplitude is ≈ 600 nm, close to the results at 100 %.

These results demonstrate that the reduction in the amplitude of the UM significantly affects the size distribution of the nanoparticles. It should be mentioned that the fact of obtaining smaller particle sizes at lower amplitudes leads to a reduction in the power consumed by the equipment in the process. It is then concluded that the optimum amplitude is 60 %.

Table. 4.11. Ultrasound milling experiments carried out at different times, 60 % amplitude, 2 coolers for n-type Bi₂Te₃. Parameters N_M, D_M and D_L indicate the maximum number density percentage, the particle size corresponding to this maximum and the lowest particle size identified, respectively.

Experiment	Power Amplitude (%)	Additive	Cooling System	Milling Time (h)	D _L (nm)	D _M (nm)	N _M (%)
Reference					991	1280	11.37
UM_60% A_2 Coolers_0.5 h	60	NO	2	0.5	594	767	12.15
UM_60% A_2 Coolers_2 h				2	523	675	10.96
UM_60% A_2 Coolers_4 h				4	460	594	11.28
UM_60% A_2 Coolers_6 h				6	460	594	11.25
UM_60% A_2 Coolers_8 h				8	675	767	10.99
UM_60% A_2 Coolers_10 h				10	523	675	11.62

Cooling system: It could be possible that less cooling is required for lower operating amplitude (60 %). This could reduce the power consumption further in the overall process. For this reason, a new set of experiments at 60 % amplitude but using only 1 cooling system was performed.

Table. 4.12, Fig. A.25 (number density) and Fig. A.24 (volume density) show that the smallest particle size is obtained at 10 h (≈ 460 nm) using only one cooling system and 60 % amplitude. This smallest particle size is exactly the same as the one produced under the same conditions but with 2 cooling systems Table. 4.11 and a significantly lower time (4 h). Therefore, as a result of these experiments, *2 cooling systems at 60 % amplitude for a duration of 4 h without additives produces powders with the smallest nanoparticles (≈ 460 nm).*

Table. 4.12. Ultrasound milling experiments carried out at different times, 60 % amplitude, 1 cooler system for n-type Bi_2Te_3 . Parameters N_M , D_M and D_L indicate the maximum number density percentage, the particle size corresponding to this maximum and the lowest particle size identified, respectively.

Experiment	Power Amplitude (%)	Additive	Cooling System	Milling Time (h)	D_L (nm)	D_M (nm)	N_M (%)
Reference					991	1280	11.37
UM_60% A_1 Cooler_0.5 h	60	NO	1	0.5	991	1130	11.91
UM_60% A_1 Cooler_2 h				2	594	767	12.01
UM_60% A_1 Cooler_4 h				4	594	872	10.54
UM_60% A_1 Cooler_6 h				6	594	872	9.48
UM_60% A_1 Cooler_8 h				8	594	872	9.23
UM_60% A_1 Cooler_10 h				10	460	594	11.35

As a summary, Fig. 4.9 (number density) and Fig. A.26 (volume density) show the conditions leading to the smallest particle size for each parameter evaluated.

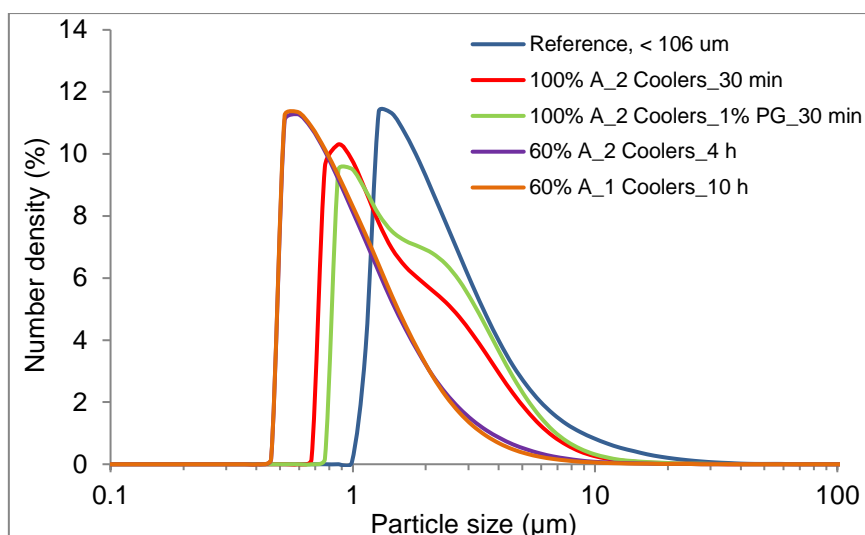


Fig. 4.9. Particle size distribution in number density of n-type Bi_2Te_3 powder after ultrasound milling experiments which produce the smallest particle size under different conditions.

Although the smallest particle size was produced at 4h (Fig. 4.9), it was decided that more suitable conditions for further fabrication of powders are 100 % amplitude for 30 min and 2 cooling systems, since the reduction in time is quite significant. The next parameter that was optimised was the concentration and it was carried out under these last conditions.

Concentration ([powder]): Here, the effect of the increase of the concentration of Bi_2Te_3 powder in the treatment is evaluated. If higher amounts of powder could be processed, this would help to more efficiently provide enough treated powder to form nanobulk disc samples. To evaluate this, different UM experiments were performed at 100 % amplitude, using 2 cooling systems, at different times and using a [powder]=0.0166 M, which is double the one utilised in all the previous experiments (see Fig. A.28 (number density) and Fig. A.27 (volume density)).

Table. 4.13. Ultrasound milling experiments carried out at different times, 100 % amplitude, 2 cooler systems and [powder]=0.0166 M for n-type Bi₂Te₃. Parameters N_M, D_M and D_L indicate the maximum number density percentage, the particle size corresponding to this maximum and the lowest particle size identified, respectively.

Experiment	Power Amplitude (%)	Additive	Cooling System	Milling Time (h)	D _L (nm)	D _M (nm)	N _M (%)
Reference					991	1280	11.37
UM_[]=0.0166M_0.5 h	100	NO	2	0.5	594	767	11.54
UM_[]=0.0166M_2 h				2	675	767	13.11
UM_[]=0.0166M_4 h				4	767	872	14.39
UM_[]=0.0166M_6 h				6	767	991	15.17
UM_[]=0.0166M_8 h				8	523	767	13.41
UM_[]=0.0166M_10 h				10	523	767	11.55

Table. 4.13 shows that the smallest particle size using [powder]=0.0166 M is produced when the UM is running for 8 and 10 h (≈ 523 nm) which is smaller than the size achieved when the concentration was half, [powder] = $8.3 \cdot 10^{-3}$ M (≈ 675 nm at 30 min) (Table 4.10). This indicates that using double powder concentration leads to a further reduction of the particle size. Furthermore, when the UM is performed for 30 min at higher concentration (0.0166 M), the smallest particle size produced was 594 nm, which is also lower than the case where half of the concentration was used. Based on these results, the final conditions adopted to perform the n-type bismuth telluride UM experiments in order to produce nanobulk disc samples are:

- Amplitude: 100 %.
- Time: 30 min.
- Cooling systems: 2.
- [powder]=0.0166 M.
- Solvent: 1-butanol, 70 mL.

As a summary, the smallest particle sizes and percentages of number of particles smaller than 1 μ m for each condition explored above are shown in Table 4.14, Fig. 4.10, Fig. A.29 and Fig. A.30. The five different conditions obtained from the optimisations performed were:

- C1 (time optimisation): UM at 100 % amplitude, 2 cooling systems for 30 min and [powder]=0.0083 M.

- C2 (additive optimisation): UM at 100 % amplitude, 2 cooling systems for 30 min, 1 % of PG and [powder]=0.0083 M.
- C3 (amplitude optimisation): UM at 60 % amplitude, 2 cooling systems for 4 h and [powder]=0.0083 M.
- C4 (cooling systems optimisation): UM at 60 % amplitude, 1 cooling system for 10 h and [powder]=0.0083 M.
- C5 ([powder] optimisation): UM at 100 % amplitude, 2 cooling systems for 30 min and [powder]=0.0166 M.

Table 4.14. Summary of the values of the smallest particle size and the number of particles smaller than 1 μm achieved for n-type Bi_2Te_3 powder treated by ultrasound milling.

Experiment	Conditions	Milling Time (h)	Smallest Particle Size (nm)	Number of Particles <1 μm (%)
Reference	Ref.		991	0.011
UM_100% A_2 Coolers	C1	0.5	675	10.58
UM_100% A_2 Coolers _1% PG	C2	0.5	767	5.94
UM_60% A_2 Coolers	C3	4	460	32.14
UM_60% A_1 Coolers	C4	10	460	33.73
UM_100% A_2 Coolers _double []	C5	0.5	594	14.39

There is a clear diminution in the smallest particle size and an increase in the percentage of particles <1 μm when the conditions C3 and C4 were used.

However, condition C5 is selected to perform further UM experiments for the production of nanobulk samples despite showing a 134 nm higher smallest particle size and approximately half percentage of particles <1 μm than C3 and C4. We believe this is worthwhile due to the much shorter time required compared to C3 and C4, which also leads to a lower electrical consumption.

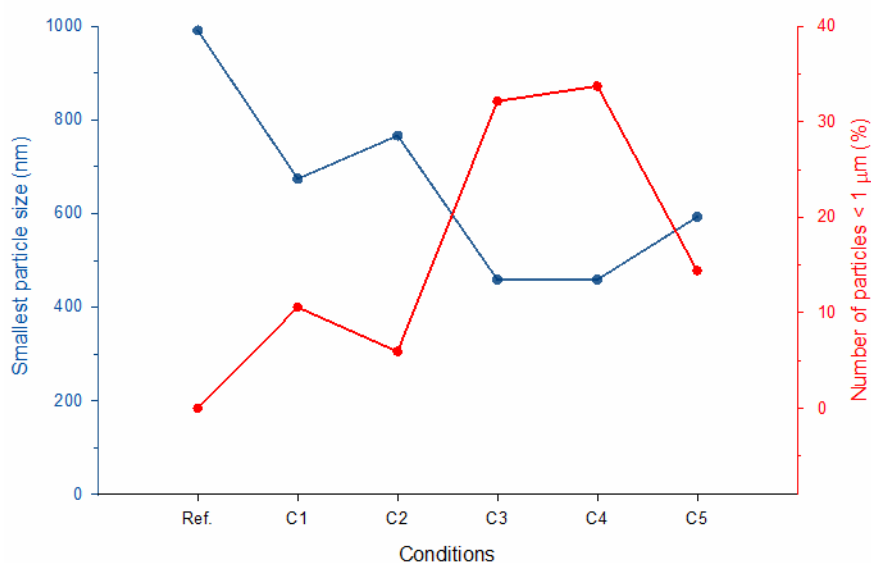


Fig. 4.10. Representation of the smallest particle size (blue) and number of particles smaller than 1 μm achieved for n-type Bi_2Te_3 after ultrasound milling experiments for different optimum conditions.

• **p-type $\text{Bi}_{0.5}\text{Sb}_{1.5}\text{Te}_3$** : Similar to the optimisation performed for the n-type bismuth telluride, in this section a similar approach is adopted in order to identify the optimum conditions for the p-type counterpart. Crushed samples (particle size < 106 μm) from p-type Bi_2Te_3 were similarly used as precursor and placed into the UM vessel. The precursor powder concentration employed was 0.0083 M unless otherwise mentioned. The solvent utilised in these tests was 1-butanol, which was already optimised above for the n-type bismuth telluride.

Use of the Additives: As in the n-type bismuth telluride, the additive used was PG and in the same proportion (1 % of the total volume). Different experiments with and without additive present and employing different times were performed. The summary of these experiments is shown in Table 4.15.

It can be identified from Table 4.15, Fig. A.32 (number density) and Fig. A.31 (volume density) that the smallest particles are achieved at 6 h (≈ 400 nm) when no additive is present, while using shorter times resulted in larger particle sizes. Longer times (8 h) produced higher particle size with a similar profile to 4 and 8 h. As for BM treatments of the p-type material, the reference sample already shows nanoparticles (≈ 750 nm) since the p-type material crushes into finer particles than the n-type counterpart.

When the PG is added, the smallest particles are produced at 8 h (≈ 350 nm), which implies that the addition of PG leads to longer milling times to obtain nanoparticles of similar size (see Fig. A.34 (number density) and Fig. A.33 (volume density)). Although the addition of PG reduces the smallest particle size by around 50 nm, there is not

much benefit in using PG due to the longer milling times required. Therefore, for further production of nanoparticles no PG is added.

Table 4.15. Ultrasound milling experiments carried out at different times at 100 % amplitude, 2 coolers and with and without the propylene glycol (PG) additive for p-type Bi₂Te₃. Parameters N_M, D_M and D_L indicate the maximum number density percentage, the particle size corresponding to this maximum and the lowest particle size identified, respectively.

Experiment	Amplitude (%)	Additive	Cooling System	Milling Time (h)	D _L (nm)	D _M (nm)	N _M (%)
Reference					767	872	13.62
UM_0.5 h	100	NO	2	0.5	767	1130	10.87
UM_2 h				2	675	872	12.94
UM_4 h				4	594	767	14.94
UM_6 h				6	405	523	13.70
UM_8 h				8	523	767	16.77
UM_0.5 h_PG	100	1 % Vol PG		0.5	460	594	12.19
UM_2 h_PG				2	460	767	11.87
UM_4 h_PG				4	523	675	13.96
UM_6 h_PG				6	594	767	16.28
UM_8 h_PG				8	357	594	13.61

Amplitude of the UM: As for the n-type bismuth telluride, the amplitude of the UM was reduced from 100 % to 60 % and different times were evaluated with the reduced amplitude. Employing 60 % amplitude the smallest particles are achieved at 6 h (\approx 350 nm), as it can be seen in Table. 4.16, Fig. A.36 (number density) and Fig. A.35 (volume density). Comparing these results to the same experiment performed at 100 % amplitude (Fig. A.32) where the smallest particle size (\approx 400 nm) was achieved at 6 h, the reduction of the amplitude produces somewhat smaller nanoparticles. This is also beneficial for the power consumption which can be reduced.

Therefore, according to these results the optimised amplitude is 60 %.

Table. 4.16. Ultrasound milling experiments carried out at different times at 60 % amplitude, 2 coolers for p-type Bi₂Te₃. Parameters N_M, D_M and D_L indicate the maximum number density percentage, the particle size corresponding to this maximum and the lowest particle size identified, respectively.

Experiment	Power Amplitude (%)	Additive	Cooling System	Milling Time (h)	D _L (nm)	D _M (nm)	N _M (%)
Reference					767	872	13.62
UM_60% A_2 Coolers_0.5 h	60	NO	2	0.5	460	675	11.06
UM_60% A_2 Coolers_2 h				2	594	767	11.31
UM_60% A_2 Coolers_4 h				4	357	594	10.41
UM_60% A_2 Coolers_6 h				6	357	460	12.07
UM_60% A_2 Coolers_8 h				8	405	594	11.13

Cooling system: To explore the influence of the cooling conditions only one cooling system was utilised in a new set of experiments and the results were compared to those obtained using 2 coolers (Table. 4.16). In the new set of experiments 60 % amplitude (optimised above) and no additive was employed. The results obtained are shown in Table. 4.17, Fig. A.38 (number density) and Fig. A.37 (volume density).

Table. 4.17. Ultrasound milling experiments carried out at different times at 60 % amplitude, 1 cooler system for p-type Bi₂Te₃. Parameters N_M, D_M and D_L indicate the maximum number density percentage, the particle size corresponding to this maximum and the lowest particle size identified, respectively.

Experiment	Power Amplitude (%)	Additive	Cooling System	Milling Time (h)	D _L (nm)	D _M (nm)	N _M (%)
Reference					767	872	13.62
UM_60% A_1 Cooler_0.5 h	60	NO	1	0.5	460	594	11.72
UM_60% A_1 Cooler_2 h				2	314	460	12.56
UM_60% A_1 Cooler_4 h				4	314	405	12.25
UM_60% A_1 Cooler_6 h				6	405	460	11.48
UM_60% A_1 Cooler_8 h				8	460	594	10.67

It can be observed that the smallest particle size is obtained at 4 h (\approx 300 nm) using only one cooler system. When 2 coolers were employed the smallest particle size (\approx 350 nm) was found at 6 h, which is not a very significant change in size. However, regarding the treatment time a reduction of 2 h in the duration of the treatment is

significantly beneficial. On the other hand, at 2 h using only 1 cooler the produced smallest particle size is similar to that at 6 h and 2 cooling systems, so by using only 1 cooler and at shorter times (4 h less) the same smallest particle size is obtained.

As a result of these experiments, *1 cooling system* has to be utilised at *60 % amplitude* for *4 h* without additive to produce the smallest nanoparticles (≈ 310 nm).

To summarise all the optimisation results, Fig. 4.11 (number density) and Fig. A.39 (volume density) show the results at the conditions identified to achieve the smallest particle size at each parameter studied. From the figure it is clear that the best conditions to obtain nanoparticles using UM technique for p-type bismuth telluride are the ones mentioned before (*60 % amplitude, 4 h, 1 cooler system*).

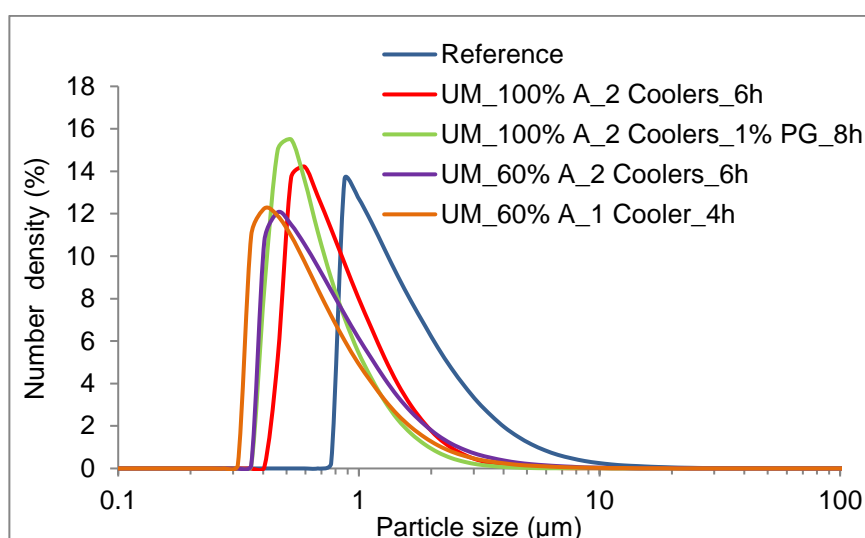


Fig. 4.11. Particle size distribution in number density of p-type Bi_2Te_3 after ultrasound milling experiments of optimum conditions.

Concentration ([powder]): The effect of the increase of the precursor powder concentration is analysed here at the optimised conditions. Double and triple concentrations were tested as described in Table 4.18.

Table 4.18. Different concentrations employed in the ultrasound milling experiments performed at 60 % amplitude, 1 cooler and during 4 h. Parameters N_M , D_M and D_L indicate the maximum number density percentage, the particle size corresponding to this maximum and the lowest particle size identified, respectively.

Experiment	Power Amplitude (%)	[Powder] (M)	Cooling System	Milling Time (h)	D_L (nm)	D_M (nm)	N_M (%)
Reference					767	872	13.62
UM_60% A_ []= 0.083 M	60	0.083	1	4	314	405	12.25
UM_60% A_ []= 0.0166 M		0.0166			276	357	11.83
UM_60% A_ []= 0.0249 M		0.0249			460	594	12.71

Table 4.18, Fig. A.41 (number density) and Fig. A.40 (volume density) show that the use of a higher concentration (0.0166 M) produced a smaller particle size (≈ 275 nm) than the previous value employed (0.0083 M). However, when the concentration is increased further to 0.0249 M an increase in the particle size occurs. Thus, the optimum concentration adopted to perform the UM treatment to produce nanobulk disc samples is 0.0166 M for the p-type bismuth telluride.

Then, the optimised parameters for p-type powder are:

- Amplitude: 60 %.
- Time: 4 h.
- Cooling system: 1.
- [powder]=0.0166 M.
- Solvent: 1-butanol, 70 mL.

The smallest particle size and percentage of number of particles smaller than 1 μm for every condition evaluated are shown in Table 4.19, Fig. 4.12, Fig. A.42 and Fig. A.43 as a summary. The conditions presented are:

- C1: UM at 100 % amplitude, 2 cooling systems for 6 h and [powder]=0.0083 M.
- C2: UM at 100 % amplitude, 2 cooling systems for 8 h, 1 % of PG and [powder]=0.0083 M.
- C3: UM at 60 % amplitude, 2 cooling systems for 6 h and [powder]=0.0083 M.
- C4: UM at 60 % amplitude, 1 cooling system for 4 h and [powder]=0.0083 M.
- C5: UM at 60 % amplitude, 1 cooling system for 4 h and [powder]=0.0166 M.

Table 4.19. Values of the smallest particle size and the number of particles smaller than 1 μm achieved for p-type Bi_2Te_3 powder under different ultrasound milling treatments.

Experiment	Conditions	Milling Time (h)	Particle Size (nm)	Number of Particles < 1 μm (%)
Reference			767	9.77
UM_100% A_2 Coolers	C1	6	405	52.5
UM_100% A_2 Coolers _1% PG	C2	8	357	66.56
UM_60% A_2 Coolers	C3	6	357	47.97
UM_60% A_1 Coolers	C4	4	314	56.55
UM_60% A_1 Coolers _double [powder]	C5	4	276	61.72

There is a clear diminution in the particle size when the UM treatment is utilised, regardless of the condition adopted. From Fig. 4.12 it can be seen that there is not a very significant different in the smallest particle sizes, however, the percentage of particles <1 μm is the highest for C2 and C5. Between both conditions C5 allows a larger amount of precursor powder, requires shorter times and hence is the most suitable for further treatments.

It can be noticed that the majority of the conditions produce a percentage of number of particles <1 μm over 50 %, which is much higher than the case of the n-type material. This could be due to the higher fragility of the p-type bismuth telluride.

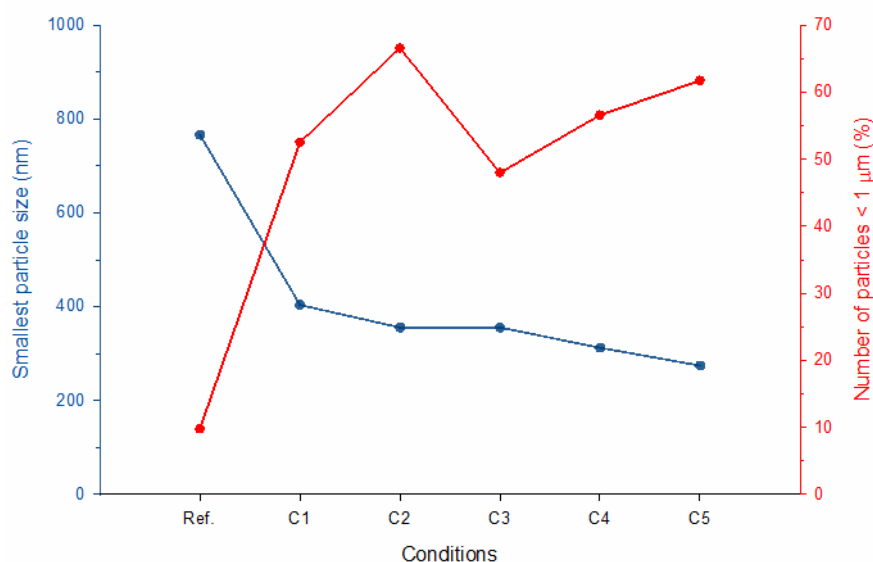


Fig. 4.12. Representation of the smallest particle size (blue) and percentage of particles smaller than 1 μm achieved for p-type Bi_2Te_3 after ultrasound milling experiments at different conditions.

4.4.2 Morphological characterisation

• n-type $\text{Bi}_2\text{Te}_{2.79}\text{Se}_{0.21} + 0.001 \text{I}_2$:

Fig. 4.13 shows SEM images obtained under different magnifications for the n-type Bi_2Te_3 before and after some of the UM processes under different conditions (amplitude of the ultrasound, time, number of coolers utilised and additive). Only the samples that produced the smallest particles at each different condition are presented in the figure. The summary of the conditions is shown in Table 4.20.

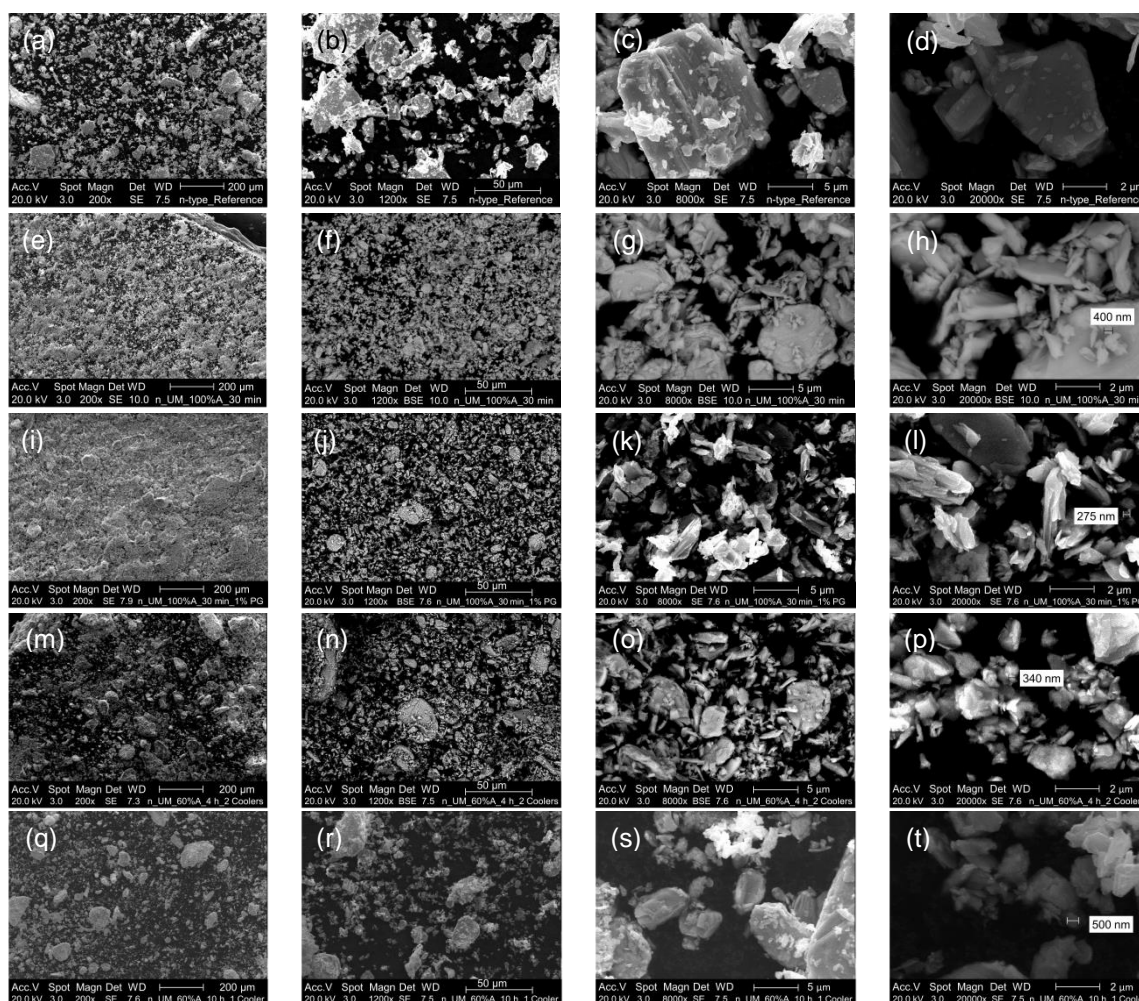


Fig. 4.13. SEM images of n- Bi_2Te_3 powder (a-d) before ultrasound milling treatment, after ultrasound milling treatment at (e-h) 100 % amplitude and 2 coolers for 30 min, (i-l) 100 % amplitude, 2 coolers and 1 % of PG for 30 min, (m-p) 60 % amplitude, 2 coolers for 4 h, and (q-t) 60 % amplitude, 1 cooler for 10 h from left to right, scale bar: 200 μm , 50 μm , 5 μm and 2 μm .

Table 4.20. Relation of SEM images from Fig. 4.13 with the different conditions that produced the smallest particle size utilised to perform ultrasound milling experiments for the n-type Bi₂Te₃.

SEM Images	Conditions	Amplitude (%)	Cooling Systems	Additive 1% PG	Milling Time (h)
(a-d)	Non treated				
(e-h)	C1	100	2	No	0.5
(i-l)	C2			Yes	
(m-p)	C3	60	1	No	4
(q-t)	C4				10

There is a clear reduction in the particle size after UM treatment for all the different conditions utilised, except the treatment performed at C4 condition, where variations in particle size is not so intense (Fig. 4.13 (q-t)). As occurred in previous cases, significant differences (up to 500 nm) are observed between the SEM images and laser diffraction results in the smallest particle sizes. The smallest particle size was obtained for the conditions C2 and C3 (\approx 300 nm, see Fig. 4.13 (l and p)). By comparison of Fig. 4.13 (h) (without additive) and Fig. 4.13 (l) (with additive) it is observed a change in the particles morphology. Shaper particles appear when additive is employed whereas rounded and smoothed shapes are observed when there is no additive. In the same way, UM process produces more rounded morphologies in the larger particles (see 1,200x magnification images in Fig. 4.13).

Since C1 condition was adopted as optimum from the laser diffraction analysis, a detailed SEM study was performed under the same UM condition but varying the treatment time (Fig. 4.14).

It can be seen from the images at 20,000x and 50,000x magnifications that there is a clear reduction in the particle size after UM treatment at all times. From the images at 200x and 1,200x magnification it can be observed that samples treated at times longer than 30 min present significantly larger particles. However, these particles are aggregates of smaller particles, as can be observed at higher magnifications. This feature was not observed in samples treated by BM process and it is a unique characteristic of the UM treatment. A detailed comparison between BM and UM processes is discussed in the next section (4.5).

At 2 h the aggregates present both larger and smaller particles (Fig. 4.14 (j-k)), whereas at larger milling times the aggregates are mainly formed by only smaller particles (see Fig. 4.14 (o-q), (t-v) and (y-a₁) at 4, 6 and 8 h, respectively). The smallest particles (\approx 100 nm) were produced at 6 and 8 h (Fig. 4. (v and a₁), respectively), and they form more homogeneous (in the 100-500 nm size range) and compacted aggregates than at shorter times. These smallest particles are not detected by laser diffraction (Fig. A.19) as occurred in previous cases.

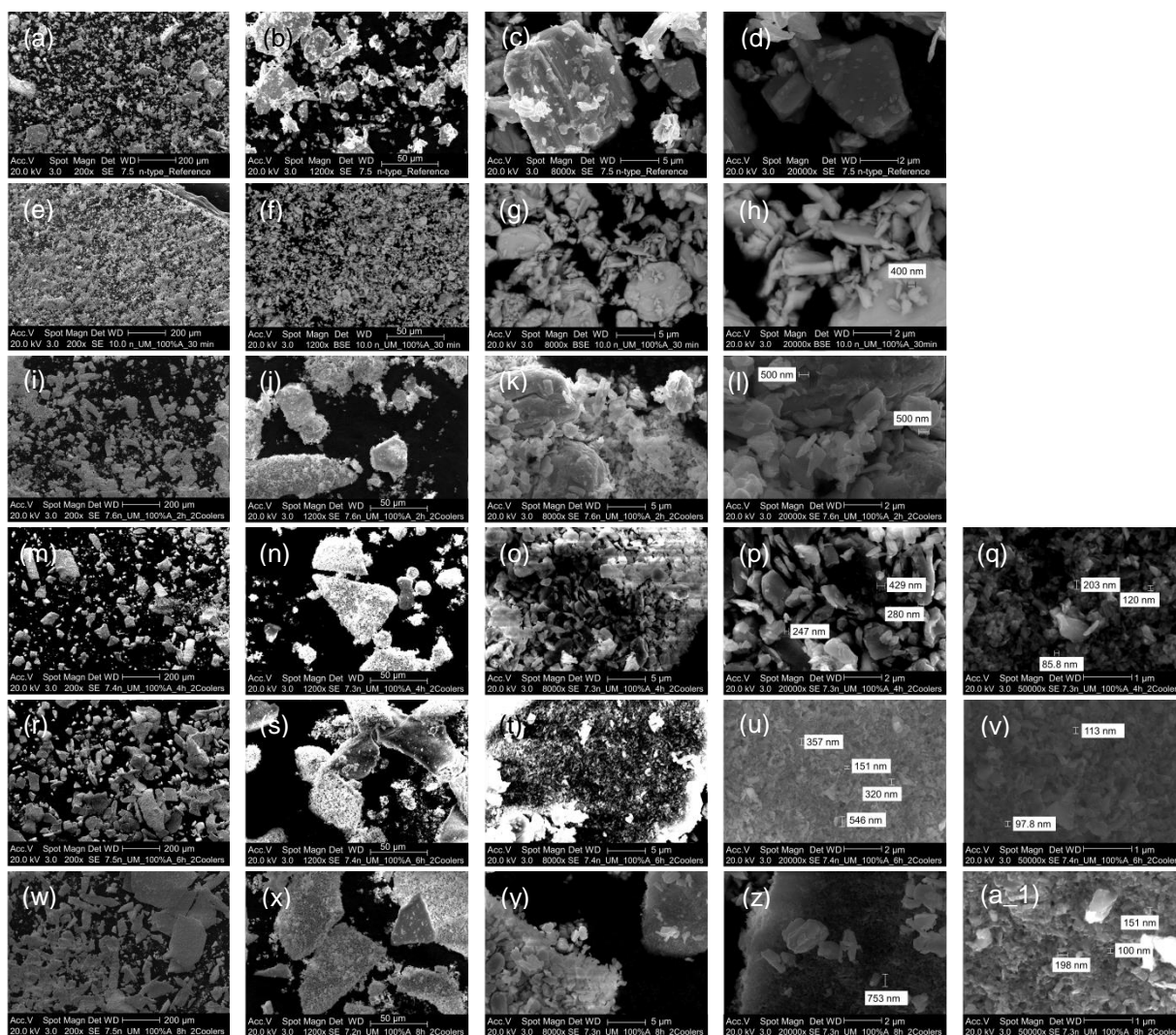


Fig. 4.14. SEM images of $n\text{-Bi}_2\text{Te}_3$ (a-d) before ultrasound milling treatment, after ultrasound milling treatment at 100 % amplitude, 2 coolers for (e-h) 30 min, (i-l) 2 h, (m-q) 4 h, (r-v) 6 h, and (w-a₁) 8 h from left to right, scale bar: 200 μm , 50 μm , 5 μm , 2 μm and 1 μm .

Additionally, some pictures were obtained of the samples treated by UM for 30 min and 8 h at 100 % amplitude and 2 coolers as shown in Fig. 4.15. After drying in air the degree of aggregation can be clearly identified. At 8 h the more significant aggregation of the particles forms a kind of curly shapes.

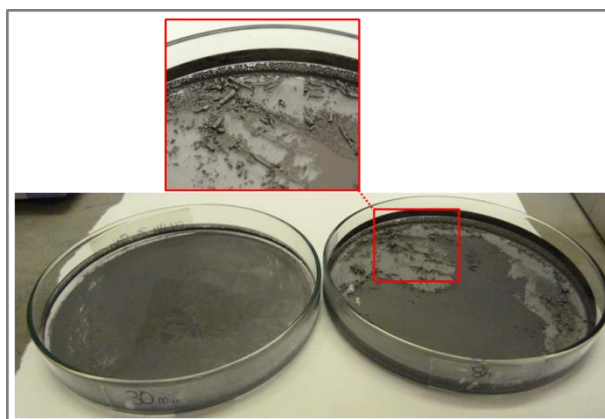


Fig. 4.15. Dried samples after ultrasound milling treatment at 30 min (left) and 8 h (right and the corresponding magnified image) with the presence of curly features.

As mentioned previously, it is more advantageous to produce a larger amount of powder from a single treatment. For this reason, the initial powder concentration was increased to 0.0166 M while keeping the rest of conditions as before (100 % amplitude and using 2 coolers). 6 and 8 h times, which produced the smallest particle sizes before, were checked. SEM images are shown in Fig. 4.16.

At the lowest magnifications (200x and 1,200x in Fig. 4.16) the increase of the concentration does not significantly modify the particle sizes compared to Fig. 4.14 (r-s and w-x). However, at 6 h higher amount of larger particles are observed than at 8 h (Fig. 4.16 (c and h)). In addition, the smallest particles achieved are larger (Fig. 4.16 (d-e and i-j)) than in the lower powder concentration case (Fig. 4.14 (v and a_1)). Most of the particles in the aggregates at this higher concentration are in the 0.5-1 μm range.

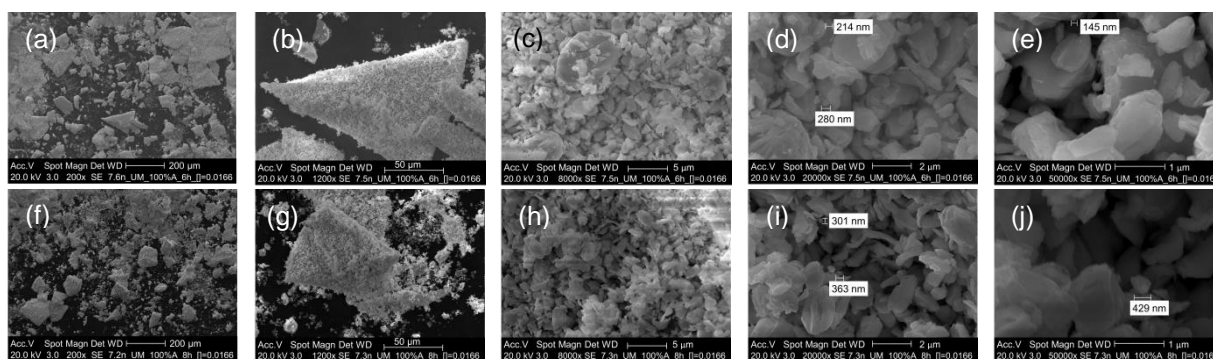


Fig. 4.16. SEM images of $n\text{-Bi}_2\text{Te}_3$ after ultrasound milling treatment at 100 % amplitude, [powder]=0.0166 M and 2 coolers for 6 h (a-e) and for 8 h (f-j) from left to right, scale bar: 200 μm , 50 μm , 5 μm , 2 μm and 1 μm .

Despite the larger particle sizes at higher concentrations, the selected condition to produce nanobulk samples are 100 % amplitude, [powder]=0.0166 M, 2 cooling systems for 8 h using 1-butanol, since this allows obtaining larger amount of powder. 8 h was selected instead of 6 h since a fewer amount of larger particles were formed.

• **p-type Bi_{0.5}Te₃Sb_{1.5}:**

Fig. 4.17 shows the SEM images obtained for the p-type Bi₂Te₃ before and after UM processes prepared under different conditions in which amplitude of the ultrasound, time, concentration, number of coolers utilised and additive (PG) were modified. In this figure only the samples that produced the smallest particles under each different condition previously evaluated, are shown. These conditions are summarised in Table 4.21.

Table 4.21. Different optimum conditions utilised to perform ultrasound milling experiments using the p-type Bi₂Te₃.

Experiment	Conditions	Amplitude (%)	Cooling System	Additives 1% PG	Milling Time (h)
(a-d)	Non treated				
(e-h)	C1	100	2	No	6
(i-l)	C2			Yes	8
(m-p)	C3	60	1	No	6
(q-t)	C4				4

Similarly to the case of the n-type samples treated by UM process, there is a clear reduction in the particle size after UM treatment at all the different conditions utilised. All samples show the characteristic aggregation of nanoparticles that also occurred at long times in the n-type material, except the powder processed at 60 % amplitude for 4h. When the amplitude is decreased from 100 to 60 %, keeping the rest of conditions fixed, not all the apparent large particles are formed by aggregates (Fig. 4.17 (f-g and n-o)). Therefore, it seems like both reducing the amplitude and the treatment time results in a small presence of aggregates.

When the UM process is performed at 100 % amplitude using PG additive, similar particle sizes and morphology are observed than in the case without additive. Thus, there is no benefit in the use of the additive and this condition (C1) was chosen as optimum since they also involve shorter times. Fine particle sizes in the range 400-1000 nm and coarse particles of few microns prevail in this sample (Fig. 4.17 (g-h)).

It should be noticed that the results from the laser diffraction analysis are not in complete agreement with the SEM evaluation, although the differences observed are less significant than in previous cases (Fig. A.31-Fig. A.38).

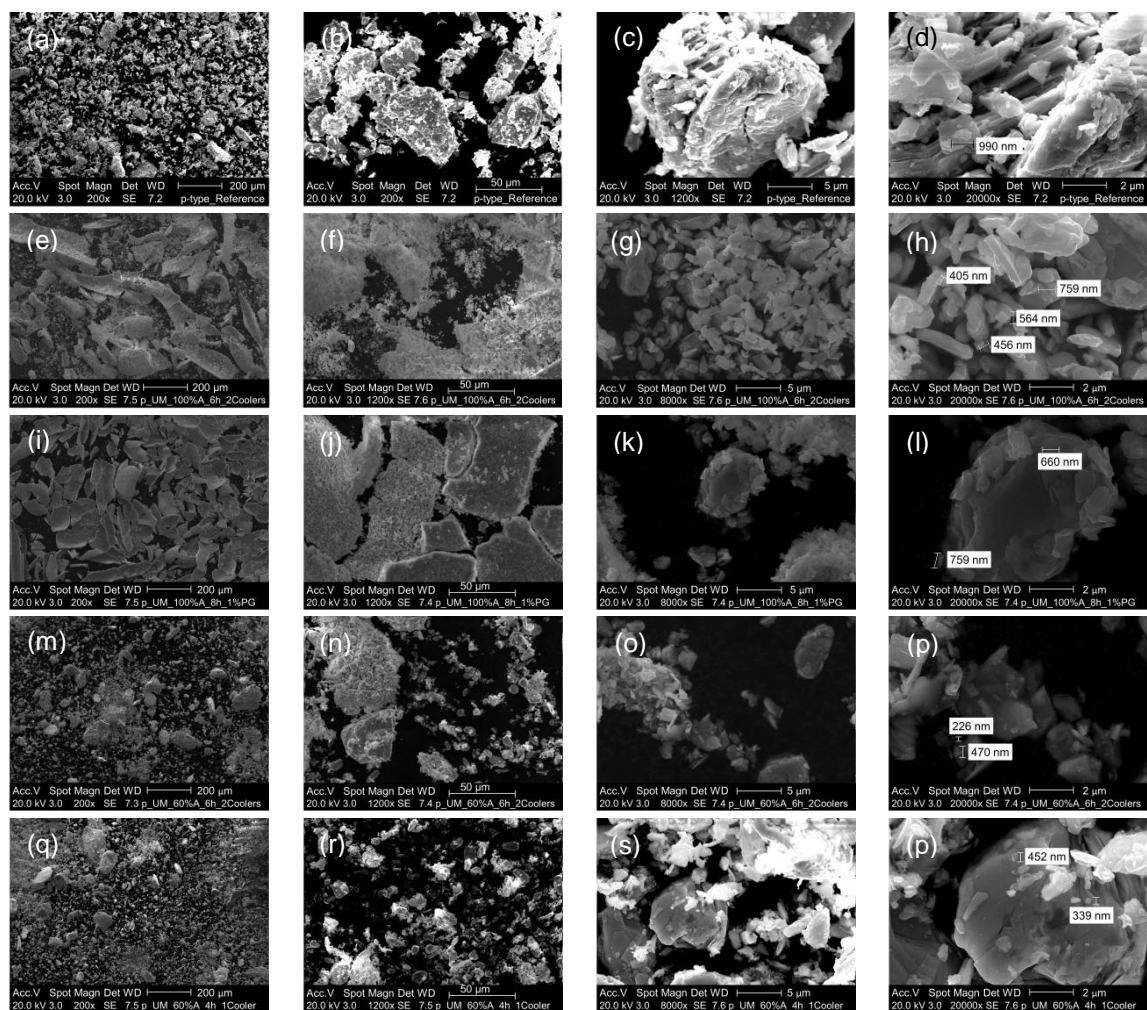


Fig. 4.17. SEM images of p-Bi₂Te₃ (a-d) before ultrasound milling treatment and after ultrasound milling at (e-h) 100 % amplitude, 2 coolers for 6 h, (i-l) 100 % amplitude, 2 coolers, 1 % of PG for 8 h, (m-p) 60 % amplitude, 2 coolers for 6 h, and (q-t) 60 % amplitude, 1 cooler for 4 h from left to right, scale bar: 200 μm, 50 μm, 5 μm, and 2 μm.

Since in the n-type material the smallest particle sizes were obtained at treatments performed at 6 and 8 h (100 % amplitude, 2 coolers), for the p-type an increase of the treatment time to 8 h and also a double increase in powder concentration is evaluated. These results are shown in Fig. 4.18. It can be seen that when the time is increased to 8 h the amount of finer particles increases with respect to the number of coarse particles (Fig. 4.18 (c and g)). This also occurs when the concentration is doubled (Fig. 4.18 (l and q)).

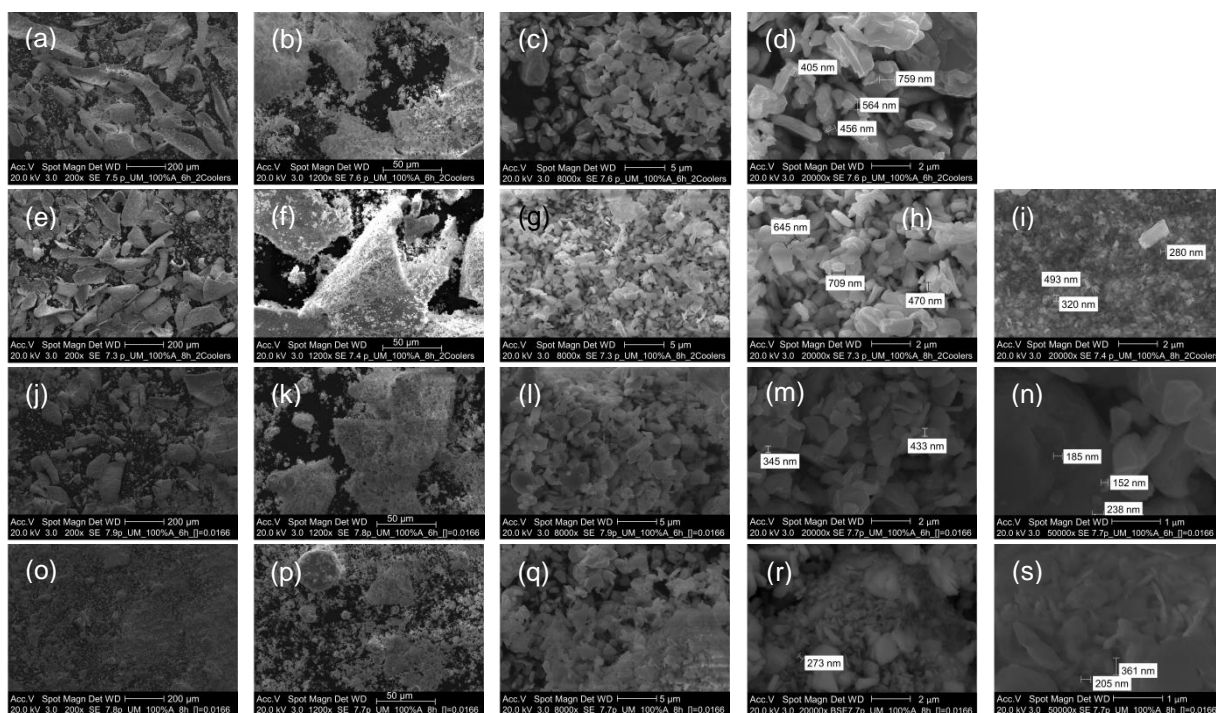


Fig. 4.18. SEM images of p-Bi₂Te₃ after ultrasound milling at (a-d) 100 % amplitude, 2 coolers, 6 and (e-i) 8 h, (j-n) 100 % amplitude, 2 coolers, [powder]=0.0166 M, 6 h and (o-s) 8 h from left to right, scale bar: 200 μ m, 50 μ m, 5 μ m, 2 μ m and 1 μ m.

It can be seen at 6 h that the increase of the concentration does not significantly modify the structure of the powders and the particle sizes (Fig. 4.18 (a-d and j-m)). However, at 8 h the formation of large aggregates is significantly reduced by the increase of the concentration (Fig. 4.18 (e-f and o-p)), although the size of the particles, observed at higher magnifications (Fig. 4.18 (g-h and q-r)), does not differ greatly. Therefore, these conditions (100 % amplitude, [powder]=0.0166 M, 2 cooling systems, 8 h and 1-butanol) were selected as optimum for the preparation of nanobulk samples and analysis of the thermoelectric properties in chapter 6. These conditions are the same than the optimised for the n-type material and both coarse particles of few microns and fine particles in the 200-1000 nm (Fig. 4.18 (q-r)) were produced.

4.4.3 Structural characterisation

XRD results for UM powders at different conditions are shown for the n and p-type materials in Fig. 4.19 and Fig. 4.20, respectively.

• *n*-type $\text{Bi}_2\text{Te}_{2.79}\text{Se}_{0.21} + 0.001 \text{I}_2$:

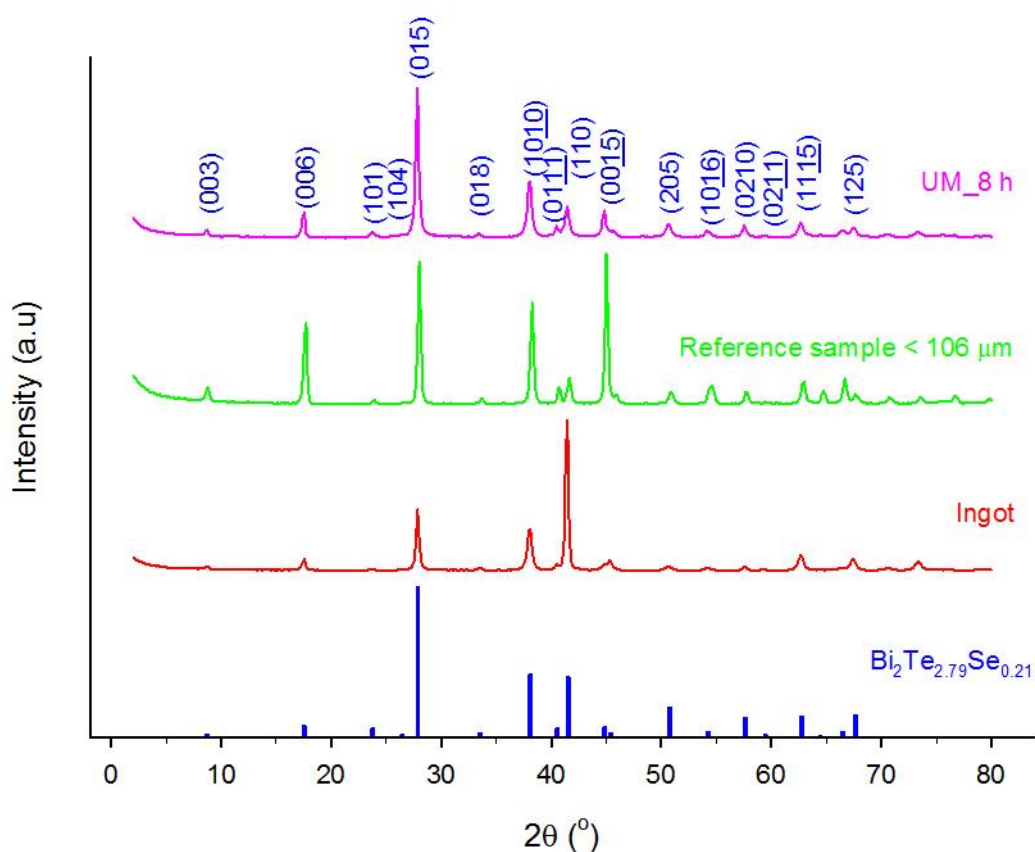


Fig. 4.19. Theoretical XRD pattern of *n*-type $\text{Bi}_2\text{Te}_{2.79}\text{Se}_{0.21}$ (blue) and patterns of the ingot sample (red), reference sample before milling (green) and after ultrasound milling treatment performed at 100 % amplitude, 2 coolers and for 8h (pink).

The XRD patterns show that all the three samples are single-phase $\text{Bi}_2\text{Te}_{2.79}\text{Se}_{0.21}$ corresponding to a rhombohedral crystal geometry (space group $R\bar{3}m$)⁽¹⁹⁶⁾ with no detectable impurities of other phases (Fig. 4.19). After UM process the same preferred orientation (015) as $\text{Bi}_2\text{Te}_{2.79}\text{Se}_{0.21}$ is maintained, while in the ingot and the reference sample <106 μm , the preferred orientation changes to (110) and (0015) respectively. The peaks of the ingot and reference samples are slightly sharper than the UM treatment, due to a reduction in the particle size induced by the ultrasound process.

• **p-type $\text{Bi}_{0.5}\text{Te}_3\text{Sb}_{1.5}$:**

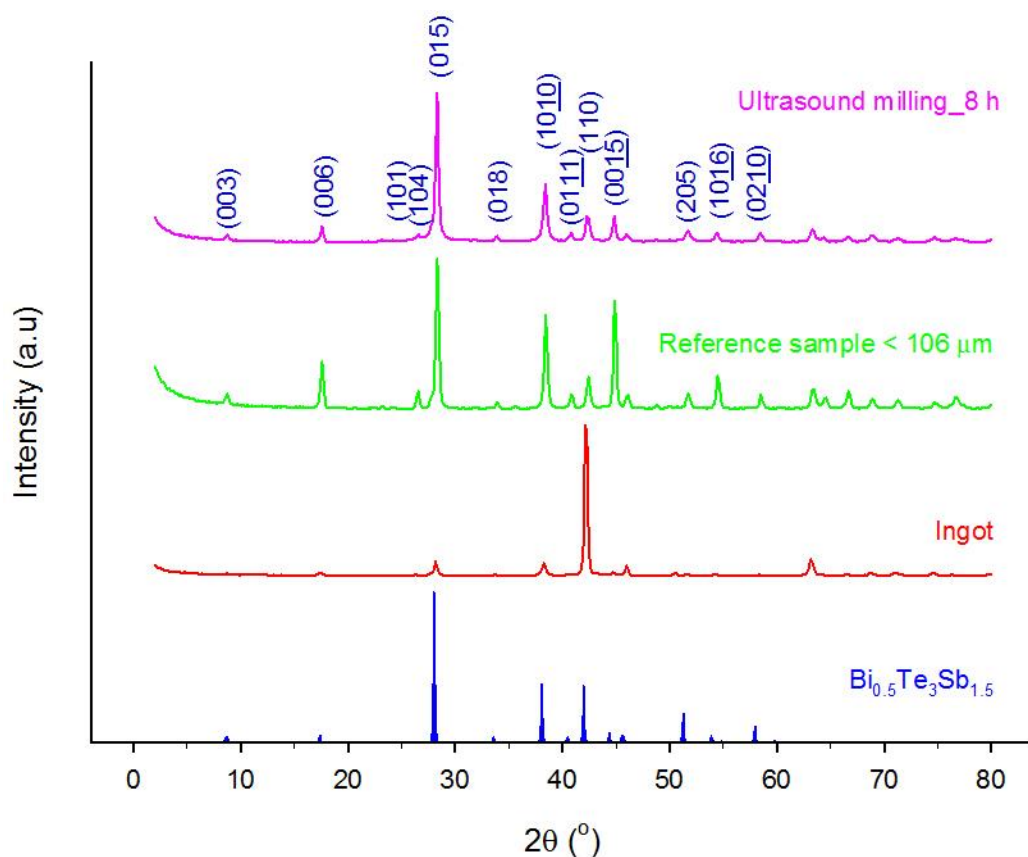


Fig. 4.20. Theoretical XRD pattern of the p-type $\text{Bi}_{0.5}\text{Te}_3\text{Sb}_{1.5}$ (blue), ingot sample (red), reference sample before milling (green) and after ultrasound milling treatment performed at 100 % amplitude, 2 coolers and for 8 h (pink).

Likewise, the treated p-type material also retains the same structure as the original untreated sample as the preferred orientation remains (015). The peaks of the ingot and reference samples are sharper and more intense than the UM sample (sample more polycrystalline), indicating a reduction in the particle size in the latter.

4.5 Comparison between ball and ultrasound milling techniques

4.5.1 Morphological characterisation

• **n-type $\text{Bi}_2\text{Te}_{2.79}\text{Se}_{0.21} + 0.001 \text{I}_2$:** Fig. 4.21 shows SEM images obtained for the n-type Bi_2Te_3 after BM process and some of the UM processes under different conditions. Only the samples that were considered as optimum for BM and UM treatments are presented, as well as the sample prepared under the condition C1 in Table 4.20.

From the SEM images at the largest magnifications, it can be observed that average sizes of the smallest particles lie around 200 nm for the BM sample (Fig. 4.21 (d)) while in the UM experiment performed at 8 h (Fig. 4.21 (l-m)) the particle size is around 300 nm. Even though with the chosen optimised conditions the UM produces slightly larger nanoparticles than the BM, it should be noted that the UM process forms similar smallest particles at shorter milling times (3 times shorter). In addition, it can be seen that UM process does not produce large particles as in the BM (Fig. 4.21 (c and k)). Interestingly, the large particles observed in the UM treatment at lower magnifications (Fig. 4.21 (i-j)) are actually an agglomeration of nanoparticles. This is a unique feature of the UM technique.

On the other hand, regarding the particles' morphology, the UM process produces more homogeneous particle sizes (Fig. 4.21 (k-m)), and smooth and rounder particles than the BM treatment (Fig. 4.21 (c-d and g-h)), which can be more clearly identified in the UM process at 30 min.

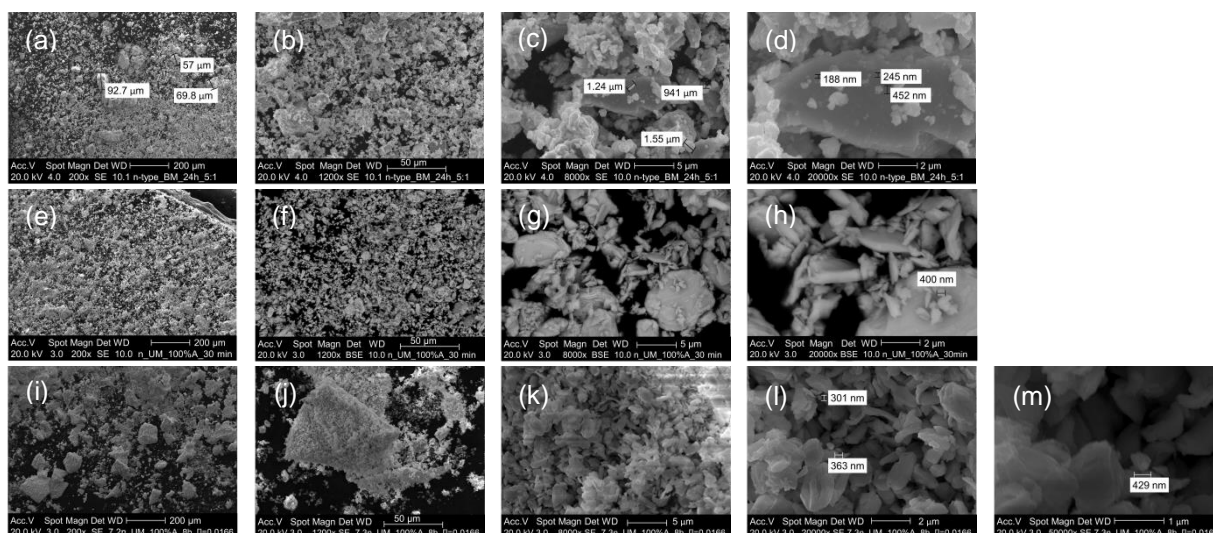


Fig. 4.21. SEM images of $n\text{-Bi}_2\text{Te}_3$ after (a-d) ball milling process at 24 h and ratio 5:1 and ultrasound milling treatment at (e-h) 100 % amplitude, 2 coolers and [powder] $=8.3 \cdot 10^{-3}$ M for 30 min, and (i-m) 100 % amplitude, 2 coolers and [powder] $=0.0166$ M for 8 h from left to right, scale bar: 200 μm , 50 μm , 5 μm , 2 μm and 1 μm .

• **p-type $\text{Bi}_{0.5}\text{Te}_3\text{Sb}_{1.5}$:** Fig. 4.22 shows SEM images obtained for the p-type Bi_2Te_3 after BM process and some of the UM processes under different conditions. Only the samples that were considered as optimum for BM and UM treatments are presented.

From the SEM images at the largest magnifications, it can be observed that average sizes of the smallest particles lie in the range 300-1000 nm for the BM sample (Fig. 4.22 (c-d)). There is also presence of larger particles of a few microns. On the other hand, fine particle sizes in the range 200-1000 nm and coarse particles of few microns are obtained in UM samples (Fig. 4.22 (h-l, m-n)). Although similar particle sizes are obtained by both

methods, the UM technique clearly produces a much larger and homogeneous amount of nanoparticles using the same treatment time (see larger magnifications in Fig. 4.22).

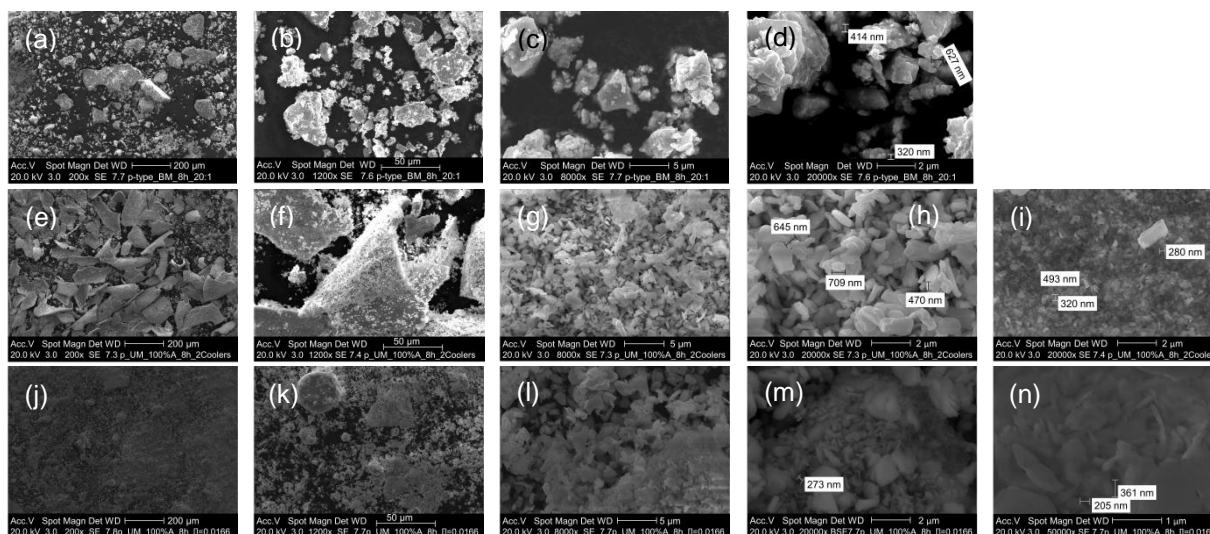


Fig. 4.22. SEM images of p-Bi₂Te₃ (a-d) after ball milling process at 8 h, ratio 20:1 and (e-j) ultrasound milling treatment at 100 % amplitude, 2 coolers, 8 h, [powder]=8.3·10⁻³ M and (j-n) [powder]=0.0166 M from left to right, scale bar: 200 μm, 50 μm, 5 μm, 2 μm and 1 μm.

Another novel feature of the UM technique is the presence of large aggregates of nanoparticles, as observed as well for the n-type (Fig. 4.21). As previously discussed this characteristic is less intense when the powder concentration is doubled (Fig. 4.22 (e-f, j-k)).

Regarding the particles morphology, smooth and rounder particles that were previously observed for the n-type material are not significant here (p-type). It has to be taken into account that the UM processes were performed in this case at larger times (8 h) than the n-type treatment (30 min), at which this difference in morphology was more pronounced.

4.5.2 Structural characterisation

In this section the XRD patterns for the ball milled sample was directly compared to the UM sample for both n- and p- type materials (Fig. 4.23 and Fig. 4.24 respectively). Only the optimum conditions of each method are shown.

Both BM and UM treatments produce the same structure and preferred orientation (015) for both types of bismuth telluride (n- and p-type). It can be noticed that the peaks corresponding to the BM treatment are slightly broader than in the UM. This might be due to a decrease of the size of the powder or/and the presence of residual strain in the material caused by a more intense mechanical stress in the BM process.^(197, 198)

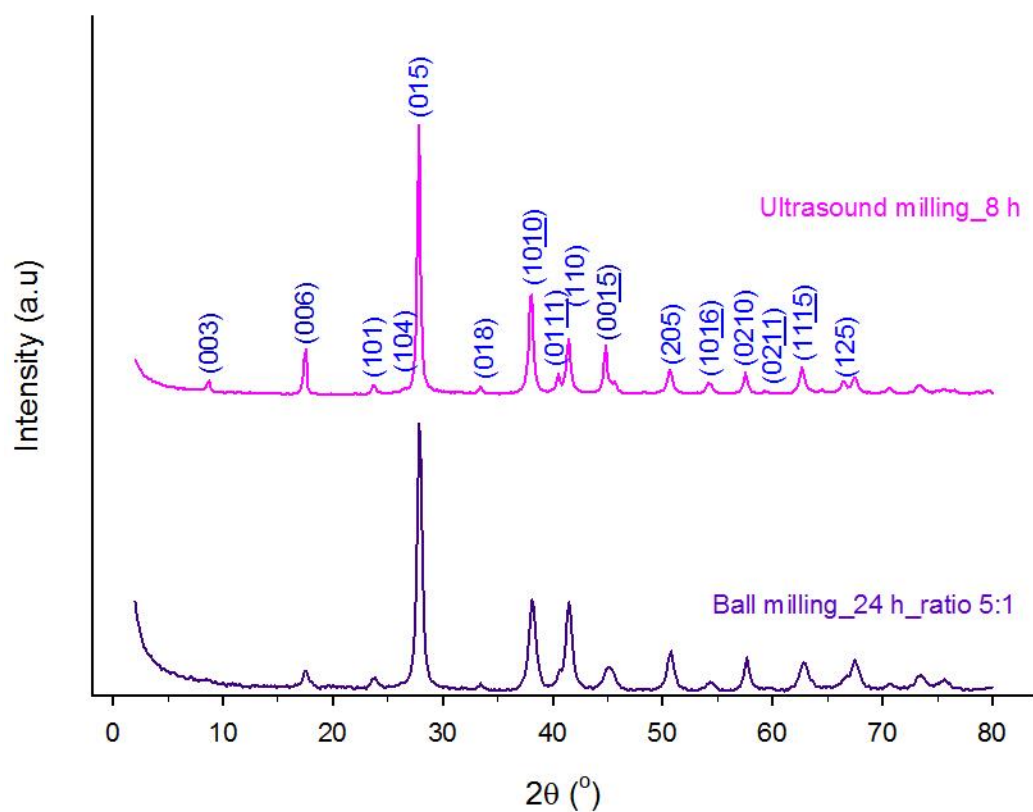


Fig. 4.23. XRD patterns of the n-type $\text{Bi}_2\text{Te}_{2.79}\text{Se}_{0.21}$ after ball milling, 24 h and ratio 5:1 (purple), and after ultrasound milling performed at 100 % amplitude, 2 coolers and 8 h (pink).

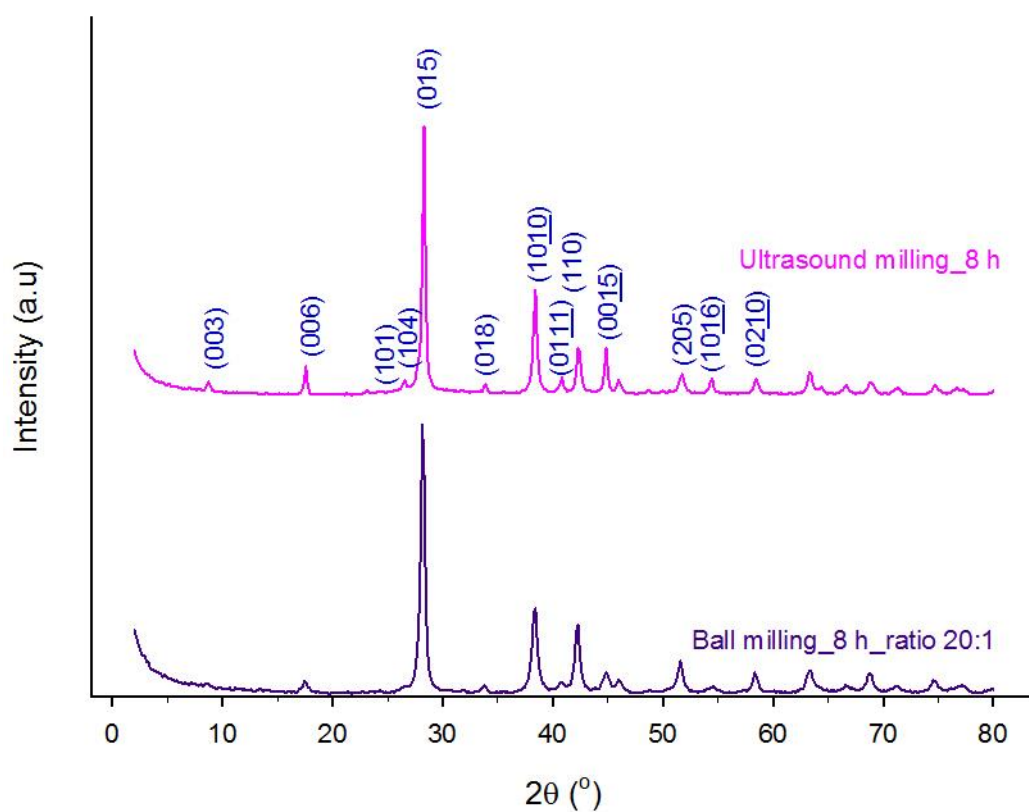


Fig. 4.24. XRD patterns of p-type $\text{Bi}_{0.5}\text{Te}_3\text{Sb}_{1.5}$ after ball milling at 8 h and ratio 20:1 (purple)

and after ultrasound milling treatment performed at 100 % amplitude, 2 coolers and for 8 h (pink).

4.6 Conclusions

The optimisation of the fabrication of bismuth telluride nanopowders by two different milling techniques, widely used BM and a new UM method was performed for both n- and p-type materials. Laser diffraction analysis, SEM and XRD measurements were employed as characterisation tools of the powders. In general, particle size analysis by laser diffraction identified larger sizes than the ones observed by SEM. For this reason, SEM results were more strongly considered when determining the final optimum conditions for the fabrication of the nanopowders.

In the BM method, treatment duration and balls:powder weight ratio were the parameters to be optimised. The balls:powder ratios that produced the smallest particle sizes in the laser diffraction analysis for the n-type and p-type materials were 5:1 and 20:1, respectively. The optimum treatment times identified by SEM analysis for the optimised ratios for the n- and p-type materials were 24 and 8 h respectively. Nanoparticles with sizes from around 200 nm and 300 nm for the n- and p-type materials respectively, were obtained for these optimum conditions. No morphological variations were identified for the non-treated sample. XRD results showed that the single phase structure found in the non-treated sample was not modified by the BM process.

In the UM method, a larger amount of parameters had to be evaluated, such as the solvent to be utilised, the presence of additive (PG), amplitude of the ultrasound, number of cooling systems and powder concentration. All the experiments performed showed a clear reduction in the particle size and the formation of nanoparticles. In addition, apparent large particles are formed, which are actually agglomerates of nanoparticles. This is a unique feature of this method.

From different solvents evaluated (1-butanol, DMF, EtOH, decane and H₂O), 1-butanol presented the highest power factor in discs compacted by cold press from the prepared powders, and it was considered as optimum. The usage of additive at short treatment times (30 min) in the n-type material does not produce a significant change in the particle size, but more rounded particles are formed when it is not present. On the other hand, the use of additive was only evaluated at longer times (8h) for the p-type material. No significant differences in the particle size and morphology were observed in this case.

Reducing the amplitude and the treatment time resulted in a minor presence of the characteristic aggregates in the p-type material, while no straightforward correlation was found for the n-type material.

Regarding the evaluation of the influence of the powder concentration, most of the large particles in the aggregates become larger when the concentration is doubled in the n-type material. In the case of the p-type material, no significant differences were observed when the concentration was doubled for a treatment time of 6 h. However, for an 8 h treatment the formation of large aggregates is significantly reduced by the increase of concentration of powder. In both cases (6 and 8 h), the size of the particles did not significantly differ.

After all the optimisation, the optimum conditions adopted were 100 % amplitude, [powder]=0.0166 M, 2 cooling systems, 8 h and 1-butanol for both n- and p-type material. At these conditions, most of the particles in the aggregates are in the 500-1000 nm range for the n-type material. For the p-type, both coarse particles of few microns and fine particles in the 200-1000 nm range were obtained. Finally, XRD analysis showed that the single phase structure identified in the non-treated sample was not modified by the UM process.

When both, BM and UM processes are compared for the n-type material, it can be observed that similar smallest particles are produced by both methods. However, UM treatment requires shorter milling times (3 times shorter), which is of great advantage since this implies a considerable reduction in time and power consumption. Moreover, in the UM samples, the presence of large particles, which it is noticeable in the BM, is considerably reduced.

For the p-type material, similar particle sizes are obtained by both methods, although the UM treatment distinctly produces a higher and homogeneous amount of nanoparticles using the same treatment time. Regarding the powders morphology, smoother and rounder particles than the BM treatment are obtained by UM in the n-type material at short times (30 min). In the p-type material, this difference in morphology is not observed since the analysis was only performed at long times (8 h).

Chapter 5 : Optimisation of the Hot Press Compaction Method

- 5.1 Introduction**
- 5.2 Construction of the hot press station**
- 5.3 Optimisation of the sintering process**
 - 5.3.1 Time and temperature optimisation
 - 5.3.2 Pressure optimisation
- 5.4 Conclusions**

Chapter 5

5.1 Introduction

In this chapter, the compaction of material powders to form high density and mechanically robust disc samples is described. High density and robustness are required to achieve bulk materials with high electrical conductivity and suitable mechanical properties for thermoelectric applications. To perform this task, hot pressing has been used as the compaction method. The construction of a hot press station from an initial standard press is described in the next section. The optimisation of the different experimental conditions of the pressing process (time, temperature and pressure) to achieve the most suitable compactness, are described in the third section. Finally, the best experimental conditions are identified, which will be used to prepare the bulk samples from the previously synthesised powders in the next chapter.

5.2 Construction of the hot press station

A standard press station available in the lab was modified to achieve a hot pressing system. The developed hot press station (Fig. 5.1) includes:

- A plastic enclosure where the argon gas is introduced to the system during the sintering process to avoid oxidation of the sample.
- A cardboard interface to minimise losses of heat and argon gas.
- A band heater (Watlow, MB1N2AN1, 4.45 cm internal diameter and 5.08 cm height) enclosing the die set to provide the required temperature needed for the sintering process. It integrates a K-type thermocouple for temperature reading.
- A hardened stainless steel die set comprising a cylindrical cavity where the powder is placed and then pressed by two rods.
- A variable auto transformer (Carroll & Meynell, CMCTV 5) was utilised to regulate the ac voltage from the mains required to power the band heater.

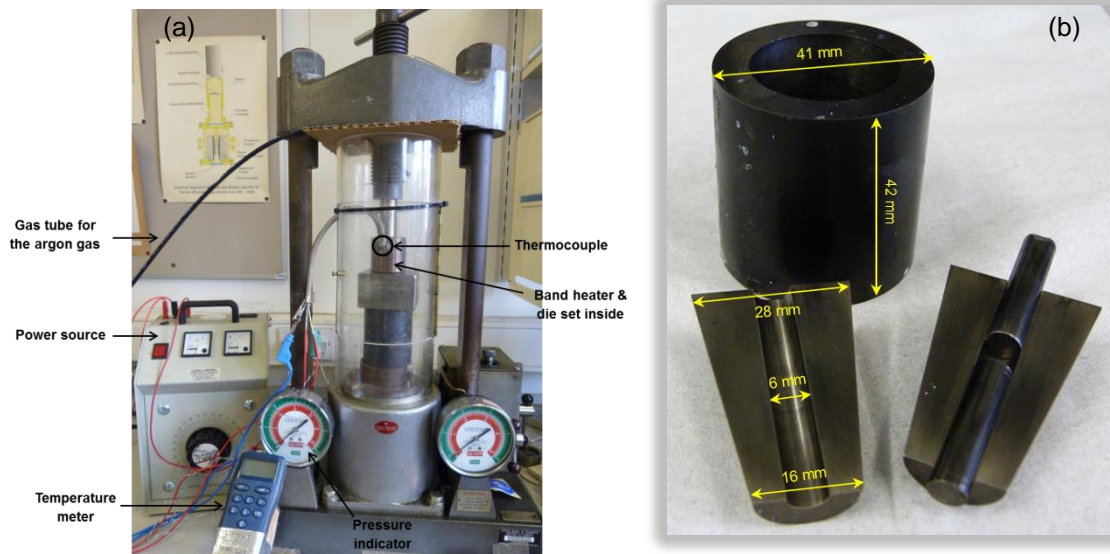


Fig. 5.1. (a) Hot pressed system built in the laboratory and (b) die set.

The fabrication of discs was achieved by placing the material powder in the die set sandwiched by the two rods. Then, the system was closed and argon gas was circulated. The required temperature for the pressing process was established with the band heater surrounding the die set and a constant pressure was applied to the rods of the die for a certain time. Finally, the pressure and the temperature were removed and the system was extracted from the press station to cool down inside the fume hood. It should be mentioned that the die set was sprayed with an anti-sticking agent (graphite spray) to avoid the bonding of the sample and facilitate its extraction from the mould. Sample discs with diameters around 6 or 13 mm were obtained by the use of die sets with different dimensions. A diagram of the fabrication process is shown in Fig. 5.2.

5.3 Optimisation of the sintering process

The material powder used for all the optimisation experiments was the n-type $\text{Bi}_2\text{Te}_{2.79}\text{Se}_{0.21}$ ($<106 \mu\text{m}$). Three samples identically processed were obtained at each experimental condition. To identify the optimal conditions different temperature and duration of the sintering process, fixing the applied pressure, were evaluated first. Then, the effect of the variation of the pressure was evaluated using the optimum time and temperature from the previous results. The density of all the processed samples were calculated using a precision balance and measuring their diameter and thickness with a calibre.

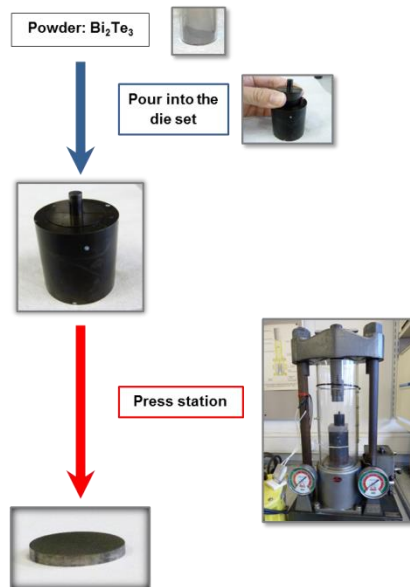


Fig. 5.2. Schematic process of fabrication of sample discs.

The density of a bulk sample which was directly cut from the ingot was measured by the Archimedes' method and used as reference. This method was utilised due to the difficulty to determine the volume of the reference sample which was not completely round. To accurately determine the density of the reference, 5 different samples from the same ingot with different volumes and shapes were measured, obtaining an average value and standard deviation of 7.75 ± 0.05 (g/cm³), very close to the value provided by the company (7.83 g/cm³) and the theoretical value (7.86 g/cm³)⁽¹⁹⁹⁾.

In addition to the density, the Seebeck coefficient and electrical conductivity of each sample were measured using the hot probe and the 4-probe techniques respectively. The power factor was calculated from these two values.

5.3.1 Time and temperature optimisation

Three different disc samples were obtained by pressing at a fixed pressure of 1513.7 MPa and employing different times (25 s, 30 min or 60 min) and temperatures as shown in the scheme of Fig. 5.3, except for samples E and F (30 min and 60 min) where only 2 and 1 sample could be obtained, respectively:

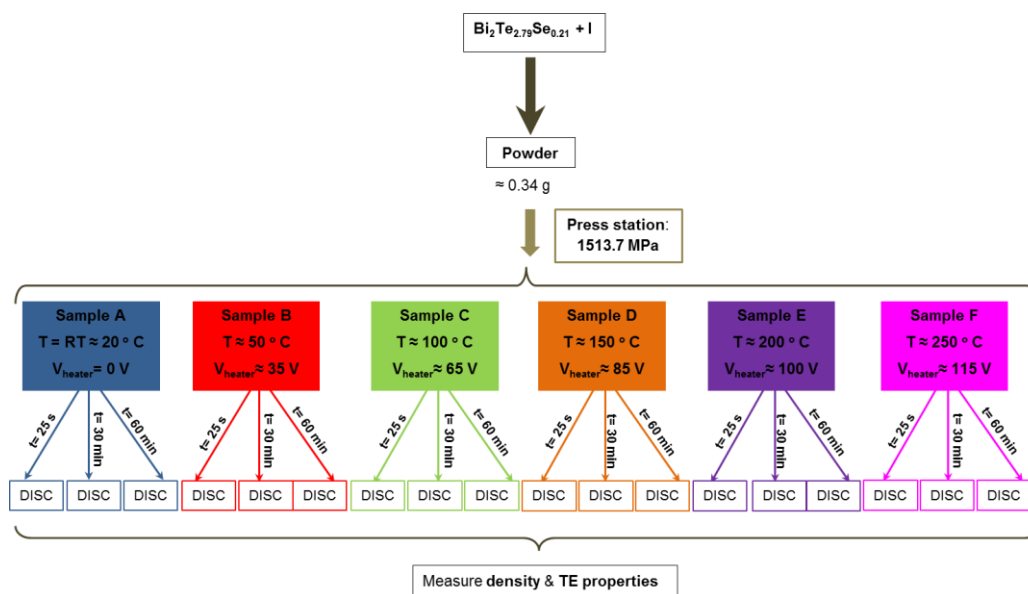


Fig. 5.3. Scheme of the experiments performed for the optimisation of time and temperature of the compaction process.

The density of the samples is represented in Fig. 5.4. The obtained values are the average of the 3 samples prepared at each condition. In the rest of the thermoelectric properties determined also the average of the 3 samples is presented.

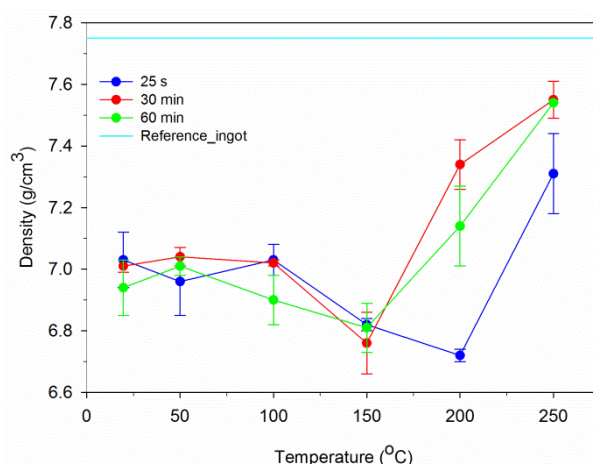


Fig. 5.4. Density vs. sintering temperature of compacted discs at different times, 25 s (blue), 30 min (red) and 60 min (green). The density value of the reference sample (cyan line) is also represented.

All the prepared samples show lower density than the ingot and present a significant increase at the highest temperatures. Temperatures higher than 150°C were required to improve the density values. The highest densities were obtained for the samples prepared at 250°C for 30 min and 60 min (7.55 and 7.54 g/cm^3 respectively). It seems that at short times (25 s) the compaction was still incomplete. On the other hand, at 250°C very similar density values were observed at 30 and 60 min, so no further improvement was achieved when longer sintering times were employed. It can be concluded from this analysis that pressing at

250 °C for 30 min are the optimal conditions for the constant pressure used. At these conditions, 97.41 % of the reference density was obtained.

The Seebeck coefficient, electrical conductivity and power factor values of the samples produced are shown in Fig. 5.5. The standard deviation values are not represented for clarity. They were smaller than 2.5 % (Seebeck coefficient), 10 % (electrical conductivity) and 12% (power factor).

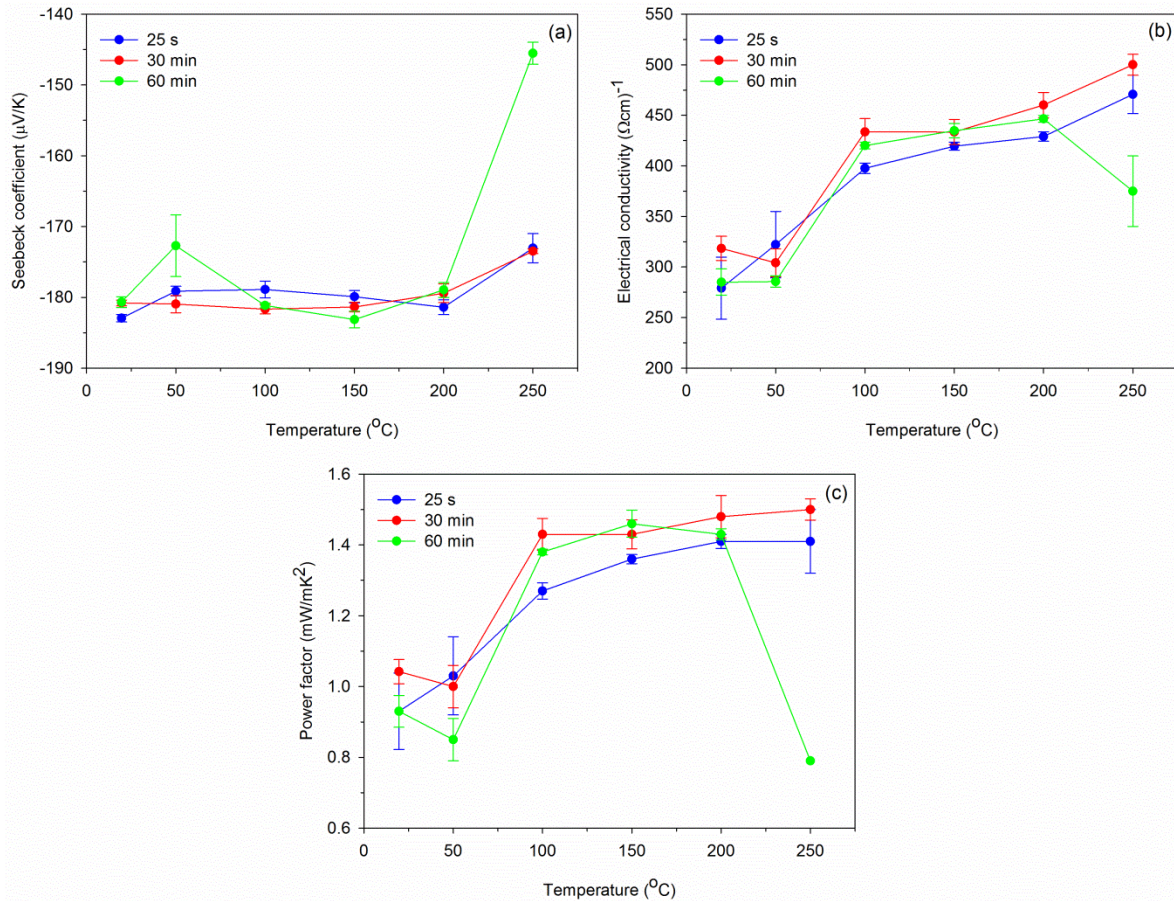


Fig. 5.5. Seebeck coefficient (a), electrical conductivity (b) and power factor (c) as a function of the sintering temperature at different times.

The absolute value of the Seebeck coefficient of all the samples is around 180 $\mu\text{V/K}$ at most of the temperatures, which is lower than the value of the reference sample (-204 $\mu\text{V/K}$). A slight reduction is observed at the highest temperatures, which becomes significant for the longer time (60 min) treatment. A similar significant decrease is also observed in the electrical conductivity for these conditions and consequently in the power factor. This could be due to the fact that in the samples sintered for 30 min and 60 min, only 2 and 1 samples respectively, thus a lower level of confidence exists for these measurements.

The electrical conductivity of the samples shows a general increase with the temperature (except the case mentioned above) as generally occurs in a sintering process. At 25 s lower conductivity values were obtained at temperatures higher than 50 °C

compared to the longer treatments, which seems to be not long enough for a suitable sintering. The highest power factor values were obtained at the highest temperatures for 30 min treatments. As occurred in the density results, the optimal conditions producing the best power factor values are 250 °C of pressing temperature for 30 min.

5.3.2 Pressure optimisation

In order to evaluate the optimal pressing pressure different powders (using the same material as above) were compacted at 250 °C for 30 min varying the applied pressure. The different pressures applied and a scheme of the process followed for the preparation of the discs is shown in Fig. 5.6:

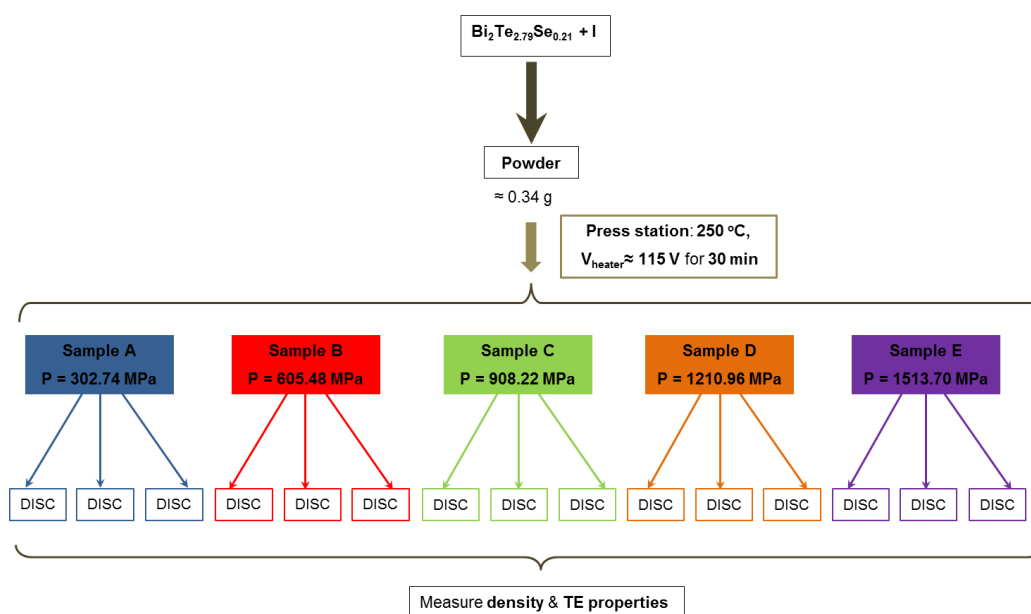


Fig. 5.6. Diagram of the procedure followed to prepare disc samples at different pressures.

The average density from 3 samples and the relative values respect to the reference sample (7.75 g/cm³) of the compacted discs are shown in Fig. 5.7.

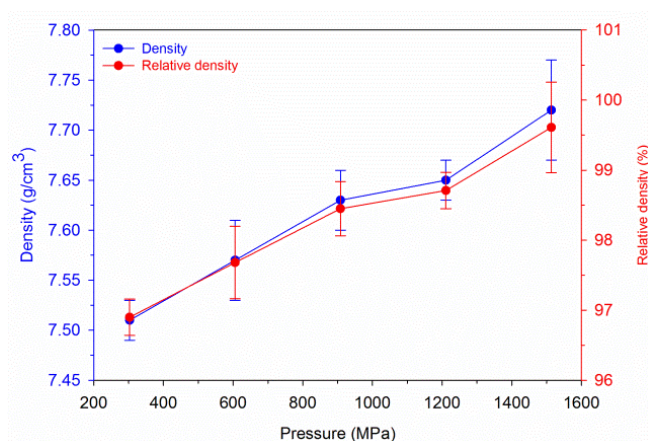


Fig. 5.7. Density (blue) and relative density (red) of powders treated at different pressures. The pressing temperature (250 °C) and the duration of the treatment (60 min) were the same for all the experiments.

A clear increase in density with pressure is observed, reaching the maximum value (7.72 g/cm³, 99.61 %) at the highest pressure (1513.7 MPa). Under these conditions, practically the same density as the reference sample was achieved.

Seebeck coefficient, electrical conductivity and power factor measurements are shown in Fig. 5.8.

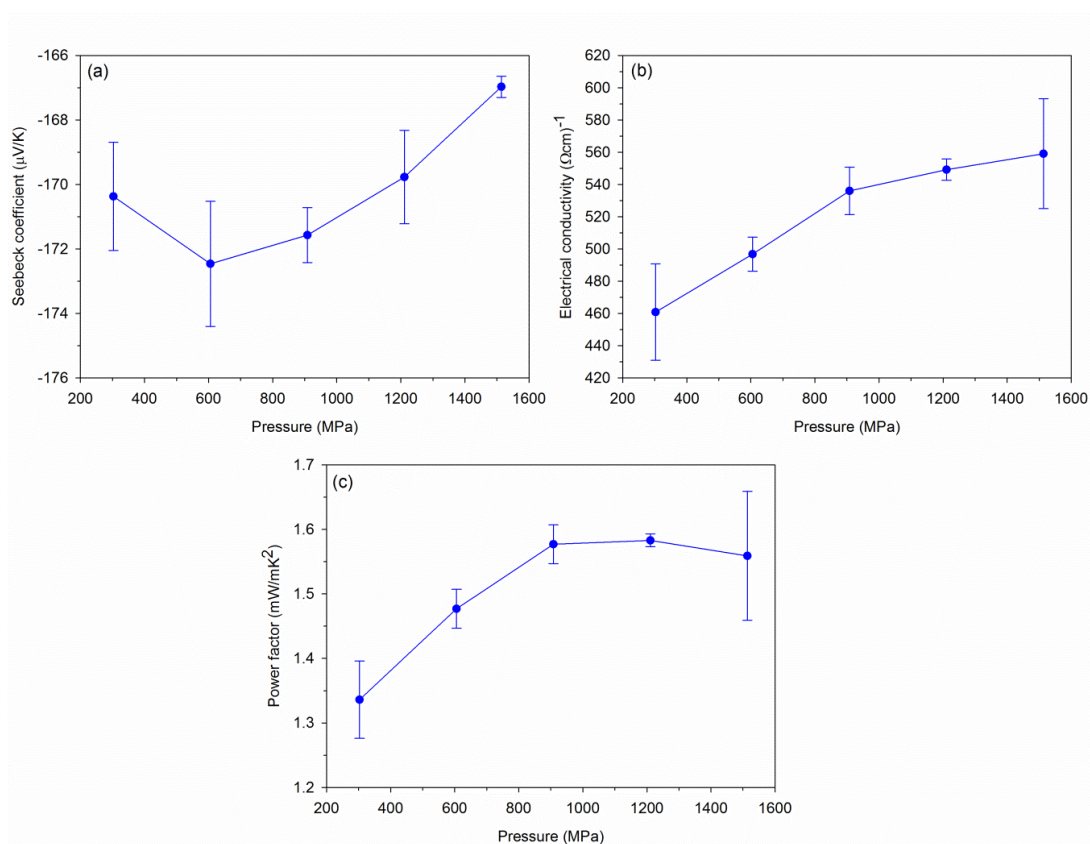


Fig. 5.8. Seebeck coefficient (a), electrical conductivity (b) and power factor (c) as a function of the sintering pressure. The same duration (30 min) and temperature (250 °C) were used in all experiments.

A reduction ($\approx 30 \mu\text{V/K}$) of the absolute value of S respect to the reference sample ($-204 \mu\text{V/K}$) was observed for all the discs, which could be due to a possible alteration in the structure of the material. In general, there is not much variation in the S values with the sintering pressure. A very slight decrease of around $6 \mu\text{V/K}$ is observed and the best S value was found for the sample sintered at 605.48 MPa.

The electrical conductivity (see Fig. 5.8b) shows an increase with pressure as occurred for the density, obtaining the highest value ($\approx 560 (\Omega\text{cm})^{-1}$) at 1513.70 MPa. It should be noted that the increase is not very significant at the highest pressures. A similar feature is observed for the power factor, which increases with pressure until a nearly constant value, due to the more significant increase of the electrical conductivity.

It can be concluded that the most suitable conditions to prepare compacted samples are at 250°C for 30 min employing a pressure of 1513.70 MPa, which produced the highest density and electrical conductivity without a significant decrease of the power factor.

Since conditions are not expected to change significantly between n- and p-type Bi_2Te_3 due to their similar chemical composition, one p-type sample was prepared using the optimised conditions identified above for the n-type material. The density obtained after the compaction process was 6.57 g/cm^3 , which is 98.40 % of the density of the reference sample ($6.68 \pm 0.21 \text{ g/cm}^3$), which was obtained by Archimedes' method from the average of 5 different samples cut from the p-type ingot. This value is very close to the one provided by the company (6.75 g/cm^3), the theoretical value (6.88 g/cm^3)⁽²⁰⁰⁾ and similar to the one obtained for the n-type. Therefore, the same conditions will be utilised for sintering both types of powders.

5.4 Conclusions

A hot press station has been developed from an available press in the lab. The detailed elements used and experimental setup was described. Different samples were compacted and the optimal conditions for the pressing process were identified, based on the density and power factor values.

Different pressing times and temperatures were initially varied keeping a fixed pressing pressure. From these experiments the highest density and power factor was obtained at 250°C of pressing temperature for 30 min. Then, using this temperature and pressing time, different pressures were tested. The most suitable pressure was 1513.70 MPa, which produced the highest density and electrical conductivity without a significant decrease of the

power factor. These conditions (250 °C, 1513.70 MPa and 30 min) are considered as optimum.

Chapter 6 : Thermoelectric Properties of Nanobulk Materials

6.1 Introduction

6.2 Characterisation of non-treated samples

6.2.1 Thermoelectric properties

6.2.2 XRD

6.2.3 Optical microscope

6.3 Characterisation of milled samples

6.3.1 Thermoelectric properties

6.3.2 XRD

6.3.3 Optical microscope

6.4 Conclusions

Chapter 6

6.1 Introduction

This chapter comprises the structural and thermoelectric characterisation of nanobulk samples prepared under the conditions optimised in the previous chapter. The different optimised powders prepared in chapter 4 by ball milling (BM), ultrasound milling (UM) and simply by the initial crushing pre-treatment (non-treated) are separated into different particle size fractions. Each fraction is hot pressed into a nanobulk disc sample which is then characterised. The main objective here is the analysis of the impact on the thermoelectric properties of the different treatments, especially the novel UM method. In order to understand the thermoelectric results, the microstructures of the samples are evaluated by microscope and XRD.

The non-treated samples are first examined in the next section. Then, both BM and UM characterisation is shown in the third section, including the comparison with each other and the non-treated samples.

We would like to remark that although the pressing conditions in chapter 5 are presented as a function of pressure, along this chapter we adopt weight (tons) instead, since this is the scale of the press station. The optimised pressure of 1513.70 MPa corresponds to 5 tons.

In the same way, as in previous chapters, the two bismuth telluride materials, n-type ($\text{Bi}_2\text{Te}_{2.79}\text{Se}_{0.21} + \text{I}$) and p-type ($\text{Bi}_{0.5}\text{Te}_3\text{Sb}_{1.5}$), were evaluated. The separation into different particle size fractions is achieved using different sieves with a shaker (see section 3.3.1). This separation is performed in order to analyse the effect of the different particle size ranges on the thermoelectric properties. The mass density also have a significant influence on the thermoelectric properties⁽¹⁹⁷⁾ and is taken into account as well along the characterisation.

6.2 Characterisation of non-treated samples

In this section the samples obtained from the powders simply treated by the initial crushing in the micro hammer-cutter mill and then sieved at 106 μm pore size (see section 4.2) were evaluated. It should be mentioned that the sintering temperature in the compaction process was increased from 250 $^{\circ}\text{C}$, which was the initially optimised temperature, to 350 $^{\circ}\text{C}$. This was performed in order to improve the electrical conductivity of the samples, which was somewhat low in the optimisation of chapter 5. Samples sintered at both temperatures are characterised.

6.2.1 Thermoelectric properties

Both Seebeck coefficient and in-plane electrical conductivity of non-treated samples were measured at room temperature by the 4-multifunctional probe apparatus (see section 3.4.3). It should be mentioned that this equipment provides an average in all directions of the sample plane where the probes are contacted (in-plane sheet resistance) and the electrical conductivity is obtained extrapolating this behaviour to the whole sample thickness. In directional samples such as bismuth telluride this can cause variations which should be taken into consideration in the interpretation of the results. The cross-plane thermal conductivity was measured by the laser flash instrument (see section 3.4.4) at room temperature as well. This instrument provides this parameter in the cross-plane direction. Measurements from samples (n and p-type) directly cut from the original ingots of materials, measured by the same equipment mentioned, were used as reference. Three samples for each particle size range and sintering temperature were prepared to evaluate repeatability. Three measurements are performed on each sample that are averaged. The reported thermoelectric properties are the average of the three averaged values from each of the three samples.

- **n-type $\text{Bi}_2\text{Te}_{2.79}\text{Se}_{0.21}$ + I:**

Density, Seebeck coefficient, in-plane electrical conductivity and power factor values of n-type discs prepared under two different sintering temperatures (250 and 350 $^{\circ}\text{C}$) for different particle size ranges are shown in Fig. 6.1. The density of the samples prepared at 250 $^{\circ}\text{C}$ is higher than at 350 $^{\circ}\text{C}$ (Fig. 6.1 (a)), and their values are 99.8 % and 98.2 % of the reference sample (cut from the ingot) density, respectively. The decrease of the density with the particle size ranges is not significant and might be due to the presence of finer particles, which increases porosity.⁽¹⁹⁷⁾

The Seebeck coefficient results show a decrease in the absolute value with respect to the reference sample (cut from ingot) at both sintering temperatures (Fig. 6.1 (b)). This could be due to an increase in the carrier concentration which induces the rise of the Fermi energy resulting in a decrease in the Seebeck coefficient.⁽²⁰¹⁾ Another possibility could be the lack of a recrystallization process which maintains residual defects in the samples, which contribute to the diminution in the Seebeck coefficient.⁽¹⁹⁸⁾ Most of the Seebeck coefficient results show no variation with the particle size ranges, which has been previously observed in the literature.⁽²⁰²⁾

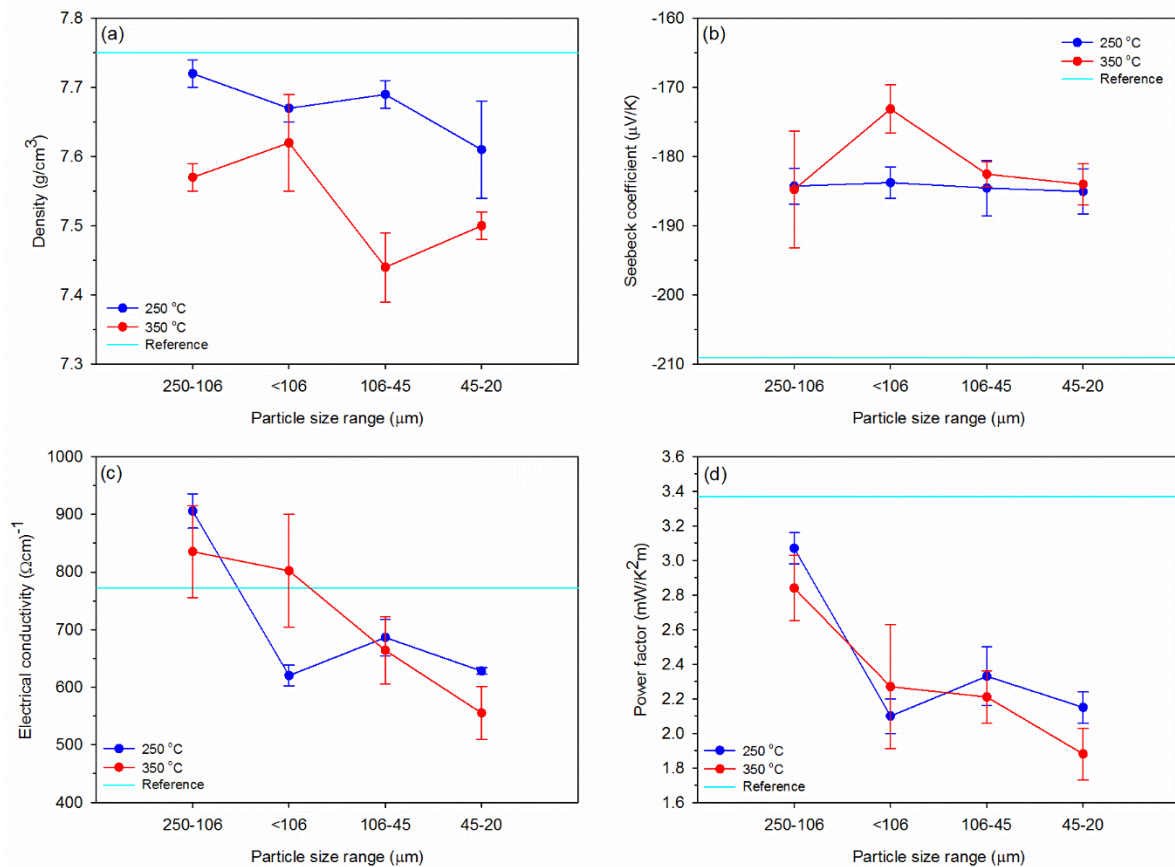


Fig. 6.1. (a) Density, (b) Seebeck coefficient, (c) in-plane electrical conductivity and (d) power factor of n-type discs prepared under two different sintering temperatures (250 and 350 °C), 5 tons of weight and for 30 min. Results are shown for samples compacted from powders of different particle size ranges.

From the in-plane electrical conductivity results in Fig. 6.1 (c) it can be observed that the electrical conductivity of the non-treated samples is higher than the reference for the larger particle sizes and lower when this parameter is decreased. In the samples prepared the electrical conductivity decreases with the particle size which is usually due to the increase of grain boundaries and/or the mass density.⁽²⁰³⁾ On the other hand, higher values of the electrical conductivity are observed for the samples sintered at 250 °C (with

the exception of the particle size <106 μm), which could be due to their somewhat higher density values.

The power factor is lower for all the non-treated samples respect to the reference as shown in Fig. 6.1 (d), mainly due to the lower Seebeck coefficient. On the other hand, it decreases with the increase of finer particles following the electrical conductivity trend at both sintering temperatures. This trend was also observed in the literature.⁽²⁰⁴⁾ The largest power factor was obtained for the sample prepared at 250 $^{\circ}\text{C}$ with a particle size range of 250-106 μm . Also, for this temperature most of the values are higher than at 350 $^{\circ}\text{C}$.

Regarding cross-plane thermal conductivity determination, it should be mentioned that it was not possible to measure it in the disc samples analysed above sintered at 250 $^{\circ}\text{C}$, due to their small diameter (around 6 mm). The thermal conductivity apparatus requires a diameter of 12.7 mm. Therefore, only thermal conductivity and ZT values are presented in Fig. 6.2 for the samples sintered at 350 $^{\circ}\text{C}$.

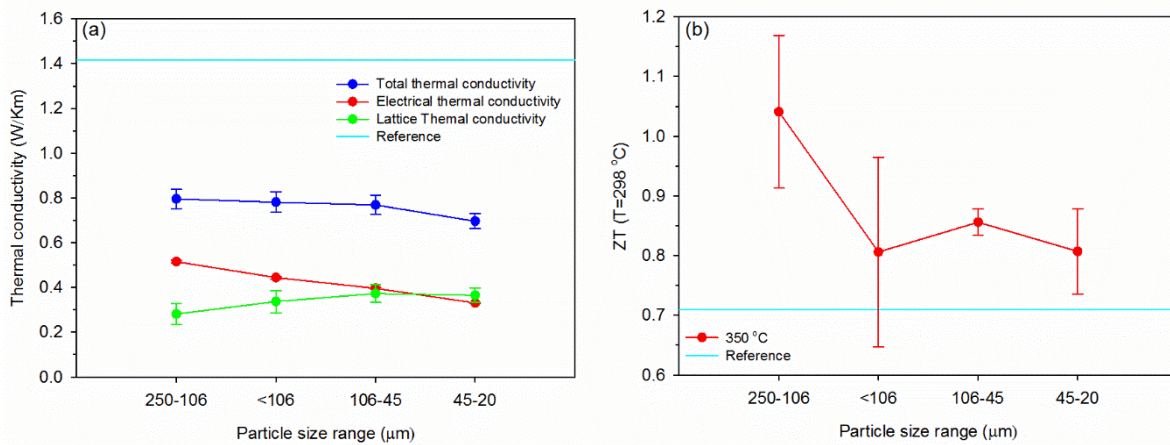


Fig. 6.2. (a) Cross-plane thermal conductivity and (b) ZT of n-type discs prepared at 350 $^{\circ}\text{C}$, 5 Tons of weight for 30 min. Results are shown for samples compacted from powders of different particle size ranges.

Fig. 6.2 (a) shows the cross-plane thermal conductivity results, including the electronic (λ_E) and lattice contributions (λ_L). The electronic contribution was obtained using the Wiedemann-Franz law ($\lambda_E=L\sigma T$, where $L=2.0 \cdot 10^{-8} \text{ V}^2/\text{K}^2$). It should be taken into account that the thermal conductivity was measured in the cross-plane direction of the samples (see Fig. 6.3).

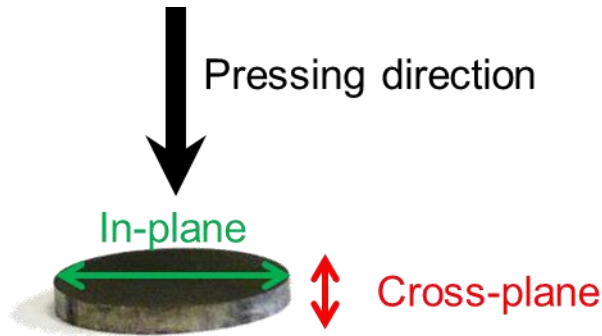


Fig. 6.3. Example of a disc sample with the different directions employed for the measurements and pressing.

The measurements performed for the different particle size ranges show a significant decrease ($\approx 50\%$) with respect to the ingot sample, which is a considerable reduction surprisingly obtained from a very simple crushing process. The values found (0.7 to 0.8 W/Km) are similar to state-of-the-art bismuth telluride materials.^(10, 58) On the other hand, the thermal conductivity does not significantly change with the different size ranges, although a slight decrease is achieved especially at the smallest size range (45-20 μm).

When comparing the electrical and lattice contribution to the thermal conductivity, it can be observed that they differ at the larger sizes but become similar at the lower size ranges. This is due to the decrease observed with the size ranges for λ_E (in agreement with electrical conductivity results) together with the opposite trend in λ_L . The slight increase in the lattice thermal conductivity with the particle size indicates that the phonons are less efficiently scattered at smaller size ranges. It should be mentioned that this discussion should be considered carefully since the electrical and thermal conductivities are evaluated in different directions (in-plane and cross-plane, respectively).

The ZT values for the samples sintered at 350 °C (Fig. 6.2 (b)) show a similar trend to the power factor (Fig. 6.2 (d)), since the thermal conductivity is predominantly constant. The highest ZT value (1.04) was obtained for the largest particle size range (250-106 μm). This value is significantly higher than the reference, mainly due to the considerable reduction of the thermal conductivity. For the rest of the size ranges, the ZT values lie around 0.80-0.85. Again, these ZT values should be considered carefully since they are obtained from the evaluation of the electrical conductivity and the thermal conductivity in different directions.

After this analysis the n-type Bi_2Te_3 , sintered at 250 °C, was identified as the most suitable condition for powder sintering into a disc with a particle size range 250-106 μm .

- **p-type $\text{Bi}_{0.5}\text{Te}_3\text{Sb}_{1.5}$:**

Density, Seebeck coefficient, in-plane electrical conductivity and power factor values for the p-type material are shown in Fig. 6.4. The density of the samples prepared at 350 °C is higher than at 250 °C, with 97.9 % and 98.9 % values respect to the reference sample cut from the ingot, respectively (Fig. 6.4 (a)). The contrary occurred to the n-type material, whose higher density was obtained for discs sintered at 350 °C. Apart from density, lower values were found for the samples sintered at 250 °C in the rest of parameters, which makes this sintering condition less adequate. At 350 °C the density does not vary significantly. Only a slight decrease is observed for the smallest particle sizes.

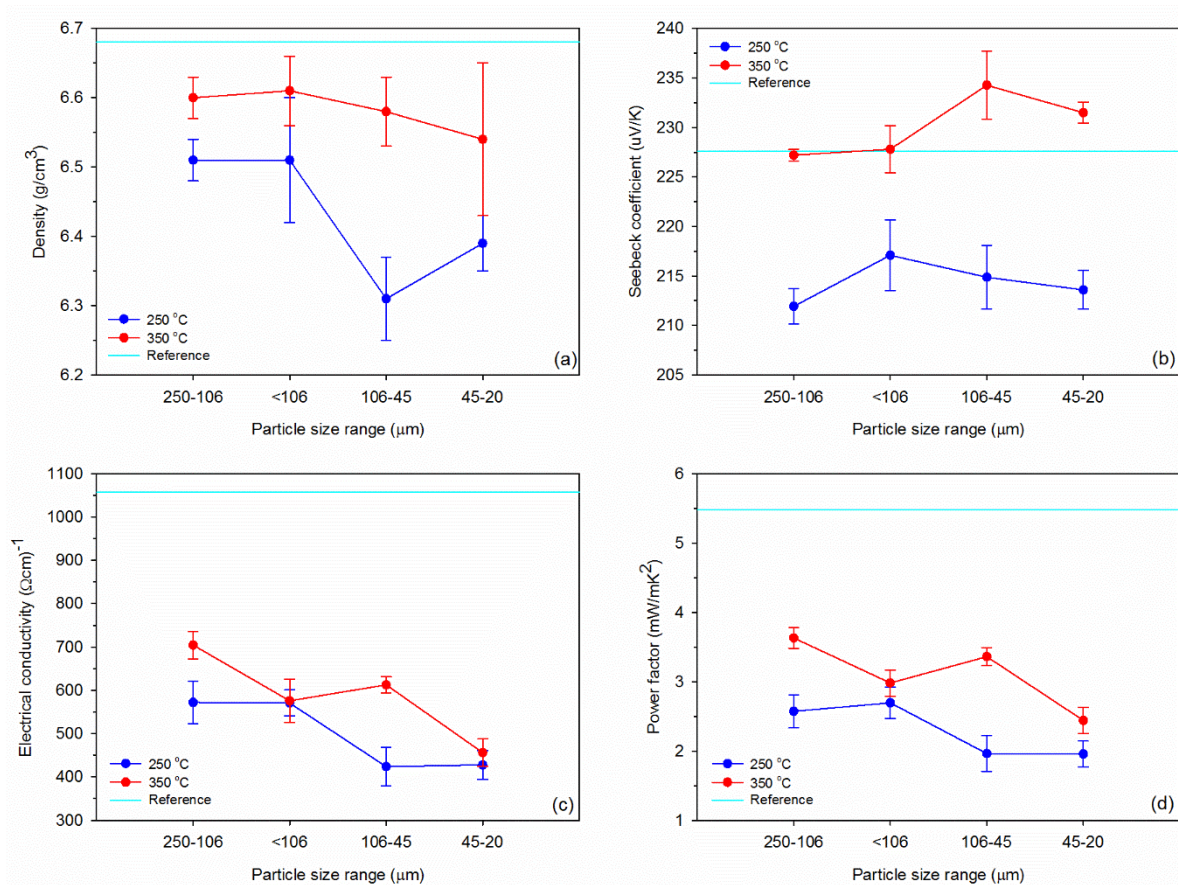


Fig. 6.4. (a) Density, (b) Seebeck coefficient, (c) in-plane electrical conductivity and (d) power factor of p-type discs prepared under two different sintering temperatures (250 and 350 °C), 5 tons of weight and for 30 min. Results are shown for samples compacted from powders of different particle size ranges.

The results from the Seebeck coefficient (Fig. 6.4 (b)) show differences between the samples sintered at 350 °C and 250 °C. At 350 °C the values are similar or above the reference sample cut from the ingot, while they are slightly lower at 250 °C. The largest Seebeck coefficient (234.27 μV/K) is observed for the sample with the particle size range

106-45 μm sintered at 350 $^{\circ}\text{C}$. No significant variations of the Seebeck coefficient with the particle size ranges is observed⁽²⁰²⁾ as in the n-type.

The behaviour of the in-plane electrical conductivity of the p-type bismuth telluride samples is shown in Fig. 6.4 (c). The non-treated samples present a significantly lower value than the reference. The electrical conductivity follows a similar trend to the n-type material with the particle size ranges. Unlike the n-type, the electrical conductivity is generally higher for the samples sintered at 350 $^{\circ}\text{C}$, which could be due to a better sintering achieved. Probably 250 $^{\circ}\text{C}$ is not enough to provide a good connection between grains. As suggested for the n-type, the behaviour of the electrical conductivity might be related to the different density values,^(197, 205) and samples with lower density (250 $^{\circ}\text{C}$) present smaller electrical conductivities. Within the samples sintered at 350 $^{\circ}\text{C}$, the largest electrical conductivity is shown for the largest particle size range 250-106 μm and it diminishes as the size range decreases.

The largest power factor was obtained for the samples prepared at 350 $^{\circ}\text{C}$ and decreases with the size range (Fig. 6.4 (d)), as observed in the n-type material (Fig. 6.1 (d)). Within the samples sintered at 350 $^{\circ}\text{C}$, the highest value was found for the 250-106 μm particle size range. For all size ranges at this temperature the power factor is lower than the reference due to the reduction in the electrical conductivity. The same occurs for the 250 $^{\circ}\text{C}$.

The cross-plane thermal conductivity measurements at room temperature are shown in Fig. 6.5. In Fig. 6.5 (a) it is observed that all samples in the different size ranges at both sintering temperatures show significantly lower thermal conductivity (<0.8 W/Km) than the reference sample (1.301 W/Km), as occurred for the n-type material. The minimum value from all the specimens is obtained for the size range 106-45 μm at 250 $^{\circ}\text{C}$ sintering temperature (0.52 W/Km). This value is considerably lower than the minimum found previously for the n-type samples (0.70 W/Km), and is lower than the state-of-the-art bismuth telluride materials, again surprisingly achieved employing a very simple crushing process.^(10, 58)

The samples sintered at 350 $^{\circ}\text{C}$ present larger thermal conductivity (0.72-0.78 W/Km) than at 250 $^{\circ}\text{C}$ (0.52-0.75 W/Km). This could be related to the slightly higher density values observed at 350 $^{\circ}\text{C}$ (Fig. 6.4 (a)). No clear trends are observed for the p-type with the size ranges, in contrast to the n-type where a nearly constant behaviour was observed (Fig. 6.2 (a)). Fig. 6.5 (b and c) also displays the electrical and lattice contributions to the thermal conductivity. It is observed that both contribute similarly to the total thermal conductivity, being λ_E somewhat smaller than λ_L . Similarly to the n-type, the λ_E decreases with the decrease in size ranges, while no clear trend can be identified for λ_L . As mentioned before, this discussion should be carefully considered due to directionality issues.

The ZT values, shown in Fig. 6.5 (f), are significantly high (≈ 1.4) for the particle size ranges 250-106 μm and 106-45 μm at 350 $^{\circ}\text{C}$ sintering temperature, improving the ZT of the starting material (reference) and within the best values reported in the literature.^(10, 58) The excellent ZT value is attributed to the improved electrical conductivity and the significant diminution in the thermal conductivity. Again, caution should be taken here for the ZT values due to samples anisotropy as previously mentioned.

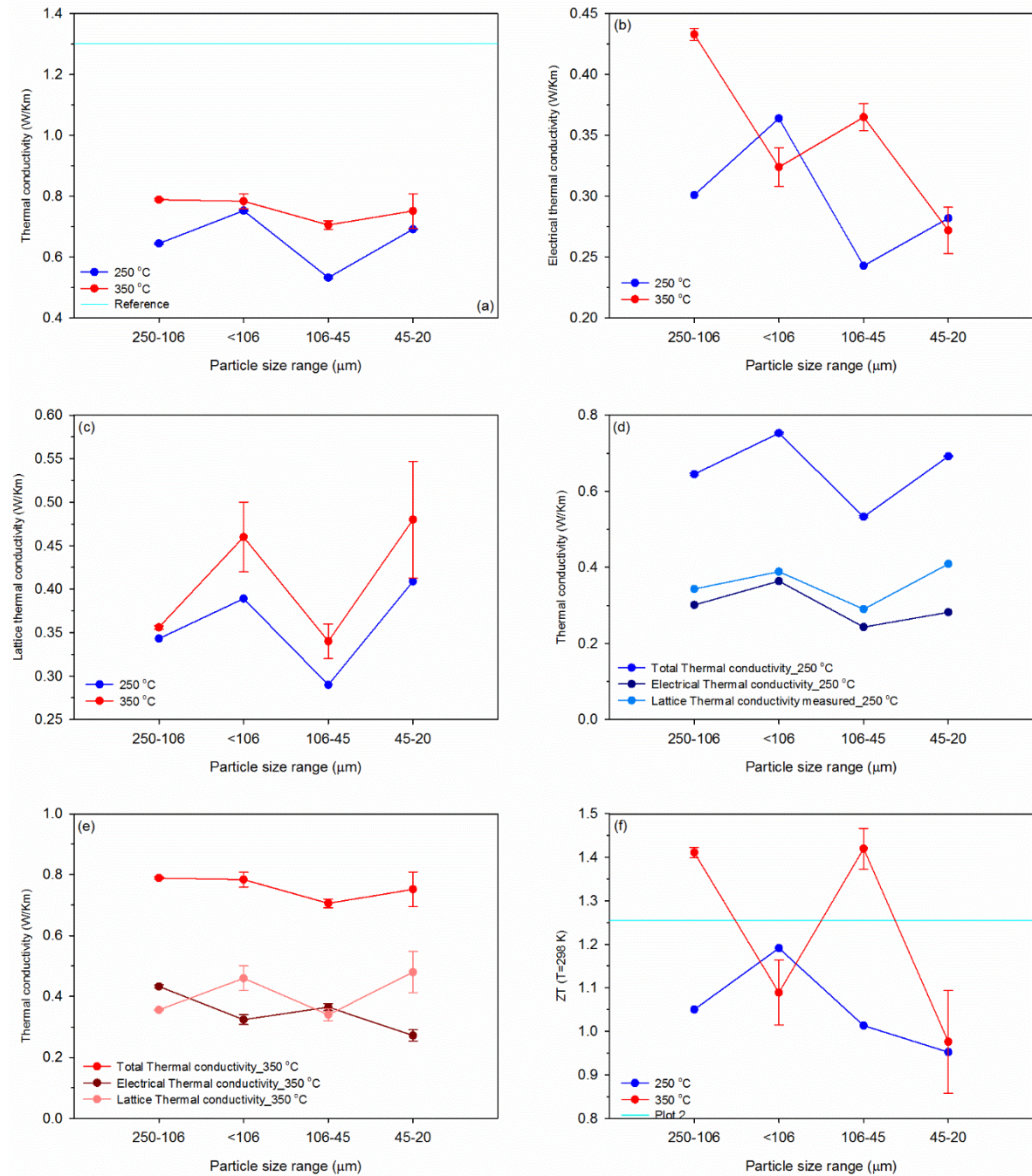


Fig. 6.5. (a) Cross-plane thermal conductivity, (b) electrical thermal conductivity and (c) lattice thermal conductivity of p-type discs prepared at 250 $^{\circ}\text{C}$ and 350 $^{\circ}\text{C}$, 5 tons of weight for 30 min from different size fractions of powder. Thermal conductivity and the different contributions at (d) 250 $^{\circ}\text{C}$ and (e) 350 $^{\circ}\text{C}$. (f) ZT values for 250 and 350 $^{\circ}\text{C}$ sintering temperatures.

After the evaluation of all the thermoelectric properties, it can be concluded that the p-type Bi_2Te_3 , sintered at 350 °C in a size range 250-106 μm leads to the best thermoelectric performance.

6.2.2 XRD

XRD measurements were performed for both types (n- and p-) of bismuth telluride in the same way as explained in section 4.2. A disc cut from the ingot served as reference in all the comparisons.

- **n-type $\text{Bi}_2\text{Te}_{2.79}\text{Se}_{0.21}$ + I:**

Fig. 6.6 presents the results of the discs sintered at 250 °C (which provided the best thermoelectric properties) at the different particle size ranges. Accordingly to the XRD patterns previously analysed from the non-sintered powders (Fig. A.44), the disc samples are also single-phase ($\text{Bi}_2\text{Te}_{2.79}\text{Se}_{0.21}$), corresponding to a rhombohedral crystal geometry (space group $R\text{-}\bar{3}m$)⁽¹⁹⁶⁾ with no detectable impurities of other phases. It should be noticed that after crushing, separation in the different particle size ranges and sintering, the preferred orientation changed from (110) for the ingot sample to (0015). This was also observed in the powder XRD patterns (Fig. A.44). Thus, there is a reorientation of the grains into this direction perpendicular to the pressing direction. Apart from this, it is significant that when the particle size is reduced, the directions (015) and (1010) become more relevant. Reduction of the particle size seems to favour these orientations. Finally, it can be noted that the XRD peaks become wider as the particle size range is reduced, proving the reduction of the grain sizes⁽⁷⁾.

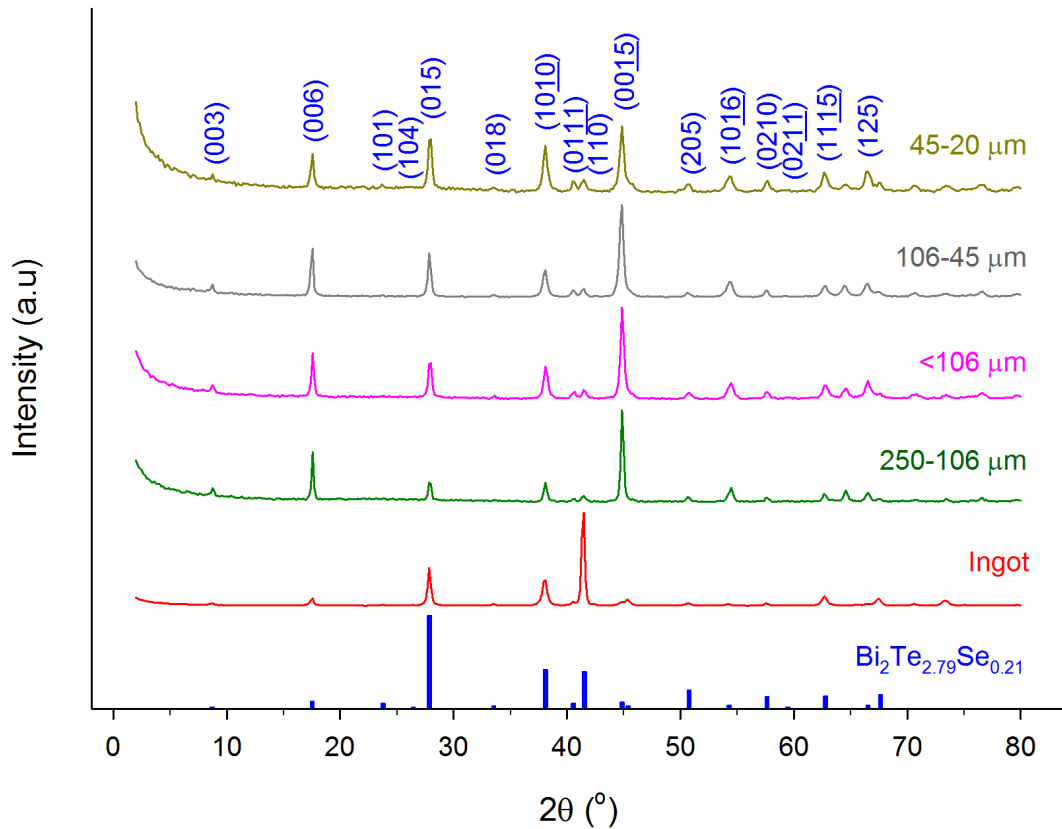


Fig. 6.6. Theoretical XRD pattern of non-treated n-type $\text{Bi}_2\text{Te}_{2.79}\text{Se}_{0.21}$ (blue), ingot sample (red), particle size 250-106 μm (green), particle size <106 μm (pink), particle size 106-45 μm (grey) and particle size 45-20 μm (dark green) discs sintered at 250 $^\circ\text{C}$ for 30 min with 5 tons of weight.

- **p-type $\text{Bi}_{0.5}\text{Te}_3\text{Sb}_{1.5}$:**

In this case, the XRD patterns presented in Fig. 6.7 correspond to the discs sintered at 350 $^\circ\text{C}$. Accordingly to the XRD patterns of the non-sintered powders (Fig. A.45), the compacted disc samples also show a single-phase $\text{Bi}_2\text{Te}_{2.79}\text{Se}_{0.21}$ corresponding to a rhombohedral crystal geometry (space group $R\bar{3}m$)⁽¹⁹⁶⁾ with no detectable impurities of other phases. After crushing, separation into different particle size ranges and sintering into a disc, three different directions became preferred orientations, (015), (1010) and (0015), in all the samples. The preferred orientation for the reference sample was (110).

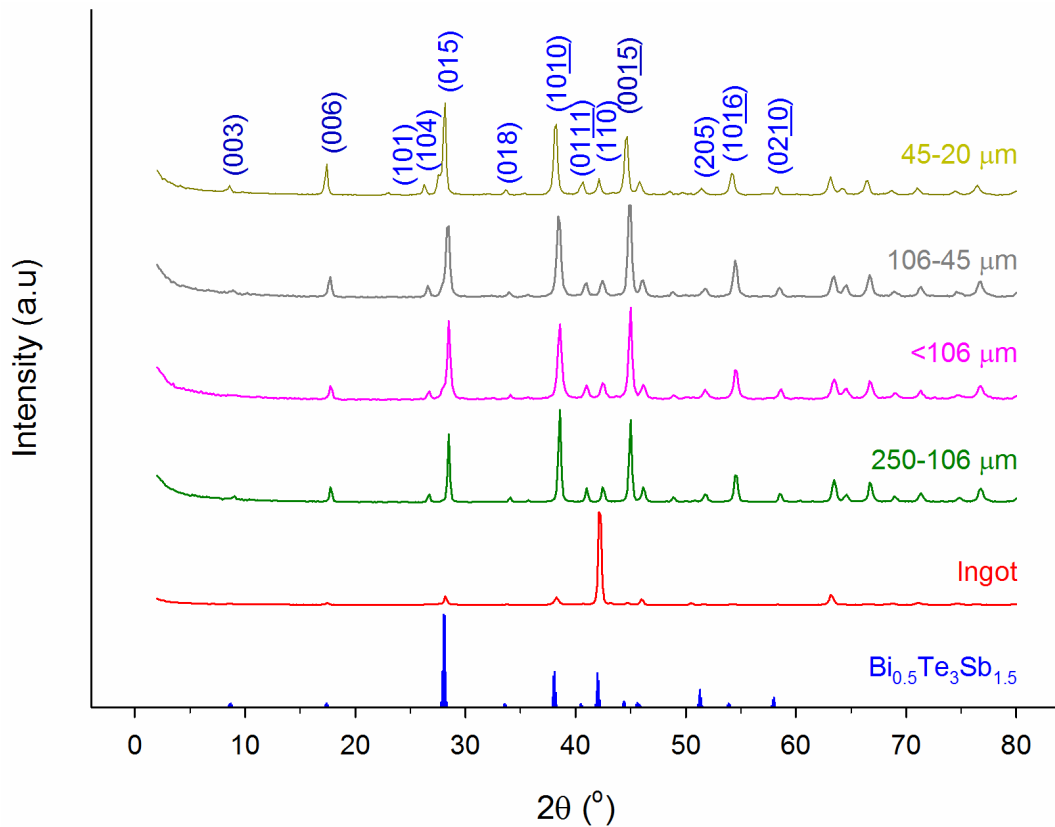


Fig. 6.7. Theoretical XRD pattern of non-treated p-type $\text{Bi}_5\text{Te}_{2.79}\text{Se}_{0.21}$ (blue), reference sample before milling (red), particle size 250-106 μm (green), particle size <106 μm (pink), particle size 106-45 μm (grey) and particle size 45-20 μm (dark green) discs sintered at 350 $^\circ\text{C}$ for 30 min with 5 tons of weight.

6.2.3 Optical microscope

In this section the microstructure of the compacted samples is analysed at the optical microscope (See section 3.3.5) and then is related to the observed thermoelectric properties. Before proceeding to the examination of the discs the microstructure should be revealed by a suitable chemical treatment. For this purpose a solution of hydrochloric acid (25 mL) and iron (III) hexahydrate (8 g) in 100 mL of water, in this way or diluted 1:10 vol. in water, was used. The sample surfaces were treated at different times. Conditions are shown in Table 6.1.

- **n-type $\text{Bi}_2\text{Te}_{2.79}\text{Se}_{0.21}$ + I:**

Table 6.1. Conditions of the stain etching treatment for the n-type non-treated disc samples.

Experiment	Solution	Time (min)
Reference	Diluted 1:10 + Without dilution	25 min + 5 min
250-106 μm	Diluted 1:10 + Without dilution	25 min + 10 min
< 106 μm	Diluted 1:10	35
106-45 μm		25
45-20 μm		

Fig. 6.8 shows the microscope images of the analysed samples. The microstructures of the reference sample show a non-uniform grain size distribution, which are formed mainly of coarse grains ($\approx 70\text{-}15\ \mu\text{m}$) even though there are some smaller sizes (Fig. 6.8 (a)). For the rest of the samples it can be noticed that there are grains that preserved the dimensions of the initial powder and also grains of much smaller size (in the order of few microns). This could be due to the existence of small particles attached to the larger ones, which pass through the sieves. Another possibility is that some particles break down during the hot pressing. It should be remarked that the hot pressing does not produce grains of larger size than the initial particles.

A clear reduction in the grain sizes can be observed between the reference and the prepared samples with the different size ranges (Fig. 6.8). We attribute this feature as responsible for the pronounced decrease in the thermal conductivity (1.4 to $\approx 0.8\ \text{W/Km}$) observed in Fig. 6.2 (a).⁽¹⁰⁾

A decrease in the electrical conductivity was observed with the diminution of the size ranges in Fig. 6.1 (c), which is in agreement with the increase in the density of grain boundaries clearly observed in Fig. 6.8 when the size ranges are reduced. However, no significant reduction in the thermal conductivity was found when the size ranges were reduced in Fig. 6.2 (a), even in the case of the smaller size range where the density of grain boundaries was significantly increased. This could be due to the fact that this further grain size reduction do not significantly influences the scattering of phonons.

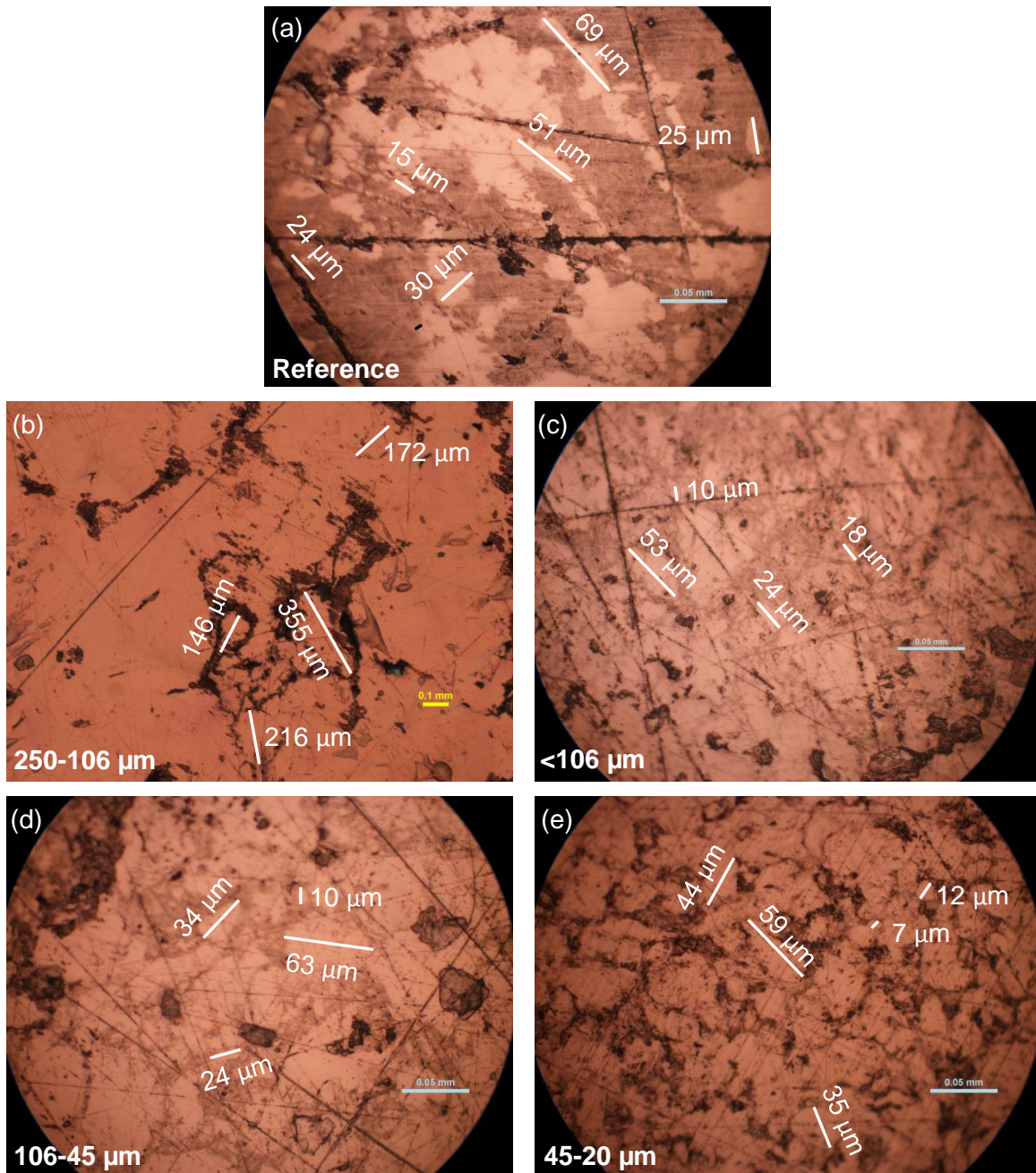


Fig. 6.8. Microscope images of n-type disc samples (a) reference, (b) size 250-106 μm , (c) size < 106 μm , (d) size 106-45 μm and size (e) 45-20 μm .

- **p-type $\text{Bi}_{0.5}\text{Te}_3\text{Sb}_{1.5}$:**

The etching conditions to reveal the microstructure of the p-type samples are shown in Table 6.2.

Table 6.2. Conditions of the stain etching treatment for the non-treated p-type disc samples.

Experiment	Solution	Time (min)
Reference	Diluted 1:10 + Without dilution	25 min + 5 min
250-106 μm	Diluted 1:10	35
< 106 μm		10
106-45 μm		25
45-20 μm	Diluted 1:10 + Without dilution	25 min + 11.5 min

Fig. 6.9 shows the microscope images of the analysed samples. The microstructure of the reference sample shows a non-uniform grain size distribution, and is formed by mainly coarse grains ($\approx 20\text{-}6\ \mu\text{m}$). For the rest of the samples, both grains with a size similar to the powder size ranges and also of a smaller size (few microns) are observed as in the n-type material. Again the hot pressing does not produce grains of larger size than the initial particles.

A clear reduction in the grain sizes can be observed between the reference and the prepared samples with the different size ranges (Fig. 6.9), which is attributed to the significant reduction in the thermal conductivity (1.3 to $\approx 0.7\ \text{W/Km}$) observed in Fig. 6.5 (a).⁽¹⁰⁾ The same behaviour was observed for the n-type above.

As occurred in the n-type, a decrease in the electrical conductivity was observed with the diminution of the size ranges Fig. 6.4 (c), which is in agreement with the increase in the density of grain boundaries clearly observed in Fig. 6.9 when the size ranges are reduced. However, no significant reduction in the thermal conductivity was found again when the size ranges were reduced (Fig. 6.5 (a)).

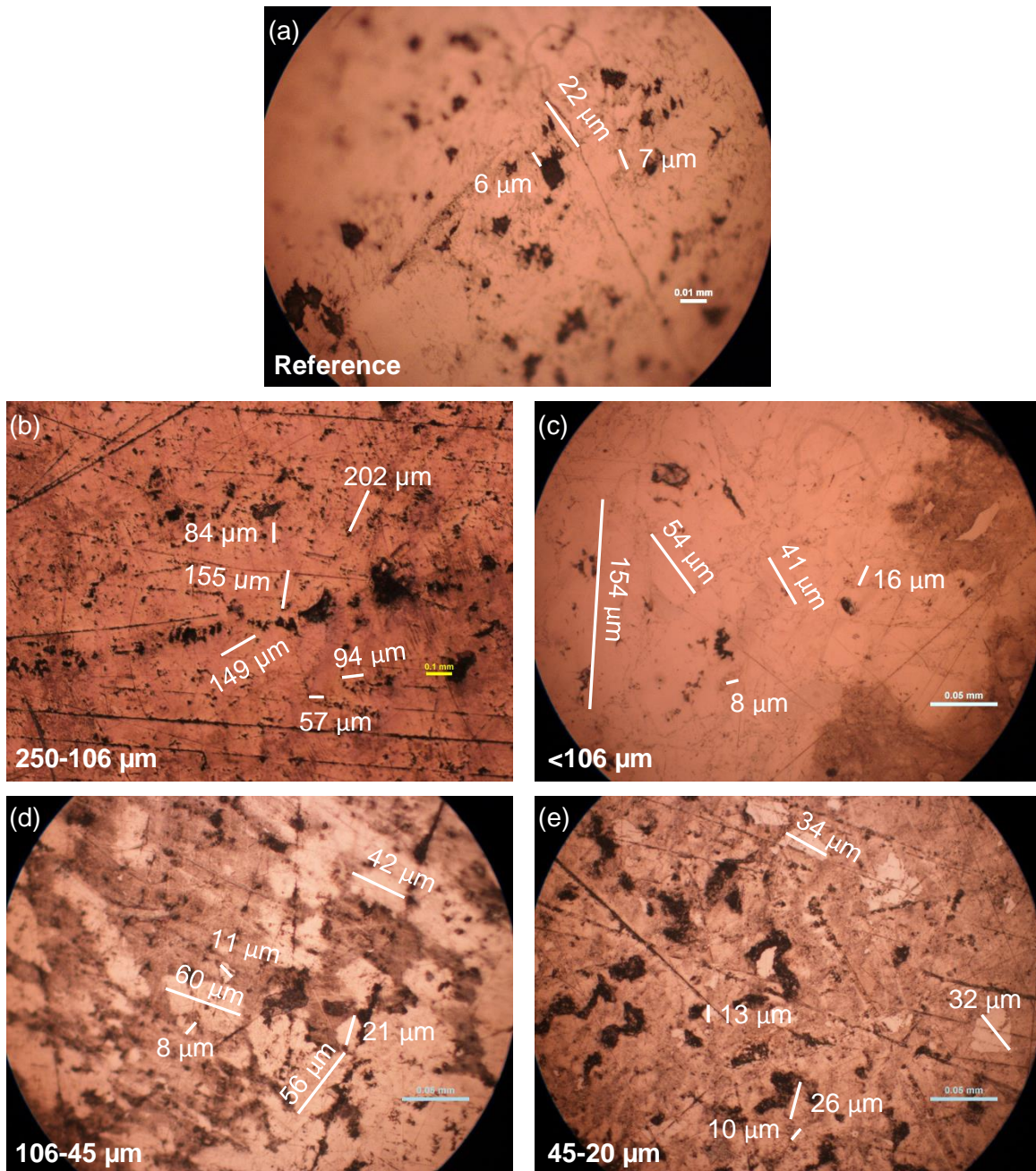


Fig. 6.9. Microscope images of p-type disc samples (a) reference, (b) size 250-106 μm , (c) size <106 μm , (d) size 106-45 μm and size (e) 45-20 μm .

6.3 Characterisation of milled samples

The optimised BM and UM powders from chapter 4 were pressed to form nanobulk samples that are characterised in this section. The same steps and equipment as in the non-treated samples were used.

6.3.1 Thermoelectric properties

Both types of material n- and p-type bismuth telluride were studied for the UM procedure but only the n-type for the BM was analysed and used for comparison between BM and UM methods. It is assumed that the p-type material process by BM will show a similar behaviour to the n-type. For this reason and due to the lower performance of the n-type sample obtained by BM, the p-type sample was not analysed. As performed for the non-treated material in the previous section, the BM powder was separated into different particle size ranges. However, this was not possible for the UM powders due to the high aggregation of the nanoparticles. On the other hand, only one sample for each particle size range of the BM powders was prepared due to the lack of material. For the UM it was possible to prepare the three samples. Accordingly, the values presented in the figures are the average of three samples for UM and only one sample for BM. Based on the optimised process in the previous chapter, the sintering temperature for the n- and p-type materials is different, 250 °C and 350 °C respectively, while the rest of the sintering conditions are equal (5 tons for 30 min under argon atmosphere).

- **n-type $\text{Bi}_2\text{Te}_{2.79}\text{Se}_{0.21}$ + I:**

Density, Seebeck coefficient, in-plane electrical conductivity and power factor values of n-type discs prepared using non-treated, BM and UM powders for different particle size ranges are shown in Fig. 6.10. The original material directly cut from the ingot is also shown as reference. The density of the BM samples (Fig. 6.10 (a)) is $\approx 95\%$ of the original sample cut from the ingot, except for the smallest particle size range (20-10 μm) that presents a significant drop to 6.34 g/cm^3 . This is likely due to the increase of porosity when the particle sizes are considerably reduced. In the case of the UM sample, the density is also reduced ($\approx 89\%$ from the cut sample from ingot), but it is somewhat higher than the sample with the lowest size range from BM. Thus, when comparing powders of similar particle size range, UM method is able to provide higher density samples than the BM process. This could be due to the characteristic higher degree of aggregation in the nanoparticles found in the UM treatment (Fig. 4.14 and Fig. 4.16). On the other hand, when compared the BM results to the non-treated samples, slightly lower densities are observed at the higher size ranges for BM treatment, but they become very similar for smaller size ranges (except the drastic drop at the lowest size range).

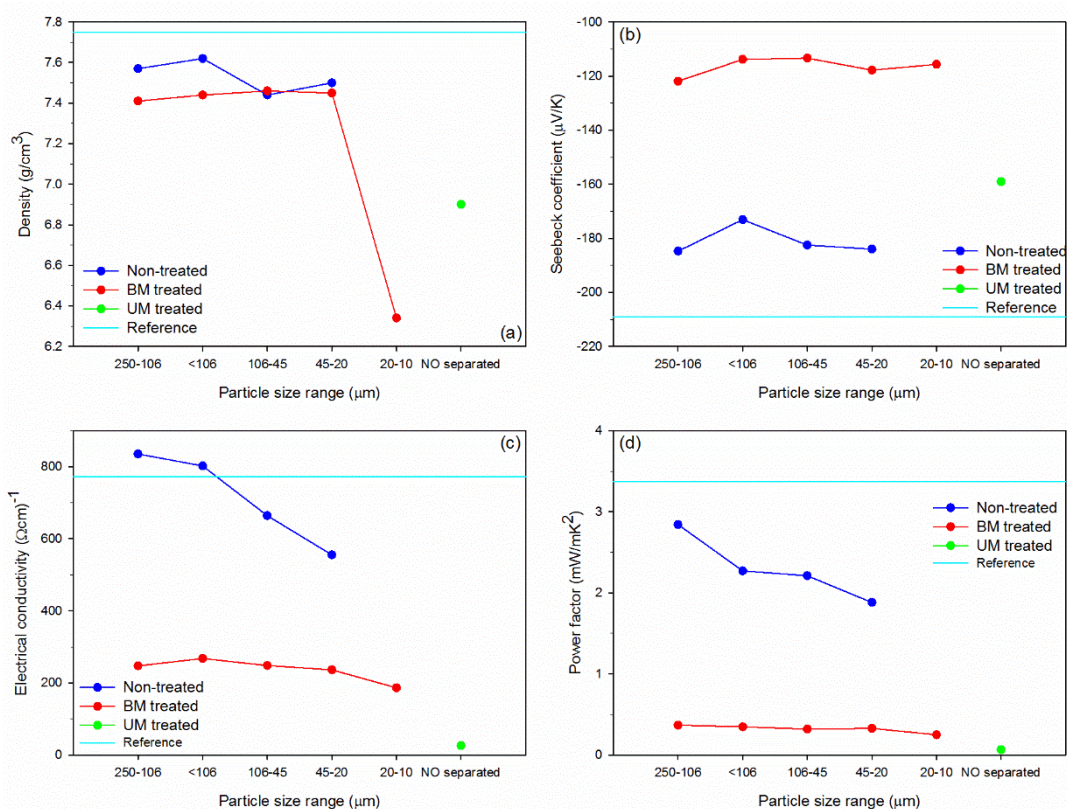


Fig. 6.10. (a) Density, (b) Seebeck coefficient, (c) electrical conductivity and (d) power factor of the n-type non-treated (350 °C) and ball milling and ultrasound milling samples prepared at 250 °C and 5 tons of weight for 30 min (optimum conditions).

Fig. 6.10 (b) shows the Seebeck coefficient results. Both BM and UM samples significantly reduce the absolute Seebeck coefficient value respect to the original ingot material and the non-treated samples. However, a less significant reduction occurs for the UM sample, which clearly provides a better Seebeck coefficient ($\approx -160 \mu\text{V/K}$) than the BM method ($\approx -120 \mu\text{V/K}$ for all the particle size ranges), as occurred with the density

The in-plane electrical conductivity results are shown in Fig. 6.10 (c). This parameter is significantly affected by the BM and UM processes, being much smaller the UM result ($26 (\Omega\text{cm})^{-1}$), as expected due to the increase in the density of grain boundaries.⁽²⁰⁶⁾ The non-treated samples provide the best values ($580\text{--}820 (\Omega\text{cm})^{-1}$). It should be noticed that the BM samples exhibit a less pronounced decrease with the size ranges than the non-treated case.

Due to the trends observed in the Seebeck coefficient and in-plane electrical conductivity values, the power factor of the samples treated by UM and BM is much lower than the non-treated samples (Fig. 6.10 (d)). The smallest power factor is observed for the UM material, mainly due to the severe decrease in the electrical conductivity.

Cross-plane thermal conductivity and its electrical and lattice contributions are shown in Fig. 6.11 (a-c). The lowest thermal conductivity value is presented for the UM sample (0.51 W/Km), which is significantly lower than the BM and non-treated samples. This

remarkably low value of the thermal conductivity is close to the lowest reported in the literature for a bismuth telluride compacted sample.^(207, 208) The cross-plane thermal conductivity of the BM samples lie in the same range as the non-treated samples. Thus, this method is not able to produce a significant additional reduction of the thermal conductivity to that already achieved in the pre-treatment (non-treated samples). On the other hand, the behaviour with the size ranges of the BM samples is somewhat random and do not display a clear trend.

It can be seen from Fig. 6.11 (c) that the main contribution to the cross-plane total thermal conductivity comes from the lattice in the BM and UM samples. The electrical contribution is significantly reduced by both methods, with a more intense decrease for UM. As remarked before, careful consideration should be taken here due to directionality issues. In the BM samples, it should be mentioned that there was no possibility to measure the thermal conductivity of the sample with size range 250-106 μm , since the sample broke before that.

Despite the low thermal conductivity values, both BM and UM samples show quite low ZT values compared to the reference and non-treated materials (Fig. 6.11 (d)). These low values are mainly attributed to the drastic decrease of the electrical conductivity and also the reduction of the Seebeck coefficient. Again, directionality issues should be taken into consideration.

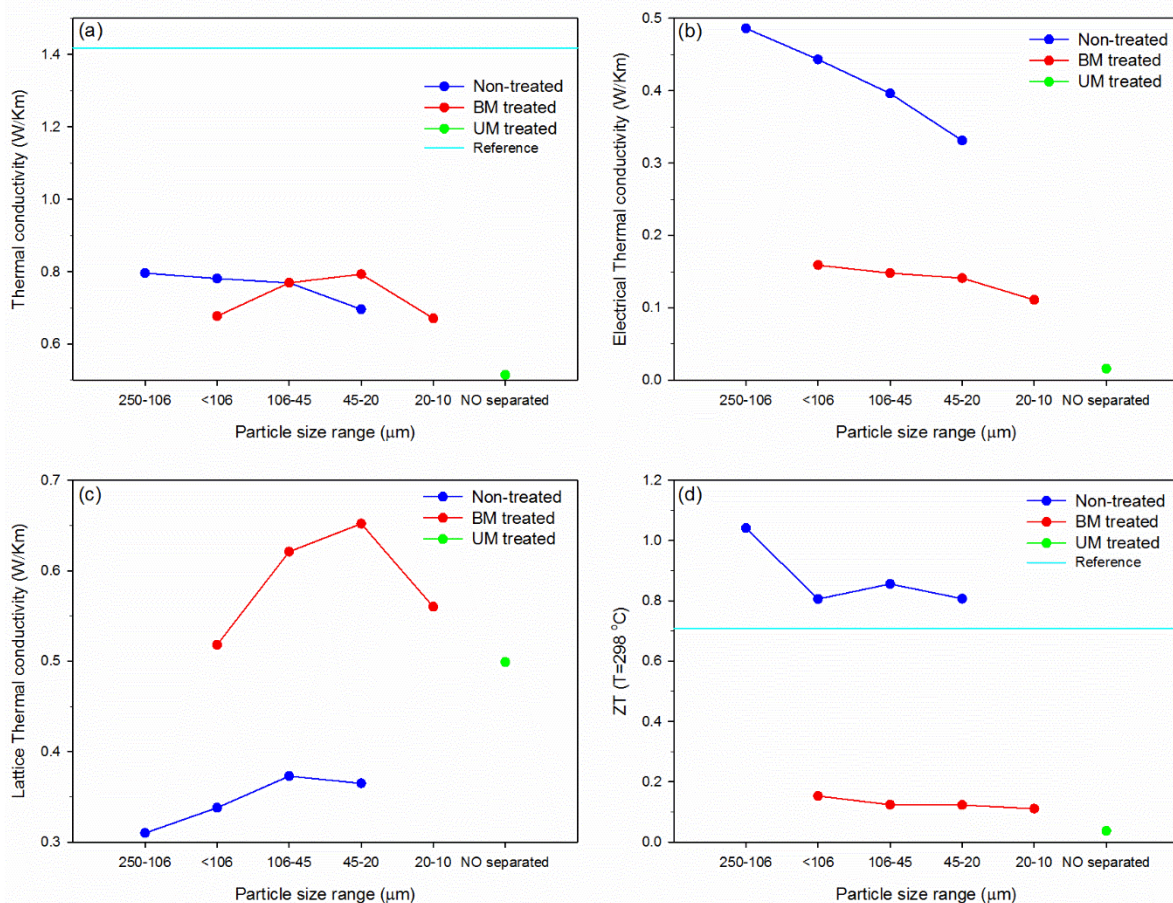


Fig. 6.11. (a) Thermal conductivity, (b) electrical thermal conductivity, (c) lattice thermal conductivity and (d) ZT of the n-type non-treated (350 °C), BM and UM samples prepared at 250 °C and 5 tons of weight for 30 min (optimum conditions).

- **p-type $\text{Bi}_{0.5}\text{Te}_3\text{Sb}_{1.5}$:**

Density, Seebeck coefficient, in-plane electrical conductivity and power factor values of p-type discs prepared using non-treated (350 °C sintering) and UM powders for different particle size ranges are shown in Fig. 6.12 compared to the reference. As in the n-type material, the UM sample present lower density ($\approx 85\%$ of the sample cut from the ingot) than the non-treated materials (see Fig. 6.12 (a)).

The Seebeck coefficient value for the UM sample ($177.03\ \mu\text{V/K}$) is almost $40\ \mu\text{V/K}$ lower than the reference and non-treated samples (Fig. 6.12 (b)). This result is similar to the n-type, although slightly higher. The electrical conductivity of the UM sample (Fig. 6.12 (c)) shows a significant decrease ($\approx 36\ (\Omega\text{cm})^{-1}$) as in the n-type material. As a result of the Seebeck coefficient and electrical conductivity values, the power factor of the UM sample is much lower ($\approx 0.1\ \text{mW/mK}^2$) than the non-treated samples ($\approx 2.4\text{-}3.7\ \text{mW/mK}^2$) and the reference. The main factor responsible for this reduction is the electrical conductivity.

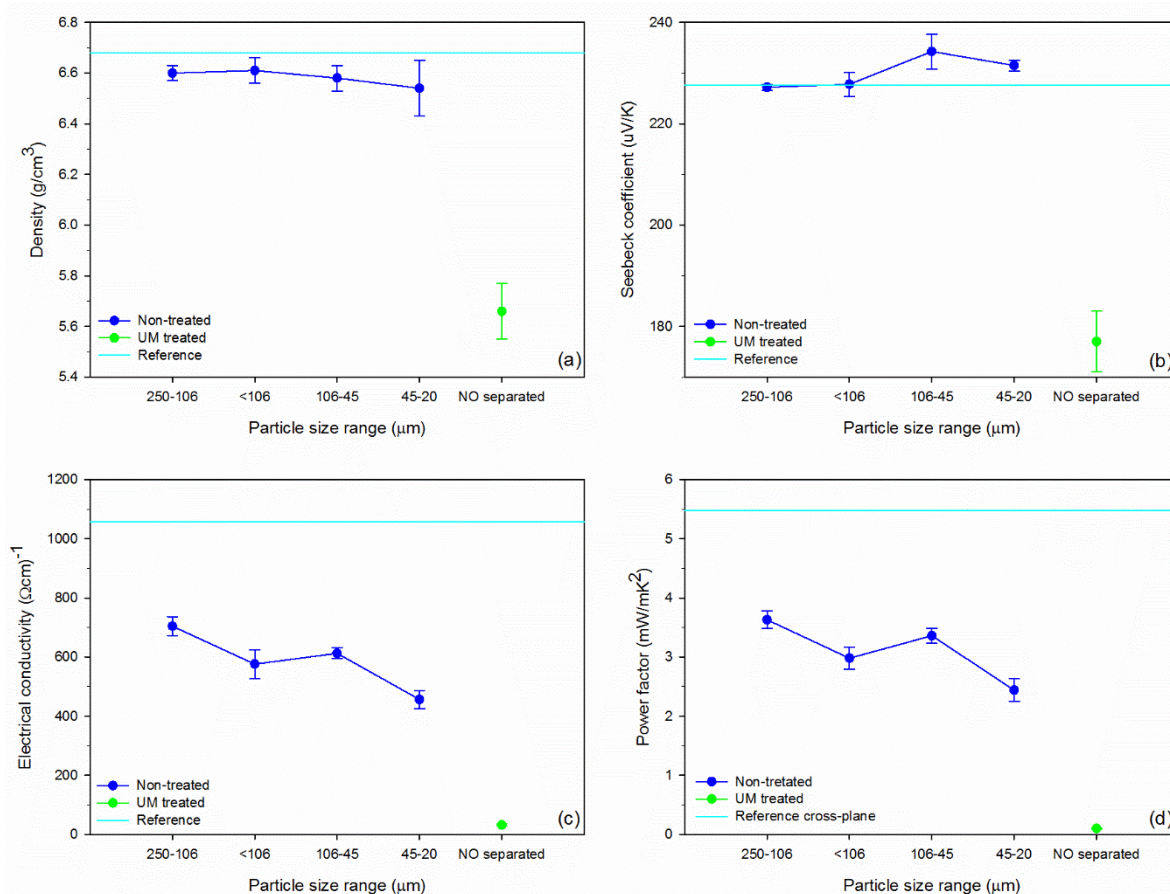


Fig. 6.12. (a) Density, (b) Seebeck coefficient, (c) electrical thermal conductivity and (d) power factor, of p-type non-treated, UM and reference samples prepared at 350 °C and 5 tons of weight for 30 min.

The cross-plane thermal conductivity values and electrical and lattice contributions are shown in Fig. 6.13 (a-c). A very low value (0.34 W/Km) was obtained for the UM sample, even significantly lower than for the n-type material (0.51 W/Km). This value is nearly similar to the smallest value reported for a bismuth telluride compacted sample⁽²⁰⁷⁾ and it is also close to the lowest thermal conductivity results in any non-polymer thermoelectric material.^(122, 209, 210) From Fig. 6.13 (b) it can be seen that the electrical contribution is nearly suppressed (0.019 W/Km). As mentioned before, consideration should be taken due to directionality differences between the measuring methods.

As for the n-type the ZT value of the UM sample is much lower (0.086) than the non-treated materials despite the ultra-low thermal conductivity result. The main limitation to the ZT is due to the severe reduction in the electrical conductivity.

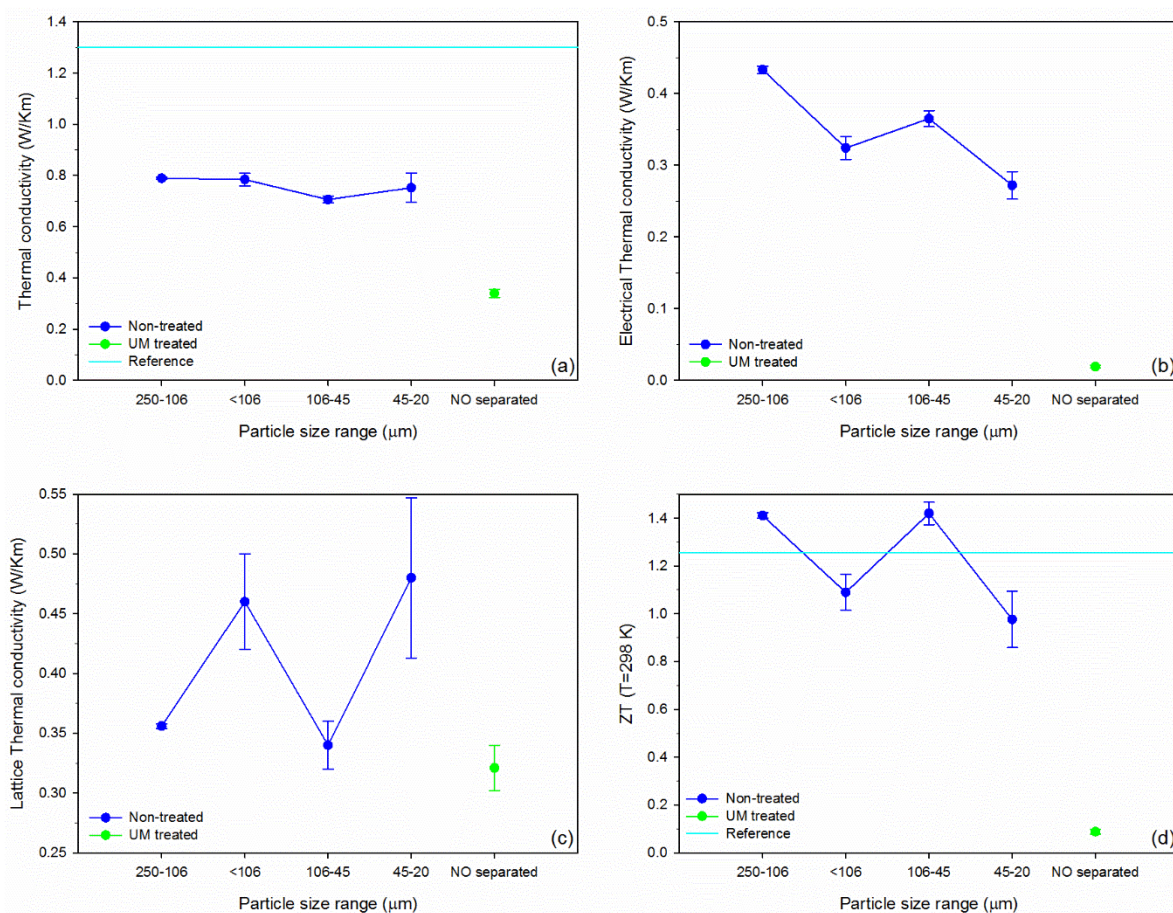


Fig. 6.13. a) Thermal conductivity, (b) electrical thermal conductivity, (c) lattice thermal conductivity and (d) ZT of p-type non-treated and UM samples prepared at 350 °C and 5 tons of weight for 30 min.

6.3.2 XRD

- **n-type $\text{Bi}_2\text{Te}_{2.79}\text{Se}_{0.21} + \text{I}$:**

Fig. 6.14 shows the XRD patterns of the discs sintered at 250 °C from the powders obtained from the BM and UM treatments and the reference sample cut from the ingot. For the BM material the discs prepared employing different particle size ranges are also included. Peak intensity was normalised in all the samples.

As in the XRD patterns obtained from the powders before sintering, all the diffraction peaks of the compacted samples were also assigned to a single-phase $\text{Bi}_2\text{Te}_{2.79}\text{Se}_{0.21}$ rhombohedral structure (space group $R\bar{3}m$),⁽¹⁹⁶⁾ with no detectable impurities of other phases. Three intense diffraction peaks, which are the same as the theoretical n-type Bi_2Te_3 pattern, for all the BM samples are present in the (015), (1010) and (110) directions. In the reference the priority direction is (110). In the case of the UM sample, apart from the main direction (015), other two directions ((1010) and (0015)) became more important. This means that a reorientation of grains in these directions occurred in

the UM sample, which is more accentuated than in the BM samples. These results are in agreement with the optimised BM (Fig. 4.7) and UM (Fig. 4.19) powder samples, which show the same priority directions (015), (10 $\bar{1}$ 0) and (110), although in the UM powder the directions (10 $\bar{1}$ 0) and (00 $\bar{1}$ 5) are not as intense as in the disc.

On the other hand, the peaks of the treated samples are wider than the reference, indicating a reduction in the grain size⁽⁷⁾ (more polycrystalline samples). This is in agreement with the SEM results that showed the reduction in the particle size by both BM (Fig. 4.5) and UM (Fig. 4.14) treatments.

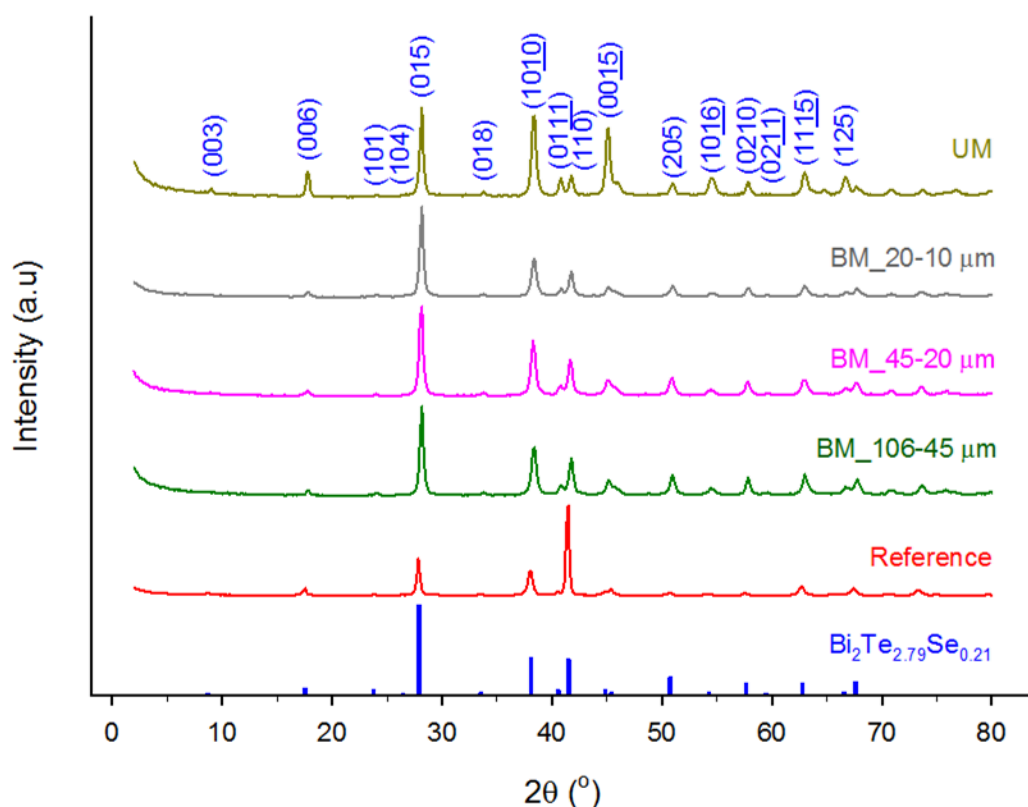


Fig. 6.14. XRD patterns of n-type $\text{Bi}_{0.5}\text{Te}_3\text{Sb}_{1.5}$ (blue), non-treated reference (red), after ball milling treatment with particle size 106-45 μm (green), 45-20 μm (pink), 20-10 μm (grey) and after ultrasound milling treatment (dark green).

- **p-type $\text{Bi}_{0.5}\text{Te}_3\text{Sb}_{1.5}$:**

The p-type XRD patterns for the UM material sintered at 350 °C and the reference sample cut from the ingot are shown in Fig. 6.15. The peak intensity was normalised in all the samples. As previously, all the XRD patterns present a single-phase $\text{Bi}_2\text{Te}_{2.79}\text{Se}_{0.21}$ corresponding to a rhombohedral crystal geometry (space group $R\bar{3}m$)⁽¹⁹⁶⁾ with no detectable impurities of other phases. The UM sample presents the same priority direction (015) than the theoretical pattern, with one more direction important (10 $\bar{1}$ 0).

These results are in agreement with the optimised UM powder sample (Fig. 4.20), which shows the same priority direction (015) than the disc.

On the other hand, the peaks of the UM sample are broader than the reference, indicating a finer grain-size particle⁽⁷⁾ (more polycrystalline). This is in agreement with the SEM images from the optimised UM powder sample (see Fig. 4.17).

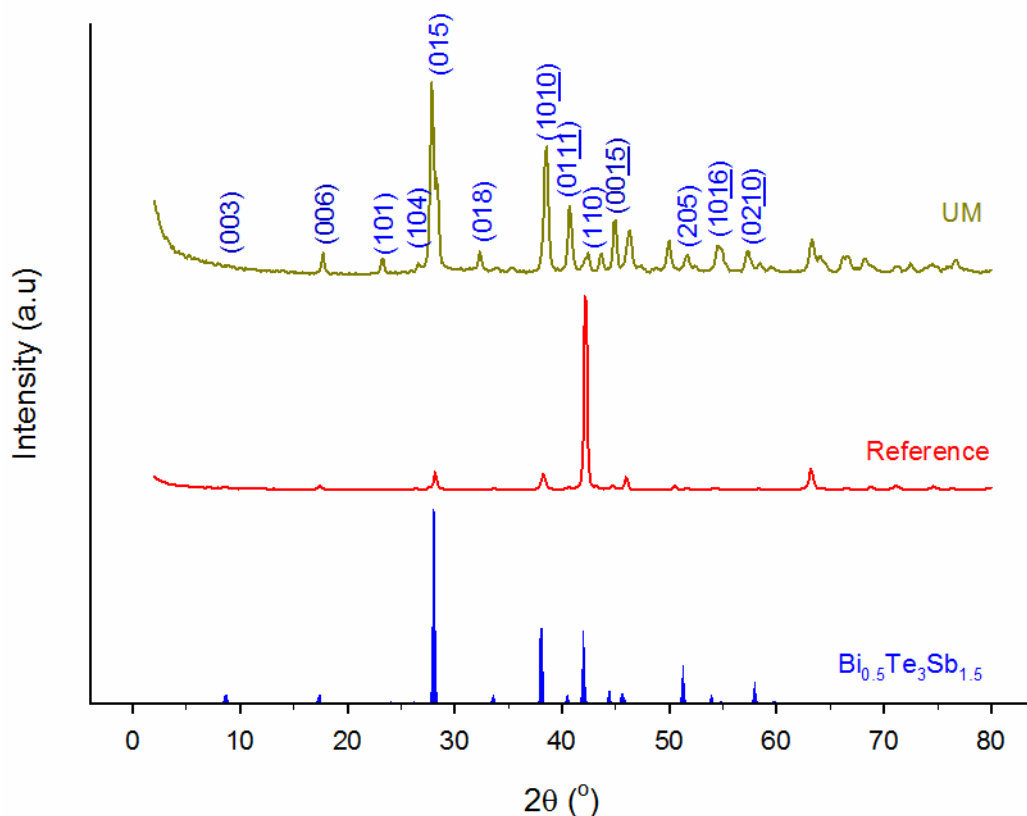


Fig. 6.15. XRD patterns of p-type $\text{Bi}_{0.5}\text{Te}_3\text{Sb}_{1.5}$ (blue), reference cut from the ingot (red) and after ultrasound milling experiment (dark green).

6.3.3 Optical microscope

- **BM_n-type $\text{Bi}_2\text{Te}_{2.79}\text{Se}_{0.21}$ + I:**

The process to reveal the microstructure of the samples, stain etching, of the samples treated by BM are described in Table 6.3.

Table 6.3. Conditions of the stain etching treatment for the n-type samples treated by BM.

Sample	Solution	Time (min)
BM_106-45 μm	Diluted 1:10 + Without dilution	25 min + 10 min
BM_45-20 μm		
BM_20-10 μm		

The microstructure of all the samples treated by BM process is shown in Fig. 6.16. It can be observed that the grains of the samples preserve the dimensions of the starting powder and also show some finer grains (in the range of few μm). As previously, the presence of these small grains may be due to the fact they can be attached to the larger grains or break down during the hot pressing. The BM samples (Fig. 6.16) present more uniform grain size distribution than the non-treated materials (Fig. 6.8 (c-f)).

A clear reduction in the grain sizes can be observed between the reference (Fig. 6.8 (a-b)) and the BM samples with the different size ranges Fig. 6.16. Although similar sizes are presented in the non-treated (Fig. 6.8) and BM samples (Fig. 6.16), the thermal conductivity of the former shows a reduction with the smaller sizes while the BM samples do not follow any trend (Fig. 6.11 (a)).

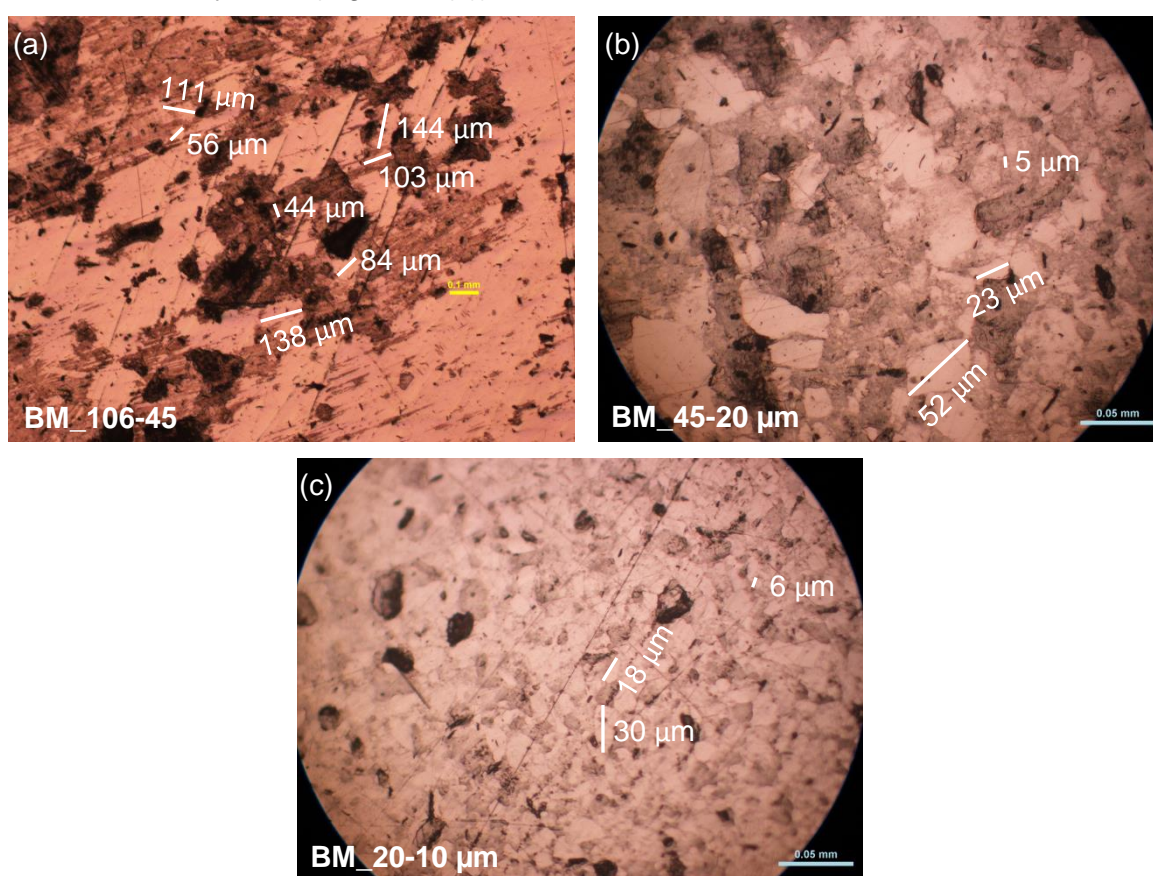


Fig. 6.16. Microscope images of n-type disc samples treated by ball milling using the optimum conditions and separated in different size ranges (a) 106-45 μm , (b) 45-20 μm and (c) 20-10 μm .

An intense decrease in the electrical conductivity was observed for all the samples after the BM but no significant differences are shown with the diminution of the size ranges (Fig. 6.10 (c)). This reduction in the electrical conductivity is attributed to the increase in the density of grain boundaries, clearly observed in Fig. 6.10 when the size ranges are reduced. The fact that in BM materials the electrical conductivity is

significantly lower than the non-treated samples (Fig. 6.10 (c)) could be due to possible oxidation reactions experienced during the milling process.

- **UM:**

The stain etching conditions (Table 6.4) to observe the microstructure of samples treated by UM process in the microscope are shown in Fig. 6.17.

Table 6.4. Conditions of the stain etching treatment for the n- and p-type samples treated by UM.

Sample	Solution	Time (min)
UM_n-type	Diluted 1:10	5 min
UM_p-type		

Fig. 6.17 shows the microstructure of all the samples treated by UM process. The grains of the UM samples present a rounder shape than the samples treated by the BM method (Fig. 6.16). Many of them are also smaller, although larger grains are also present. However, by looking at the largest magnifications (Fig. 6.17 (b and d)), it can be seen that the large grains are actually formed by very fine grains, which provide a kind of granular texture, more significant in the p-type material (Fig. 6.17 (d)). The large reduction observed in the thermal and electrical conductivities in the UM samples (Fig. 6.11 (a) and Fig. 6.10 (c) for the n-type and Fig. 6.13 (a) and Fig. 6.12 (c) for the p-type) can be attributed to this granular texture, which effectively scatters the electrons and achieve a drastic reduction in the electronic thermal conductivity (Fig. 6.11 (b) and Fig. 6.13 (b) for n- and p-type respectively).

This granular texture, originated from the agglomerates identified in the UM powders (Fig. 4.14 and Fig. 4.17 for n- and p-type respectively) is not produced in the BM method and it is a unique feature of the UM process, which provides the capability to achieve ultra-low thermal conductivity values, although significantly lowering the electrical conductivity. The existence of nano-grains can be deduced from the largest magnification images (larger magnifications were not possible due to equipment limitations) and apparently the nanoparticles of the powders are maintained when they are pressed into discs.

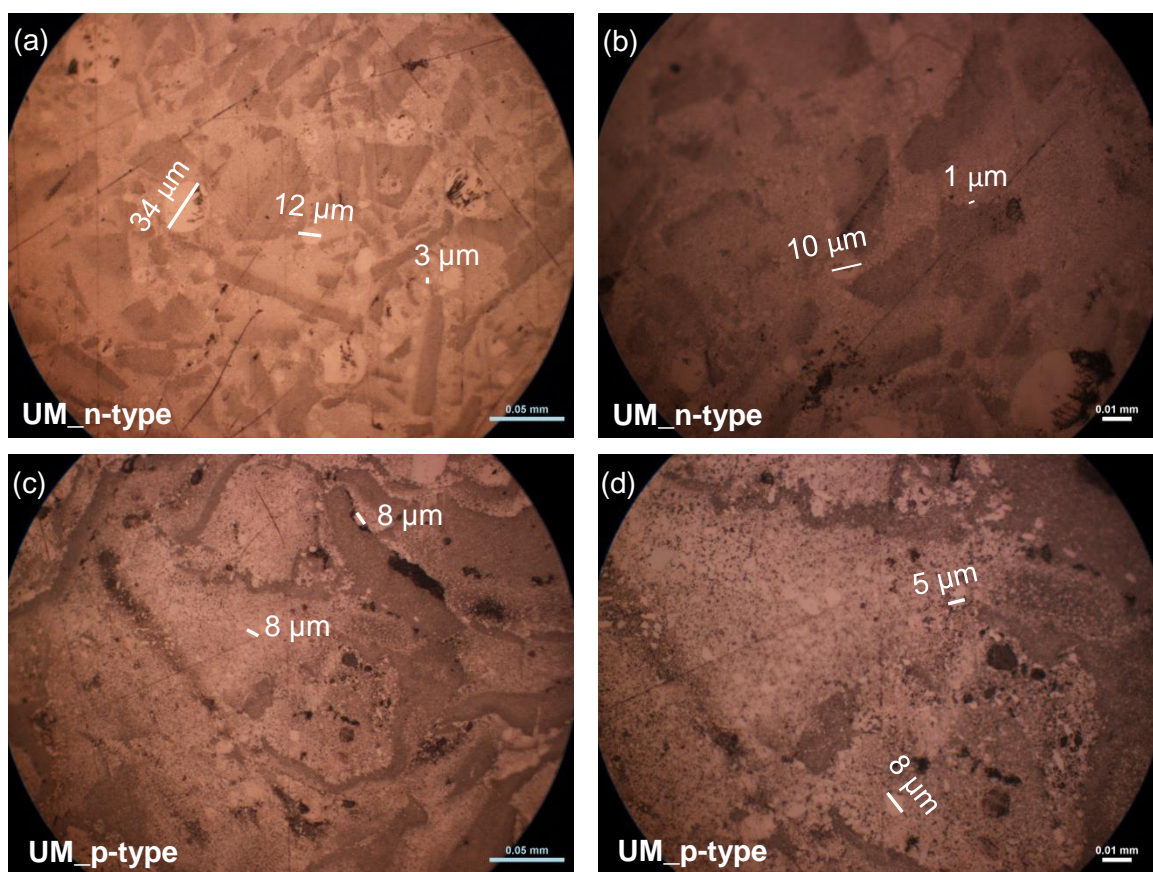


Fig. 6.17. Microscope images of n- (a-b) and p-type (c-d) disc samples treated by ultrasound milling.

6.4 Conclusions

The thermoelectric, structural and morphological characterisation of bismuth telluride discs prepared from a very simple crushing pre-treatment (non-treated samples), BM and UM powders, were performed in this chapter for both n-type and p-type materials (except for the BM where only the n-type was analysed). For non-treated and BM powders, a separation into different particle size fractions was performed before compaction.

For the non-treated samples the absolute value of the Seebeck coefficient is reduced with respect to the ingot reference sample in the case of the n-type material, and slightly improved in the p-type counterpart. The in-plane electrical conductivity is higher than the reference for the n-type samples at the larger particle size ranges, but lower when size is reduced. For the p-type all the samples significantly reduced (around 50 %) their electrical conductivity and also a decrease of this parameter with the particle size ranges was observed. A remarkable reduction of the cross-plane thermal conductivity in both n- and p-type samples respect to the ingot was achieved. The lowest values achieved for the n- and p-type materials were 0.70 and 0.52 W/Km, respectively. The latter is lower than state-of-

the-art bismuth telluride materials. The highest ZT obtained for the n-type material was 1.04, significantly higher than the reference. For the p-type material the highest ZT value was 1.42, close to state-of-the-art bismuth telluride materials and higher than for the best bismuth telluride samples prepared by ball milling method. However, these should be considered carefully due to possible anisotropy in the samples.

For the nanostructured bulk materials prepared by UM method the absolute value of the Seebeck coefficient was reduced with respect to the reference for both n- and p-type samples, but this reduction was less significant than for the samples obtained by BM. The in-plane electrical conductivity was drastically reduced by the UM process, reaching values of 26 and 36 (Ωcm)⁻¹ for the n- and p-type samples, respectively. Although samples treated by BM also significantly reduced their electrical conductivity, it was not so pronounced as in the UM method. The cross-plane thermal conductivity presented remarkably low results (0.51 and 0.34 W/Km for the n- and p-type samples, respectively) for UM samples, which are lower than in state-of-the-art bismuth telluride materials. Moreover, the value for the p-type sample is similar to the lowest reported in the literature and close to the lowest found for non-polymer thermoelectric materials. The microstructure analysis revealed that a unique feature in the UM samples is the presence of very fine grains, which provide a granular texture, more significantly in the p-type material. Despite the ultra-low thermal conductivity values achieved, UM samples show quite low ZT values compared to the reference and BM materials, mainly attributed to the drastic decrease of the electrical conductivity.

The BM materials presented higher values of cross-plane thermal conductivity than UM samples and similar to the ones obtained from the samples prepared by the simple crushing pre-treatment. Their ZT values lie around 0.1, higher than UM but much lower than the reference and the samples obtained with the pre-treatment.

As a novel technique for the fabrication of nanostructured bismuth telluride materials, UM provides better results than BM for the Seebeck coefficient and especially the thermal conductivity. However, the method drastically reduces the electrical conductivity and due to this there is no overall gain in the ZT. If the electrical conduction could be improved, it could represent a promising method for nanostructuring bulk thermoelectric materials.

Chapter 7 : Thermoelectric Modules Fabrication

- 7.1 Introduction
- 7.2 Module fabrication procedure
- 7.3 Module characterisation
- 7.4 Conclusions

Chapter 7

7.1 Introduction

This chapter includes the fabrication and characterisation of thermoelectric modules fabricated employing the materials characterised in the previous chapter. The main objective is to demonstrate the integration of the materials into a device and the enhancement in the performance when the optimised materials fabricated in this thesis are used.

The fabrication procedure is first described in the next section. Then, the modules fabricated employing the original (ingot) and optimised materials, are characterised by the module ZT using impedance spectroscopy. Finally the main conclusions are made.

7.2 Module fabrication procedure

Thermoelectric modules consisting of nine couples of $\text{Bi}_2\text{Te}_{2.79}\text{Se}_{0.21}$ n-type and $\text{Bi}_{0.5}\text{Te}_3\text{Sb}_{1.5}$ p-type thermoelements, from the original ingots (used as a reference) and optimised nanobulk discs were fabricated. The sides of the discs that are going to join the Cu strips on the ceramic plates were metallised using a nickel plating pen (Hunter Products Inc., see Fig. 7.1. (a)). Then, the metallised disc (goldish colour) was fixed onto a plate using wax (Aquabond 65, Importe) to be diced. Each dice was cut with a cross sectional area of 1.7 mm x 1.7 mm using a Struers Accutum-100 cutter (Fig. 7.1. (a)). Then, the wax was removed using a hot solution (100 °C) of 2 g of Aquaclean900 in tap water (200 mL).

A next step consists in the preparation of the substrates (Fig. 7.1. (b)). They are 16 mm x 13 mm alumina plates with attached Cu strips (2 mm x 5 mm with a 0.15 mm thickness) provided by European Thermodynamics Ltd. The Cu strips were covered by soldering flux paste purchased from RS. Onto the Cu strips, a solder material (Sn/Pb, 60/40 with a melting point of 188 °C) previously cut to a similar cross-sectional area to the thermoelements was attached (Fig. 7.1. (b)). The solder material was then covered with the same soldering flux paste. Apart from the conventional Sn/Pb solder, a solder paste was

also employed in some cases ($\text{Sn}_{42}\text{Bi}_{58}$ with lowest melting point=138 °C). This paste does not require the use of flux.

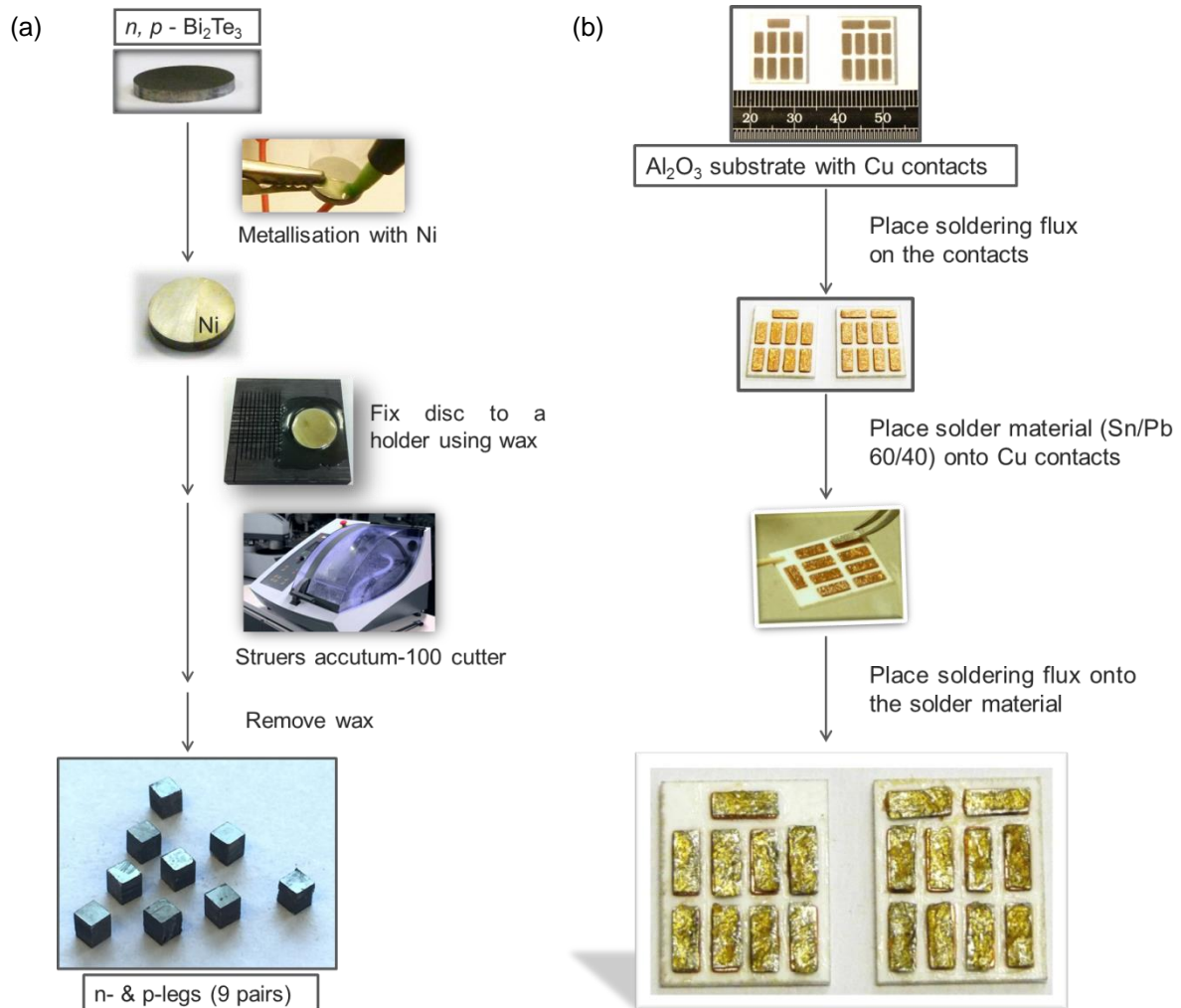


Fig. 7.1. Schemes of (a) material and (b) substrate preparation for the thermoelectric module fabrication.

Once the legs were cut and the substrates ready with the soldering flux and the soldering material, the next step is the assembly of all the parts (Fig. 7.2). Firstly, all the elements of the assembly kit were sprayed with graphite spray to prevent the solder to join to the components of the assembly kit. Then, all the kit elements were placed in the assembly forming a grid where the n- and p- legs were alternatively positioned in the grid gaps. A thick lid is placed onto the assembled module to provide some pressure to the assembly (see Fig. 7.2). Once assembled, the set up was placed into a quartz tube furnace under argon atmosphere for soldering. The soldering conditions are optimised in the next section. After the soldering process, the set up was removed from the interior of the furnace and cooled down to room temperature under Ar atmosphere. Then, the assembly kit was carefully extracted and the kit elements removed until the fabricated module is obtained.

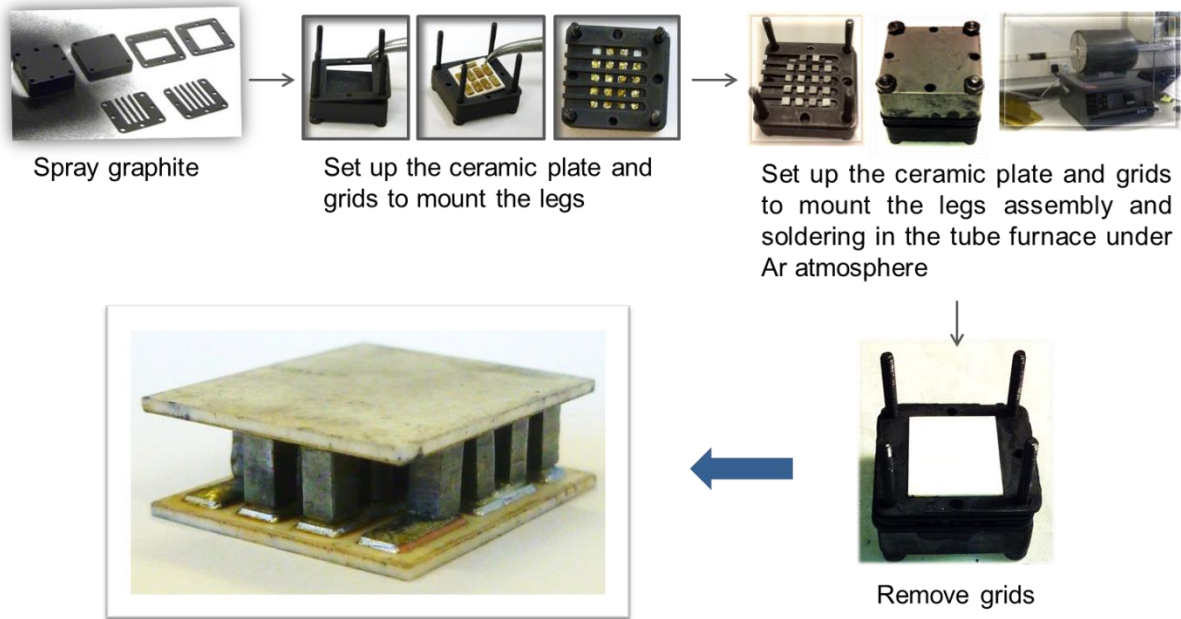


Fig. 7.2. Scheme of the assembly process for the module fabrication.

7.3 Module characterisation

Several modules were prepared utilising the original ingot materials (used as reference) and the n- and p-type materials with the best performance from chapter 6 (size range 250-106 μm for both n- and p-type non-treated materials). The length of the legs corresponds to the thickness of the disc (cross-plane operation). These modules were characterised by impedance spectroscopy. This technique can be considered as an advanced Harman method and is able to determine the module ZT .⁽¹⁹⁴⁾ The characteristic impedance response of a thermoelectric module is shown in Fig. 3.15.⁽¹⁹⁴⁾

The module ZT value can be calculated by $(ZT)_{\text{module}} = \frac{R_{TE}}{R_{\Omega}}$, as described in section 3.4.5, with R_{TE} the thermoelectric resistance, given by the difference between the high and low frequency intercepts with the real impedance axis (Fig. 3.15). R_{Ω} is the total ohmic resistance of the device and it is given by the high frequency intercept.

For the optimisation of the soldering conditions the $(ZT)_{\text{module}}$ value was used as guidance. The temperature (read at the furnace display) and treatment duration were the soldering conditions evaluated. The use of the $\text{Sn}_{42}\text{Bi}_{58}$ solder paste was also explored.

In an initial step, different modules were fabricated employing the reference material (n- and p-type bismuth telluride directly cut from the ingot). The conditions and the $(ZT)_{\text{module}}$ values obtained for each module are shown in Table 7.1.

Table 7.1. Experimental conditions, total ohmic resistance, leg length and $(ZT)_{\text{module}}$ results for different modules prepared with original ingot materials.

Experiment	Temperature (°C)	Time (min)	R_{Ω} (Ω)	Length (mm)	Solder material	$(ZT)_{\text{module}}$
A	370	30	0.08	2.00	Sn/Pb 60/40	0.47
B		20	0.26	1.62		0.27
C		15	0.53	2.00		0.29
D	400	10	0.56	1.92		0.13
E	340	10	0.34	1.92	Sn ₄₂ Bi ₅₈ paste	0.29

In experiments A, B and C the soldering temperature was fixed and different times evaluated for the Sn/Pb solder. The increase of the ohmic resistance when the soldering time was reduced indicates a higher contact resistance contribution (poor soldering). The highest $(ZT)_{\text{module}}$ was 0.47 and the lowest ohmic resistance 0.08 Ω , both obtained for module A. When the temperature was increased and the time shortened the module performance was degraded, providing the lowest $(ZT)_{\text{module}}$ value (0.13) and highest ohmic resistance (0.56 Ω). The use of the soldering paste did not enhance the performance and the conditions of module A are considered as optimum.

In a second step the best performing bismuth telluride materials identified in the previous chapter (non-treated n- and p-type discs with a size range 250-106 μm) were employed to fabricate modules under the optimised conditions. The results are shown in Table 7.2. It should be mentioned that module F burnt (Fig. 7.3. (a)) after the soldering treatment, so the soldering time was reduced in the next experiments to 25 min, where shinier joints were observed (see Fig. 7.3. (b)).

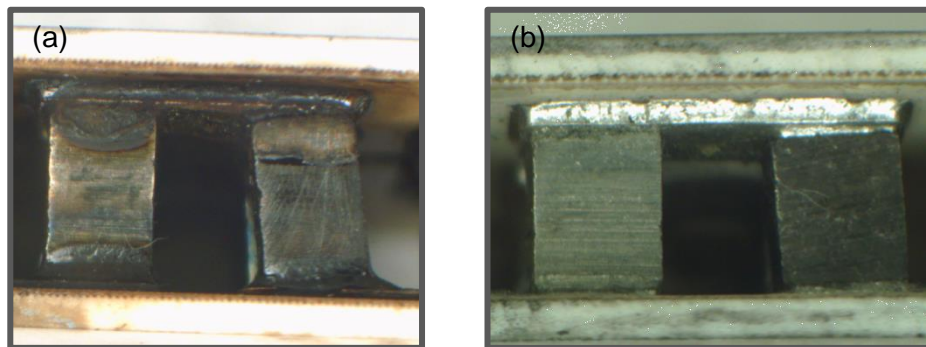


Fig. 7.3. (a) Burnt and (b) shiny joints in the fabricated modules after soldering treatment for 30 and 25 min, respectively.

Table 7.2. Experimental conditions, total ohmic resistance, leg length and $(ZT)_{\text{module}}$ results for the modules prepared using materials prepared from powders with particle size (250-106 μm).

Experiment	Temperature ($^{\circ}\text{C}$)	Time (min)	R_{Ω} (Ω)	Length (mm)	$(ZT)_{\text{module}}$
F	370	30	0.89	2.49	0.23
G		25	0.87	2.97	0.27
H			0.44	1.89	0.35
I			0.48	1.88	0.26

The highest $(ZT)_{\text{module}}$ obtained corresponds to 0.35 for module H, which also shows the lowest total ohmic resistance. Unexpectedly, this value is lower than for the best module fabricated with the ingot materials (0.47). The explanation to this behaviour is not very clear. A possible reason is a higher contact resistance for module H (non-treated material), since its ohmic resistance is significantly higher (0.44 Ω) than in module A (0.08 Ω , ingot sample). In addition, it could be due to the electrical conductivity results obtained when the materials were characterised in the previous chapter. The equipment employed for this is not able to determine independently the cross-plane electrical conductivity, which is the direction evaluated in the $(ZT)_{\text{module}}$.

In Fig. 7.4 the impedance results of the modules with the largest $(ZT)_{\text{module}}$ from both the reference and prepared materials are shown.

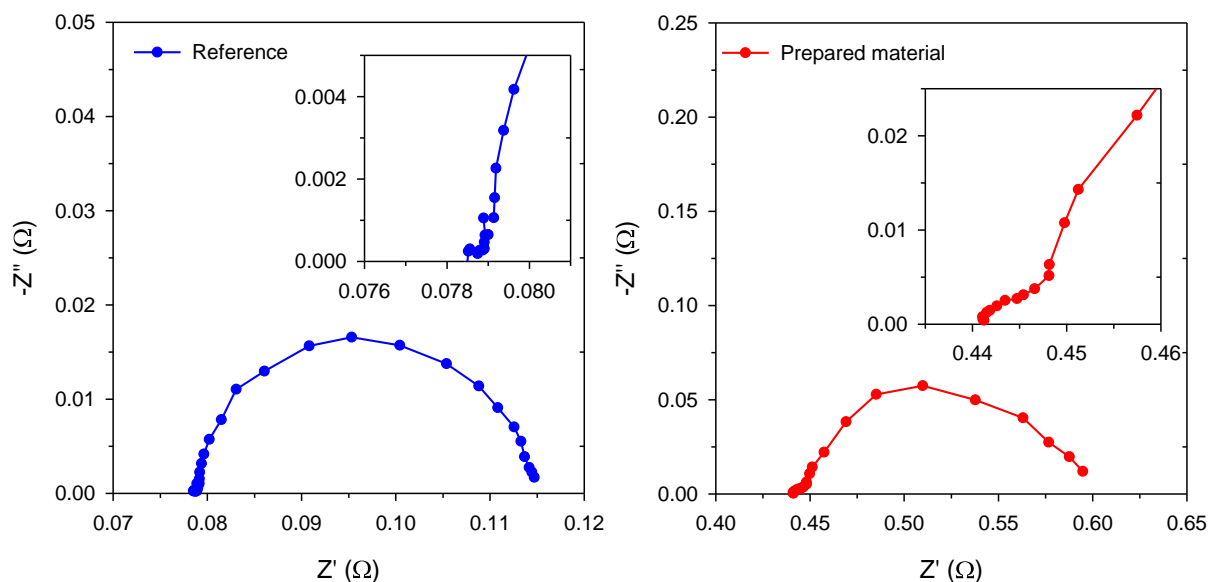


Fig. 7.4. Impedance spectra of the best modules prepared with the (blue) reference and (red) prepared material with particle size range 250-106 μm .

7.4 Conclusions

Thermoelectric modules were fabricated using the original ingot materials and the best performing materials prepared in this thesis. Their performance was evaluated by the module ZT calculated by impedance spectroscopy. The module fabrication method is described and the optimum conditions for the soldering process evaluated (soldering temperature and duration and the use of different solders) using the original materials. Although the prepared materials present higher ZT values than the ingot materials, their $(ZT)_{\text{module}}$ is lower. A possible reason is a higher contact resistance for the module from the prepared materials. On the other hand, it could be due to the electrical conductivity measurements of the discs samples which were not calculated in the same direction than the current flow in the modules.

Chapter 8 : Conclusions and Future Work

8.1 Conclusions

8.2 Future work

Chapter 8

8.1 Conclusions

The main objective of the work presented in this thesis was the evaluation of a novel technique, ultrasound milling, for the preparation of nanostructured bismuth telluride powder and its use to prepare nanobulk thermoelectric materials. The production of nanoparticles is mainly useful in reducing the thermal conductivity of materials to enhance the figure of merit. This objective has been reached for both n- and p-type bismuth telluride through a systematic experimental work where solvent to be used, time of the milling process, the presence of additive, amplitude of the ultrasound, number of cooling systems and powder concentration were optimised.

The principal attainments are as follows:

- A systematic experimental investigation was conducted to analyse the feasibility of producing bismuth telluride nanoparticles by ultrasound milling. Changes in the parameters mentioned before were performed to obtain the minimum particle size. From the experimental results, the optimised conditions to produce nanoparticles for n- and p-type bismuth telluride using ultrasound milling were 100 % amplitude, [powder]=0.0166 M, 2 cooling systems, 8 h and 1-butanol as solvent. At these conditions, most of the particles are in the 500-1000 nm range for the n-type material. For the p-type, both coarse particles of few microns and fine particles in the 200-1000 nm range were obtained.
- Nanoparticles in the ultrasound milling powders appear to form characteristic aggregates that look like large particles. This is not observed by ball milling method and it is a unique feature of the ultrasound milling technique. It was evaluated by XRD analysis that the single phase structure of the original Bi_2Te_3 materials is not altered by the ultrasound milling method.

- The well-known ball milling technique was also employed, only for comparison, to produce nanoparticles. An optimisation of the ball milling was conducted for the n- and p-type bismuth telluride where treatment duration and balls:powder weight ratio were evaluated. In this case, the optimised conditions were different for both materials, 24 h and 5:1 balls:powder weight ratio and 8 h and 20:1 ratio for the n- and p-type materials, respectively. The smallest particle sizes achieved under the optimised conditions were 200 nm and 300 nm for n- and p-type bismuth telluride. Similarly to the ultrasound milling process, the ball milling technique did not modify the single phase structure of the initial sample, as it was shown from XRD results.
- The time consumed in the milling processes to prepare similar smallest particle sizes is 3 times shorter in the case of ultrasound milling technique than in the ball milling for the n-type material. In the p-type material, similar milling times and particle sizes were obtained, but larger amounts of more homogeneous nanoparticles are produced by the ultrasound milling method. The reduction in the milling time when ultrasound milling method is employed for some materials implies a substantial decrease in time and power consumption, which is an important consideration.
- Regarding morphology, the powders produced by ultrasound milling process showed rounder and smoother particles than the ball milling treatment for the n-type material at short times (30 min). In the p-type material, this difference in morphology is not observed since the analysis was only conducted at longer times (8 h).
- A standard press station was remodelled to fabricate a hot press and the optimal conditions to prepare highly compacted samples, based on the density and power factor values, were identified. Pressure, time and temperature were the parameters optimised using the n-type material. A pressure of 1513.70 MPa applied for 30 min at 250 °C were the optimum parameters.
- The performance of the nanostructured bulk samples prepared from the ultrasound milling powders was evaluated. Ultrasound milling produces very low thermal conductivity materials, within the lowest values reported in the literature (0.50 and 0.35 for n- and p-type respectively). This reduced thermal conductivity values are due to the presence of the highly aggregated nanoparticles that form a uniform granular microstructure after compaction. Unfortunately, electrical conductivity is also reduced significantly, which led to no significant final improvement in ZT.
- The ultrasound milling process is preceded by a simple crushing pre-treatment performed employing a micro hammer-cutter mill, producing mainly micrometre size

powder. Powders obtained in this way, separated in different particle sizes, provided ZT values (≈ 1.4 for p-type material) close to the best ones reported in the literature.

- Thermoelectric modules were fabricated using the best performing nanobulk samples prepared in this thesis. The module fabrication method was described and the optimum conditions for the soldering process evaluated, obtaining a soldering temperature of 370 °C and 30 min soldering time for Sn/Pb 60/40 solder. Their performance was analyzed by impedance spectroscopy to determine of the module ZT. Although the prepared materials present higher ZT values than the ingot materials, their $(ZT)_{\text{module}}$ is lower, which could be due to a higher contact resistance and/or the anisotropy in their electrical conductivity, difficult to identify by the four probe method utilised in the characterisation.

8.2 Future work

As a new technique, the use of ultrasound milling offers a lot of possibilities for future investigations. Here we present some of the possible studies for future work:

- Bismuth telluride has been analysed in this thesis but this method could be applied to other established materials such as silicides, SiGe, etc. It should be very interesting to test if the same or similar features produced in Bi_2Te_3 can be achieved in other materials.
- The usage of different solvents in the ultrasound milling process could significantly modify the results achieved, especially solvents of higher viscosity could be interesting since the ultrasound waves will possibly propagate differently.
- The use of atomic precursors (Bi, Te) instead of formed compounds (Bi_2Te_3) could be interesting, as frequently performed in ball milling.
- To identify a process to remove possible organic compounds from the solvent that could be adsorbed on the surface of the nanoparticles limiting the electrical conductivity.
- Potential improvement in the electrical conductivity could be obtained by performing the ultrasound milling process in an inert atmosphere, which could avoid possible oxidation reactions.
- Measuring the electrical conductivity of the disc samples in the direction of operation with a more suitable method for a more precise evaluation of the performance should be considered.

- Examining the thermoelectric properties of a sample prepared from powder produced by the simple crushing pre-treatment without size separation (all sizes produced together) could be interesting. Possibly, a good performance could be also obtained without the need to perform a separation process.
- Further optimisation of the soldering conditions to prepare a thermoelectric modules using the material fabricated in this thesis should be taken into account to enhance the $(ZT)_{\text{module}}$.

References

- [1] M. C.-C. Martin-Gonzalez, O. and Diaz-Chao, P., *Renewable and Sustainable Energy Reviews* 2013, 24, 288.
- [2] J. P. Heremans, B. Wiendlocha, C. A.M., *Energy & environmental science* 2012, 5, 5510.
- [3] Y. Pei, H. Wang, G. J. Snyder, *Advanced Materials* 2012, 24, 6125.
- [4] G. A. Slack, *Solid States Physics*, ed. by H. Ehrenreich, F. Seitz and D. Turnbull, Academic Press, New York. 1979, 34, 1.
- [5] L.D. Hicks, M. S. Dresselhaus, *Physical Review B* 1993, 47, 12727.
- [6] D. M. Rowe, V. S. Shukla, N. Savvides, *Nature* 1981, 290, 765.
- [7] D. Mei, H. Wang, Y. Li, Z. Yao, T. Zhu, *Journal of Materials Research* 2015, 30, 2585.
- [8] D. Kraemer, J. Sui, K. McEnaney, H. Zhao, Q. Jie, Z. F. Ren, G. Chen, *Energy & Environmental Science* 2015.
- [9] Y. Lan, A. J. Minnich, G. Chen, Ren, *Advanced Functional Materials* 2010, 20, 357.
- [10] B. Poudel, Q. Hao, Y. Ma, Y. Lan, A. Minnich, B. Yu, X. Yan, D. Wang, A. Muto, D. Vashaee, X. Chen, J. Liu, M. S. Dresselhaus, G. Chen, Z. Ren, *Science* 2008, 320, 634.
- [11] T. J. Seebeck, *Abhandlungen der Deutschen Akademie der Wissenschaften zu Berlin* 1822, 1820-21, 289.
- [12] *Manual on the Use of Thermocouples in Temperature Measurement*, American Society for Testing and Materials, 2003.
- [13] h. t. c. e. t. h. h. a. o. 2/08/2015).
- [14] A. F. Ioffe, *Semiconductor Thermoelements and Thermoelectric Cooling*, Infosearch, London 1957.
- [15] *Nature* 1879, 20, 301.
- [16] E. Altenkirch, *Physikalische Zeitschrift* 1909, 10, 560.
- [17] E. Altenkirch, *Physikalische Zeitschrift* 1911, 12, 920.
- [18] M. Telkes, *Journal of Applied Physics* 1947, 18, 1116.
- [19] M. V. Vedernikov, E. K. Iordanishvili, "A.F. Ioffe and origin of modern semiconductor thermoelectric energy conversion", presented at *Proceedings ICT 98. XVII International Conference* 24-28 May, 1998.
- [20] W. Thomson, *Proceedings of the Royal Society of Edinburgh* 1951, 91.
- [21] D. M. Rowe, *CRC Handbook of Thermoelectric*, 1995.
- [22] T. M. Tritt, in *Semiconductors and Semimetals*, Vol. Volume 70 (Ed: M. T. Terry), Elsevier, 2001, ix.
- [23] L. E. Bell, *Science* 2008, 321, 1457.
- [24] D. M. Rowe, C. M. Bhandari, *Holt Technology* 1983.
- [25] G. Joshi, H. Lee, Y. Lan, X. Wang, G. Zhu, D. Wang, R. W. Gould, D. C. Cuff, M. Y. Tang, M. S. Dresselhaus, G. Chen, Z. Ren, *Nano Letters* 2008, 8, 4670.
- [26] X. W. Wang, H. Lee, Y. C. Lan, G. H. Zhu, G. Joshi, D. Z. Wang, J. Yang, A. J. Muto, M. Y. Tang, J. Klatsky, S. Song, M. S. Dresselhaus, G. Chen, Z. F. Ren, *Applied Physics Letters* 2008, 93, 193121.

- [27] D. M. Rowe, A. W. Cook, Ed., 28th Consultative Conference, to be published on behalf of the V.K. Watt Committee on Energy by IEE 1992.
- [28] K. Matsuura, D. M. Rowe, K. Koumoto, G. Min, and, A. Tsuyoshi, XIth International conference on Thermoelectrics, University of Texas at Arlington 1992.
- [29] L.D. Hicks, M. S. Dresselhaus, *Physical Review B* 1993, 47, 16631.
- [30] L.D. Hicks, T.C. Harman, X. Sun, M. S. Dresselhaus, *Physical Review B* 1996, 53, R10493.
- [31] D. Vashaee, A. Shakouri, *Physical Review Letters* 2004, 92, 106103.
- [32] T.C. Harman, P. J. Taylor, M. P. Walsh, B. E. L. Forge, *Science* 2002, 297, 2229.
- [33] K. Kadel, L. Kumari, W.Z. Li, J.Y. Huang, P. P. Provencio, *Nanoscale Research Letters* 2010, 6, 57.
- [34] A. I. Boukai, Y. Bunimovich, J. Tahir-Kheli, J.-K. Yu, W. A. Goddard Iii, J. R. Heath, *Nature* 2008, 451, 168.
- [35] G. Slack, Fall Materials Research Society meeting 1998.
- [36] L. I. Anatyshuk, M. S. Moldavasky, V. V. Rasinkov, T. N.K., *Proc. Xth Int. Conf. Thermoelectrics, Cardiff, Wales, September 10-12 1991*, 108.
- [37] A. W. Van Herwaarden, D. C. Van Duyn, B. W. Van Oudheusden, and, P. M. Sarro, *Sensors and actuators* 1989, A21-A23, 621.
- [38] D. W. Rowe, U.K. Patent No. 87 1988, 14698.
- [39] H. J. Goldsmid, *Electronic refrigeration*, London, U.K. 1986.
- [40] J. C. Peltier, *Ann. Chim* 1834, LV1, 371.
- [41] S. J. Poon, *Semiconductors and semimetals* 2001, 70, 37.
- [42] G. Min, D. M. Rowe, K. Kontostavlakis, *Journal of Physics D: Applied Physics* 2004, 37, 1301.
- [43] D. M. Rowe, *CRC Handbook of Thermoelectrics: Micro to Nano*, 2005.
- [44] D. M. Rowe, G. Min, *Journal of Power Sources* 1998, 73, 193.
- [45] G. Min, N. M. Yatim, *Journal of Physics D: Applied Physics* 2008, 41, 222001.
- [46] J. W. Fergus, *Journal of the European Ceramic Society* 2012, 32, 525.
- [47] O. Bubnova, X. and Crispin, *Energy & environmental science* 2012, 5, 9345.
- [48] G. Min, D. M. Rowe, *J. Power Sources* 1992, 38, 253.
- [49] G. Min, D. M. Rowe, *Proceedings of first Young Scientists Conference, Yunnan Province, P R China* 1992, 130.
- [50] G. Min, D. M. Rowe, *CRC Handbook of Thermoelectric*, D.M. Rowe. CRC Press, New York 1995, 479.
- [51] D. M. Rowe, G. Min, W. S.G.K., *Proceedings of 14th International conference on Thermoelectrics, St. Petersburg, Russia* 1995, 291.
- [52] D. M. Rowe, G. Min, *IEE Proc. Sci. Meas. Technol.* 1996, 143(6), 351.
- [53] D. M. Rowe, G. Min, *Journal of Power Sources* 1998, 73, 193.
- [54] G. Min, D. M. Rowe, *Energy Conversion and Management* 2002, 43, 221.
- [55] G. Min, D. M. Rowe, O. Assis, S. G. K. Williams, *Proceedings of 11th International conference on Thermoelectrics, Arlington, TX* 1992, 210.
- [56] G. Min, D. M. Rowe, *Proceedings of 14th International conference on Thermoelectrics, Long Beach, CA* 2002, 365.
- [57] X. Li, H. Ren, Y. and Luo, *Applied Physics Letters* 2011, 98, 083113.
- [58] S. I. Kim, K. H. Lee, H. A. Mun, H. S. Kim, S. W. Hwang, J. W. Roh, D. J. Yang, W. H. Shin, X. S. Li, Y. H. Lee, G. J. Snyder, S. W. Kim, *Science* 2015, 348, 109.
- [59] X. B. Xiao, T. J. Zhu, X. H. Ji, *Thermoelectrics Handbook: Macro to nano* (Ed: D.M. Rowe), CRC, Boca Raton, FL 2006, 25.
- [60] R. Venkatasubramanian, E. Siivola, T. Colpitts, B. O'Quinn, *Nature* 2001, 413, 597.
- [61] J. R. Sootsman, D. Y. Chung, M. G. Kanatzidis, *Angewandte Chemie International Edition* 2009, 48, 8616.
- [62] K. Hoang, S. D. Mahanti, *Physical Review B* 2008, 78, 085111.
- [63] S. D. Mahanti, K. Hoang, S. Ahmad, *Physica B: Condensed Matter* 2007, 401–402, 291.

- [64] K. Hoang, S. D. Mahanti, P. Jena, *Physical Review B* 2007, 76, 115432.
- [65] S. Ahmad, S. D. Mahanti, K. Hoang, M. G. Kanatzidis, *Physical Review B* 2006, 74, 155205.
- [66] J. P. Heremans, V. Jovovic, E. S. Toberer, A. Saramat, K. Kurosaki, A. Charoenphakdee, S. Yamanaka, G. J. Snyder, *Science* 2008, 321, 554.
- [67] P. Yanzhong, S. Xiaoya, L. Aaron, W. Heng, C. Lidong, S. G. Jeffrey, *Nature* 2011, 473, 7345.
- [68] G. S. Nolas, G. A. Slack, D. T. Morelli, T. M. Tritt, A. C. Ehrlich, *Journal of Applied Physics* 1996, 79, 4002.
- [69] N. G.S, D. T. Morelli, T. M. Tritt, *Annual Revision Matter Science* 1999, 29, 89.
- [70] C. Uher, *Semiconductors and Semimetals* 2000, 69, 139.
- [71] X. Tang, Q. Zhang, L. Chen, T. Goto, T. Hirai, *Journal of Applied Physics* 2005, 97, 093712.
- [72] M. Puyet, A. Dauscher, B. Lenoir, M. Dehmas, C. Stiewe, E. Müller, J. Hejtmanek, *Journal of Applied Physics* 2005, 97, 083712.
- [73] J. S. Dyck, W. Chen, C. Uher, L. Chen, X. Tang, T. Hirai, *Journal of Applied Physics* 2002, 91, 3698.
- [74] M. Puyet, B. Lenoir, A. Dauscher, M. Dehmas, C. Stiewe, E. Müller, *Journal of Applied Physics* 2004, 95, 4852.
- [75] S. R. Culp, S. J. Poon, N. Hickman, T. M. Tritt, J. Blumm, *Applied Physics Letters* 2006, 88, 042106.
- [76] C. Uher, J. Yang, S. Hu, D. T. Morelli, G. P. Meisner, *Physical Review B* 1999, 59, 8615.
- [77] Y. Xia, S. Bhattacharya, V. Ponnambalam, A. L. Pope, S. J. Poon, T. M. Tritt, *Journal of Applied Physics* 2000, 88, 1952.
- [78] S. Bhattacharya, A. L. Pope, R. T. Littleton, T. M. Tritt, V. Ponnambalam, Y. Xia, S. J. Poon, *Applied Physics Letters* 2000, 77, 2476.
- [79] H. Hohl, A. P. Ramirez, C. Goldmann, G. Ernst, B. Wölfing, E. Bucher, *Journal of Physics: Condensed Matter* 1999, 11, 1697.
- [80] S. Sportouch, P. Larson, M. Bastea, P. Brazis, J. Ireland, C. R. Kannewurf, S. D. Mahanti, C. Uher, M. G. Kanatzidis, *Materials Research Society Symposium - Proceedings* 1999, 545, 421.
- [81] S. Ögüt, K. M. Rabe, *Physical Review B* 1995, 51, 10443.
- [82] F. G. Aliev, N. B. Brandt, V. V. Moschalkov, V. V. Kozyrkov, R. V. Skolozdra, A. I. Belogorokhov, *Zeitschrift für Physik B* 1989, 75, 167.
- [83] J. Tobola, J. Pierre, S. Kaprzyk, R. V. Skolozdra, M. A. Kouacou, *Journal of Physics: Condensed Matter* 1998, 10, 1013.
- [84] S. Sakurada, N. Shutoh, *Applied Physics Letters* 2005, 86, 082105.
- [85] M. I. Fedorov, D. A. Pshenay-Severin, V. K. Zaitsev, S. Sano, M. V. Vedernikov, *Twenty-second international conference on thermoelectrics (ICT). IEEE France* 2003, 142.
- [86] V. K. Zaitsev, M. I. Fedorov, E. A. Gurieva, I. S. Eremin, P. P. Konstantinov, A. Y. Samunin, *International conference on thermoelectrics. IEEE* 2005, 189.
- [87] G. N. Isachenko, V. K. Zaitsev, M. I. Fedorov, E. A. Gurieva, I. S. Eremin, P. P. Konstantinov, *Twenty-sixth international conference on thermoelectrics. IEEE Jeju Island, Korea (South)* 2007, 248.
- [88] X. Zhang, Q.-m. Lu, L. Wang, F.-p. Zhang, J.-x. Zhang, *Journal of Electronic Materials* 2010, 39, 1413.
- [89] Q. Zhang, T. J. Zhu, A. J. Zhou, H. Yin, X. B. Zhao, *Physica Scripta* 2007, T129, 126.
- [90] M. I. Fedorov, V. K. Zaitsev, G. N. Isachenko, *Seventeenth international conference on solid compounds of transition elements. Durnten-Zurich: Trans Tech* 2011, 286.
- [91] M. I. Fedorov, V. K. Zaitsev, I. S. Eremin, E. A. Gurieva, A. T. Burkov, P. P. Konstantinov, *Physics of Solid State* 2006, 48, 1486.
- [92] T. Aizawa, R. Song, A. Yamamoto, *Materials Transactions, JIM* 2006, 47, 1058.
- [93] J.-i. Tani, H. Kido, *Intermetallics* 2013, 32, 72.
- [94] H. J. Goldsmid, *Introduction to thermoelectricity*. New York: Springer 2009.
- [95] Q. Zhang, J. He, X. B. Zhao, S. N. Zhang, T. J. Zhu, H. Yin, T. M. Tritt, *Journal of Physics D: Applied Physics* 2008, 41, 185103.

- [96] D. J. Braun, W. Jeitschko, *Journal of the Less-Common Metals* 1980, 72, 147.
- [97] S. Bathula, M. Jayasimhadri, N. Singh, A. K. Srivastava, J. Pulikkotil, A. Dhar, R. C. Budhani, *Applied Physics Letters* 2012, 101, 213902.
- [98] R. Funahashi, S. Urata, *International Journal of Applied Ceramics Technology* 2007, 4, 297.
- [99] W. Koshibae, K. Tsutsui, S. and Maekawa, *Phys. Rev. B* 2000, 62, 6869.
- [100] Y. Wang, N. S. Rogado, R. J. Cava, N. P. and Ong, *Nature* 2003, 423, 425.
- [101] K. Fujita, T. Mochida, K. Nakamura, *Japanese Journal of Applied Physics* 2001, 40, 4644.
- [102] M. Ohtaki, Y. Nojiri, E. Maed, *Proc. 19th Int. Conf. Thermoelectrics, IEEE, Wales* 2000, 190.
- [103] I. Terasaki, *Proc. 21st Int. Conf. Thermoelectrics* 2002, 185.
- [104] R. Funahashi, I. Matsuhara, H. Ikuta, T. Takeuchi, U. Mizutani, S. Sodeoka, *Japanese Journal of Applied Physics* 2000, 39, L1127.
- [105] T. Yamamoto, K. Uchinokura, I. Tsukada, *Physical Review B* 2002, 65, 184434.
- [106] R. Funahashi, I. Matsubara, *Applied Physics Letters* 2001, 79, 362.
- [107] T. Itoh, I. Terasaki, *Japanese Journal of Applied Physics* 2000, 39, 6658.
- [108] S. Hébert, S. Lambert, D. Pelloquin, A. Maignan, *Physical Review B* 2001, 64, 172101.
- [109] D. Pelloquin, A. Maignan, S. Hébert, C. Martin, M. Hervieu, C. Michel, L. B. Wang, B. Raveau, *Chemistry of Materials* 2002, 14, 3100.
- [110] K. Koumoto, I. Terasaki, R. Funahashi, *Materials Research Society Bulletin* 2006, 31, 206.
- [111] C. Hamann, *Physica Status Solidi B* 1967, 20, 481.
- [112] Y.W. Park, A. Denenstien, C.K. Chiang, A.J. Heeger, A. G. MacDiarmid, *Solid State Communications* 1979, 29, 747.
- [113] N. Toshima, *Macromolecules Symposium* 2002, 186, 81.
- [114] Y. Shinohara, K. Ohara, Y. Imai, I. Isoda, H. Nakanishi, *Thermoelectrics, 2003 Twenty-Second International Conference on - ICT 2003*, 298.
- [115] X. Gao, K. Uehara, D. D. Kluga, J. S. Tse, *Computer Materials Science* 2006, 36, 49.
- [116] O. Bubnova, X. Crispin, *Energy & Environmental Science* 2012, 5, 9345.
- [117] J. Yang, H.-L. Yip, A. K. Y. Jen, *Advanced Energy Materials* 2013, 3, 549.
- [118] Q. Zhang, Y. Sun, W. Xu, D. Zhu, *Advanced Materials* 2014, 26, 6829.
- [119] A. J. Heeger, *Angewandte Chemie International Edition* 2001, 40, 2591.
- [120] G. H. Kim, L. Shao, K. Zhang, K. P. Pipe, *Nat Mater* 2013, 12, 719.
- [121] Y. Sun, P. Sheng, C. Di, F. Jiao, W. Xu, D. Qiu, D. Zhu, *Advanced Materials* 2012, 24, 932.
- [122] L.-D. Zhao, S.-H. Lo, Y. Zhang, H. Sun, G. Tan, C. Uher, C. Wolverton, V. P. Dravid, M. G. Kanatzidis, *Nature* 2014, 508, 373.
- [123] X. Lu, D. T. Morelli, Y. Xia, F. Zhou, V. Ozolins, H. Chi, X. Zhou, C. Uher, *Advanced Energy Materials* 2013, 3, 342.
- [124] M. J. Kirkham, A. M. dos Santos, C. J. Rawn, E. Lara-Curzio, J. W. Sharp, A. J. Thompson, *Physical Review B* 2012, 85, 144120.
- [125] H. Zhao, J. Sui, Z. Tang, Y. Lan, Q. Jie, D. Kraemer, K. McEnaney, A. Guloy, G. Chen, Z. Ren, *Nano Energy* 2014, 7, 97.
- [126] H. Zhao, J. Sui, Z. Tang, Y. Lan, Q. Jie, D. Kraemer, K. McEnaney, A. Guloy, G. Chen, Z. F. Ren, *Nano Energy* 2014, 7, 97.
- [127] J. P. Heremans, B. Wiendlocha, A. M. Chamoire, *Energy & Environmental Science* 2012, 5, 5510.
- [128] Y. Pei, H. Wang, G. J. Snyder, *Advanced Materials* 2012, 24, 6125.
- [129] Y. Pei, X. Shi, A. LaLonde, H. Wang, L. Chen, G. J. Snyder, *Nature* 2011, 473, 66.
- [130] J. P. Heremans, V. Jovic, E. S. Toberer, A. Saramat, K. Kurosaki, A. Charoenphakdee, S. Yamanaka, G. J. Snyder, *Science* 2008, 321, 554.
- [131] C. M. Jaworski, B. Wiendlocha, V. Jovic, J. P. Heremans, *Energy & Environmental Science* 2011, 4, 4155.
- [132] K. Biswas, J. He, I. D. Blum, C.-I. Wu, T. P. Hogan, D. N. Seidman, V. P. Dravid, M. G. Kanatzidis, *Nature* 2012, 489, 414.

- [133] H. J. Goldsmid, *Application of thermoelectricity*, Methuen, New York 1960.
- [134] W. Xie, X. Tang, Y. Yan, Q. Zhang, T. M. Tritt, *Applied Physics Letters* 2009, 94, 102111.
- [135] C. Dames, G. Chen, *Thermoelectrics Handbook: Macro to Nano* (Ed: D. M. Rowe), CRC/Taylor & Francis, Boca Raton, FL 2006, Ch. 42.
- [136] J. He, M. G. Kanatzidis, V. P. Dravid, *Materials Today* 2013, 16, 166.
- [137] J. He, S. N. Girard, M. G. Kanatzidis, V. P. Dravid, *Advanced Functional Materials* 2010, 20, 764.
- [138] R. W. Seigel, *MRS Bulletin* 1990, 15, 60.
- [139] H. Gleiter, *Progress in Materials Science* 1990, 33, 223.
- [140] R. Herr, U. Birringer, H. Gleiter, *Transactions of the Japan Institute of Metals Supplement* 1986, 27, 43.
- [141] B. W. Dodson, L. J. Schowalter, J. E. Cunningham, F. E. Pollak, *Materials Research Society Symposium Proceedings* 1989, 160.
- [142] T. M. Bessman, B. M. Bessman, *Materials Research Society Symposium Proceedings* 1990, 168.
- [143] L. M. Goldman, B. Blanpain, F. Spaepen, *Journal of Applied Physics* 1986, 60, 1374.
- [144] D. S. Lashmore, R. Oberle, M. P. Dariel, L. H. Bennett, L. Swartzendruber, *Materials Research Society Symposium Proceedings* 1989, 132, 219.
- [145] C. C. Koch, *Nanostructured Materials* 1993, 2, 109.
- [146] P. matteazzi, D. Basset, F. Miani, G. Le Caër, *Nanostructured Materials* 1993, 2, 217.
- [147] G. Wasserman, *Proceedings of the 4th International Conference on Strength of Metals and Alloys* 1976, 3, 1343.
- [148] J. D. Embury, *Strengthening Methods in Crystals* (A. Kelly and R.B. Nicholson, eds). Applied Science Publishing, London 1971, 331.
- [149] E. Ashalley, H. Chen, X. Tong, H. Li, Z. Wang, *Front. Mater. Sci.* 2015, 9, 103.
- [150] <https://ninithi.com/gas-phase-synthesis/>.
- [151] <https://duepublico.uni-duisburg-essen.de/servlets/DerivateServlet/Derivate-5148/03Kap3.pdf>.
- [152] http://engg.scu.ac.ir/_Engineering/Documents/Inert%20gas%20condensation_20140428_002109.pdf.
- [153] D. M. Mattox, *Handbook of Physical Vapor Deposition (PVD) Processing* (Second Edition) 2010.
- [154] <http://www.imicromaterials.com/technical/lithography-process-overview>.
- [155] <http://www.lithoguru.com/scientist/lithobasics.html>.
- [156] H. J. Levinson, *Lithography Process Control*. Tutorial texts in Optical Engineering SPIE Optical Engineering Press. 1999, TT28.
- [157] S. B. Mooney, J. B. and Radding, *Ann. Rev. Mater. Sci.* 1982, 12, 81.
- [158] K. S. Suslick, M. Fang, T. Hyeon, *Journal of the American Chemical Society* 1996, 118, 11960.
- [159] M. a. S. Paunovic, M., *FUNDAMENTALS OF ELECTROCHEMICAL DEPOSITION SECOND EDITION*. Wiley-interscience a John Wiley & Sons, INC., PUBLICATION 2006.
- [160] J. Eskult, *Electrochemical Deposition of Nanostructured Metal/Metal-Oxide Coatings*. ACTA UNIVERSITATIS UPSALIENSIS UPPSALA. 2007.
- [161] S. S. a. C. Djokic, P.L., *Chapter 6_Electroless Deposition: Theory and Applications*. Springer Science +Business Media. 2010, 251.
- [162] C. J. Brumlik, V. P. Menon, C. R. Martin, *Journal of Materials Research* 1994, 268, 1174.
- [163] C.-G. Wu, T. Bein, *Science* 1994, 264, 1757.
- [164] P. M. Ajayan, O. Stephan, P. Redlich, C. Colliex, *Nature* 1995, 375, 564.
- [165] W. Han, S. Fan, Q. Li, Y. Hu, *Science* 1997, 277, 1287.
- [166] G. O. Mallory, J. B. Hajde, *Electroless Plating: Fundamentals and Applications*, American Electroplaters and Surface Finishers Society, Orlando, FL. 1990.

- [167] K. a. Y. Byrappa, M., Handbook of hydrothermal technology. Noyes publications. William Andrew Publishing. 2000.
- [168] J. R. a. H. Creighton, P., ASM International 2001, 1.
- [169] S. D. Allen, J. Appl. Phys. 1981, 52, 6501.
- [170] S. K. Roy, Bull. Mater. Sci 1998, 11, 129.
- [171] R. M. Osgood, H. H. Gilgen, Annual Review of Materials Science 1985, 15, 549.
- [172] R. L. Abber, Handbook of Thin-Film Deposition Processes and Techniques, ed., K.K. Schuegraf, Noyes, Park Ridge, NJ. 1988.
- [173] <http://www.enea.it/it/pubblicazioni/EAI/anno-2011/n.%204-5%202011%20Luglio-ottobre2011/Bacteria-endosimbionts-a-source-of-innovation-in-biotechnology-for-vector-borne-diseases-control%20>.
- [174] <http://www.onecentralpress.com/wp-content/uploads/2015/01/CHAPTER-15-MF-LATEST.pdf>.
- [175] I. Morjan, Carbon 2003, 41, 2913.
- [176] C. Wang, D. Chen, X. Jiao, Science and Technology of Advanced Materials 2009, 10, 023001.
- [177] H. P. Hentze, M. Antonietti, Current Opinion in Solid State and Materials Science 2001, 5, 343.
- [178] M. Tiemann, Chem. Mater. 2008, 20, 961.
- [179] www.directhotpressing.com.
- [180] M. Tokia, Journal of the Society of Powder Metallurgy, Japan 1993, 30, 790.
- [181] K. C. Cho, R. H. Woodman, B. R. Klotz, R. J. Dowding, Materials and Manufacturing Processes 2004, 19, 619.
- [182] J. R. Groza, In ASM Handbook: Powder Metallurgy, ASM: Materials Park, OH 1998, 7, 583.
- [183] www.hielscher.com/mill_01.htm (access on 30/03/2016).
- [184] M. Hodnett, www.sensorsmag.com/sensors/acoustic-ultrasound/measuring-cavitation-ultrasonic-cleaners-and-processors-8161 2011.
- [185] E. B. Flint, K. S. Suslick, Science 1991, 253, 1397.
- [186] J. García-Cañadas, G. Min, Review of Scientific Instruments 2014, 85, 043906.
- [187] D. K. Schroeder, Semiconductor Material and Device Characterisation, Wiley. 1990.
- [188] L. J. Van der Pauw, Philips Research Reports 1958, 13, 1.
- [189] D. Platzek, G. Karpinski, C. Stiewe, P. Ziolkowski, C. Drasar, E. Muller, Proceedings of 24th International Conference on Thermoelectrics (IEEE, Piscataway) 2005, 13.
- [190] W. J. Parker, R. J. Jenkins, C. P. a. Butler, G. L. Abbott, Journal of Applied Physics 1966, 32, 1679.
- [191] M. Hosokawa, K. Nogi, M. N. and, T. Yokoyama, Nanoparticle Technology Handbook. Elsevier 2012.
- [192] <http://carleton.columbia.edu/netzsch-nanoflash-thermal-diffusivity-analyzer>.
- [193] J. García-Cañadas, G. Min, AIP Advances 2016, 6, 035008.
- [194] J. García-Cañadas, G. Min, Journal of Applied Physics 2014, 116, 174510.
- [195] <https://cds.dl.ac.uk/cds/datasets/crys/icsd/llicsd.html>.
- [196] A. Soni, Z. Yanyuan, Y. Ligen, M. K. K. Aik, M. S. Dresselhaus, Q. Xiong, Nano Letters 2012, 12, 1203.
- [197] S. K. Yoon, O.-J.; Ahn, S.; Kim, J.-Y.; Koo, H.; Bae, S.-H.; Cho, J.-Y.; Kim, J.-S.; Park, C, Journal of Electronic Materials 2013, 42, 3390.
- [198] S.-J. Jung, K. S. K., H.-H. Park, D.-B. Hyun, S.-H. Baek, J.-S. Kim, Journal of Nanomaterials 2013, 2013.
- [199] C. Xinzhi, F. Xian, R. Zhenzhou, Y. Fan, G. Zhanghua, L. Guangqiang, Journal of Physics D: Applied Physics 2014, 47, 115101.
- [200] J.-J. Shen, T.-J. Zhu, X.-B. Zhao, S.-N. Zhang, S.-H. Yang, Z.-Z. Yin, Energy & Environmental Science 2010, 3, 1519.
- [201] G. J. a. T. Snyder, E. S., Nature Materials 2008, 7, 105.

- [202] K. a. K. Kishimoto, T., *Journal of Applied Physics* 2002, 92, 2544.
- [203] J. I. Jaklovszky, R.; Nistor, N. and Chiculita, A., *Physica Status Solidi* 1975, 27, 329.
- [204] L. D. Z. Zhao, B. P; Liu, W. S. and Li, J. F., *Journal of Applied Physics* 2009, 105, 023704.
- [205] C. W. Nan, *Progress in Materials Science* 1993, 37, 1.
- [206] S. M. S. Toprak, C.; Platzek, D.; Williams, S.; Bertini, L.; Muller, E.; Gatti, C. Zhang, Y.; Rowe, M. and Muhammed, M., *Advanced Functional Materials* 2004, 14, 1189.
- [207] S. Grasso, N. Tsujii, Q. Jiang, J. Khaliq, S. Maruyama, M. Miranda, K. Simpson, T. Mori, M. J. Reece, *Journal of Materials Chemistry C* 2013, 1, 2362.
- [208] R. J. Mehta, Y. Zhang, C. Karthik, B. Singh, R. W. Siegel, T. Borca-Tasciuc, G. Ramanath, *Nature Materials* 2012, 11, 233.
- [209] K. Tyagi, B. Gahtori, S. Bathula, A. K. Srivastava, A. K. Shukla, S. Auluck, A. Dhar, *Journal of Materials Chemistry A* 2014, 2, 15829.
- [210] P. Qiu, T. Zhang, Y. Qiu, X. Shi, L. Chen, *Energy & Environmental Science* 2014, 7, 4000.

Appendix A

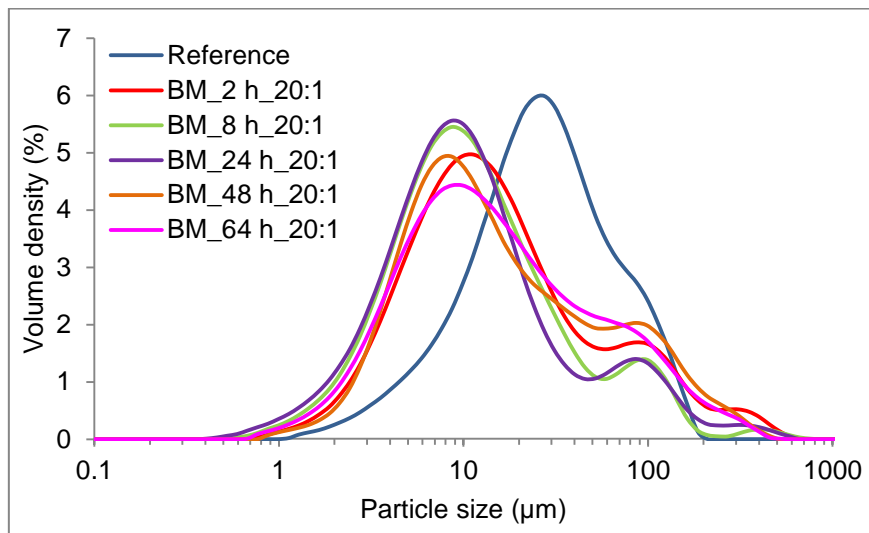


Fig. A.1. Particle size distribution in volume density of n-type Bi₂Te₃ after ball milling using balls:material ratio 20:1 at different times.

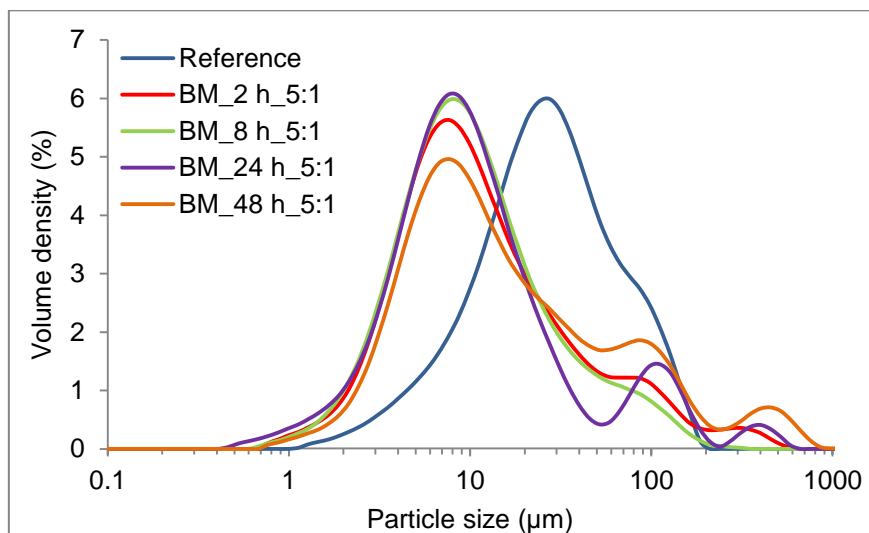


Fig. A.2. Particle size distribution in volume density of n-type Bi₂Te₃ after ball milling using balls:material ratio 5:1 at different times.

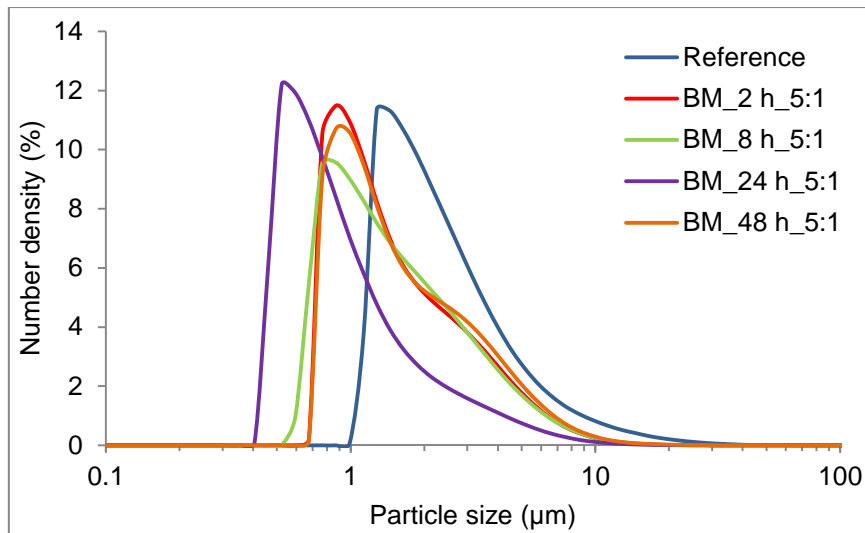


Fig. A.3. Particle size distribution in number density of n-type Bi_2Te_3 after ball milling using balls:material ratio 5:1 at different times.

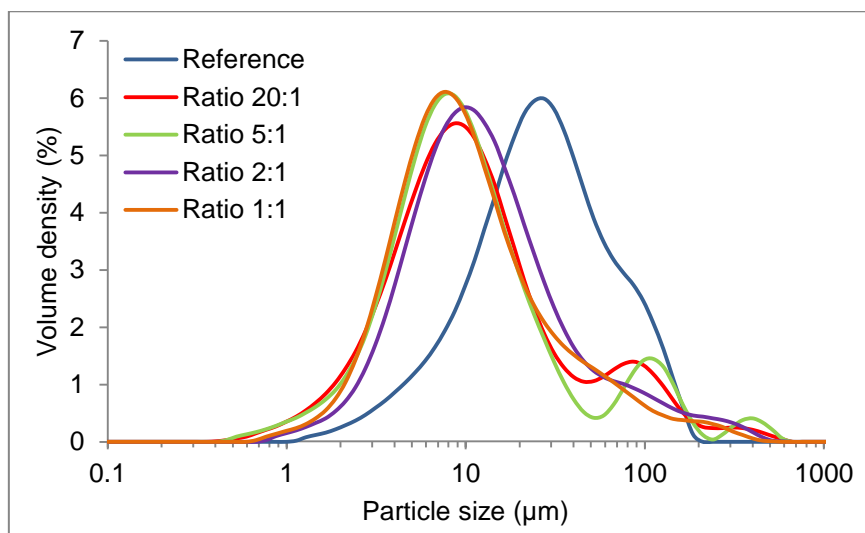


Fig. A.4. Particle size distribution in volume density of n-type Bi_2Te_3 after ball milling using different balls:material ratio at 24 h.

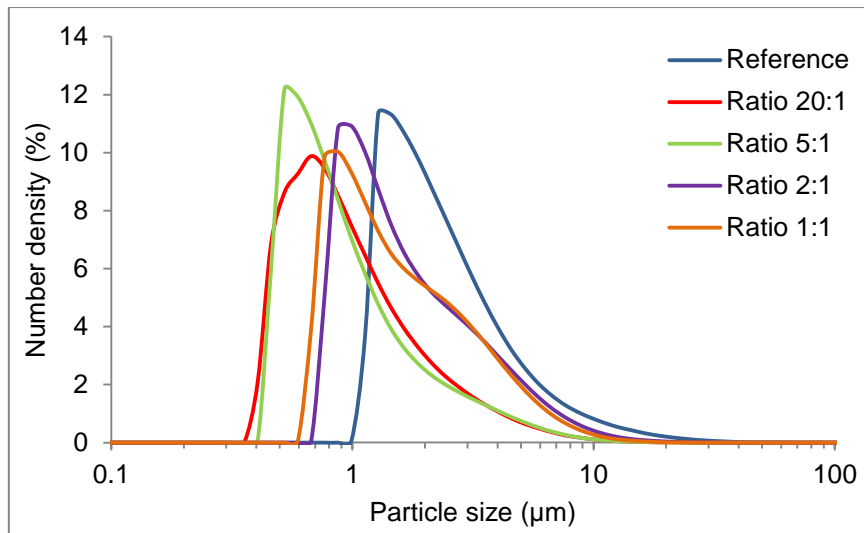


Fig. A.5. Particle size distribution in number density of n-type Bi_2Te_3 after ball milling using different balls:material ratios at 24 h.

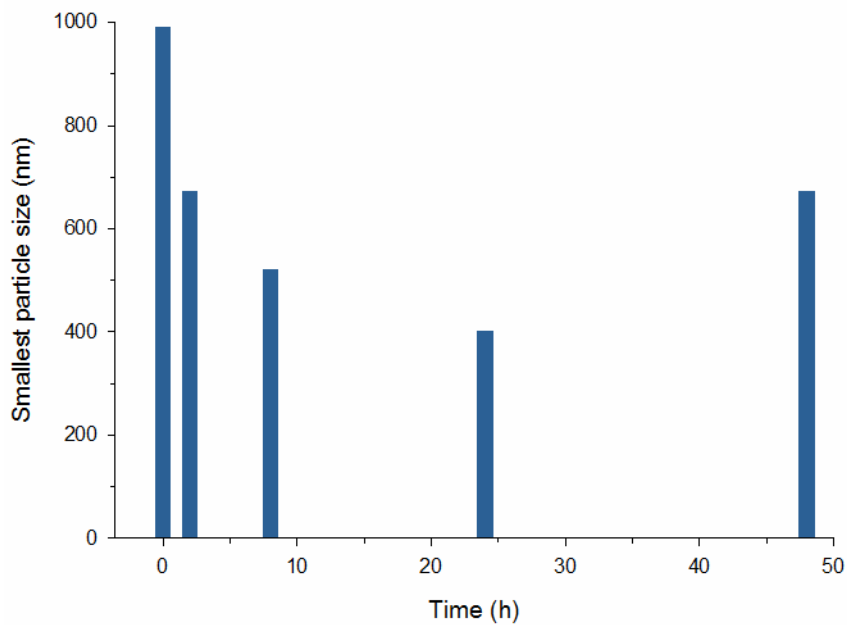


Fig. A.6. Representation of the smallest particle size achieved for n-type Bi_2Te_3 after ball milling under different times and ratio balls:material 5:1.

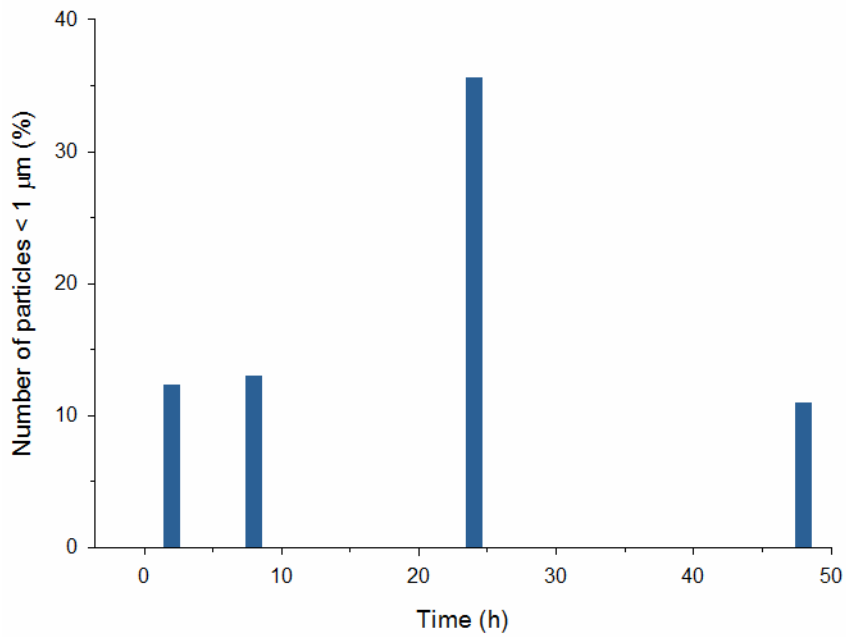


Fig. A.7. Representation of the number of particles with a size smaller than 1 μm achieved for n-type Bi₂Te₃ after ball milling under different times and ratio balls:material 5:1.

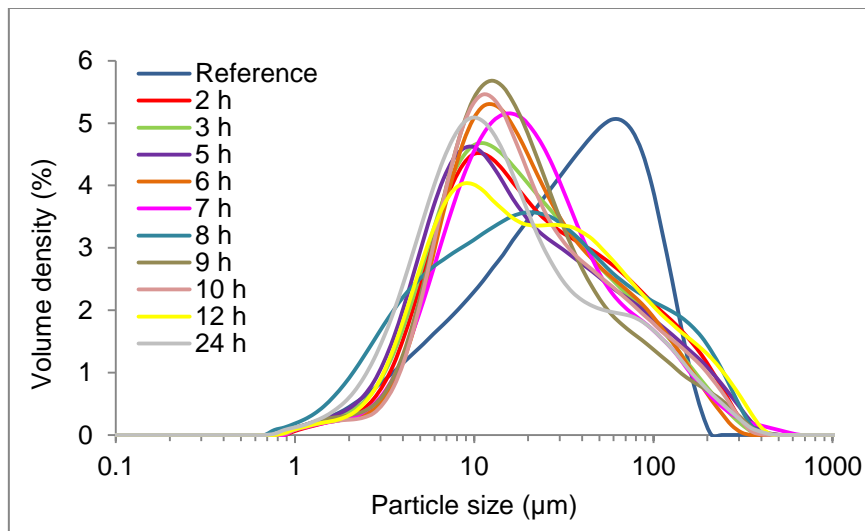


Fig. A.8. Particle size distribution in volume density of p-type Bi₂Te₃ after ball milling using balls:material ratio 20:1 at all the different times performed.

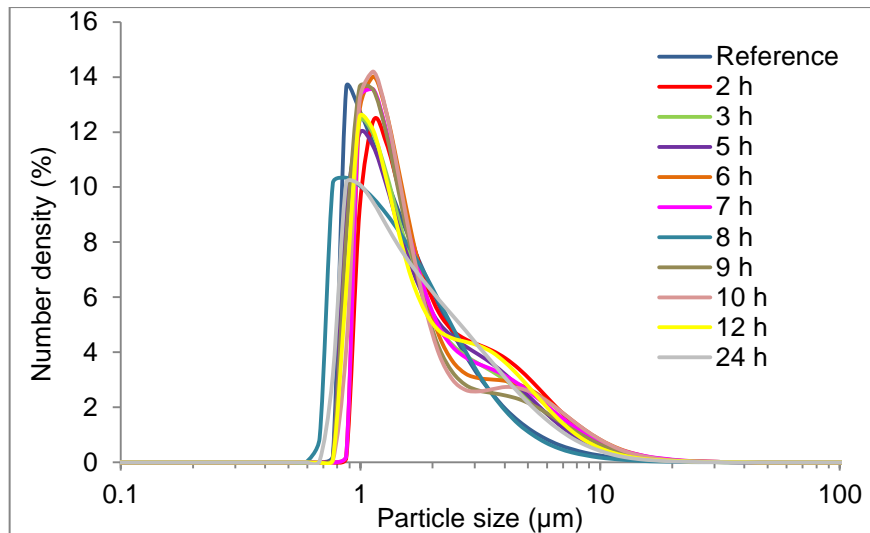


Fig. A.9. Particle size distribution in number density of p-type Bi_2Te_3 after ball milling using balls:material ratio 20:1 at all the different times performed.

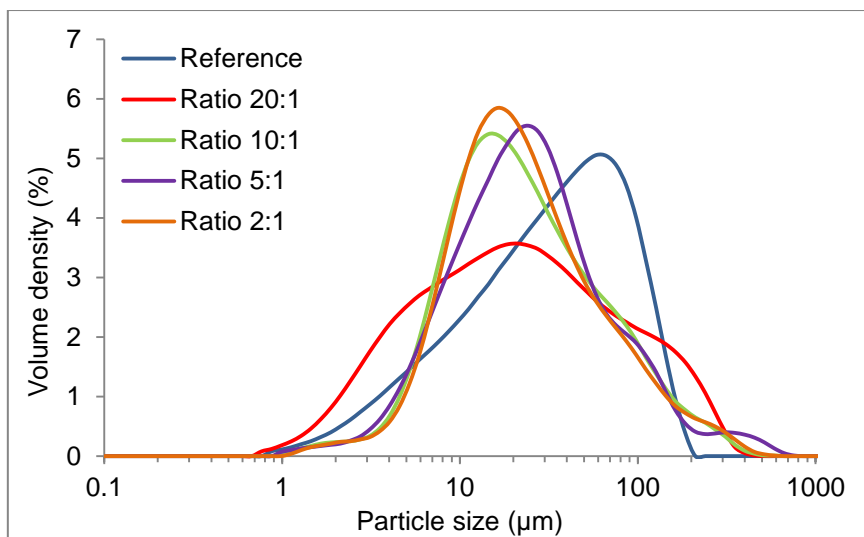


Fig. A.10. Particle size distribution in volume density of p-type Bi_2Te_3 after ball milling using different balls:material ratio at 8 h.

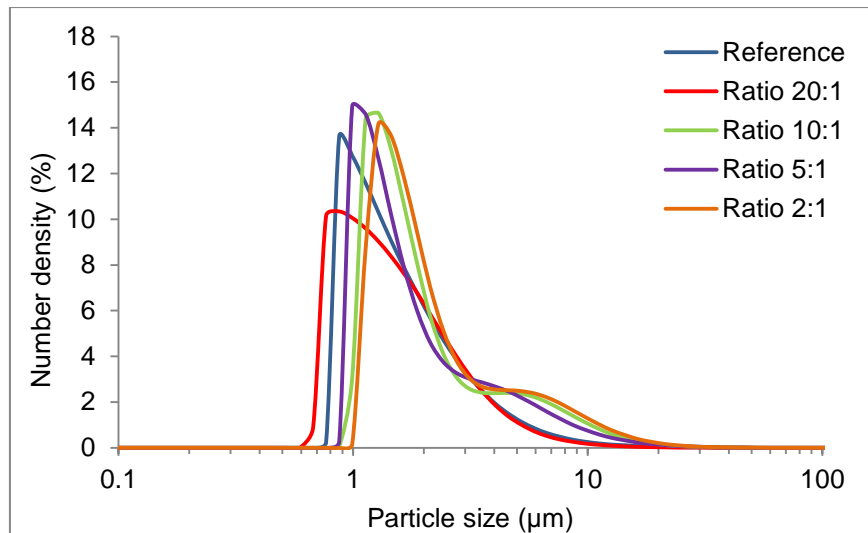


Fig. A.11. Particle size distribution in number density of p-type Bi_2Te_3 after ball milling using different balls:material ratio at 8 h.

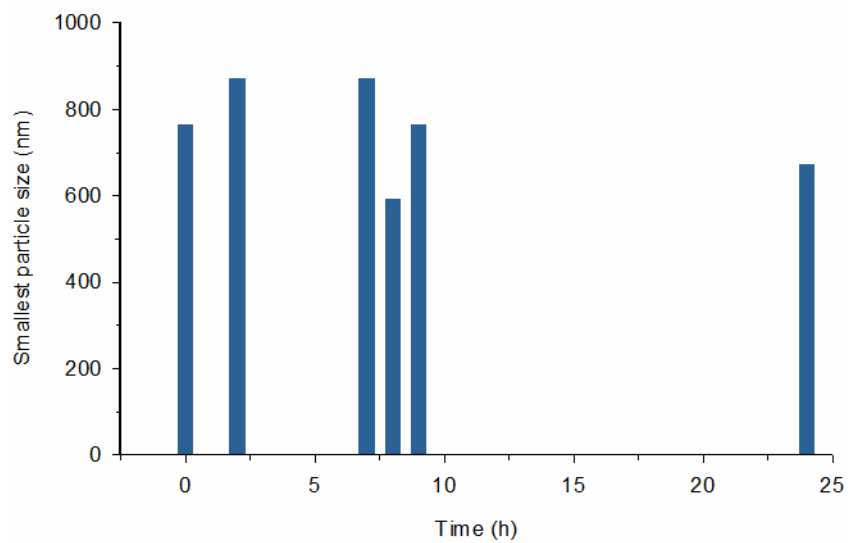


Fig. A.12. Representation of the smallest particle size achieved for p-type Bi_2Te_3 after ball milling under different times and ratio balls:material 20:1.

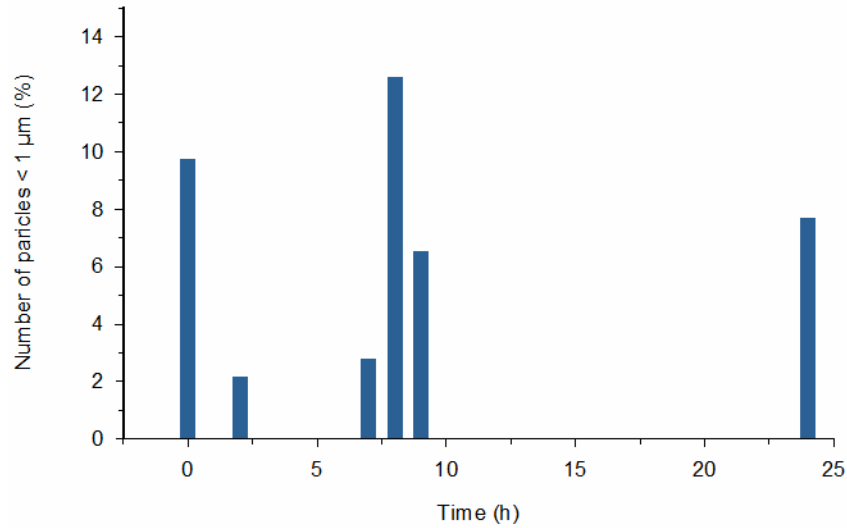


Fig. A.13. Representation of the number of particles with a size smaller than 1 μm achieved for p-type Bi_2Te_3 after ball milling under different times and ratio balls:material 20:1.

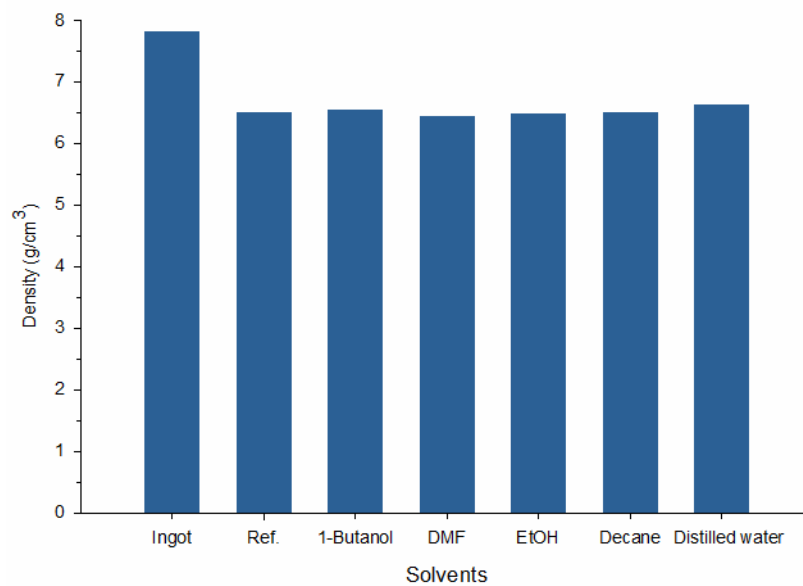


Fig. A.14. Density measurements of the n-type Bi_2Te_3 discs prepared by ultrasound milling (2 h, 100 % amplitude and 2 coolers) using different solvents.

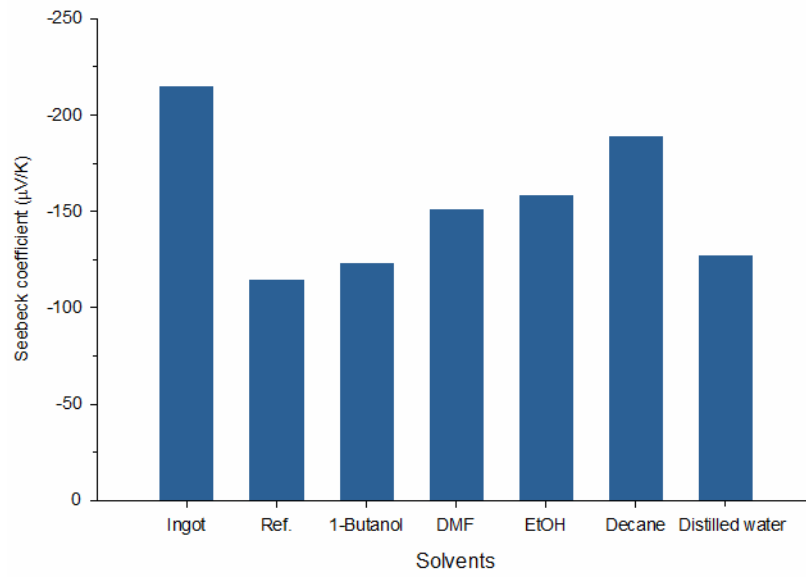


Fig. A.15. Seebeck coefficient results of the n-type Bi_2Te_3 discs prepared by ultrasound milling (2 h, 100 % amplitude and 2 coolers) using different solvents.

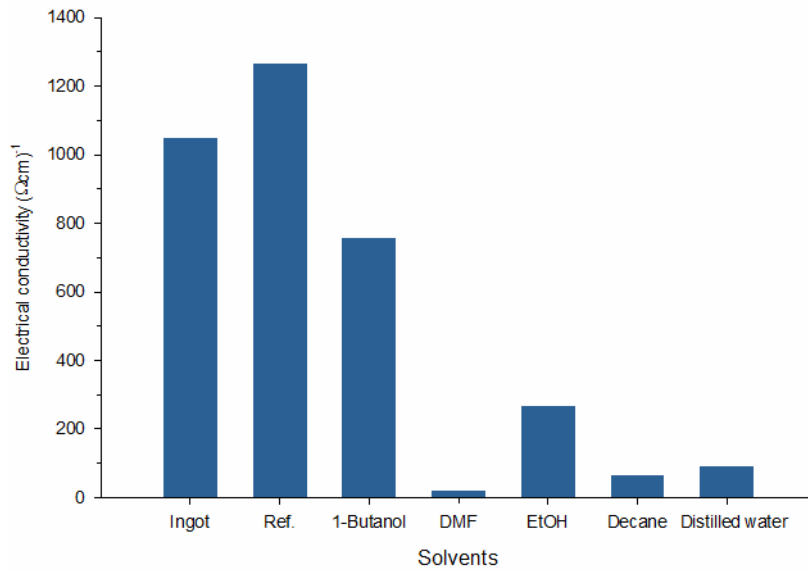


Fig. A.16. Electrical conductivity results of the n-type Bi_2Te_3 discs prepared by ultrasound milling (2 h, 100 % amplitude and 2 coolers) using different solvents.

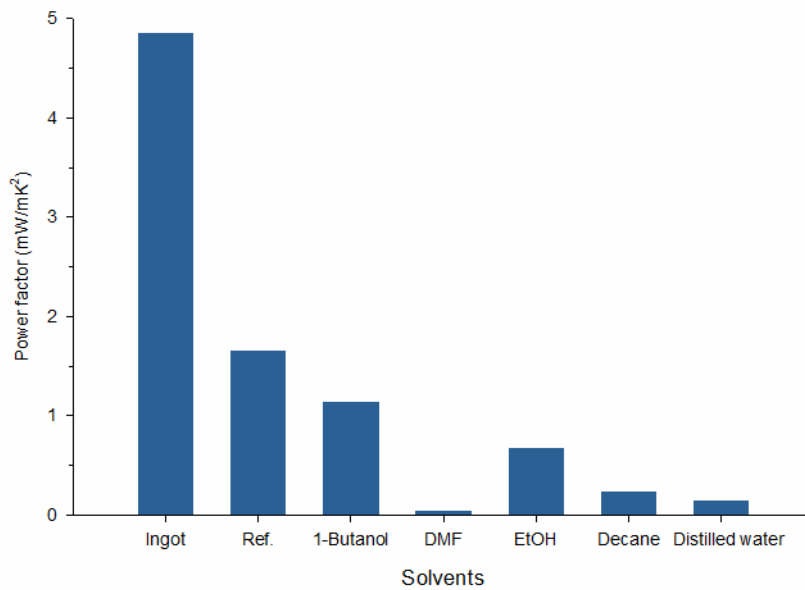


Fig. A.17. Power factor results of the n-type Bi₂Te₃ discs prepared by ultrasound milling (2 h, 100 % amplitude and 2 coolers) using different solvents.

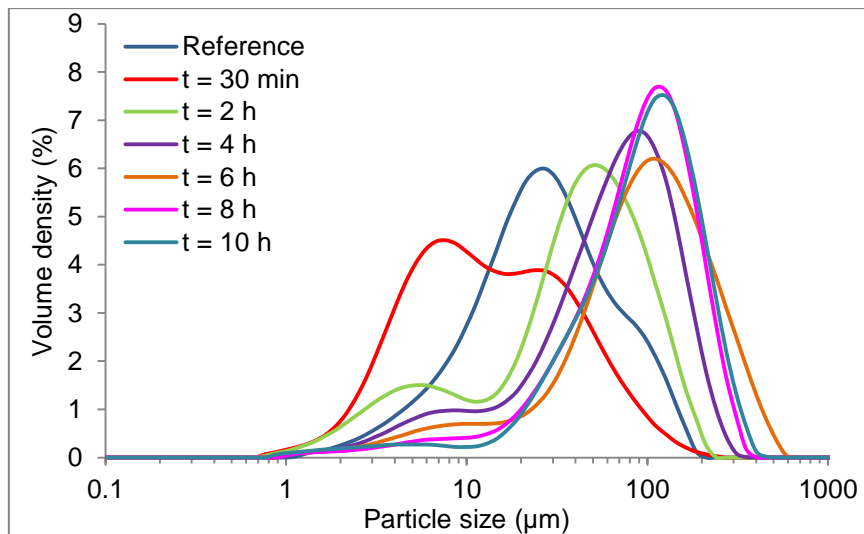


Fig. A.18. Particle size distribution in volume density of n-type Bi₂Te₃ powder after ultrasound milling treatment performed without PG additive at 100 % amplitude, 2 coolers and at different times.

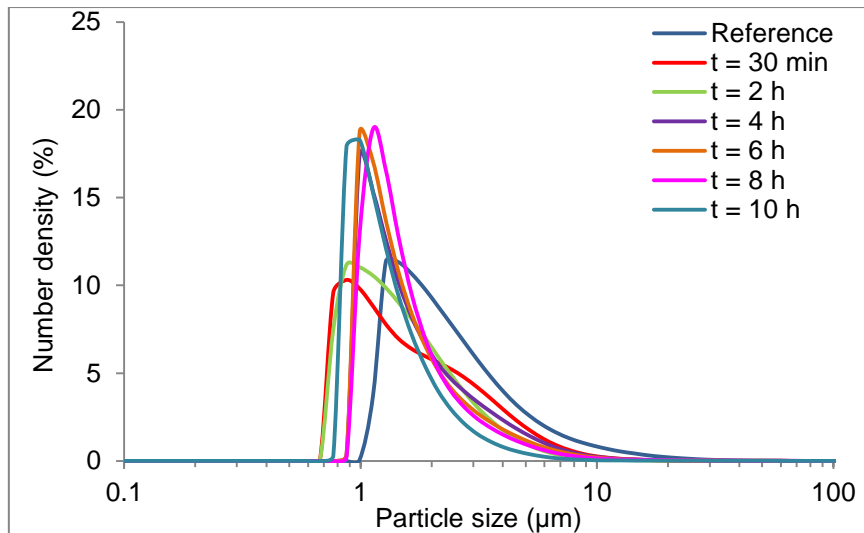


Fig. A.19. Particle size distribution in number density of n-type Bi_2Te_3 powder after ultrasound milling treatment performed without PG additive at 100 % amplitude, 2 coolers and at different times.

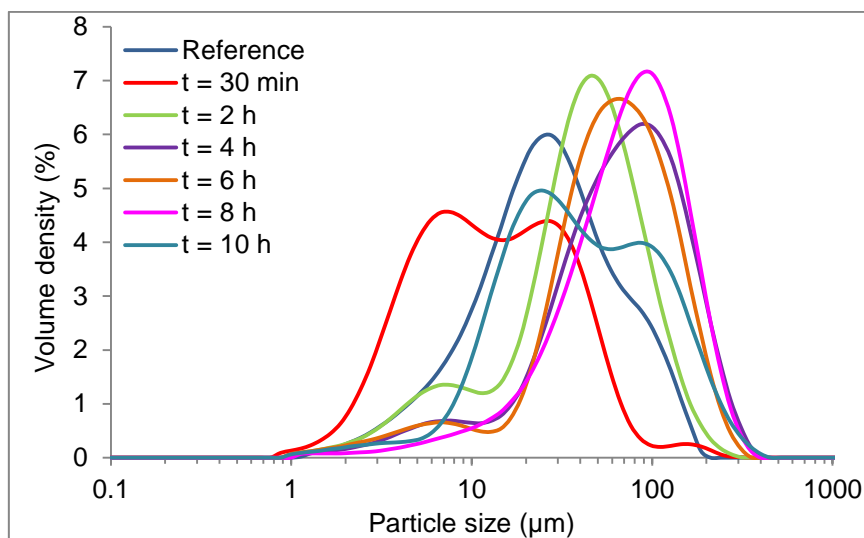


Fig. A.20. Particle size distribution in volume density of n-type Bi_2Te_3 after ultrasound milling performed at 100 % amplitude, 2 coolers, 1 % of additive PG and at different times.

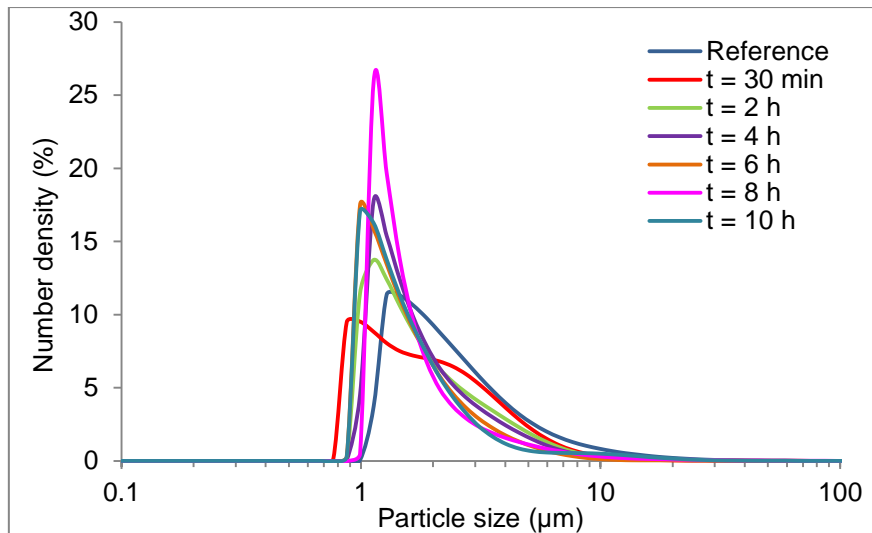


Fig. A.21. Particle size distribution in number density of n-type Bi₂Te₃ powder after ultrasound milling experiments performed at 100 % amplitude, 2 coolers, 1 % of PG additive and at different times.

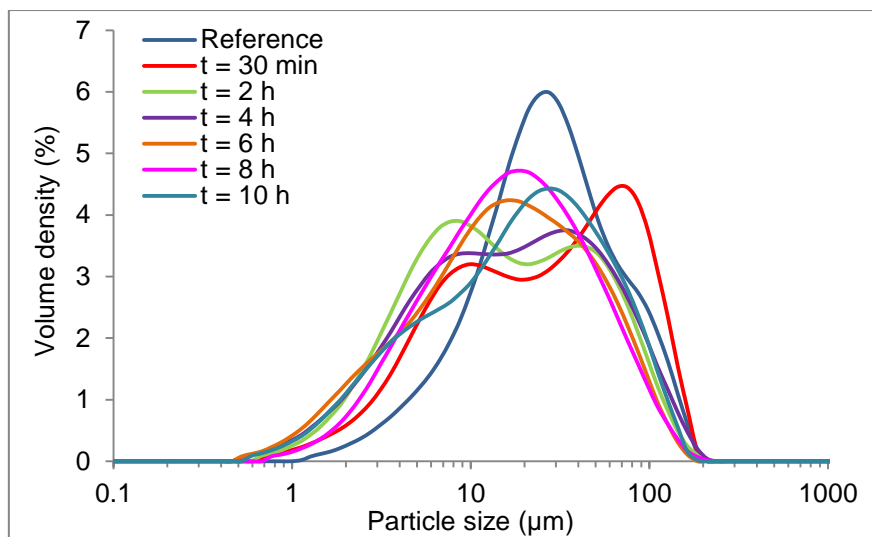


Fig. A.22. Particle size distribution in volume density of n-type Bi₂Te₃ after ultrasound milling performed at 60 % amplitude, 2 coolers and at different times.

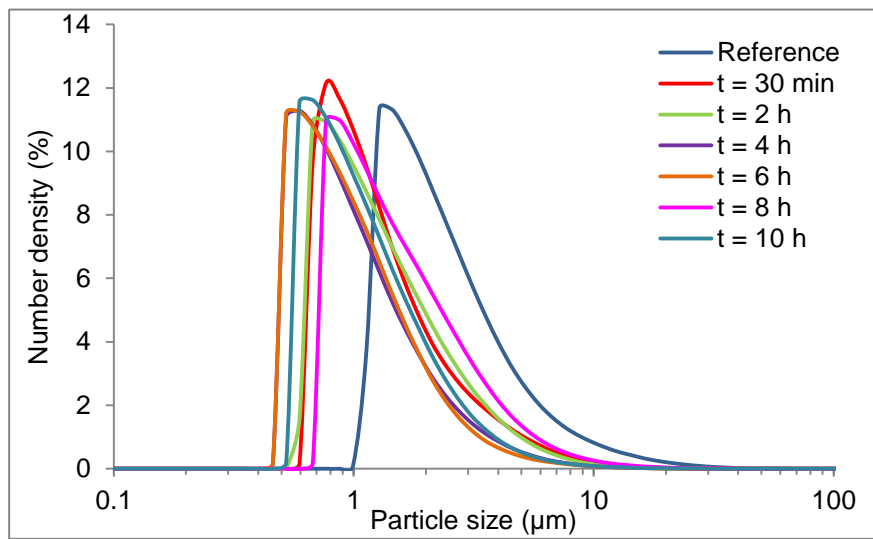


Fig. A.23. Particle size distribution in number density of n-type Bi₂Te₃ after ultrasound milling experiments performed at 60 % amplitude, 2 coolers and at different times.

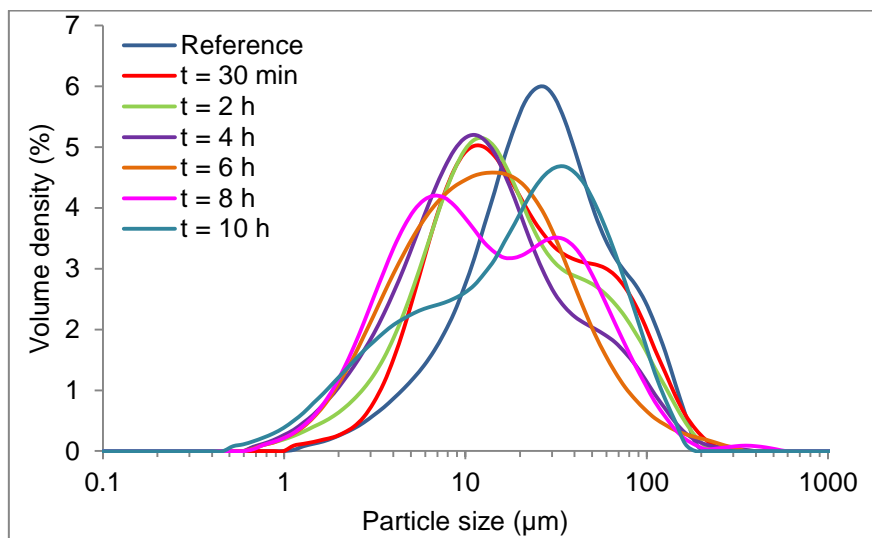


Fig. A.24. Particle size distribution in volume density of n-type Bi₂Te₃ after ultrasound milling performed at 60 % of amplitude, 1 cooler and at different times.

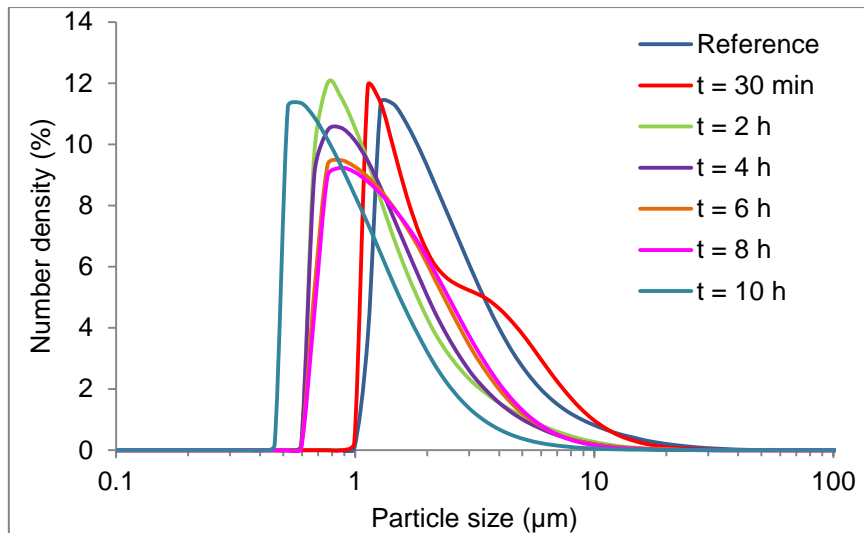


Fig. A.25. Particle size distribution in number density of n-type Bi_2Te_3 after ultrasound milling performed at 60 % amplitude, 1 cooler and at different times.

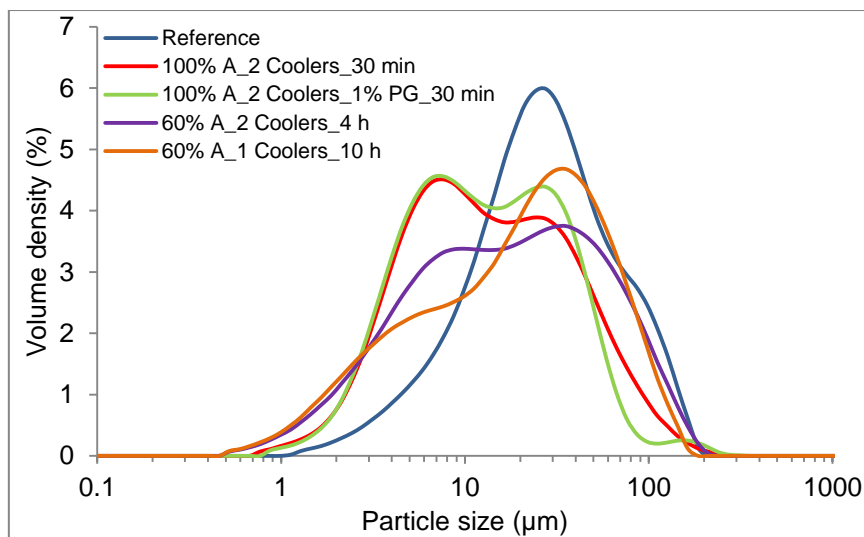


Fig. A.26. Particle size distribution in volume density of n-type Bi_2Te_3 powder after ultrasound milling experiments which produce the smallest particle size under different conditions.

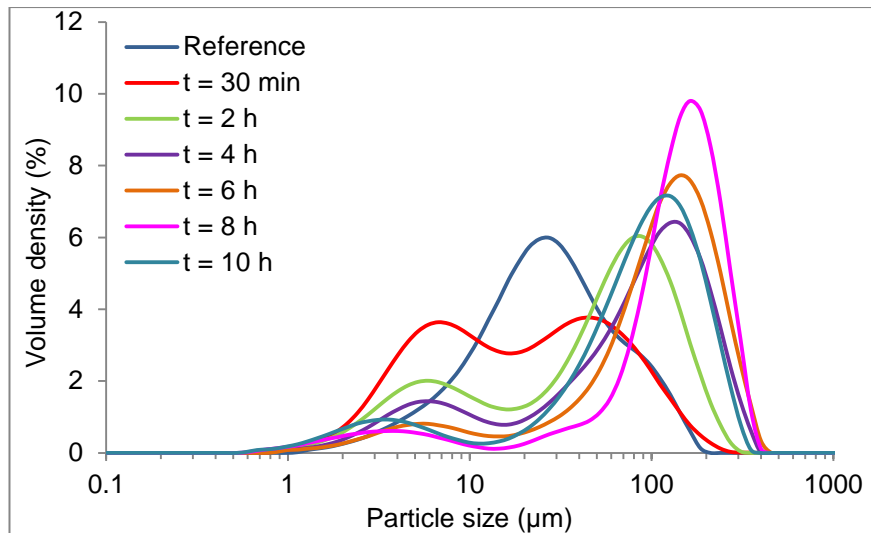


Fig. A.27. Particle size distribution in volume density of n-type Bi_2Te_3 after ultrasound milling experiments performed at 100 % amplitude, 2 coolers, double powder concentration (0.0166 M) and at different times.

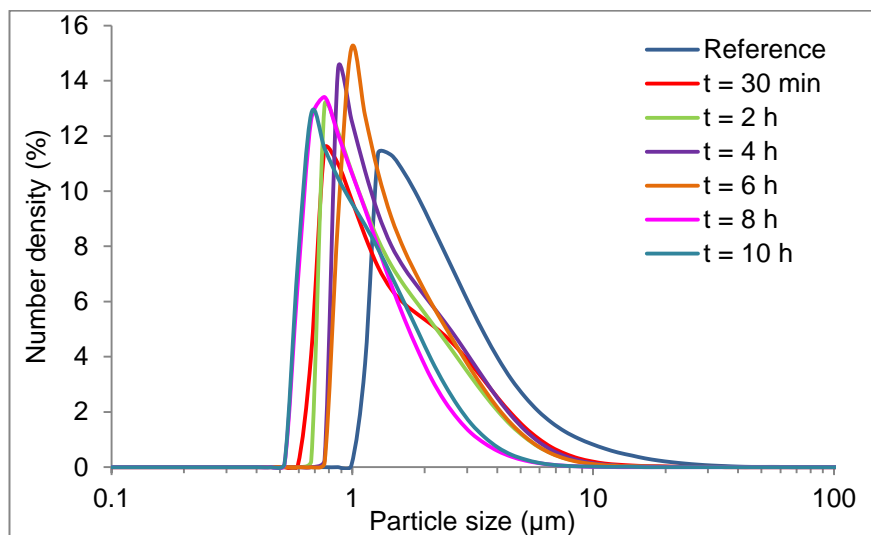


Fig. A.28. Particle size distribution in number density of n-type Bi_2Te_3 after ultrasound milling experiments performed at 100 % amplitude, 2 coolers, double powder concentration (0.0166 M) and at different times.

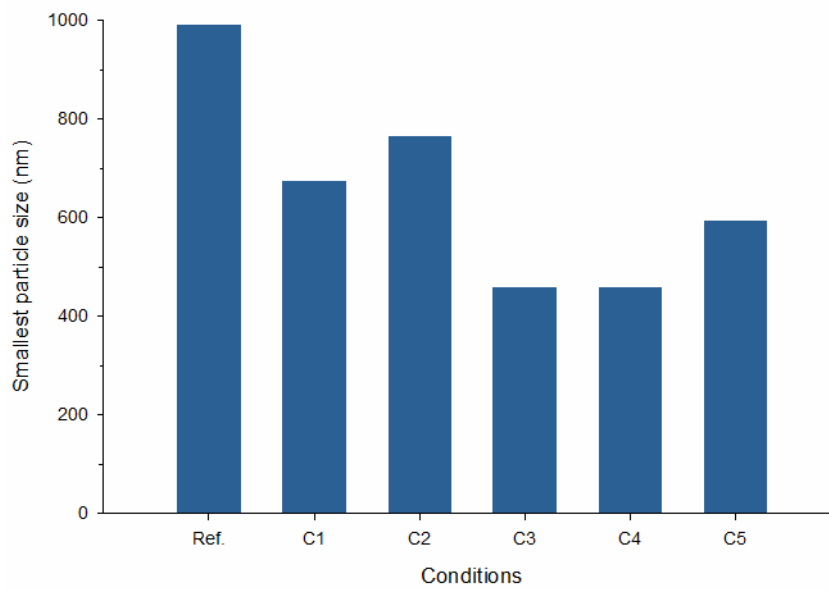


Fig. A.29. Representation of the smallest particle size achieved for n-type Bi₂Te₃ after ultrasound millings which the smallest particle size is achieved for every different variable changed.

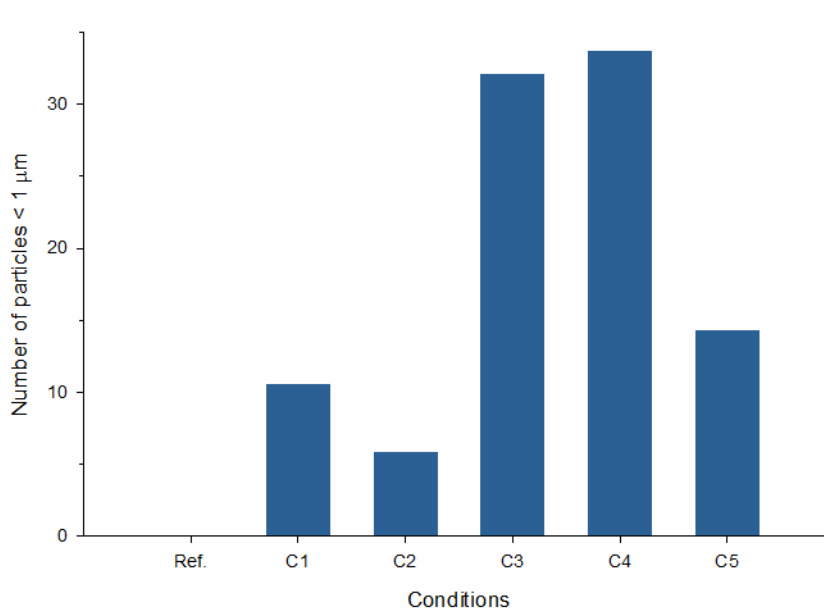


Fig. A.30. Representation of the number of particles smaller than 1 μm achieved for n-type Bi₂Te₃ after ultrasound millings which the smallest particle size is achieved for every different variable changed.

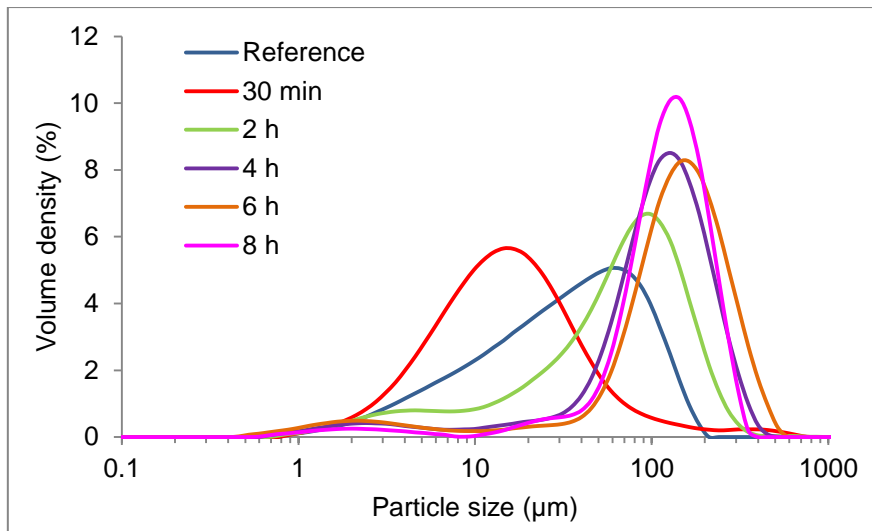


Fig. A.31. Particle size distribution in volume density of p-type Bi_2Te_3 after ultrasound milling experiments performed at 100 % amplitude, 2 coolers and at different times without PG additive.

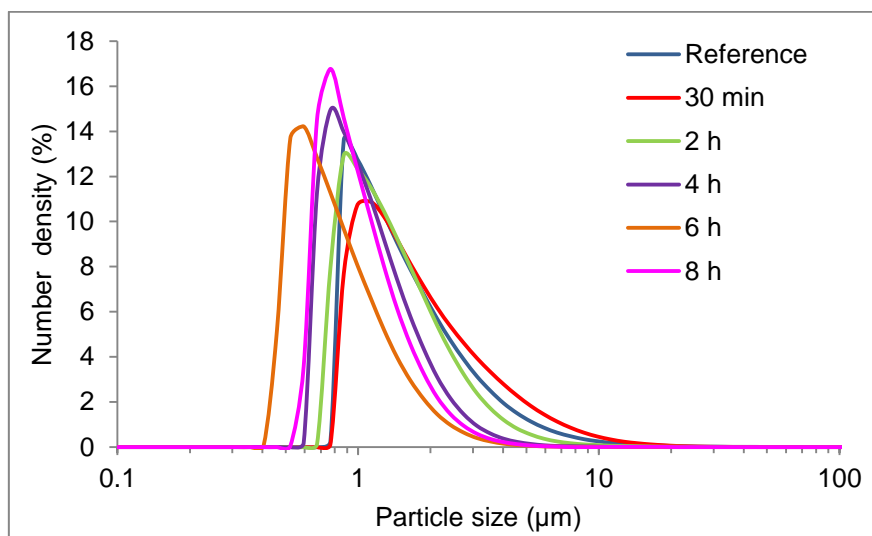


Fig. A.32. Particle size distribution in number density of p-type Bi_2Te_3 after ultrasound milling experiments performed at 100 % amplitude, 2 coolers and at different times without PG additive.

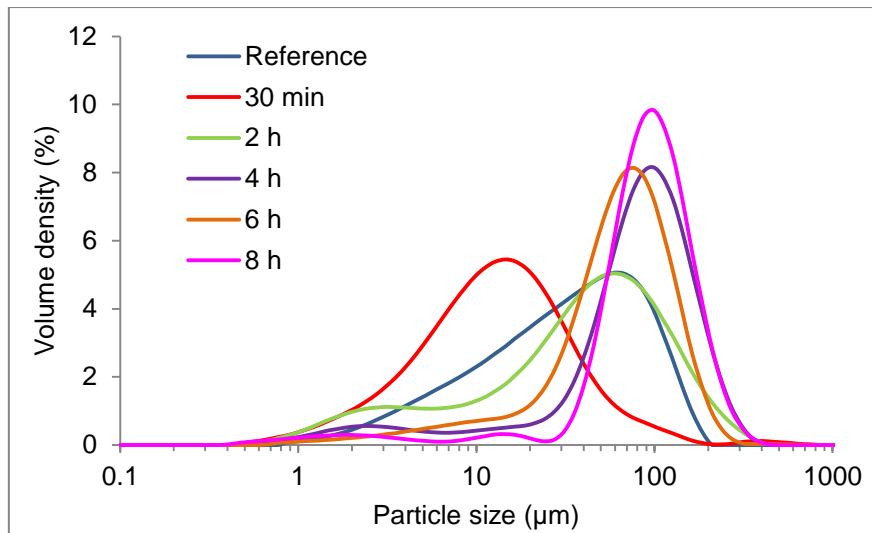


Fig. A.33. Particle size distribution in volume density of p-type Bi₂Te₃ after ultrasound milling experiments performed at 100 % amplitude, 2 coolers, 1% of additive (PG) and at different times.

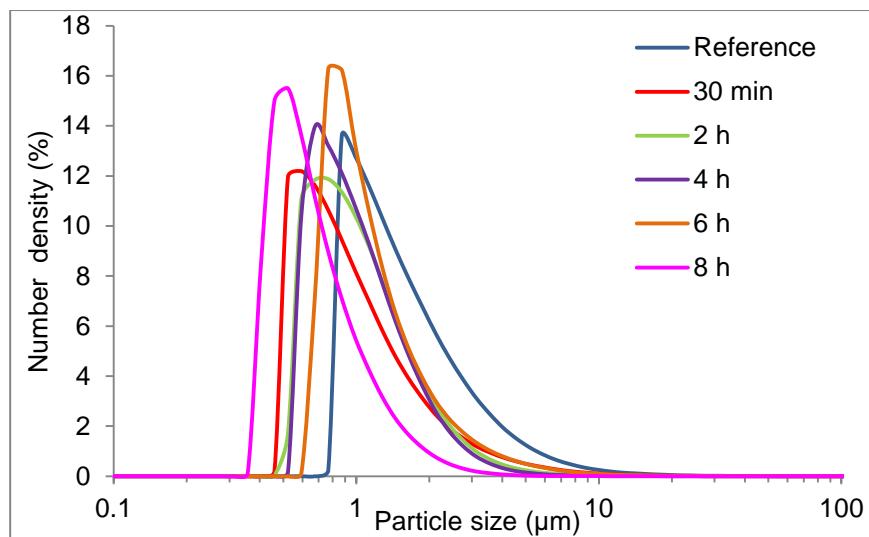


Fig. A.34. Particle size distribution in number density of p-type Bi₂Te₃ after ultrasound milling experiments performed at 100 % amplitude, 2 coolers, 1% of additive (PG) and at different times.

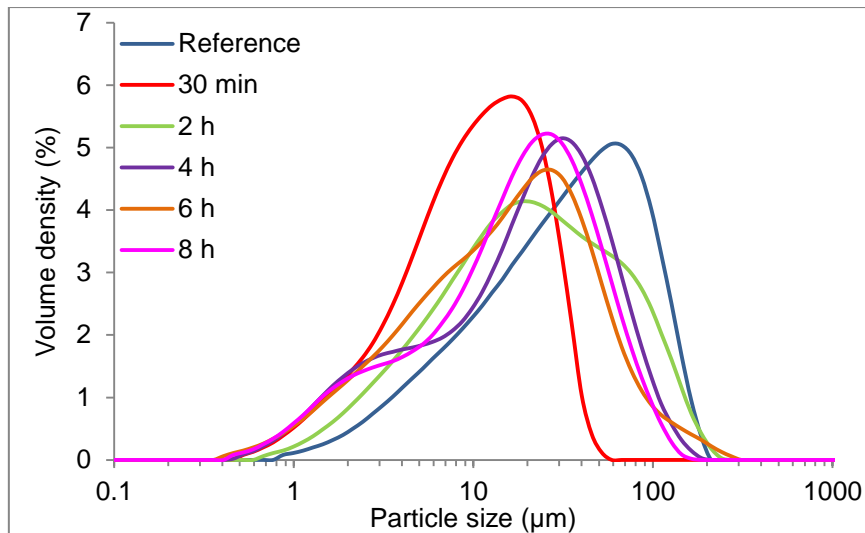


Fig. A.35. Particle size distribution in volume density of p-type Bi_2Te_3 after ultrasound milling experiments performed at 60 % amplitude, 2 coolers and at different times.

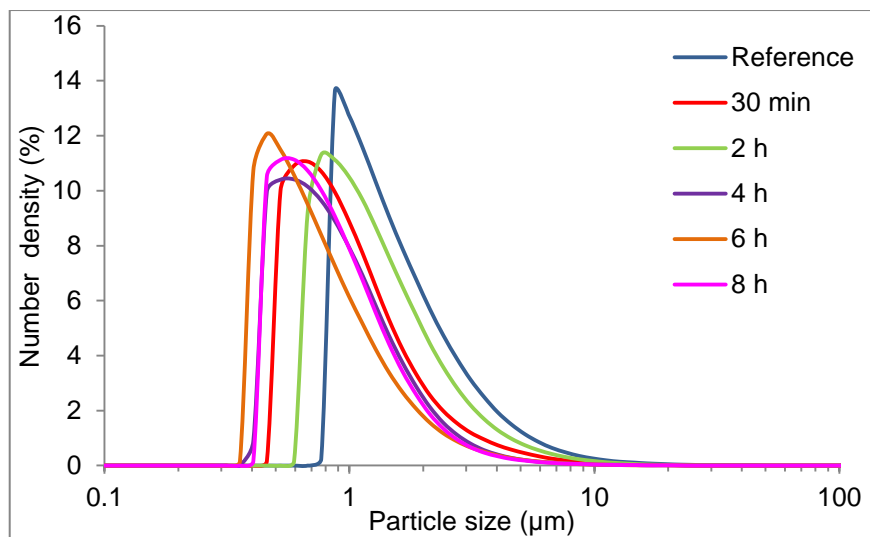


Fig. A.36. Particle size distribution in number density of p-type Bi_2Te_3 after ultrasound milling experiments performed at 60 % amplitude, 2 coolers and at different times.

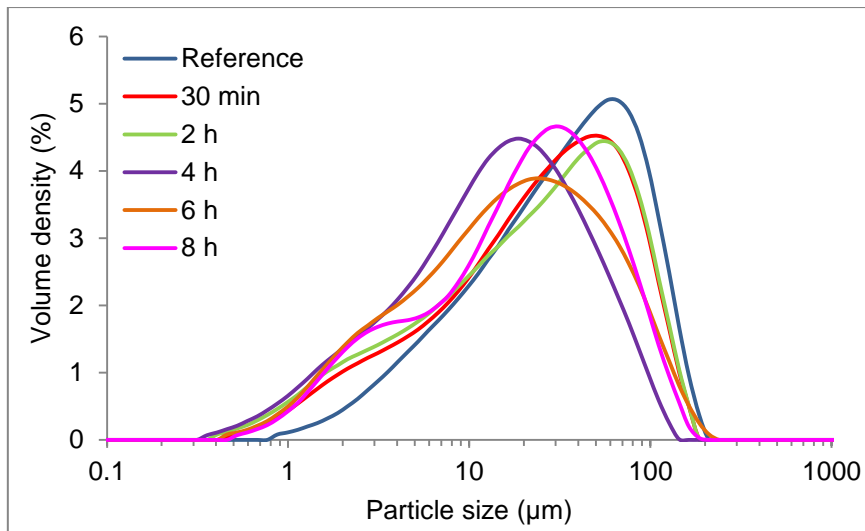


Fig. A.37. Particle size distribution in volume density of p-type Bi₂Te₃ after ultrasound milling experiments performed at 60 % amplitude, 1 cooler and at different times.

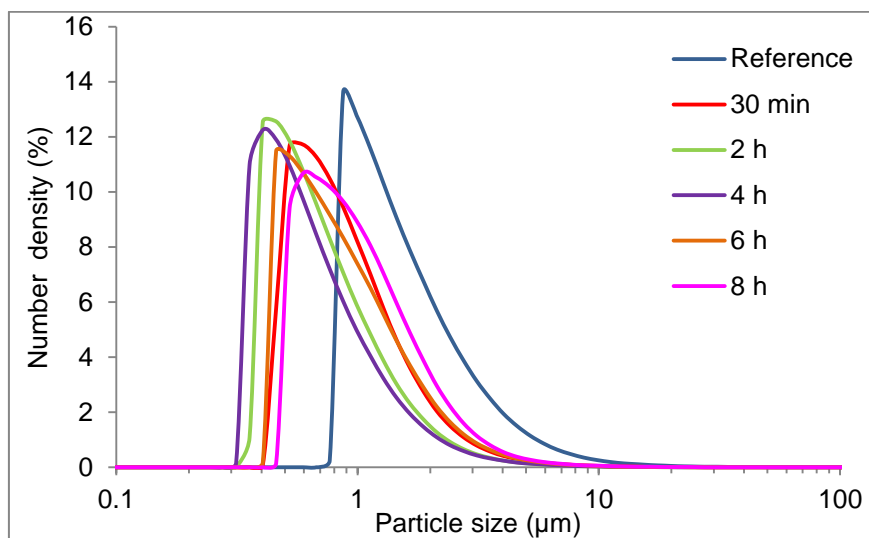


Fig. A.38. Particle size distribution in number density of p-type Bi₂Te₃ after ultrasound milling experiments performed at 60 % amplitude, 1 cooler and at different times.

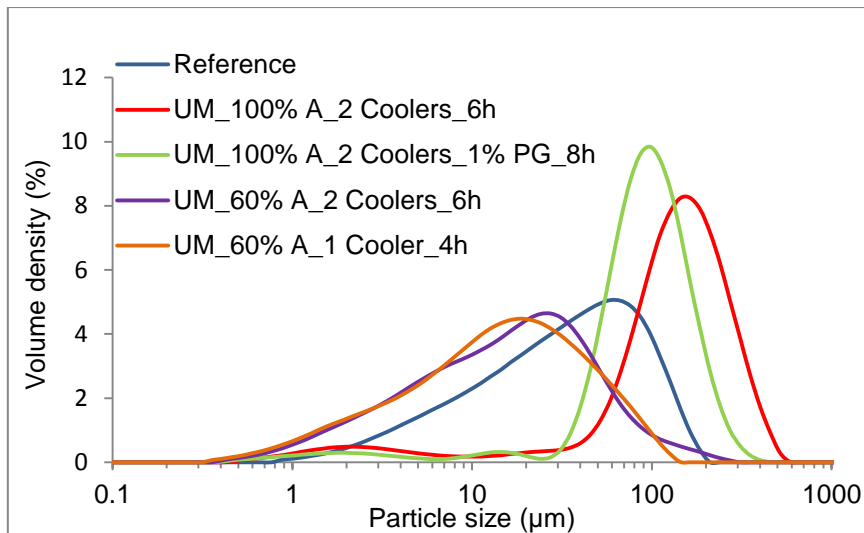


Fig. A.39. Particle size distribution in volume density of p-type Bi_2Te_3 after ultrasound millings experiments of optimum conditions.

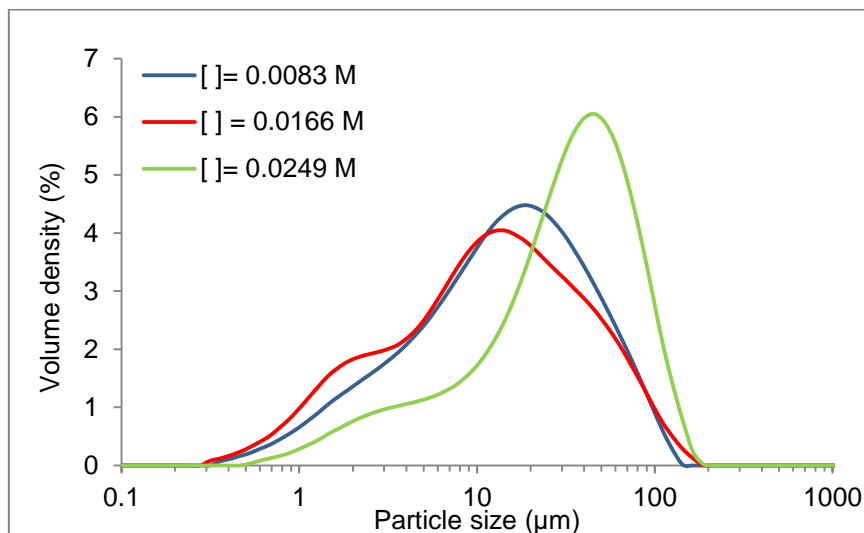


Fig. A.40. Particle size distribution in volume density of p-type Bi_2Te_3 after ultrasound milling experiments performed at 60% amplitude, 1 cooler, 4 h and at different concentrations.

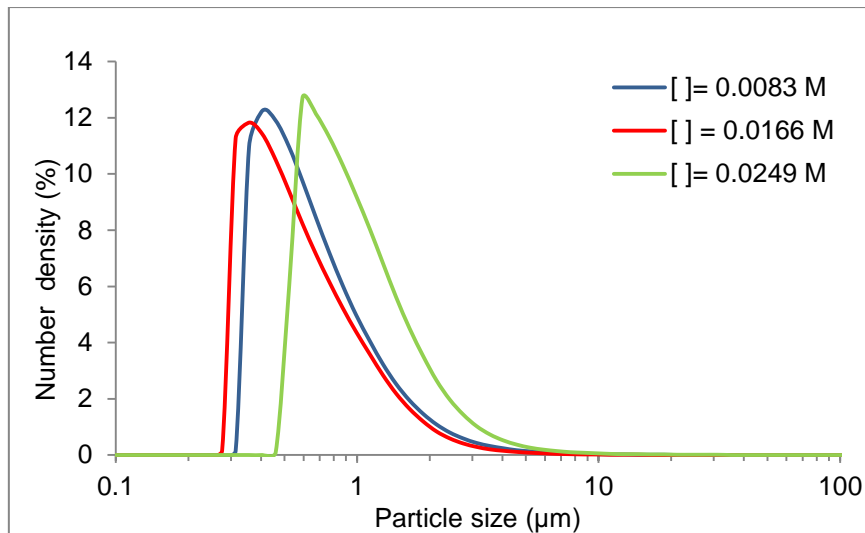


Fig. A.41. Particle size distribution in number density of p-type Bi_2Te_3 after ultrasound milling experiments performed at 60 % amplitude, 1 cooler, 4 h and at different concentrations.

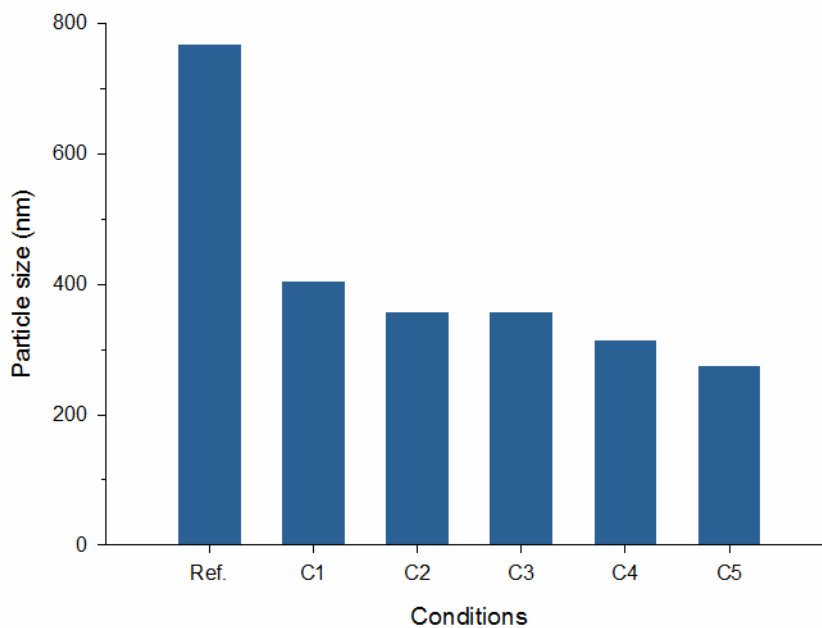


Fig. A.42. Representation of the smallest particle size achieved for p-type Bi_2Te_3 after ultrasound millings which the smallest particle size is achieved for every different variable changed.

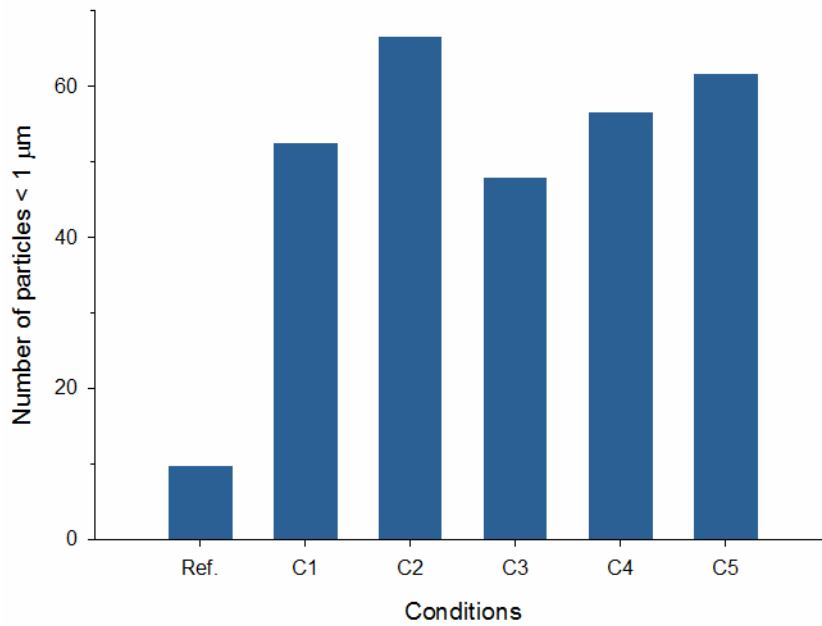


Fig. A.43. Representation of the number of particles smaller than 1 μm achieved for p-type Bi₂Te₃ after ultrasound millings which the smallest particle size is achieved for every different variable changed.

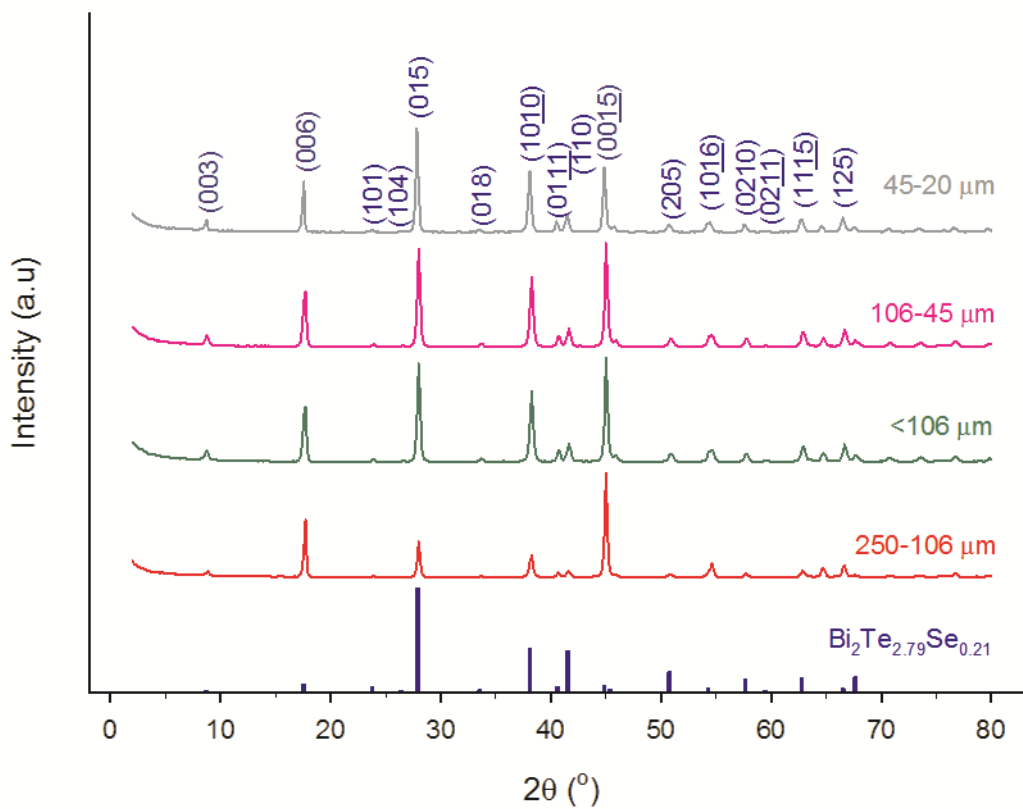


Fig. A.44. Theoretical XRD pattern of non-treated n-type Bi₂Te_{2.79}Se_{0.21} (blue), particle size 250-106 μm (red), particle size <106 μm (green), particle size 106-45 μm (pink) and particle size 45-20 μm (grey) powder.

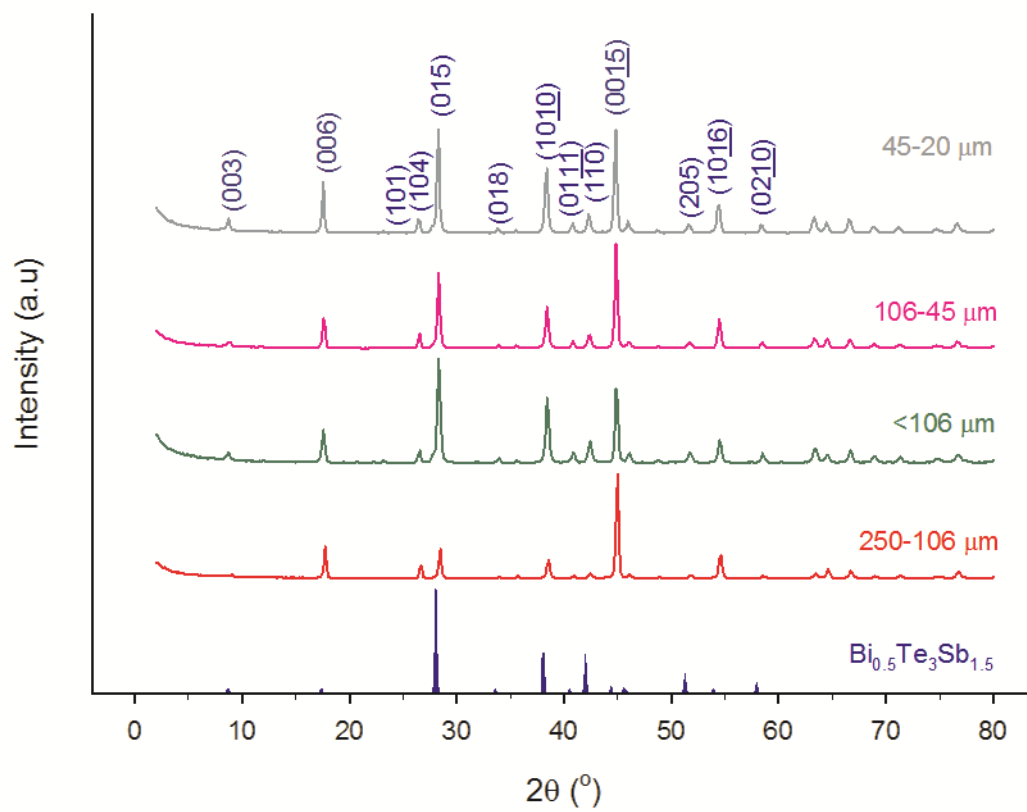


Fig. A.45. Theoretical XRD pattern of non-treated p-type $\text{Bi}_{0.5}\text{Te}_3\text{Se}_{1.5}$ (blue), particle size 250-106 μm (red), particle size <106 μm (green), particle size 106-45 μm (pink) and particle size 45-20 μm (grey) powder.

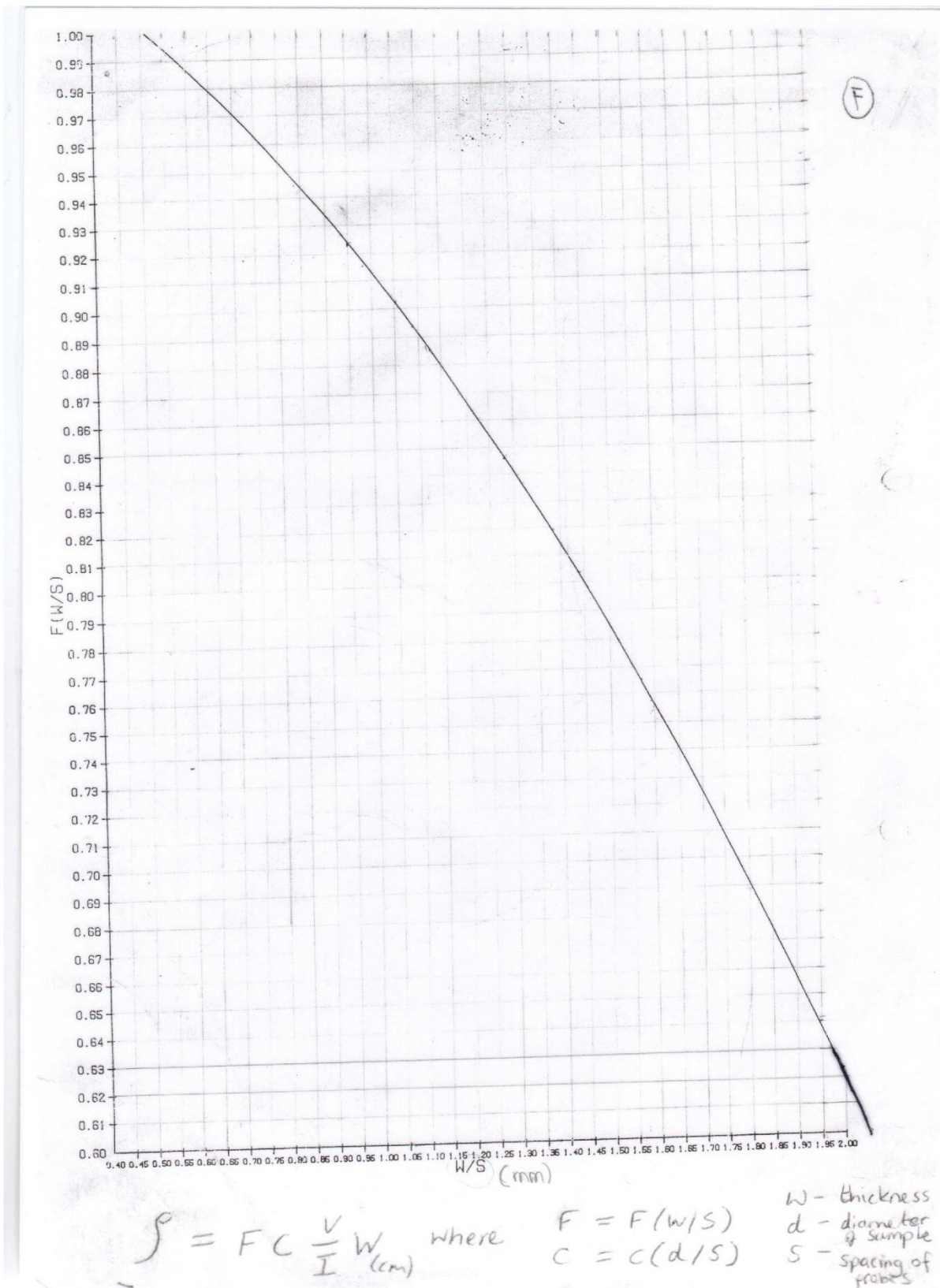


Fig. A.46. F value corrections to calculate the electrical conductivity measured by 4-probe technique.

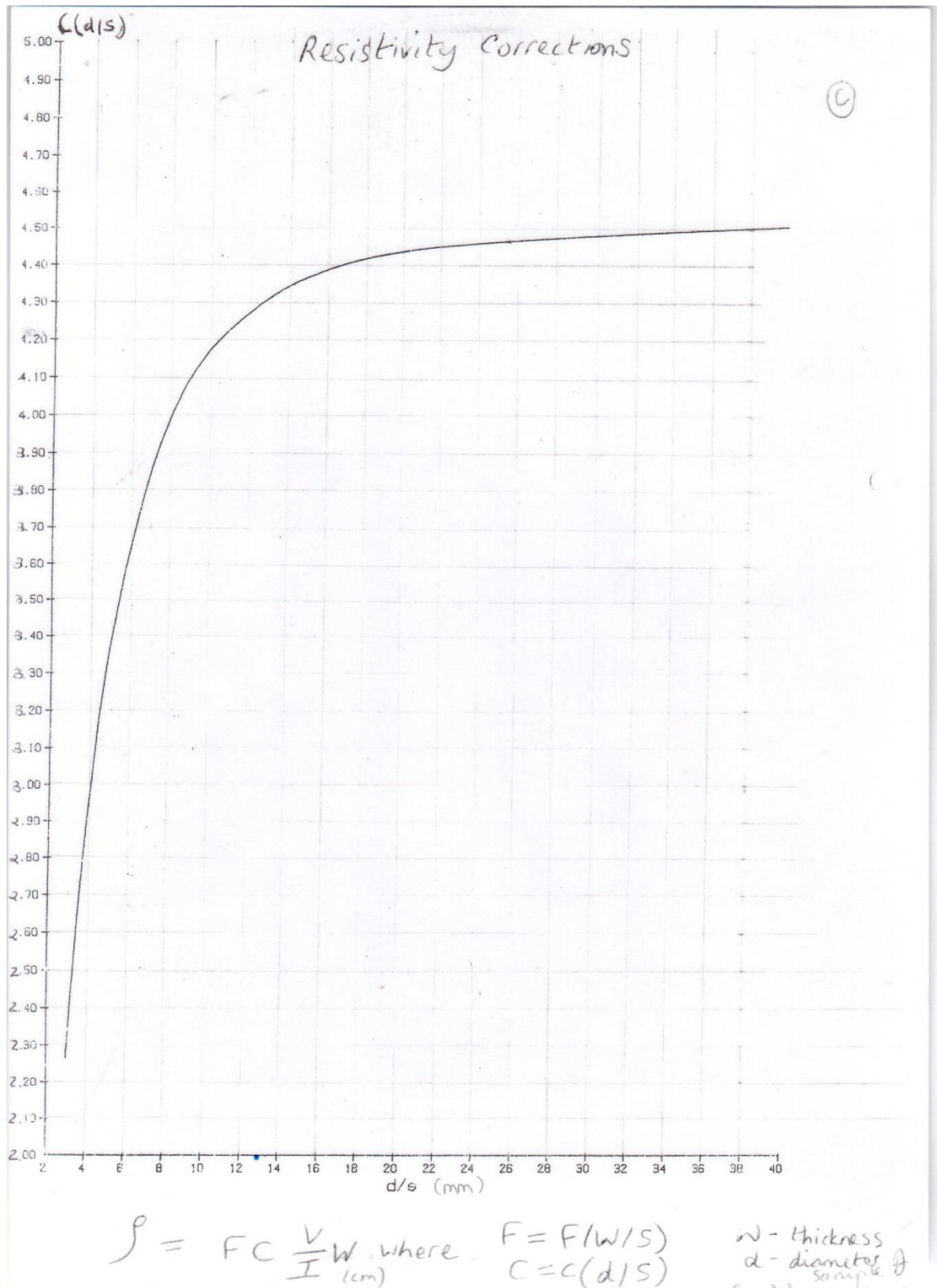


Fig. A.47. C value corrections to calculate the electrical conductivity measured by 4-probe technique.

